








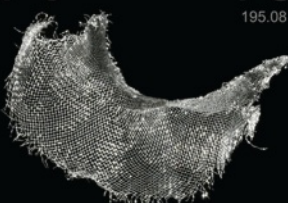

# Конденсированные среды и межфазные границы

РЕЦЕНЗИРУЕМЫЙ НАУЧНЫЙ ЖУРНАЛ

# Condensed Matter and Interphases

PEER-REVIEWED SCIENTIFIC JOURNAL

Том  
Vol. 27, № 2  
2025

<div>Co2758.933</div> <div></div> <div>Cobalt</div>	<div>Ni2858.693</div> <div></div> <div>Nickel</div>	<div>Cu2963.546</div> <div></div> <div>Copper</div>
<div>Rh45102.91</div> <div></div> <div>Rhodium</div>	<div>Pd46106.42</div> <div></div> <div>Palladium</div>	<div>Ag47107.87</div> <div></div> <div>Silver</div>
<div>Ir77192.22</div> <div></div> <div>Iridium</div>	<div>Pt78195.08</div> <div></div> <div>Platinum</div>	<div>Au79196.97</div> <div></div> <div>Gold</div>



# Condensed Matter and Interphases

## Kondensirovannyye sredy i mezhfaznyye granitsy

Peer-reviewed scientific journal

Published since January 1999

Periodicity: Quarterly

Volume 27, No. 2, 2025

Full-text version is available in the Russian language on the website: <https://journals.vsu.ru/kcmf>

**Condensed Matter and Interphases** (Kondensirovannyye Sredy i Mezhfaznyye Granitsy) publishes articles in Russian and English dedicated to key issues of condensed matter and physicochemical processes at interfaces and in volumes.

**The mission of the journal** is to provide open access to the results of original research (theoretical and experimental) at the intersection of contemporary condensed matter physics and chemistry, material science and nanoindustry, solid state chemistry, inorganic chemistry, and physical chemistry, and to share scientific data in the **following sections**: atomic, electron, and cluster structure of solids, liquids, and interphase boundaries; phase equilibria and defect formation processes; structure and physical and chemical properties of interphases; laser thermochemistry and photostimulated processes on solid surfaces; physics and chemistry of surface, thin films and heterostructures; kinetics and mechanism of formation of film structures; electrophysical processes in interphase boundaries; chemistry of surface phenomena in sorbents; devices and new research methods.

**The journal accepts for publication:** reviews, original articles, short communications by leading Russian scientists, foreign researchers, lecturers, postgraduate and undergraduate students.

### FOUNDER AND PUBLISHER:

Voronezh State University

The journal is registered by the Russian Federal Service for Supervision of Communications, Information Technology and Mass Media, Certificate of Registration ПИ № ФС77-78771 date 20.07.2020

The journal is included in the List of peer reviewed scientific journals published by the Higher Attestation Commission in which major research results from the dissertations of Candidates of Sciences (PhD) and Doctor of Science (DSc) degrees are to be published. Scientific specialties of dissertations and their respective branches of science are as follows: 1.4.1. – Inorganic Chemistry (Chemical sciences); 1.4.4. – Physical Chemistry (Chemical sciences); 1.4.6. – Electrochemistry (Chemical sciences); 1.4.15. – Solid State Chemistry (Chemical sciences); 1.3.8. – Condensed Matter Physics (Physical sciences).

The journal is indexed and archived in: Russian Scientific Index Citations, Scopus, Chemical Abstract, EBSCO, DOAJ, CrossRef

Editorial Board and Publisher Office:  
1 Universitetskaya pl., Voronezh 394018  
Phone: +7 (432) 2208445  
<https://journals.vsu.ru/kcmf>  
E-mail: [kcmf@main.vsu.ru](mailto:kcmf@main.vsu.ru)

When reprinting the materials, a reference to the Condensed Matter and Interphases must be cited

The journal's materials are available under the Creative Commons "Attribution" 4.0 Global License



© Voronezh State University, 2025

### EDITOR-IN-CHIEF:

**Victor N. Semenov**, Dr. Sci. (Chem.), Full Professor, Voronezh State University (Voronezh, Russian Federation)

### VICE EDITORS-IN-CHIEF:

**Evelina P. Domashevskaya**, Dr. Sci. (Phys.–Math.), Full Professor, Voronezh State University (Voronezh, Russian Federation)

**Polina M. Volovitch**, Ph.D. (Chem.), Associate Professor, Institut de Recherche de Chimie (Paris, France)

### EDITORIAL BOARD:

**Nikolay N. Afonin**, Dr. Sci. (Chem.), Voronezh State Pedagogical University (Voronezh, Russian Federation)

**Vera I. Vasil'eva**, Dr. Sci. (Chem.), Full Professor, Voronezh State University (Voronezh, Russian Federation)

**Aleksandr V. Vvedenskii**, Dr. Sci. (Chem.), Full Professor, Voronezh State University (Voronezh, Russian Federation)

**Victor V. Gusarov**, Dr. Sci. (Chem.), Associate Member of the RAS, Ioffe Physical-Technical Institute RAS (St. Petersburg, Russian Federation)

**Vladimir E. Guterman**, Dr. Sci. (Chem.), Full Professor, Southern Federal University (Rostov-on-Don, Russian Federation)

**Boris M. Darinskii**, Dr. Sci. (Phys.–Math.), Full Professor, Voronezh State University (Voronezh, Russian Federation)

**Vladimir P. Zlomanov**, Dr. Sci. (Chem.), Full Professor, Moscow State University (Moscow, Russian Federation)

**Valentin M. Levlev**, Dr. Sci. (Phys.–Math.), Full Member of the RAS, Moscow State University (Moscow, Russian Federation)

**Oleg A. Kozaderov**, Dr. Sci. (Chem.), Associate Professor, Voronezh State University (Voronezh, Russian Federation)

**Andrey I. Marshakov**, Dr. Sci. (Chem.), Full Professor, Frumkin Institute of Physical Chemistry and Electrochemistry RAS (Moscow, Russian Federation)

**Irina Ya. Mittova**, Dr. Sci. (Chem.), Full Professor, Voronezh State University (Voronezh, Russian Federation)

**Victor V. Nikonenko**, Dr. Sci. (Chem.), Full Professor, Kuban State University (Krasnodar, Russian Federation)

**Oleg V. Ovchinnikov**, Dr. Sci. (Phys.–Math.), Full Professor, Voronezh State University (Voronezh, Russian Federation)

**Sergey N. Saltykov**, Dr. Sci. (Chem.), Associate Professor, Novolipetsk Steel (Lipetsk, Russian Federation)

**Vladimir F. Selemenev**, Dr. Sci. (Chem.), Full Professor, Voronezh State University (Voronezh, Russian Federation)

**Pavel V. Seredin**, Dr. Sci. (Phys.–Math.), Associate Professor, Voronezh State University (Voronezh, Russian Federation)

**Evgeny A. Tutov**, Dr. Sci. (Chem.), Associate Professor, Voronezh State Technical University (Voronezh, Russian Federation)

**Vitaly A. Khonik**, Dr. Sci. (Phys.–Math.), Full Professor, Voronezh State Pedagogical University (Voronezh, Russian Federation)

**Andrey B. Yaroslavl'tsev**, Dr. Sci. (Chem.), Full Member of the RAS, Kurnakov Institute of General and Inorganic Chemistry RAS (Moscow, Russian Federation)

### INTERNATIONAL MEMBERS OF THE EDITORIAL BOARD:

**Mahammad Babanly**, Dr. Sci. (Chem.), Associate Member of the ANAS, Institute of Catalysis and Inorganic Chemistry ANAS (Baku, Azerbaijan)

**Tiziano Bellezze**, Dr. Sci. (Chem.), Marche Polytechnic University (Ancona, Italy)

**Mane Rahul Maruti**, Ph.D. (Chem.), Shivaji University (Kolhapur, India)

**Nguyen Anh Tien**, Ph.D. (Chem.), Associate Professor, University of Pedagogy (Ho Chi Minh City, Vietnam)

**Vladimir V. Pankov**, Dr. Sci. (Chem.), Full Professor, Belarusian State University (Minsk, Belarus)

**Fritz Scholz**, Dr. Sci., Professor, Institut für Biochemie Analytische Chemie und Umweltchemie (Greifswald, Germany)

**Mathias S. Wickleder**, Dr. Sci., Professor, University of Cologne (Köln, Germany)

**Vladimir Sivakov**, Dr. rer. nat., Leibniz Institute of Photonic Technology (Jena, Germany)

### EXECUTIVE SECRETARY:

**Vera A. Logacheva**, Cand. Sci. (Chem.), Voronezh State University (Voronezh, Russian Federation)

## CONTENTS

**Review***Bui C. D., Nalimova S. S., Nguyen V. T. A.*

Graphitic carbon nitride: properties and applications in gas sensing. Review

177

*Velmuzhov A. P., Sukhanov M. V., Tyurina E. A., Shiryayev V. S.*

Advanced methods for preparing especially pure glasses based on germanium and gallium chalcogenides. Part 2. Synthesis using chemical transport reactions. Review

190

**Original articles***Belonogov E. K., Kushev S. B., Serikov D. V., Soldatenko S. A., Turaeva T. L.*

On the mechanism of recrystallization of bismuth chalcogenides during photonic treatment with incoherent radiation

203

*Bordonskiy G. S., Kazantsev V. A., Kozlov A. K.*  
Investigation of the possibility of ice film 0 formation on the dielectric surface in a microwave resonator

211

*Kamorn D. M., Simagin A. S., Kazantsev O. A., Slivkin A. I., Zamyshlyayeva O. G., Emasheva A. A., Melnikova N. B.*

Self-assembly of cationic polymers in mixed polymer-lipid monolayers at the liquid-air interface

217

*Kareem R. O., Hamad O. A.*

The potential corrosion inhibition properties of acetyl benzoic acid derivatives with substituted alkali metals (Na, K, Li): DFT approach

226

*Kareem R. O.*

DFT analysis: correlation of epinephrine HOMO-LUMO, refractive index, optical electronegativity, and electrical conductivity with Substituted Halogens (F, Cl, Br)

237

*Kuzenko D. V.*

Influence of external influences on the activation of domain walls of ferroelectric perovskites

251

*Polkovnikova Y. A., Tulskeya U. A., Semyonov V. N., Slivkin A. I.*

Modeling of Desloratadine release process from alloys with Polyethylene glycol-6000 by Molecular dynamics method

260

*Proydakova V. Yu., Voronov V. V., Kuznetsov S. V., Nekrylov I. N., Zavrazhnov A. U., Fedorov P. P.*  
Phase diagram of the system  $\text{Na}_2\text{SO}_4 - \text{In}_2(\text{SO}_4)_3$ . Comparative analysis of  $\text{Na}_2\text{SO}_4 - \text{R}_2(\text{SO}_4)_3$  systems (R = Al, Ga, Fe, In, Sc, Yb)

267

*Pronin I. A., Komolov A. S., Lenshin A. S., Yakushova N. D., Karmanov A. A.*

Investigation of the transformation of the surface architecture of zinc oxide powders synthesized by grinding during etching with argon ions

278

*Prokhorov D. A., Rybin M. G., Zuev S. M.*

Analysis of anisotropic heat and thermal diffusivity of thermally expanded graphite

284

*Radaykin D. G., Moshnikov V. A.*

Structures for photocatalysis based on ZnO with Ag nanoparticles

293

*Rembeza E. S., Zaynobidinov S. Z., Rasulova M. B.*  
Structural and optical properties of Mg-doped ZnO films obtained by spray pyrolysis

302

*Seredin P. V., Kosheleva O. K., Goloshchapov D. L., Builov N. S., Peshkov Ya. A., Mizerov A. M., Timoshnev S. N., Sobolev M. S., Sharofidinov Sh. Sh.*  
Diffraction studies of the PA MBE grown of GaN layers on silicon substrates without their nitridation and an intermediate AlN nucleation layers

308

*Tyutyunik A. S., Gurchenko V. S., Mazinov A. S.*  
Effect of the re-emitting layer of organic thin film on the efficiency of silicon solar cells

316

**Short communication***Semyonov V. N., Volkov V. V., Samofalova T. V.*  
Complexation processes in aqueous solutions of lead acetate and thiourea

323

**Chronicle**Pavel Pavlovich FEDOROV  
(April 16, 1950 – March 31, 2025)

329



# Condensed Matter and Interphases

Kondensirovannye Sredy i Mezhfaznye Granitsy  
<https://journals.vsu.ru/kcmf/>

## Review

Review article

<https://doi.org/10.17308/kcmf.2025.27/12763>

## Graphitic carbon nitride: properties and applications in gas sensing. Review

C. D. Bui<sup>1✉</sup>, S. S. Nalimova<sup>1</sup>, V. T. A. Nguyen<sup>2</sup>

<sup>1</sup>Saint Petersburg Electrotechnical University «LETI»,  
5 ul. Professora Popova, Saint Petersburg 197022, Russia Federation

<sup>2</sup>Peter the Great St. Petersburg Polytechnic University,  
29 ul. Politehnicheskaya, Saint Petersburg 195251, Russia Federation

### Abstract

**Purpose:** Nowadays gas sensors are of great interest for disease detection and assessment of treatment efficacy based on exhaled breath analysis. One of the promising materials for gas sensors are composites of graphitic carbon nitride with metal oxides.

**Experimental:** The article considers the basic properties of g-C<sub>3</sub>N<sub>4</sub> and provides a review of methods that can be effective for obtaining its composites with metal oxides.

**Conclusions:** The study presents the mechanism of interaction of g-C<sub>3</sub>N<sub>4</sub> with gases of different nature. In addition, it gives some examples of sensors based on composites of g-C<sub>3</sub>N<sub>4</sub> with metal oxides.

**Keywords:** Graphitic carbon nitride, Gas sensing, Nanocomposites

**For citation:** Bui C. D., Nalimova S. S., Nguyen V. T. A. Graphite carbon nitride: properties and applications in gas sensing. Review. *Condensed Matter and Interphases*. 2025;27(2): 177–189. <https://doi.org/10.17308/kcmf.2025.27/12763>

**Для цитирования:** Буй К. Д., Налимова С. С., Нгуен В. Т. А. Графитоподобный нитрид углерода: свойства и применение в газовой сенсорике. Обзор. *Конденсированные среды и межфазные границы*. 2025;27(2): 177–189. <https://doi.org/10.17308/kcmf.2025.27/12763>

✉ Bui Cong Doan, e-mail: [congdoan6997@gmail.com](mailto:congdoan6997@gmail.com)

© Bui C. D., Nalimova S. S., Nguyen V. T. A., 2025



The content is available under Creative Commons Attribution 4.0 License.



## 1. Introduction

Gas sensors are widely used to detect low concentrations of flammable, explosive or toxic gases and to monitor environmental pollution. Generally, the main requirements for a gas-sensitive material are as follows: high sensitivity, fast performance and good selectivity. Development of inexpensive and reliable sensor devices for gas detection, especially at room temperature, is an important scientific and technological task. For its solution, sensors operating on the basis of various principles are used. In regard to this, semiconductor adsorption sensors are favorably characterized by simple construction, low cost and a wide choice of materials of the primary sensing element [1, 2]. The principle of their operation is based on the change in the resistance of the material when chemical reactions of interaction with oxidizing or reducing gases occur on its surface [3, 4]. The sensing material should be selected so that it has a large surface available for interaction with gas molecules, suitable active centers for their adsorption. The main advantage of semiconductor gas sensors is their high sensitivity, but their wide application is limited by low selectivity and high operating temperatures [5]. The problems of selectivity can be solved by using different sensitive materials and realizing multisensor systems [6], as well as thermomodulation mode [7, 8]. To reduce operating temperatures, heating is replaced by exposure to ultraviolet or visible light [9, 10]. Over the years, the gas-sensitive properties of *n*-type semiconductor oxides such as SnO<sub>2</sub> [11], ZnO [12], TiO<sub>2</sub> [13], Fe<sub>2</sub>O<sub>3</sub> [14] и WO<sub>3</sub> [15] have been widely studied. To a lesser extent, *p*-type oxides such as CuO [16], NiO [17] и Co<sub>3</sub>O<sub>4</sub> [18] have also been investigated. Studies on mixed metal oxides (perovskites [19] and cubic spinels, such as ferrites [20] and orthostannates [21]), have shown that they can have much higher response in some cases. In the last decade, two-dimensional (2D) materials [22] with nanoscale thickness and large surface-to-volume ratio have shown great promise for gas sensors. Efficient gas sensors can be obtained by combining the advantages of different groups of materials and creating composites of metal oxides with 2D materials [23, 24].

Nanomaterials based on graphitic carbon nitride (g-C<sub>3</sub>N<sub>4</sub>) have found wide applications in various types of catalysis due to their low density, high chemical stability, tunable morphology and low consumption [25]. The g-C<sub>3</sub>N<sub>4</sub> has a hierarchical structure and consists of an aromatic plane and a  $\pi$ -conjugated s-triazine unit composed of hybridized multiple sp, sp<sup>2</sup> and sp<sup>3</sup> carbon and nitrogen atoms [26].

These materials are usually fabricated by thermal condensation of nitrogen-containing precursors such as melamine, dicyandiamide and urea [27, 28]. The morphology of g-C<sub>3</sub>N<sub>4</sub> can be easily controlled, which allows increasing the specific surface area and the number of adsorption centers for reactions with target gases.

Based on the mechanism of gas sensitivity, the large specific surface area and a larger number of adsorption centers in g-C<sub>3</sub>N<sub>4</sub> allow more gas molecules to participate in reactions with target gases. In addition, simple and inexpensive methods of obtaining g-C<sub>3</sub>N<sub>4</sub> are advantages of its application in the field of gas sensing. Since the band gap of g-C<sub>3</sub>N<sub>4</sub> is 2.7 eV, the valence band electrons easily move to the conduction band when exposed to visible light, which leads to excellent catalytic activity and allows reducing the activation energy of the chemical reaction leading to a sensor response.

Nitrogen atoms give g-C<sub>3</sub>N<sub>4</sub> semiconducting properties and complexation ability, making it to some extent a more efficient catalyst than graphene. However, some drawbacks remain, limiting its further application in this field. The g-C<sub>3</sub>N<sub>4</sub> obtained by direct calcination of the precursor usually has a dense structure and low specific surface area [29]. The low charge carrier mobility and low electrical conductivity of pure g-C<sub>3</sub>N<sub>4</sub> result in long response time and poor fast performance [30]. Pure g-C<sub>3</sub>N<sub>4</sub> has low sensitivity, high operating temperature and low selectivity [31]. Creating composites of g-C<sub>3</sub>N<sub>4</sub> with metal oxides allows increasing the surface area, creating more surface active centers. The formation of a heterojunction between the material and g-C<sub>3</sub>N<sub>4</sub> can provide electron transfer. Thus, SnO<sub>2</sub>/g-C<sub>3</sub>N<sub>4</sub> composites show higher sensitivity and selectivity to ethanol compared to SnO<sub>2</sub> [32]. The g-C<sub>3</sub>N<sub>4</sub>/ZnO based sensor has been shown to have excellent performance for CH<sub>4</sub> detection [33].

The aim of this study is to analyze the properties of  $g\text{-C}_3\text{N}_4$ , review the main methods of obtaining its composites with metal oxides and the achieved results on their application in gas sensing.

## 2. The structure of $g\text{-C}_3\text{N}_4$

The strong covalent bonding between N and C atoms in the  $g\text{-C}_3\text{N}_4$  layer provides its high chemical and thermal stability [34]. Two-dimensional  $\pi$ -bonded polymer systems including triazine or tri-s-triazine (s-heptazine) blocks linked by tertiary amines make  $g\text{-C}_3\text{N}_4$  stable at room temperature (see Fig. 1) [35].

The individual layers are linked to each other by weak van der Waals forces. Under ambient conditions,  $g\text{-C}_3\text{N}_4$  is thermally and chemically stable, biocompatible, environmentally friendly and resistant to acidic and alkaline environments [36].

The  $g\text{-C}_3\text{N}_4$  obtained by thermal condensation of N-containing precursors has low crystallinity due to the appearance of defects connected with insufficient deamination during thermal condensation and the formation of heptazine-based melon. In melon, layers of one-dimensional chains of NH-linked melem monomers are connected by hydrogen bonds in a zigzag shape. As a result, the charge carriers generated by photon exposure are concentrated in certain regions, which reduces the conductivity [37].

## 3. The properties of $g\text{-C}_3\text{N}_4$

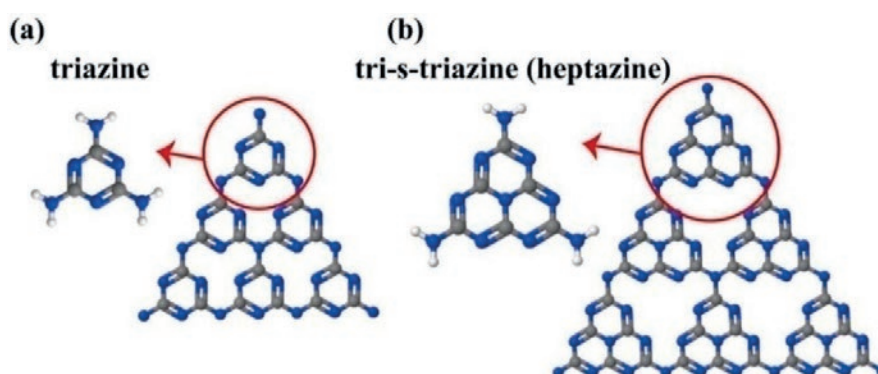
Graphitic carbon nitride ( $g\text{-C}_3\text{N}_4$ ) has recently attracted the interest of researchers due to its outstanding properties including low cost, large

surface area, abundance in nature, fast electron transfer,  $\pi$ - $\pi$  bond pairing, and absence of metals [38]. It is an excellent polymeric semiconductor operating in the visible region of the spectrum, with biocompatibility and excellent catalytic properties.

Pacha et al. synthesized bulk and thin film  $g\text{-C}_3\text{N}_4$  by thermal polycondensation of melamine [39]. X-ray photoelectron spectroscopy was used to determine the chemical composition of bulk and thin films of  $g\text{-C}_3\text{N}_4$ . Peaks corresponding to C 1s, N 1s, as well as a peak of O 1s of weak intensity, are observed in the spectra (see Fig. 2).

The paper shows the C-V characteristics of the ITO/ $g\text{-C}_3\text{N}_4$ /Al structure from -5 V to 5 V for a wide frequency range from 1 kHz to 1 MHz. At 1 kHz, the capacitance is 3.42 nF, and it decreases to 3.18 nF as the frequency increases up to 100 kHz. The decrease in capacitance at high frequencies can be explained by the low conductivity of  $g\text{-C}_3\text{N}_4$ . Moreover, the paper shows the frequency dependence of dielectric constant of  $g\text{-C}_3\text{N}_4$  thin film, the values of which are 8.05–7.17 in the frequency range from 100 Hz to 100 kHz.

Giusto et al. observed that  $g\text{-C}_3\text{N}_4$  film has a refractive index ( $n_D = 2.43$ ) which is the highest for polymeric materials [40]. The highly oriented and conjugated  $g\text{-C}_3\text{N}_4$  films exhibit intense blue photoluminescence (PL) under UV excitation. The PL spectra of  $g\text{-C}_3\text{N}_4$  films differ from those of powders due to the large number of allowed radiative transitions between different energy levels upon light excitation. When the film thickness is more than 1  $\mu\text{m}$ , the absorption spectra are similar to the absorption spectra of



**Fig. 1.** (a) Triazine and (b) tri-s-triazine (heptazine) two-dimensional network based on  $g\text{-C}_3\text{N}_4$  (white, gray, and blue balls denote H, C, and N, respectively) [35]



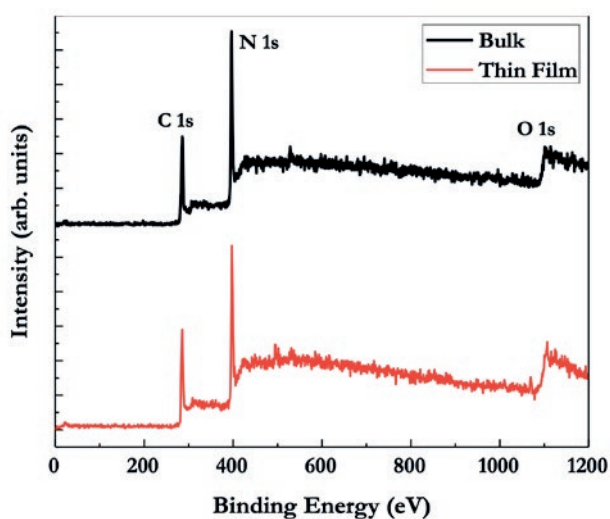


Fig. 2. X-ray photoelectron spectrum of bulk and thin-film  $g\text{-C}_3\text{N}_4$  [31]

bulk powder. The optical absorption edge shows the thickness dependence of absorption [41].

The absorption spectra of  $g\text{-C}_3\text{N}_4$  powders show that the absorption edge of the material is around  $\lambda = 450$  nm [42]. By contrast,  $g\text{-C}_3\text{N}_4$  films exhibit thickness dependent absorption spectra. A 55 nm thick  $g\text{-C}_3\text{N}_4$  film exhibits intense absorption bands at  $\lambda = 307$  nm and two additional bands at  $\lambda = 366$  and 386 nm; they are due to  $\pi\text{-}\pi^*$ ,  $\pi\text{-}\pi^*$  and LP- $\pi^*$  transitions, respectively, where  $\pi^*$  are the levels of excited  $\pi$ -orbitals. The differences

between the wavelengths of the calculated and measured absorption bands are related to the size of the monoatomic sheets and the thickness of the films. Theoretical calculations show that the energy bands will be separated into discrete energy levels.

Being a carbon/nitrogen compound with tri-s-triazines linked via tertiary amines,  $g\text{-C}_3\text{N}_4$  has corresponding band positions (conduction band (CB) at  $\approx -1.1$  eV and valence band (VB) at  $\approx +1.6$  eV relative to the standard hydrogen electrode (NHE) at pH = 0) [43]. The chemical potential allows  $g\text{-C}_3\text{N}_4$  to exhibit redox properties in various photocatalytic reactions under visible light irradiation. As shown in Fig. 3, the energy conversion process under sunlight in bulk  $g\text{-C}_3\text{N}_4$  mainly involves four factors, namely, photon excitation, generation/separation of photogenerated charge carriers, and surface redox reactions involving electrons/holes [44].

The disadvantages of bulk  $g\text{-C}_3\text{N}_4$  are high bulk or surface recombination. It limits the ability of pure  $g\text{-C}_3\text{N}_4$  to achieve high photocatalytic performance.

To overcome the drawbacks of pure  $g\text{-C}_3\text{N}_4$ , its composites with other materials are prepared and investigated. In particular, composites with metal oxides are used to improve sensor and photocatalytic performance.

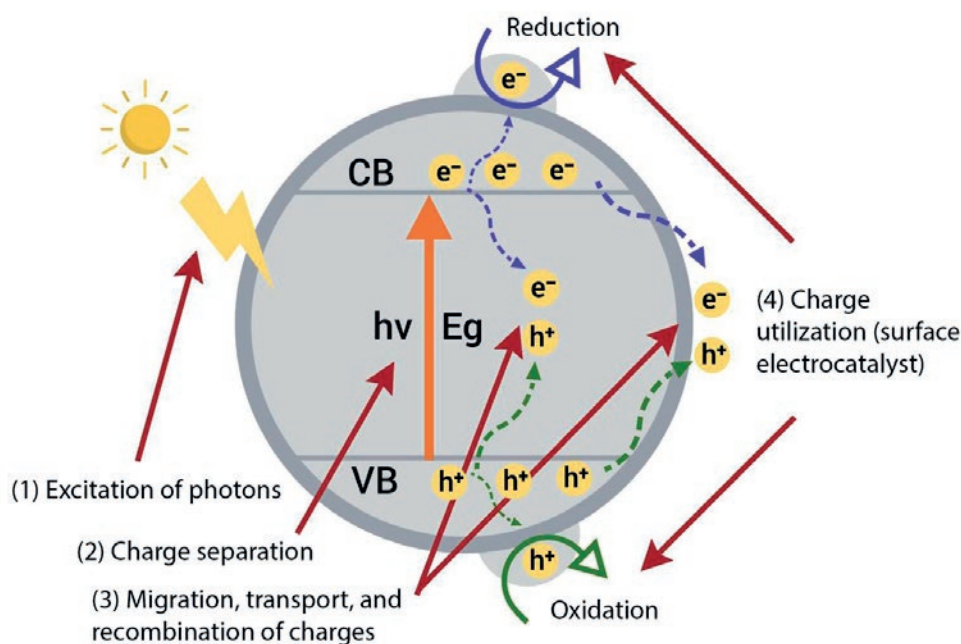


Fig. 3. Four main processes of  $g\text{-C}_3\text{N}_4$  photocatalysis

#### 4. Synthesis methods of metal oxide composites with g-C<sub>3</sub>N<sub>4</sub>

The synthesis of g-C<sub>3</sub>N<sub>4</sub> composites with various compounds, including TiO<sub>2</sub> [45], ZnO [46], CdS [47], Bi<sub>2</sub>WO<sub>6</sub> [48], Bi<sub>2</sub>MoO<sub>6</sub> [49], In<sub>2</sub>O<sub>3</sub> [50], Ag<sub>3</sub>PO<sub>4</sub> [51], AgBr [52] и MoS<sub>2</sub> [53], has been reported in the literature. The heterostructure formed based on g-C<sub>3</sub>N<sub>4</sub> cannot be formed with all materials. Since the efficiency of the heterostructure stimulated by visible light depends on the ability to hybridize bonds, the main criteria for material selection are the corresponding band structure. In addition, band bending occurs at the interface due to the potential difference between the semiconductors in contact. The photogenerated electrons and holes move in the opposite directions due to the internal field created by the band bending. As a result, pairs of electrons and holes are effectively separated and combined on the opposite sides of the heterojunction. ultrasonic mixing, precipitation-calcination, ultrasonic dispersion, hydrothermal method, and ultrasonic deposition are the methods for synthesizing g-C<sub>3</sub>N<sub>4</sub> composites.

Ultrasonication is the simplest method for producing g-C<sub>3</sub>N<sub>4</sub>-based composites. The method involves mixing g-C<sub>3</sub>N<sub>4</sub> powders (derived from nitrogen-containing precursors such as urea, melamine) with appropriate metals or metal oxides in water or an organic solvent. In this process, it is possible to form composites in which the metal oxide is distributed on the surface of g-C<sub>3</sub>N<sub>4</sub> during the stirring process.

The nanocomposite is extracted after complete evaporation of the solvent or water during heat treatment. In addition, other factors such as mechanical stirring and particle movement in the ultrasonic field can modify the deposition and dissolution process. A simple precipitation-calcination procedure was used by Yuan et al. [46] to obtain nanocomposites consisting of ZnO on g-C<sub>3</sub>N<sub>4</sub> nanosheets (see Fig. 4).

Nanocomposites based on g-C<sub>3</sub>N<sub>4</sub> can be obtained by heat treatment at high temperatures (calcination) of metal oxides with g-C<sub>3</sub>N<sub>4</sub> precursors. Due to its advantages including low time, low cost, simplicity and high yield, this method is a popular method for fabricating g-C<sub>3</sub>N<sub>4</sub>-based nanocomposites. However, the obtained composites have small specific surface area, large size particles, inhomogeneous particle distribution, etc., because there is no mixing of precursors in aqueous medium in this method, and higher calcination temperatures are required. The formation of heterostructure between the components in the fabricated nanocomposite reduces the probability of recombination of electron-hole pairs.

The hydrothermal method has become a promising technology for the creation of nanocomposite materials [54]. In this method, the crystallite size, morphology and crystallinity of materials can be improved due to the fact that the process takes place at relatively low temperatures. In addition, there are other parameters such as pressure, reaction temperature, pH, additives, solvent types, reaction time and precursor

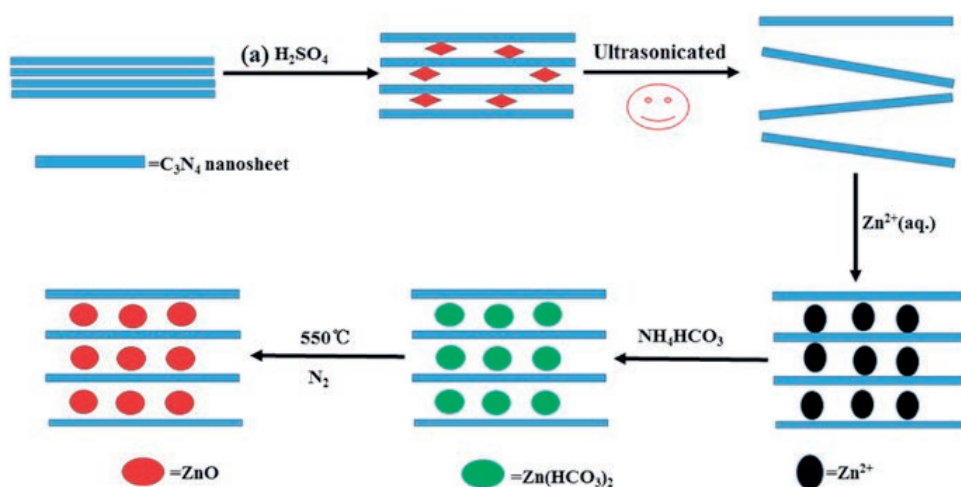


Fig. 4. Fabrication process of nanocomposites from g-C<sub>3</sub>N<sub>4</sub> and ZnO nanosheets [46]



composition that determine the surface chemistry and play an important role in the synthesis process. Idresse et al. [55] used the hydrothermal method to form niobium pentoxide ( $\text{Nb}_2\text{O}_5$ )/ $\text{g-C}_3\text{N}_4$  heterostructure (see Fig. 5).

Due to the low temperature used in this process, the particles obtained by hydrothermal synthesis have higher specific surface area, smaller size and better stability compared to those obtained by solid-state technology.

The synthesis of nanomaterials using the microwave method has become widespread due to the homogeneous heating of precursors at a high rate. This results in the formation of crystallites with a narrow size distribution, which is explained by the sequential nucleation and rapid crystal growth [56].  $\text{g-C}_3\text{N}_4$  is unstable as an organic polymer and decomposes at high temperatures. The formation of contact between  $\text{g-C}_3\text{N}_4$  and semiconductor promotes oxygen activation and hence its decomposition [57].

Thus, in this work, methods for synthesizing materials based on  $\text{g-C}_3\text{N}_4$  from various precursors are considered, which are aimed at investigating methods for synthesizing  $\text{g-C}_3\text{N}_4$  in the form of quantum dots, nanosheets or thin films, as well as composite heterostructures of  $\text{g-C}_3\text{N}_4$  with other materials.

## 5. Application of $\text{g-C}_3\text{N}_4$ in the development of gas sensors

The high adsorption capacity and unique surface morphology of  $\text{g-C}_3\text{N}_4$  contribute to high sensitivity. The high efficiency of charge transfer in  $\text{g-C}_3\text{N}_4$  in the context of interaction with various target gas molecules depends largely on the type of electrical conductivity. It is suggested that the sensitivity mechanism can be explained by the self-protonation of  $\text{g-C}_3\text{N}_4$  nanosheets. The sensing mechanism of  $\text{g-C}_3\text{N}_4$  is shown in Fig. 6.

The type of electrical conductivity in  $\text{g-C}_3\text{N}_4$  strongly depends on the presence of functional groups on its surface. In [59], treatment of  $\text{g-C}_3\text{N}_4$  fibers in  $\text{H}_2\text{SO}_4$  promotes their protonation and provides hole conductivity. In addition, in the process of high-temperature annealing, decomposition of residual  $\text{SO}_4^{2-}$  groups to  $\text{SO}_3$  is likely, which leads to the oxidation of  $\text{g-C}_3\text{N}_4$  fibers with the formation of oxygen-containing groups such as  $\text{C=O}$  and  $\text{O=C-OH}$ , which exhibit electron-acceptor properties. It contributes to an increase in the hole concentration.

Carbon nitrides contain amino groups that attract oxygen molecules [60]. When  $\text{NO}_2$  molecules interact with amino groups in  $\text{g-C}_3\text{N}_4$ , they capture more electrons due to their higher electronegativity compared to carbon atoms.

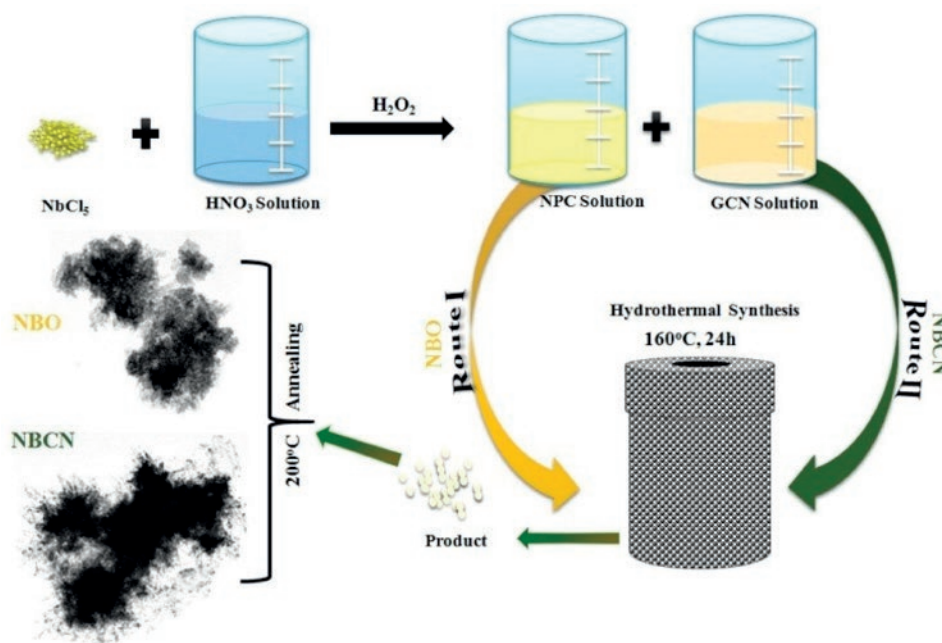
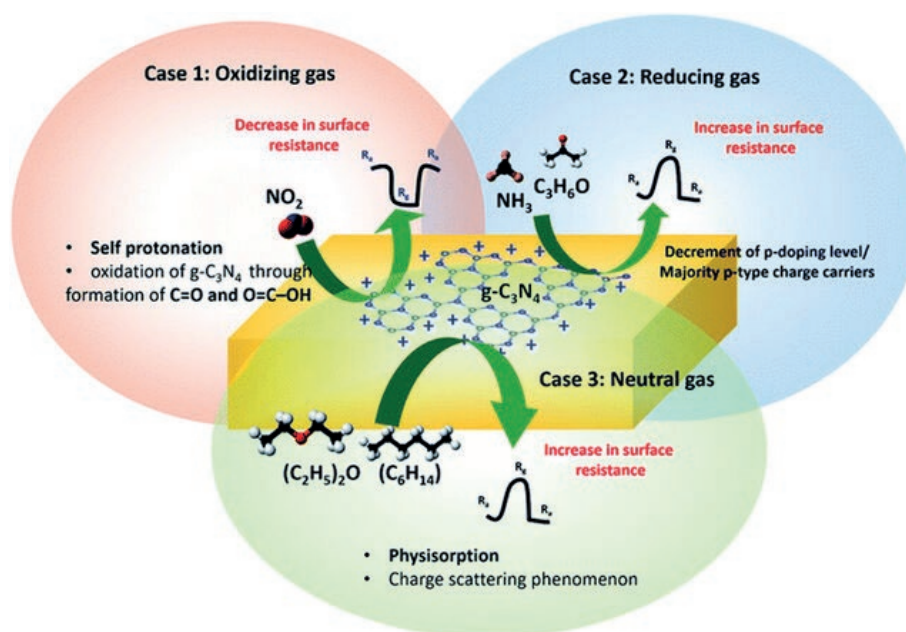


Fig. 5. Scheme of the hydrothermal method for synthesis of  $\text{Nb}_2\text{O}_5$  and  $\text{Nb}_2\text{O}_5/\text{g-C}_3\text{N}_4$  [55]



**Fig. 6.** Sensitivity mechanism of g-C<sub>3</sub>N<sub>4</sub> in the detection of oxidizing (case 1), reducing (case 2) and neutral gas (case 3) [58]

This is followed by the process of charge transfer from the N atom in g-C<sub>3</sub>N<sub>4</sub> to the NO<sub>2</sub> atom. When NO<sub>2</sub>, a typical electron acceptor gas, is adsorbed, the resistance of g-C<sub>3</sub>N<sub>4</sub> decreases. In addition, NO<sub>2</sub> can react with water vapor in the air to form HNO<sub>3</sub>, which can protonate the g-C<sub>3</sub>N<sub>4</sub> fibers, thereby reducing the resistance. For comparison, the obtained sensors were also used to detect gases with weak ability to give up electrons, such as NH<sub>3</sub> and acetone. In contrast, when reducing gases interact with g-C<sub>3</sub>N<sub>4</sub>, its surface resistivity increases, which is a typical property of a p-type semiconductor. However, when exposed to a neutral gas (hexane or ether), the effect of charge carrier scattering on the surface becomes dominant due to physically adsorbed molecules on the surface of g-C<sub>3</sub>N<sub>4</sub>, which leads to an increase in the surface resistivity. Thus, the large pore area and volume as well as the surface area of pure g-C<sub>3</sub>N<sub>4</sub> are the main factors for the high response of the sensor based on it [58].

Gas sensors based on g-C<sub>3</sub>N<sub>4</sub> are separated depending on the oxidation or reduction process on the surface of this material. This leads to a corresponding change in the surface resistivity value of the material. In the case of reducing gas, g-C<sub>3</sub>N<sub>4</sub> has proven its ability to detect toxic gases, industrial and domestic emissions such

as acetic acid, n-butanol, carbon monoxide [32]. In addition, there are capabilities to detect other gases such as acetone, methane, ethanol, hydrogen, and toluene [61]. In the case of oxidizing gases, g-C<sub>3</sub>N<sub>4</sub> has been investigated and proved to be applicable for the detection of NO<sub>2</sub> and CO<sub>2</sub> gases. In addition, g-C<sub>3</sub>N<sub>4</sub> can detect ambient humidity. However, the application of gas sensors based on pure g-C<sub>3</sub>N<sub>4</sub> is very limited. This has led to the modification of g-C<sub>3</sub>N<sub>4</sub> to improve its applicability in gas sensors. Techniques such as morphology modification, doping and formation of heterostructures have been used to improve the electrical structure of g-C<sub>3</sub>N<sub>4</sub> material. The main focus is the combined surface structure modification and heterostructure formation with metal oxides. Since this increases the surface area where the reaction takes place, the concentration of charge carriers increases and the recombination of electrons and holes is minimized. Table 1 summarizes the main works on gas sensors using g-C<sub>3</sub>N<sub>4</sub>.

It was shown in [66] that the addition of carbon to g-C<sub>3</sub>N<sub>4</sub> contributes to the increase in sensitivity to NO<sub>2</sub>, which is due to the contact between the carbon and the g-C<sub>3</sub>N<sub>4</sub> network. This is due to delocalized  $\pi$ -bonds leading to modification of the electronic structure of C/g-C<sub>3</sub>N<sub>4</sub> and improved electron movement. The gas sensitivity of g-C<sub>3</sub>N<sub>4</sub>



with the addition of carbon 10 wt% is 3 times higher than that of the original g-C<sub>3</sub>N<sub>4</sub>.

There are a number of publications devoted to the development of gas sensors based on composites of g-C<sub>3</sub>N<sub>4</sub> and metal oxides. For example, ZnO/rGO/g-C<sub>3</sub>N<sub>4</sub> nanocomposite for ethanol detection was obtained in [72]. The developed sensor showed excellent performance: sensitivity to 100 ppm ethanol at 300 °C ~ 178 ( $R_a/R_g$ ), detection limit below 500 ppb. The addition of g-C<sub>3</sub>N<sub>4</sub> leads to a 2-fold increase in sensitivity, which is attributed to the electron sensitization mechanism. The improved sensitivity of the ZnO/rGO/g-C<sub>3</sub>N<sub>4</sub> nanocomposite-based sensor to ethanol is mainly due to the combined effects of the small size of ZnO, the superior electronic conductivity of rGO, the formation of a p-n heterojunction between ZnO and rGO, and the improved generation of electrons and holes due to the wide band gap of g-C<sub>3</sub>N<sub>4</sub>.

The authors of [68] synthesized an efficient acetone sensor based on g-C<sub>3</sub>N<sub>4</sub>/WO<sub>3</sub> nanocomposites, the  $R_a/R_g$  response of which to 100 ppm acetone at 340 °C was 35. The obtained value is approximately 3 times higher than the response of pure WO<sub>3</sub>. The unique sensing properties are attributed to the synergistic effects combining ultrathin nanosheets, suitable crystalline phase and porous surface of WO<sub>3</sub>, as well as the increase in specific surface area and change in electrical properties after g-C<sub>3</sub>N<sub>4</sub> modification.

The hierarchical structure of ZnO decorated with g-C<sub>3</sub>N<sub>4</sub> was synthesized in [33]. The results

showed that the response ( $R_a/R_g$ ) of g-C<sub>3</sub>N<sub>4</sub>/ZnO to 1000 ppm CH<sub>4</sub> at 320 °C was 11.9 and exceeds that of ZnO under the same conditions by 2.2 times. The factors determining the improvement of sensing properties are increase of specific surface area and formation of p-n heterojunction. Different lattice parameters of ZnO and g-C<sub>3</sub>N<sub>4</sub>, involved in the formation of the p-n junction, lead to the formation of a large number of defects between ZnO and g-C<sub>3</sub>N<sub>4</sub>, which are potential active centers. The different positions of the Fermi level in ZnO and g-C<sub>3</sub>N<sub>4</sub> play an important role in providing improved sensing properties. Since the Fermi level in g-C<sub>3</sub>N<sub>4</sub> is located higher than in ZnO, at the interface between g-C<sub>3</sub>N<sub>4</sub> and ZnO, electrons will transfer from g-C<sub>3</sub>N<sub>4</sub> to ZnO until their Fermi levels are equalized. Thus, when the composite sensor is exposed to CH<sub>4</sub>, the electrons that were captured by the chemisorbed oxygen anions are transferred back to ZnO. The supply of additional electrons from g-C<sub>3</sub>N<sub>4</sub> leads to a more significant reduction in the depleted charge region. The authors of [73] showed an increase in the sensitivity to acetone during the formation of CuO/g-C<sub>3</sub>N<sub>4</sub> heterostructures. Thus, the response of composites containing 4 wt% g-C<sub>3</sub>N<sub>4</sub> to 1000 ppm acetone at room temperature is almost 30 times higher than that of a pure CuO sample. At the same time, the same factors listed above are cited as reasons for the improved properties.

There are a number of studies confirming the efficiency of photoactivation of gas sensitivity

**Table 1.** Main works on gas sensors using g-C<sub>3</sub>N<sub>4</sub>

Materials	Target gas	Working conditions	Response	Ref.
g-C <sub>3</sub> N <sub>4</sub> (8 %)/ZnO	Ethanol, 104 ppm	RT, UV	$\{(I_b - I_a)/I_a\} = 3.26$	[61]
Графен/g-C <sub>3</sub> N <sub>4</sub> (15 %)	NO <sub>2</sub> , 500 ppm	$T = 100\text{ }^{\circ}\text{C}$	$R_a/R_g = 2$	[62]
g-C <sub>3</sub> N <sub>4</sub> (10 %)/TiO <sub>2</sub>	CO <sub>2</sub> , 1500 ppm	$T = 450\text{ }^{\circ}\text{C}$	$R_a/R_g = 0.88$	[63]
$\alpha$ -Fe <sub>2</sub> O <sub>3</sub> /g-C <sub>3</sub> N <sub>4</sub> (60 %)	Ethanol, 100 ppm	$T = 340\text{ }^{\circ}\text{C}$	$R_a/R_g = 7.76$	[64]
g-C <sub>3</sub> N <sub>4</sub> /Co <sub>3</sub> O <sub>4</sub>	Toluene, 100 ppm	$T = 220\text{ }^{\circ}\text{C}$	$R_g/R_a = 25.8$	[65]
C (10 %)/ g-C <sub>3</sub> N <sub>4</sub>	NO <sub>2</sub> , 50 ppm	$T = 200\text{ }^{\circ}\text{C}$	$(R_g - R_a)/R_a = 0.71$	[66]
g-C <sub>3</sub> N <sub>4</sub> (10 %)/ SnO <sub>2</sub>	Acetic acid, 1000 ppm	$T = 185\text{ }^{\circ}\text{C}$	$R_a/R_g = 87.7$	[67]
g-C <sub>3</sub> N <sub>4</sub> (1 %)/ WO <sub>3</sub>	Acetone, 100 ppm	$T = 340\text{ }^{\circ}\text{C}$	$R_a/R_g = 35$	[68]
g-C <sub>3</sub> N <sub>4</sub> /NiO	NO <sub>2</sub> , 50 ppm	RT	$R_a/R_g = 25.4$	[69]
ZnO/ g-C <sub>3</sub> N <sub>4</sub> (30 %)	NO <sub>2</sub> , 10 ppm	$T = 180\text{ }^{\circ}\text{C}$	$(R_g - R_a)/R_a = 14.6$	[70]
g-C <sub>3</sub> N <sub>4</sub> (12 %)/ In <sub>2</sub> O <sub>3</sub>	Formaldehyde, 100 ppm	$T = 119\text{ }^{\circ}\text{C}$	$R_a/R_g = 1405$	[71]

at room temperature in “metal oxide/g-C<sub>3</sub>N<sub>4</sub>” nanocomposites due to the separation of photogenerated charge carriers. For example, this has been shown in the detection of ethanol upon exposure to UV light by sensors based on ZnO/g-C<sub>3</sub>N<sub>4</sub> [61], TiO<sub>2</sub>-C/g-C<sub>3</sub>N<sub>4</sub> [74] composites. Determination of NO<sub>2</sub> presence at room temperature and visible light exposure is possible with sensors based on 2D/2D ZnO/g-C<sub>3</sub>N<sub>4</sub> [75], In<sub>2</sub>O<sub>3</sub>/g-C<sub>3</sub>N<sub>4</sub>/Au [76].

A sensor based on a nanocomposite of graphene and g-C<sub>3</sub>N<sub>4</sub> [62] showed its efficiency in NO<sub>2</sub> detection due to the synergetic effect, in which graphene with high mobility of charge carriers plays the role of a channel for signal transmission, while g-C<sub>3</sub>N<sub>4</sub> with an active surface takes part in the interaction with analyte molecules.

The creation of composites based on two-dimensional materials and metal oxides has become an important area in gas sensing.

In [77], composites of reduced graphene oxide (rGO) and ZnO showed a sensitivity of 25.6 % to 5 ppm NO<sub>2</sub> at room temperature. At the same time, the response of rGO starts to be observed only at higher concentrations of NO<sub>2</sub>.

The gas-sensitive properties of the graphene/SnO<sub>2</sub> composite material have been investigated [78]. At an optimum operating temperature of 150 °C, the response value to 1 ppm NO<sub>2</sub> was 24.7, while the response of pure SnO<sub>2</sub> was less than 10.

In [79], gas-sensitive ZnO/MoS<sub>2</sub> composites were developed. The response value of the obtained sensor to 50 ppm ethanol reached 42.8 at an operating temperature of 260 °C. For pure ZnO, the optimum temperature was 240 °C, and the response to the same concentration of ethanol was ~ 24.

MoS<sub>2</sub>-TiO<sub>2</sub> composites obtained in [80] demonstrated excellent sensing properties and high sensitivity to ethanol vapors at low operating temperatures, and their response was almost 11 times higher than that of TiO<sub>2</sub> nanotubes. At the optimum operating temperature of 150 °C, the response to 100 ppm ethanol reached ~ 14.2.

Analysis of the current developments in gas sensors showed that the main disadvantage of metal oxide-based sensors is the high operating temperature, and 2D materials show unsatisfactory selectivity. Effective strategies

for further improvement (to increase selectivity, reduce operating temperature, improve sensitivity and other properties) include the creation of composite structures. To date, research on 2D metal oxides is still at an early stage. It is necessary to further study the mechanisms of their interaction with gas molecules.

## 6. Conclusions

Currently, g-C<sub>3</sub>N<sub>4</sub> is a material with great potential for gas sensor applications. The structure and basic properties such as electrical and optical properties of g-C<sub>3</sub>N<sub>4</sub> are summarized in this review. The mechanism of g-C<sub>3</sub>N<sub>4</sub> in gas sensors is discussed and specific gas sensor applications are listed.

From this, the following conclusions can be drawn about the properties of g-C<sub>3</sub>N<sub>4</sub> for gas sensor applications. The high specific surface area of g-C<sub>3</sub>N<sub>4</sub> provides more active centers for interaction with gases and hence improves sensitivity. The surface catalytic properties of g-C<sub>3</sub>N<sub>4</sub> improve the sensor performance in oxidation of target gases, ultimately minimizing the operating temperature. Controlling the mesoporosity of g-C<sub>3</sub>N<sub>4</sub> through optimal pore size and volume provides a percolation pathway for diffusion of gas molecules, which in turn leads to increased sensor efficiency. The formation of heterojunction between g-C<sub>3</sub>N<sub>4</sub> and metal oxides changes the charge transfer properties. The possibility of the existence of metal oxides in multiple phases (e.g. γ-WO<sub>3</sub> and ε-WO<sub>3</sub>) with g-C<sub>3</sub>N<sub>4</sub> enhances the sensing response due to electron transfer between the homojunction (γ-WO<sub>3</sub> and ε-WO<sub>3</sub>) and heterojunction (WO<sub>3</sub>/g-C<sub>3</sub>N<sub>4</sub>). Since the metal or metal oxide has a higher work function than g-C<sub>3</sub>N<sub>4</sub>, electrons move from the conduction band of g-C<sub>3</sub>N<sub>4</sub> to the metal/metal oxide, resulting in band bending. A larger surface area and higher electrical conductivity can be achieved by using a composite of 2D-2D materials (graphene and g-C<sub>3</sub>N<sub>4</sub>) to effectively interact with gases.

## Contribution of the authors

The authors contributed equally to this article.

## Conflict of interests

The authors declare that they have no known competing financial interests or personal



relationships that could have influenced the work reported in this paper.

## References

1. Dey A. Semiconductor metal oxide gas sensors: a review. *Materials Science and Engineering: B*. 2018;229: 206–217. <https://doi.org/10.1016/j.mseb.2017.12.036>
2. Yamazoe N. Oxide semiconductor gas sensors. *Catalysis Surveys from Asia*. 2003;7(1): 63–75. <https://doi.org/10.1023/a:1023436725457>
3. Nikolić M. V., Milovanović V., Vasiljević Z. Ž., Stamenković Z. Semiconductor gas sensors: materials, technology, design, and application. *Sensors*. 2020;20(22): 6694. <https://doi.org/10.3390/s20226694>
4. Ryabko A. A., Bobkov A. A., Nalimova S. S., ... Terukov E. I. Gas sensitivity of nanostructured coatings based on zinc oxide nanorods under combined activation. *Technical Physics*. 2020;92(5): 644–649. <https://doi.org/10.21883/tp.2022.05.53683.314-21>
5. Li Q., Zeng W., Li Y. Metal oxide gas sensors for detecting NO<sub>2</sub> in industrial exhaust gas: recent developments. *Sensors and Actuators B: Chemical*. 2022;359: 131579. <https://doi.org/10.1016/j.snb.2022.131579>
6. Rabchinskii M. K., Sysoev V. V., Varezchnikov A. S., ... Brunkov P. N. Toward on-chip multisensor arrays for selective methanol and ethanol detection at room temperature: capitalizing the graphene carbonylation. *ACS Applied Materials & Interfaces*. 2023;15(23): 28370–28386. <https://doi.org/10.1021/acsami.3c02833>
7. Ryabtsev S. V., Obvintseva N. Yu., Chistyakov V. V., ... Domashevskaya E. P. Features of the resistive response to ozone of semiconductor PdO sensors operating in thermomodulation mode. *Condensed Matter and Interphases*. 2023;25(3): 392–397. <https://doi.org/10.17308/kcmf.2023.25/11263>
8. Shaposhnik A. V., Zvyagin A. A., Dyakonova O. V., Ryabtsev S. V., Ghareeb D. A. Semiconductor metal oxide sensor for hydrogen sulphide operating under non-stationary temperature conditions. *Condensed Matter and Interphases*. 2021;23(4): 637–643. <https://doi.org/10.17308/kcmf.2021.23/3684>
9. Ryabko A. A., Nalimova S. S., Mazing D. S., Korepanov O. A., ... Aleshin A. N. Sensitization of ZnO nanorods by AgInS<sub>2</sub> colloidal quantum dots for adsorption gas sensors with light activation. *Technical Physics*. 2022;92(6): 717–722. <https://doi.org/10.21883/tp.2022.06.54418.15-22>
10. Nalimova S. S., Ryabko A. A., Maximov A. I., Moshnikov V. A. Light-activation of gas sensitive layers based on zinc oxide nanowires. *Journal of Physics: Conference Series*. 2020;1697(1): 012128. <https://doi.org/10.1088/1742-6596/1697/1/012128>
11. Domènech-Gil G., Samà J., Fàbrega C., ... Romano-Rodríguez A. Highly sensitive SnO<sub>2</sub> nanowire network gas sensors. *Sensors and Actuators B: Chemical*. 2023;383: 133545. <https://doi.org/10.1016/j.snb.2023.133545>
12. Pham Q. T., Syrkov A. G., Silivanov M. O., Ngo Q. K. Preparation of zinc nanooxide and its application for antibacterial coatings. *Tsvetnye Metally*. 2023;(9): 51–56. <https://doi.org/10.17580/tsm.2023.09.06>
13. Rzaiz J. M., Abass A. M. Review on: TiO<sub>2</sub> thin film as a metal oxide gas sensor. *Journal of Chemical Reviews*. 2020;2(2): 114–121. <https://doi.org/10.33945/sami/jcr.2020.2.4>
14. Umar A., Alduraibi M., Al-Dossary O. M. Development of ethanol gas sensor using A-Fe<sub>2</sub>O<sub>3</sub> nanocubes synthesized by hydrothermal process. *Journal of Nanoelectronics and Optoelectronics*. 2020;15(1): 59–64. <https://doi.org/10.1166/jno.2020.2742>
15. Dong C., Zhao R., Yao L., Yan R., Zhang X., Wang Y. A review on WO<sub>3</sub> based gas sensors: morphology control and enhanced sensing properties. *Journal of Alloys and Compounds*. 2020;820: 153194. <https://doi.org/10.1016/j.jallcom.2019.153194>
16. Chaloeipote G., Prathumwan R., Subannajui K., Wisitsoraat A., Wongchoosuk C. 3D printed CuO semiconducting gas sensor for ammonia detection at room temperature. *Materials Science in Semiconductor Processing*. 2021;123: 105546. <https://doi.org/10.1016/j.mssp.2020.105546>
17. Kushchenko A. N., Syrkov A. G., Ngo Q. K. Inorganic synthesis of highly hydrophobic metals containing surface compounds with electron acceptor modifiers: process features. *Tsvetnye Metally*. 2023;(8): 62–72. <https://doi.org/10.17580/tsm.2023.08.11>
18. Kumarage G. W. C., Comini E. Low-dimensional nanostructures based on cobalt oxide (Co<sub>3</sub>O<sub>4</sub>) in chemical-gas sensing. *Chemosensors*. 2021;9(8): 197. <https://doi.org/10.3390/chemosensors9080197>
19. Chumakova V., Marikutsa A., Platonov V., Khmelevsky N., Rumyantseva M. N. Distinct roles of additives in the improved sensitivity to CO of Ag- and Pd-modified nanosized LaFeO<sub>3</sub>. *Chemosensors*. 2023;11(1): 60. <https://doi.org/10.3390/chemosensors11010060>
20. Njoroge M. A., Kirimi N. M., Kuria K. P. Spinel ferrites gas sensors: a review of sensing parameters, mechanism and the effects of ion substitution. *Critical Reviews in Solid State and Materials Sciences*. 2021;47(6): 807–836. <https://doi.org/10.1080/10408436.2021.1935213>
21. An D., Wang, Q., Tong, X., ... Li Y. Synthesis of Zn<sub>2</sub>SnO<sub>4</sub> via a co-precipitation method and its gas-sensing property toward ethanol. *Sensors and Actuators B: Chemical*. 2015;213: 155–163. <https://doi.org/10.1016/j.snb.2015.02.042>
22. Buckley D. J., Black N. C. G., Castanon E., Melios C., Hardman M., Kazakova O. Frontiers of graphene and 2D material-based gas sensors for environmental monitoring. *2D Materials*. 2020;7(3): 032002. <https://doi.org/10.1088/2053-1583/ab7bc5>
23. Platonov V., Malinin N. I., Vasiliev R. B., Rumyantseva M. N. Room temperature UV-activated NO<sub>2</sub> and NO detection by ZnO/rGO composites. *Chemosensors*. 2023;11(4): 227. <https://doi.org/10.3390/chemosensors11040227>
24. Simonenko E. P., Simonenko E. P., Mokrushin A. S., ... Kuznecov N. T. Application of titanium carbide MXENES in chemiresistive gas sensors. *Nanomaterials*. 2023;13(5): 850. <https://doi.org/10.3390/nano13050850>
25. Cui S., Li R., Pei J., Wen, Y., Li Y., Xing X. Automobile exhaust purification over g-C<sub>3</sub>N<sub>4</sub> catalyst material. *Materials Chemistry and Physics*. 2020;247: 122867. <https://doi.org/10.1016/j.matchemphys.2020.122867>
26. Ray D., Nepak D., Vinodkumar T., Subrahmanyam Ch. g-C<sub>3</sub>N<sub>4</sub> promoted DBD plasma assisted dry reforming of methane. *Energy*. 2019;183: 630–638. <https://doi.org/10.1016/j.energy.2019.06.147>

27. Yang W., Jia L., Wu P., Zhai H., He J., Liu C. Effect of thermal program on structure–activity relationship of g-C<sub>3</sub>N<sub>4</sub> prepared by urea pyrolysis and its application for controllable production of g-C<sub>3</sub>N<sub>4</sub>. *Journal of Solid State Chemistry*. 2021;304: 122545. <https://doi.org/10.1016/j.jssc.2021.122545>
28. Pati S., Acharya R. An overview on g-C<sub>3</sub>N<sub>4</sub> as a robust photocatalyst towards the sustainable generation of H<sub>2</sub> energy. *Materials Today: Proceedings*. 2021;35: 175–178. <https://doi.org/10.1016/j.matpr.2020.04.178>
29. Xiong Z., Wang Z., Murugananthan M., Zhang Y. Construction of an in-situ Fenton-like system based on a g-C<sub>3</sub>N<sub>4</sub> composite photocatalyst. *Journal of Hazardous Materials*. 2019;373: 565–571. <https://doi.org/10.1016/j.jhazmat.2019.03.114>
30. Cao M., Wang K., Tudela I., Fan X. Improve photocatalytic performance of g-C<sub>3</sub>N<sub>4</sub> through balancing the interstitial and substitutional chlorine doping. *Applied Surface Science*. 2021;536: 147784. <https://doi.org/10.1016/j.apsusc.2020.147784>
31. Zhao R., Wang Z., Zou T., Wang Z., Yang Y., Xing X. Synthesis and enhanced sensing performance of g-C<sub>3</sub>N<sub>4</sub>/SnO<sub>2</sub> composites toward isopropanol. *Chemistry Letters*. 2018;47(7): 881–882. <https://doi.org/10.1246/cl.180296>
32. Cao J., Qin C., Wang Y., Zhang H., Sun G., Zhang Z. Solid-state method synthesis of SnO<sub>2</sub>-decorated g-C<sub>3</sub>N<sub>4</sub> nanocomposites with enhanced gas-sensing property to ethanol. *Materials*. 2017;10(6): 604. <https://doi.org/10.3390/ma10060604>
33. Li X., Li Y., Sun G., Luo N., Zhang B., Zhang Z. Synthesis of a flower-like g-C<sub>3</sub>N<sub>4</sub>/ZnO hierarchical structure with improved CH<sub>4</sub> sensing properties. *Nanomaterials*. 2019;9(5): 724. <https://doi.org/10.3390/nano9050724>
34. He F., Wang Z., Li Y., Peng S., Liu B. The nonmetal modulation of composition and morphology of g-C<sub>3</sub>N<sub>4</sub>-based photocatalysts. *Applied Catalysis B: Environmental*. 2020;269: 118828. <https://doi.org/10.1016/j.apcatb.2020.118828>
35. Zhao G., Yang H., Liu M., Xu X. Metal-free graphitic carbon nitride photocatalyst goes into two-dimensional time. *Frontiers in Chemistry*. 2018;6. <https://doi.org/10.3389/fchem.2018.00551>
36. Zhang Y., Gao H., Kuai Y., ... You W. Effects of Y additions on the precipitation and recrystallization of Al–Zr alloys. *Materials Characterization*. 2013;86: 1–8. <https://doi.org/10.1016/j.matchar.2013.09.004>
37. Naseri A., Samadi M., Pourjavadi A., Ramakrishna S. Graphitic carbon nitride (g-C<sub>3</sub>N<sub>4</sub>)-based photocatalysts for solar hydrogen generation: recent advances and future development directions. *Journal of Materials Chemistry A*. 2017;5(45): 23406–23433. <https://doi.org/10.1039/c7ta05131j>
38. Idris A. O., Oseghe E. O., Msagati T. A. M., Kuva-rega A. T., Feleni U., Mamba B. B. Graphitic carbon nitride: a highly electroactive nanomaterial for environmental and clinical sensing. *Sensors*. 2020;20(20): 5743. <https://doi.org/10.3390/s20205743>
39. Patra P. C., Mohapatra Y. N. Dielectric constant of thin film graphitic carbon nitride (g-C<sub>3</sub>N<sub>4</sub>) and double dielectric Al<sub>2</sub>O<sub>3</sub>/g-C<sub>3</sub>N<sub>4</sub>. *Applied Physics Letters*. 2021;118(10). <https://doi.org/10.1063/5.0045911>
40. Giusto P., Cruz D., Heil T., ... Antonietti M. Shine bright like a diamond: new light on an old polymeric semiconductor. *Advanced Materials*. 2020;32(10). <https://doi.org/10.1002/adma.201908140>
41. Bian J., Li Q., Huang C., Li J., Gou Y., Zaw M., Qi F. Thermal vapor condensation of uniform graphitic carbon nitride films with remarkable photocurrent density for photoelectrochemical applications. *Nano Energy*. 2015;15: 353–361. <https://doi.org/10.1016/j.nanoen.2015.04.012>
42. Wang Y., Wang X., Antonietti M. Polymeric graphitic carbon nitride as a heterogeneous organocatalyst: from photochemistry to multipurpose catalysis to sustainable chemistry. *Angewandte Chemie International Edition*. 2011;51(1): 68–89. <https://doi.org/10.1002/anie.201101182>
43. Cao S., Low J., Wang Y., Jaroniec M. Polymeric photocatalysts based on graphitic carbon nitride. *Advanced Materials*. 2015;27(13): 2150–2176. <https://doi.org/10.1002/adma.201500033>
44. Liu M., Wageh S., Al-Ghamdi A. A., ... Wang Y. Quenching induced hierarchical 3D porous g-C<sub>3</sub>N<sub>4</sub> with enhanced photocatalytic CO<sub>2</sub> reduction activity. *Chemical Communications*. 2019;55(93): 14023–14026. <https://doi.org/10.1039/c9cc07647f>
45. Li C., Sun Z., Xue Y., Yao G., Zheng S. A facile synthesis of g-C<sub>3</sub>N<sub>4</sub>/TiO<sub>2</sub> hybrid photocatalysts by sol–gel method and its enhanced photodegradation towards methylene blue under visible light. *Advanced Powder Technology*. 2016;27(2): 330–337. <https://doi.org/10.1016/j.appt.2016.01.003>
46. Yuan X., Zhou C., Jing Q., Tang Q., Mu Y., Du A. K. Facile synthesis of g-C<sub>3</sub>N<sub>4</sub> nanosheets/ZnO nanocomposites with enhanced photocatalytic activity in reduction of aqueous chromium (VI) under visible light. *Nanomaterials*. 2016;6(9): 173. <https://doi.org/10.3390/nano6090173>
47. Cheng F., Yin H., Xiang Q. Low-temperature solid-state preparation of ternary CdS/g-C<sub>3</sub>N<sub>4</sub>/CuS nanocomposites for enhanced visible-light photocatalytic H<sub>2</sub>-production activity. *Applied Surface Science*. 2017;391: 432–439. <https://doi.org/10.1016/j.apsusc.2016.06.169>
48. Ge L., Han C., Liu J. Novel visible light-induced g-C<sub>3</sub>N<sub>4</sub>/Bi<sub>2</sub>WO<sub>6</sub> composite photocatalysts for efficient degradation of methyl orange. *Applied Catalysis B: Environmental*. 2011;108–109: 100–107. <https://doi.org/10.1016/j.apcatb.2011.08.014>
49. Liang Q., Zhang M., Yao C., Liu C., Xu S., Li Z. High performance visible-light driven photocatalysts of Bi<sub>2</sub>MoO<sub>6</sub>-g-C<sub>3</sub>N<sub>4</sub> with controllable solvothermal fabrication. *Journal of Photochemistry and Photobiology A: Chemistry*. 2017;332: 357–363. <https://doi.org/10.1016/j.jphotochem.2016.09.012>
50. Cao S., Liu X., Yuan Y., ... Xue C. Solar-to-fuels conversion over In<sub>2</sub>O<sub>3</sub>/g-C<sub>3</sub>N<sub>4</sub> hybrid photocatalysts. *Applied Catalysis B: Environmental*. 2014;147: 940–946. <https://doi.org/10.1016/j.apcatb.2013.10.029>
51. Liu L., Qi Y., Lu J., ... Cui W. A stable Ag<sub>3</sub>PO<sub>4</sub>@g-C<sub>3</sub>N<sub>4</sub> hybrid core@shell composite with enhanced visible light photocatalytic degradation. *Applied Catalysis B: Environmental*. 2016;183: 133–141. <https://doi.org/10.1016/j.apcatb.2015.10.035>
52. Yang Y., Guo W., Guo Y., Zhao Y., Yuan X., Guo Y. Fabrication of Z-scheme plasmonic photocatalyst Ag@AgBr/g-C<sub>3</sub>N<sub>4</sub> with enhanced visible-light photocatalytic activity. *Journal of Hazardous Materials*. 2014;271: 150–159. <https://doi.org/10.1016/j.jhazmat.2014.02.023>



53. Peng W., Li X. Synthesis of  $\text{MoS}_2/\text{g-C}_3\text{N}_4$  as a solar light-responsive photocatalyst for organic degradation. *Catalysis Communications*. 2014;49: 63–67. <https://doi.org/10.1016/j.catcom.2014.02.008>
54. Bhati V. S., Hojamberdiev M., Kumar M. Enhanced sensing performance of ZnO nanostructures-based gas sensors: A review. *Energy Reports*. 2020;6: 46–62. <https://doi.org/10.1016/j.egy.2019.08.070>
55. Idrees F., Dillert R., Bahnemann D. W., Butt F. K., Tahir M. N. In-situ synthesis of  $\text{Nb}_2\text{O}_5/\text{g-C}_3\text{N}_4$  heterostructures as highly efficient photocatalysts for molecular  $\text{H}_2$  evolution under solar illumination. *Catalysts*. 2019;9(2): 169. <https://doi.org/10.3390/catal9020169>
56. Yin H., Yamamoto T., Wada Y., Yanagida S. Large-scale and size-controlled synthesis of silver nanoparticles under microwave irradiation. *Materials Chemistry and Physics*. 2004;83(1): 66–70. <https://doi.org/10.1016/j.matchemphys.2003.09.006>
57. Li T., Zhao L., He Y., Cai J., Luo M., Lin J. Synthesis of  $\text{g-C}_3\text{N}_4/\text{SmVO}_4$  composite photocatalyst with improved visible light photocatalytic activities in RhB degradation. *Applied Catalysis B: Environmental*. 2013;129: 255–263. <https://doi.org/10.1016/j.apcatb.2012.09.031>
58. Bhati V. S., Takhar V., Raliya R., Kumar M., Banerjee R. Recent advances in  $\text{g-C}_3\text{N}_4$  based gas sensors for the detection of toxic and flammable gases: a review. *Nano Express*. 2022;3(1): 014003. <https://doi.org/10.1088/2632-959x/ac477b>
59. Li S., Wang Z., Wang X., ... Huang W. Orientation controlled preparation of nanoporous carbon nitride fibers and related composite for gas sensing under ambient conditions. *Nano Research*. 2017;10(5): 1710–1719. <https://doi.org/10.1007/s12274-017-1423-8>
60. Wang D., Gu W., Zhang Y., Hu Y., Zhang T., Tao X., Chen W. Novel C-rich carbon nitride for room temperature  $\text{NO}_2$  gas sensors. *RSC Advances*. 2014;4(35): 18003–18006. <https://doi.org/10.1039/c4ra02127d>
61. Zhai J., Wang T., Wang C., Liu D. UV-light-assisted ethanol sensing characteristics of  $\text{g-C}_3\text{N}_4/\text{ZnO}$  composites at room temperature. *Applied Surface Science*. 2018;441: 317–323. <https://doi.org/10.1016/j.apsusc.2018.02.026>
62. Hang N. T., Zhang S. Efficient exfoliation of  $\text{g-C}_3\text{N}_4$  and  $\text{NO}_2$  sensing behavior of graphene/ $\text{g-C}_3\text{N}_4$  nanocomposite. *Sensors and Actuators B: Chemical*. 2017;248: 940–948. <https://doi.org/10.1016/j.snb.2017.01.199>
63. Karthik P., Gowthaman P., Venkatachalam M., Saroja M. Design and fabrication of  $\text{g-C}_3\text{N}_4$  nanosheets decorated  $\text{TiO}_2$  hybrid sensor films for improved performance towards  $\text{CO}_2$  gas. *Inorganic Chemistry Communications*. 2020;119: 108060. <https://doi.org/10.1016/j.inoche.2020.108060>
64. Zhang Y., Zhang D., Guo W., Chen S. The  $\alpha\text{-Fe}_2\text{O}_3/\text{g-C}_3\text{N}_4$  heterostructural nanocomposites with enhanced ethanol gas sensing performance. *Journal of Alloys and Compounds*. 2016;685: 84–90. <https://doi.org/10.1016/j.jallcom.2016.05.220>
65. Yue J., Xu J., Hong B., ... Wang X. Synthesis and calcination-temperature-dependent gas-sensing performance of  $\text{g-C}_3\text{N}_4/\text{Co}_3\text{O}_4$  heterojunctions for toluene gas sensors. *Journal of Materials Science: Materials in Electronics*. 2023;34(21). <https://doi.org/10.1007/s10854-023-10957-y>
66. Govind A., Bharathi P., Mathankumar G., ... Navaneethan M. Enhanced charge transfer in 2D carbon-rich  $\text{g-C}_3\text{N}_4$  nanosheets for highly sensitive  $\text{NO}_2$  gas sensor applications. *Diamond and Related Materials*. 2022;128: 109205. <https://doi.org/10.1016/j.diamond.2022.109205>
67. Zhang Y., Liu J., Chu X., Liang S., Kong L. Preparation of  $\text{g-C}_3\text{N}_4\text{-SNO}_2$  composites for application as acetic acid sensor. *Journal of Alloys and Compounds*. 2020;832: 153355. <https://doi.org/10.1016/j.jallcom.2019.153355>
68. Wang D., Huang S., Li H., ... Yang J. Ultrathin  $\text{WO}_3$  nanosheets modified by  $\text{g-C}_3\text{N}_4$  for highly efficient acetone vapor detection. *Sensors and Actuators B: Chemical*. 2019;282: 961–971. <https://doi.org/10.1016/j.snb.2018.11.138>
69. Ullah M., He L., Liu Z., ... Shi K. Rational fabrication of a  $\text{g-C}_3\text{N}_4/\text{NiO}$  hierarchical nanocomposite with a large surface area for the effective detection of  $\text{NO}_2$  gas at room temperature. *Applied Surface Science*. 2021;550: 149368. <https://doi.org/10.1016/j.apsusc.2021.149368>
70. Patrick D. S., Govind A., Bharathi P., ... Navaneethan M. Hierarchical  $\text{ZnO/g-C}_3\text{N}_4$  nanocomposites for enhanced  $\text{NO}_2$  gas sensing applications. *Applied Surface Science*. 2023;609: 155337. <https://doi.org/10.1016/j.apsusc.2022.155337>
71. Sun D., Wang W., Zhang N., ... Ruan S.  $\text{g-C}_3\text{N}_4/\text{In}_2\text{O}_3$  composite for effective formaldehyde detection. *Sensors and Actuators B: Chemical*. 2022;358: 131414. <https://doi.org/10.1016/j.snb.2022.131414>
72. Meng F., Chang Y., Qin W., ... Ibrahim M.  $\text{ZnO}$ -reduced graphene oxide composites sensitized with graphitic carbon nitride nanosheets for ethanol sensing. *ACS Applied Nano Materials*. 2019;2(5): 2734–2742. <https://doi.org/10.1021/acsanm.9b00257>
73. Akhtar A., Cheng J., Chu X., Liang S., Dong Y., He L. Acetone sensing properties of the  $\text{g-C}_3\text{N}_4\text{-CuO}$  nanocomposites prepared by hydrothermal method. *Materials Chemistry and Physics*. 2021;265: 124375. <https://doi.org/10.1016/j.matchemphys.2021.124375>
74. Hou M., Gao J., Yang L., Guo S., Hu T., Li Y. Room temperature gas sensing under UV light irradiation for  $\text{Ti}_3\text{C}_2\text{T}_x$  MXene derived lamellar  $\text{TiO}_2\text{-C/g-C}_3\text{N}_4$  composites. *Applied Surface Science*. 2021;535: 147666. <https://doi.org/10.1016/j.apsusc.2020.147666>
75. Wang H., Bai J., Meng D., ... Lu G. Visible light activated excellent  $\text{NO}_2$  sensing based on 2D/2D  $\text{ZnO/g-C}_3\text{N}_4$  heterojunction composites. *Sensors and Actuators B: Chemical*. 2020;304: 127287. <https://doi.org/10.1016/j.snb.2019.127287>
76. Han C., Li X., Liu J., ... Liu Y.  $\text{In}_2\text{O}_3/\text{g-C}_3\text{N}_4/\text{Au}$  ternary heterojunction-integrated surface plasmonic and charge-separated effects for room-temperature ultrasensitive  $\text{NO}_2$  detection. *Sensors and Actuators B: Chemical*. 2022;371: 132448. <https://doi.org/10.1016/j.snb.2022.132448>
77. Liu S., Yu B., Zhang H., Fei T., Zhang T. Enhancing  $\text{NO}_2$  gas sensing performances at room temperature based on reduced graphene oxide-ZnO nanoparticles hybrids. *Sensors and Actuators B: Chemical*. 2014;202: 272. <https://doi.org/10.1016/j.snb.2014.05.086>
78. Kim H. W., Na H. G., Kwon Y. J., ... Kim S. S. Microwave-assisted synthesis of graphene-SnO<sub>2</sub> nanocomposites and their applications in gas sensors. *ACS Appl. Mater. Interfaces*. 2017;9(37): 31667. <https://doi.org/10.1021/acsami.7b02533>

79. Yan H., Song P., Zhang S., Yang Z., Wang Q. Facile synthesis, characterization and gas sensing performance of ZnO nanoparticles-coated MoS<sub>2</sub> nanosheets. *Journal of Alloys and Compounds*. 2016;662: 118. <https://doi.org/10.1016/j.jallcom.2015.12.066>

80. Zhao P. X., Tang Y., Mao J., ... Zhang X. M. One-dimensional MoS<sub>2</sub>-decorated TiO<sub>2</sub> nanotube gas sensors for efficient alcohol sensing. *Journal of Alloys and Compounds*. 2016;674: 252. <https://doi.org/10.1016/j.jallcom.2016.03.029>

### Information about the authors

*Bui Cong Doan*, postgraduate student, Department of Micro- and Nanoelectronics, Saint Petersburg Electrotechnical University “LETI” (St. Petersburg, Russian Federation).

<https://orcid.org/0000-0002-9937-9078>

[congdoan6997@gmail.com](mailto:congdoan6997@gmail.com)

*Nalimova Svetlana Sergeyevna*, Cand. Sci. (Phys.–Math.), Associate Professor, Department of Micro- and Nanoelectronics, Saint Petersburg Electrotechnical University “LETI” (St. Petersburg, Russian Federation).

<https://orcid.org/0000-0003-3065-3961>

[sskarpova@list.ru](mailto:sskarpova@list.ru)

*Nguyen Van Tu Anh*, postgraduate student, Department of Physical Electronics, Peter the Great St. Petersburg Polytechnic University (St. Petersburg, Russian Federation).

<https://orcid.org/0009-0004-7198-6329>

[anh.spbpu@gmail.com](mailto:anh.spbpu@gmail.com)

*Received 05.04.2024; approved after reviewing 10.07.2024; accepted for publication 15.07.2024; published online 25.06.2025.*



## Review

Review article

<https://doi.org/10.17308/kcmf.2025.27/12770>

## Advanced methods for preparing especially pure glasses based on germanium and gallium chalcogenides. Part 2. Synthesis using chemical transport reactions. Review

A. P. Velmuzhov✉, M. V. Sukhanov, E. A. Tyurina, V. S. Shiryaev

G. G. Devyatykh Institute of Chemistry of High-Purity Substances, Russian Academy of Sciences,  
49 Tropinina st., Nizhny Novgorod 603137 Russian Federation

### Abstract

**Purpose:** The second part of the review presents the results of preparing especially pure glasses based on germanium and gallium chalcogenides with chemical transport reactions.

**Experimental part:** Deep purification and vacuum loading of metallic gallium, gallium(III) telluride and rare-earth elements (REE) using gallium(III) iodide as a transport agent made it possible to reduce the content of hydrogen, oxygen impurities and heterogeneous inclusions in glasses by 1–2 orders of magnitude compared to tradition direct glass synthesis. We have theoretically justified and experimentally confirmed the high efficiency of REEs as getters for binding and subsequent removal of oxygen impurities from the chalcogenide melt.

**Conclusions:** The key result achieved by reducing the impurity content is mid-infrared (IR) laser generation in bulk samples of REE-doped chalcogenide glasses and in optical fibers based on them, which was previously not possible in these materials.

**Keywords:** Chalcogenide glasses; Especially pure substances; Optical materials; Synthesis; Chemical transport reactions; Laser generation

**Funding:** The research was carried out with the financial support of the national project “Science and Universities” at the laboratory “High-purity chalcogenide glasses for mid-IR photonics”, state order FFSR-2024-0001 and the Research and Education Centre of the Nizhny Novgorod region within the framework “Technoplatfrom 2035” project.

**For citation:** Velmuzhov A. P., Sukhanov M. V., Tyurina E. A., Shiryaev V. S. Advanced methods for preparing especially pure glasses based on germanium and gallium chalcogenides. Part 2. Synthesis using chemical transport reactions. Review. *Condensed Matter and Interphases*. 2025;27(2): 190–202. <https://doi.org/10.17308/kcmf.2025.27/12770>

**Для цитирования:** Вельмузов А. П., Суханов М. В., Тюрина Е. А., Ширяев В. С. Современные способы получения особо чистых стекол на основе халькогенидов германия и галлия. Часть 2. Синтез с применением реакций химического транспорта. Обзор. *Конденсированные среды и межфазные границы*. 2025;27(2): 190–202. <https://doi.org/10.17308/kcmf.2025.27/12770>

✉ Alexander P. Velmuzhov, e-mail: [velmuzhov.ichps@mail.ru](mailto:velmuzhov.ichps@mail.ru)

© Velmuzhov A. P., Sukhanov M. V., Tyurina E. A., Shiryaev V. S., 2025



The content is available under Creative Commons Attribution 4.0 License.



## 1. Introduction

The development of luminescent and laser sources of radiation in the mid-infrared (IR) range is a promising practical application of glasses based on germanium and gallium chalcogenides [1, 2]. Until recently, research in this area was limited to the evaluation of potential capabilities of chalcogenide glasses doped with rare-earth elements (REEs) as laser materials [3, 4]. In cooperation with Devyatikh Institute of Chemistry of High-Purity Substances of the Russian Academy of Sciences (ICHPS RAS), Dianov Fiber Optics Research Centre (FORC) and Prokhorov General Physics Institute of the Russian Academy of Sciences (GPI RAS), for the first time, laser generation at a wavelength  $\geq 5 \mu\text{m}$  was achieved first in bulk samples of REE-doped chalcogenide glasses [5] and then in optical fibers based on them [6–8].

In recent years, there has been increasing interest in germanium and gallium telluride glasses due to their optical transparency in a wide spectral range up to  $35 \mu\text{m}$  for bulk samples [9] and  $16 \mu\text{m}$  for optical fibers [10]. This makes such glasses promising for the transmission of  $\text{CO}_2$  laser radiation with operating wavelengths at  $9.3$  and  $10.6 \mu\text{m}$  [11]. Optical devices based on telluride glasses can be used to solve problems related to space exploration [12–14].

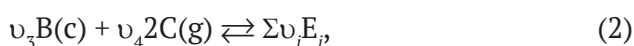
The main difficulty in preparing especially pure glasses, containing gallium and REE, is the extremely low volatility of these metals in the form of simple substances and chalcogenides [15, 16]. This virtually excludes the possibility of purification of the glass-forming melt by distillation, which is the most important step in preparing low impurity chalcogenide glasses [17].

The purpose of this review is to systematize the scientific fundamentals of the methods for preparing especially pure chalcogenide glasses developed at the Institute of Chemistry of High-Purity Substances of the Russian Academy of Sciences for the last 15 years. The first part of the review presents the results of batch synthesis via volatile iodides of *p*-elements, germanium monochalcogenides, and thermal decomposition of germanium sulfide and selenide iodides [18]. The second part focuses on the application of chemical transport reactions for preparing low impurity chalcogenide

glasses. The article presents data on REEs as effective getters for binding oxygen impurities in telluride glasses.

## 2. Preparation of chalcogenide glasses with chemical transport reactions

Chemical transport is one of the most effective methods for the deep purification of substances [19, 20]. The method is based on the interaction of the vapors of the transport agent with the target low volatile substance, resulting in the formation of one or more highly volatile compounds. For the “main substance – impurity” system, chemical transport reactions can be written in the following form:



where *A* – main substance; *B* – impurity; *C* – transport agent;  $D_i$  – product of interaction with the main substance;  $E_i$  – product of interaction with the impurity;  $\nu_i$  – stoichiometric coefficient. If at  $T_2$  the reactions (1) and (2) proceed mainly in the forward direction and at  $T_1$  in the reverse direction, then by creating a temperature gradient  $T_2 \rightarrow T_1$  it is possible to ensure the transport of components *A* and *B* from the zone with  $T_2$  to the zone with  $T_1$ . If the thermodynamic or kinetic reaction (1) is more favorable, component *A* will be transported preferentially. This leads to a spatial separation of the main substance and impurity, which provides the purification effect.

The partition coefficient  $\alpha$  for chemical purification methods is determined by the ratio:

$$\alpha = \frac{x^*}{x^* + x} / \frac{y^*}{y^* + y}, \quad (3)$$

where  $x, x^*$  – concentrations of the main substance and impurity in the starting reagents;  $y, y^*$  – concentrations of the main substance and impurity in the reaction products. If the impurity is transported less efficiently than the main substance, the reaction products are impoverished by the impurity compared to the initial reagents, and  $\alpha > 1$ . For the simplified case, when all stoichiometric coefficients of the reactions (1) and (2) are equal to 1,  $\alpha$  can be estimated by standard thermodynamic functions of chemical transport participants [20]:

$$\ln \alpha = \ln \frac{K_1^0}{K_2^0} = \frac{\Delta_r H_2^0 - \Delta_r H_1^0}{RT} - \frac{\Delta_r S_2^0 - \Delta_r S_1^0}{R}, \quad (4)$$

where  $K_1^0$  and  $K_2^0$  – standard equilibrium constants of reactions;  $\Delta_r H_1^0$  and  $\Delta_r H_2^0$  – changes in the standard enthalpies of reactions;  $\Delta_r S_1^0$  and  $\Delta_r S_2^0$  – changes in the standard entropies of reactions;  $R$  – universal gas constant; index 1 refers to the reaction involving the main substance, index 2 to the reaction involving the impurity. When modeling chemical transport by the method of minimizing thermodynamic potentials, the partition coefficient is estimated directly from the calculated equilibrium concentrations of the system components. It should be noted that the above calculation method is an estimation, since in reality chemical transport of substances occurs under conditions far from thermodynamic equilibrium. The separation effect in chemical transport can be based not only on differences in equilibrium constants, but also on differences in the rate constants of reactions involving the main substance and impurity.

### 2.1 Chemical transport of gallium

Gallium(III) iodide is a convenient reagent for vacuum loading of gallium into a reactor with a chalcogenide batch with chemical transport. The transport agent can be prepared by passing iodine vapor over metallic gallium in a vacuum reactor and further purified by multiple distillation. Chemical transport is based on the reaction:



At higher temperatures, the reaction proceeds in the forward direction, transferring non-volatile gallium to the vapor phase in the form of monoiodide. In the lower temperature region of the reactor, gallium monoiodide disproportionates, releasing metallic gallium and  $\text{GaI}_3$ . The main impurities limiting the optical properties of chalcogenide glasses contained in especially pure gallium are  $\text{Ga}_2\text{O}_3$  and  $\text{Ga}(\text{OH})_3$ . They have absorption bands in the range 10, 15–20  $\mu\text{m}$  [21, 22] and may be in the form of heterogeneous inclusions at concentrations above the solubility limit. These impurities are formed when manipulating (weighing, loading, storage) metallic gallium and are not controlled in commercial high purity samples. To evaluate the optimal conditions of chemical transport

ensuring high efficiency of gallium loading and its purification from oxide impurities, the  $\text{GaI}_3$  –  $\text{Ga} - \text{Ga}_2\text{O}_3$  system was modeled using the method of minimization of thermodynamic potentials in the IVTANTERMO software package [23]. The quantitative evaluation of the efficiency of the purification of gallium from oxygen impurities was carried out on the basis of the calculation of the separation coefficient  $\alpha_{[\text{O}]}(T)$ , which was determined from the ratio of the initial concentration of this impurity in the condensed phase  $n_{[\text{O}]}^0$  to the equilibrium pressure in the vapor phase  $p_{[\text{O}]}(T)$  at a given temperature:

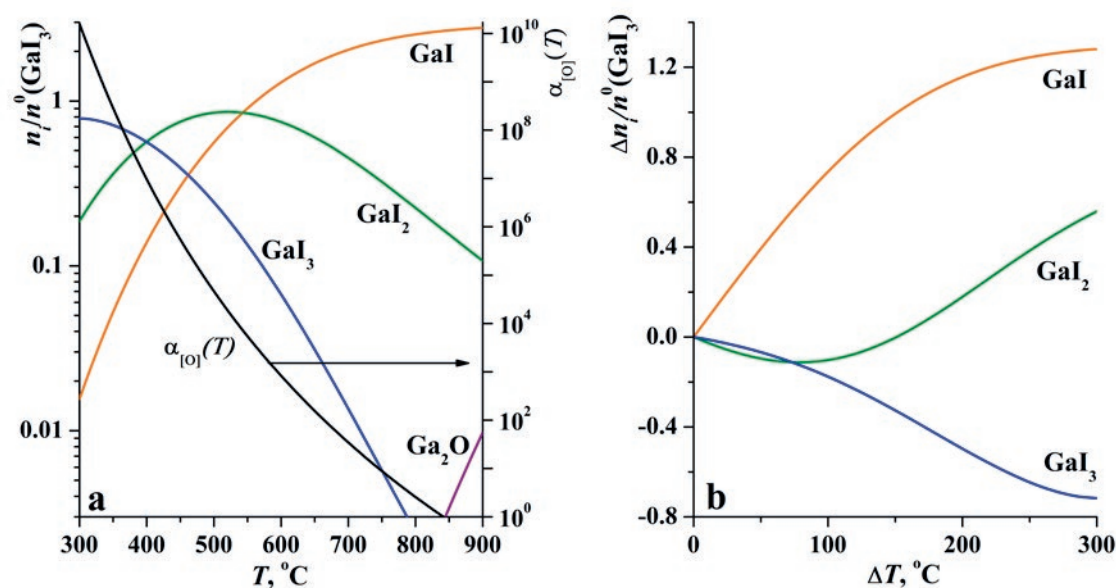
$$a_{[\text{O}]}(T) = \frac{n_{[\text{O}]}^0}{\sum n_i^0} / \frac{p_{[\text{O}]}(T)}{\sum p_i(T)} \quad (6)$$

where  $n_i^0$  – initial content of the  $i$ -th component in the condensed phase;  $p_i(T)$  – equilibrium pressure of the  $i$ -th component at temperature  $T$ .

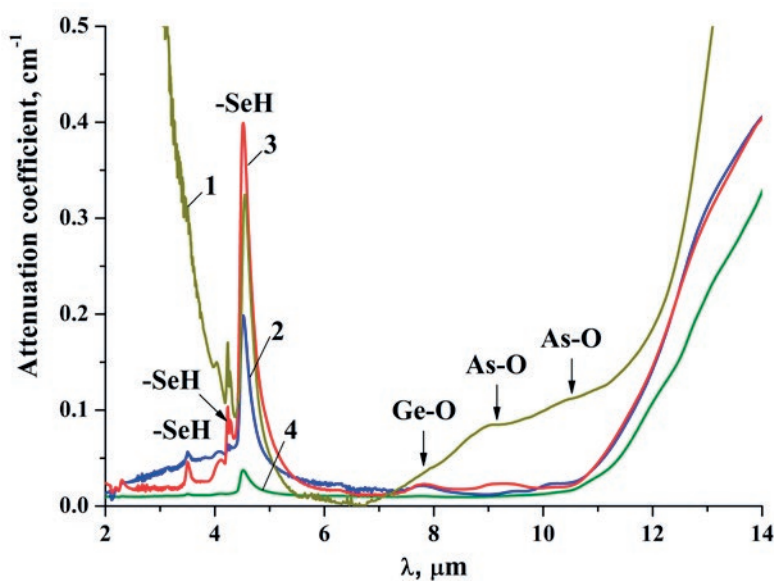
Fig. 1a shows the results of modeling in terms of temperature dependence of the relative concentrations of the vapor phase components and oxygen impurity partition coefficient. The high content of gallium monoiodide in the system is reached at temperatures  $> 600$  °C. From the dependence of the concentration differences of the vapor phase components at 600 °C and a given temperature  $T$  (flow method [19]), it follows that efficient transport is observed at  $\Delta T > 250$  °C (Fig. 1b). The oxygen-containing component of the vapor phase is gallium(I) oxide. At 600 °C, the partition coefficient is about  $10^3$ , indicating the high efficiency of chemical transport to purify gallium from oxygen impurities. The data obtained was used as reference values for the development of the gallium loading method.

The method was used to prepare glasses of the  $\text{Ga} - \text{Ge} - \text{As} - \text{Se}$  system [24]. The optimum conditions for chemical transport are as following: the temperature in the ampoule with gallium 600–650 °C; temperature of the  $\text{GaI}_3$  evaporator 220–240 °C; the temperature of the gallium receiver 250–280 °C. The  $\text{Ge} - \text{As} - \text{Se}$  batch, previously alloyed with aluminum and  $\text{TeCl}_4$  to bind oxygen and hydrogen impurities, was fed into the gallium reactor by vacuum distillation. The glass synthesis was carried out at 800 °C for 4 hours in a rocking furnace.

Figure 2 shows the absorption spectra of four glass samples prepared by different methods.



**Fig. 1.** Thermodynamically determined composition of the  $\text{GaI}_3 - \text{Ga} - \text{Ga}_2\text{O}_3$  system (a) and the dependence of the amount of the transferred vapor phase component on the temperature difference  $\Delta T = 600^\circ\text{C} - T$  (b)



**Fig. 2.** Absorption spectra of glasses prepared by different methods: 1 – the  $\text{Ga}_3\text{Ge}_{16}\text{As}_{17}\text{Se}_{64}$  sample, prepared by melting simple high purity substances; 2 – the  $\text{Ge}_{16}\text{As}_{17}\text{Se}_{67}$  sample, prepared with the addition of getters and distillation purification of the melt; 3 – the  $\text{Ga}_3\text{Ge}_{16}\text{As}_{17}\text{Se}_{64}$  sample, prepared from sample 1 with the addition of gallium by the usual loading; 4 – the  $\text{Ga}_3\text{Ge}_{16}\text{As}_{17}\text{Se}_{64}$  sample, prepared by the method of sample 1 with the addition of gallium by the chemical transport method [69]

Sample 1, with the  $\text{Ga}_3\text{Ge}_{16}\text{As}_{17}\text{Se}_{64}$  composition, was prepared by melting simple, especially pure substances without additional purification. Sample 2, with the  $\text{Ge}_{16}\text{As}_{17}\text{Se}_{67}$  composition was prepared by adding getters and purification of the melt by distillation. The other two samples,

with the  $\text{Ga}_3\text{Ge}_{16}\text{As}_{17}\text{Se}_{64}$  composition were synthesized using the same technique with the addition of metallic gallium by conventional loading (sample 3) and chemical transport (sample 4). In sample 1, along with the high intensity of the absorption bands, we observe a significant



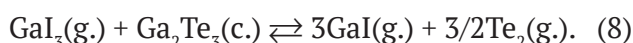
scattering in the short wavelength region of the spectrum. This is due to the presence of gallium(III) oxide impurities in the form of heterogeneous inclusions. The addition of gallium to the  $\text{Ge}_{16}\text{As}_{17}\text{Se}_{67}$  glass by the conventional method leads to a 2-fold increase in the intensity of the absorption bands of the SeH- groups, germanium and arsenic oxides – by a factor of 3. This is due to the incorporation of  $\text{Ga}_2\text{O}_3$  and  $\text{Ga}(\text{OH})_3$  impurities (or a more complex composition) present in the initial metallic 7N gallium. In the glass prepared with Ga loading with chemical transport, the intensity of the impurity absorption bands is lower by an order of magnitude. Consequently, the developed method has high efficiency for preparing gallium-containing chalcogenide glasses with the low impurity content.

### 1.2. Chemical transport of gallium telluride(III)

The high chemical activity of gallium towards the silica glass reactor is a disadvantage of chemical transport in the form of a simple substance. This facilitates the formation of relatively volatile lower iodides of gallium and silicon, which enter the glass-forming melt:

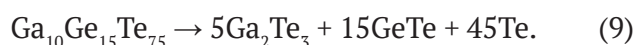


To avoid contact of metallic gallium with the reactor walls when preparing glasses of the Ga – Ge – Te system, a method of transport loading of gallium(III) telluride has been developed [25, 26]. The method is based on the reaction:



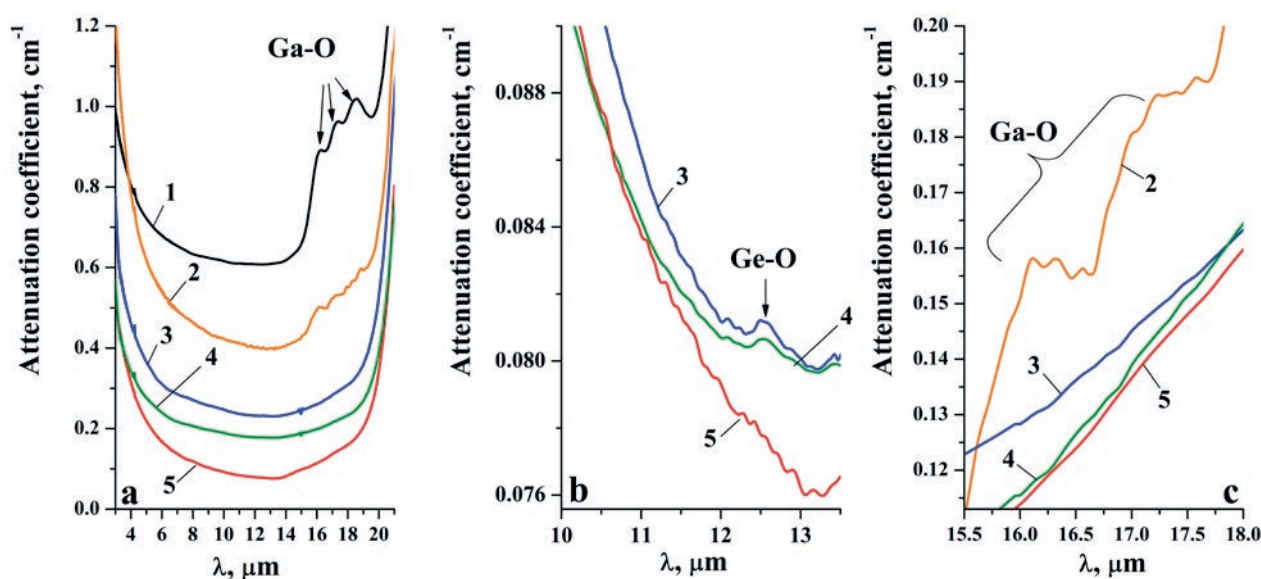
According to the results of thermodynamic modeling [25], a significant transition of gallium to the vapor phase in the form of GaI happens at temperatures above 600 °C. The minimum value of  $\Delta T$  for effective chemical transport of gallium telluride(III) at 750 °C is 250 °C. The oxygen impurity content can theoretically be reduced by a factor of  $10^3$ – $10^4$  at transport temperatures of 680–700 °C. It has been experimentally determined that the optimum conditions for chemical transport of gallium telluride are: the temperature in the ampoule with  $\text{Ga}_2\text{Te}_3$  is 680–720 °C; the temperature of the  $\text{GaI}_3$  vaporizer is 220–240 °C; the temperature of the  $\text{Ga}_2\text{Te}_3$  receiver is 250–280 °C. The average loading rate of  $\text{Ga}_2\text{Te}_3$  under these conditions was  $0.3 \text{ g}\cdot\text{h}^{-1}\cdot\text{cm}^{-2}$ .

A specific task in the transport loading of gallium(III) telluride for preparing especially pure chalcogenide glasses is the synthesis of this compound. The interaction of simple substances in the intermediate reactor requires the subsequent extraction of the synthesized telluride and its introduction into the chemical transport unit. These operations have a high probability of contaminating the reactant with atmospheric impurities. The tellurium vapor passing over metallic gallium, analogous to the synthesis of GeTe [27], is inefficient because the resulting layer of non-volatile  $\text{Ga}_2\text{Te}_3$  prevents further reaction. In view of these difficulties, a method of  $\text{Ga}_2\text{Te}_3$  synthesis has been developed which consists in preparing a glass with the composition  $\text{Ga}_{10}\text{Ge}_{15}\text{Te}_{75}$  by the interaction of simple substances and its subsequent thermal decomposition. According to the results of X-ray diffraction phase analysis and atomic emission spectrometry with inductively coupled plasma [28], the decomposition of  $\text{Ga}_{10}\text{Ge}_{15}\text{Te}_{75}$  glass at a temperature of 750 °C can be described by a chemical reaction:



The method was used to synthesize the especially pure  $\text{Ga}_{10}\text{Ge}_{15}\text{Te}_{75}$  and  $\text{Ga}_{10}\text{Ge}_{15}\text{Te}_{75}\text{I}_2$  glasses. In the first step, the  $(\text{GeTe})_x\text{Te}_{100-x}$  batch was prepared by passing tellurium vapor over a mixture of germanium granules with aluminum and loaded into an ampoule with metallic gallium. The ampoule was sealed, and the batch was melted at 800 °C for five hours without being disconnected from the vacuum post. Tellurium and germanium(II) telluride were then extracted from the resulting  $\text{Ga}_{10}\text{Ge}_{15}\text{Te}_{75}$  melt at 750 °C. Gallium(III) telluride was left in the evaporator. In the next step, the transport loading of gallium(III) telluride into the batch reactor was carried out by passing of gallium(III) iodide. To obtain  $\text{Ga}_{10}\text{Ge}_{15}\text{Te}_{75}\text{I}_2$  glasses with improved stability against crystallization, the calculated amount of gallium(III) iodide was returned to the batch. The ampoule containing the batch was sealed-off and melted at 850 °C for five hours. The melt was quenched in water and annealed at 170 °C to relieve mechanical stress.

Fig. 3 shows the absorption spectra of glasses of the Ga – Ge – Te – I system, prepared



**Fig. 3.** Absorption spectra of Ga – Ge – Te – I glasses prepared by different methods: in a wide spectral range (a), in the absorption range of germanium oxide impurity (b), in the absorption range of gallium oxides (c). 1 – the  $\text{Ga}_{10}\text{Ge}_{15}\text{Te}_{75}\text{I}_2$  sample, prepared by melting simple substances and germanium(IV) iodide; 2 – the  $\text{Ga}_{10}\text{Ge}_{15}\text{Te}_{75}$  sample, prepared with preliminary synthesis of  $\text{Ga}_2\text{Te}_3$  in an individual reactor and subsequent chemical transport; 3 – the  $\text{Ga}_{10}\text{Ge}_{15}\text{Te}_{75}\text{I}_2$  sample, prepared with preliminary synthesis of  $\text{Ga}_2\text{Te}_3$  by passing tellurium vapor over gallium and subsequent chemical transport; 4 – the  $\text{Ga}_{10}\text{Ge}_{15}\text{Te}_{75}\text{I}_2$  sample, prepared with loading of metallic gallium by chemical transport [28]; 5 – the  $\text{Ga}_{10}\text{Ge}_{15}\text{Te}_{75}$  sample, prepared with preliminary synthesis of  $\text{Ga}_2\text{Te}_3$  by decomposition of  $\text{Ga}_{10}\text{Ge}_{15}\text{Te}_{75}$  and subsequent chemical transport [25]

by different techniques, in a broad spectral range (a), in the impurity absorption region of germanium oxides (b), in the absorption region of gallium oxides (c). The lowest intensity of the impurity absorption bands is observed for the sample prepared with  $\text{Ga}_2\text{Te}_3$  chemical transport, synthesized by thermal decomposition of the  $\text{Ga}_{10}\text{Ge}_{15}\text{Te}_{75}$  glass. The intensities of the impurity bands in this sample are below the detection limit obtained for samples up to 30 mm in length. The estimated Ge–O impurity content calculated from the absorption in the 12.5 μm region is <1 ppb(wt). This is by far the best result for germanium and gallium telluride-based glasses. The absence of a known absorption coefficient for oxygen impurity in the form of gallium oxides makes it difficult to estimate its content.

### 2.3 Chemical transport of REE

The interest in REE-doped chalcogenide glasses is due to the possibility of achieving mid-IR laser generation in them. REEs have been shown to be a significant source of hydrogen

impurities and heterogeneous inclusions in chalcogenide glasses [29]. Hydrogen in REEs is present in dissolved form and as stable hydrides [30]. The difficulty in purifying REEs from hydrogen by conventional heating in vacuum is due to the thermal stability and refractoriness of the hydrides: most of them decompose significantly only above the melting point (> 1000 °C). Hydrogen impurity can have a significant negative effect on the luminescence and generation properties of doped chalcogenide glasses due to radiation-free impurity relaxation [31]. This is due to the spectral proximity of the absorption bands of SH- and SeH groups and the emission bands of REEs.

To prepare especially pure glasses, we proposed to use a method of vacuum alloying of metals with gallium for purifying REEs from hydrogen impurities [32]. The addition of gallium significantly reduces the decomposition temperature of REE hydrides due to the formation of fusible intermetallics, e.g.  $\text{Ga}_3\text{Tm}$ ,  $\text{Ga}_2\text{Pr}$ ,  $\text{Ga}_2\text{Tb}$ . This ensures efficient purification at

temperatures of 700–750 °C. In combination with germanium loading via monochalcogenides, the method made it possible to significantly reduce the content of hydrogen impurities in the form of SH- and SeH- groups in REE-doped  $\text{Ga}_5\text{Ge}_{36}\text{S}_{59}$  and  $\text{Ga}_5\text{Ge}_{36}\text{Se}_{59}$  glasses from  $(10-26) \pm 2$  ppm(at.) to  $(0.16-0.22) \pm 0.02$  ppm(at.) (Fig. 4) [32]. In the Tb-doped  $\text{Ga}_5\text{Ge}_{36}\text{Se}_{59}$  sample prepared by the developed method, laser generation in the 5  $\mu\text{m}$  range was achieved for the first time for chalcogenide glasses [5].

To prepare REE-doped optical fibers, the requirements for the content of heterogeneous impurities, which have a negative effect on the optical losses, increase significantly. The doping of chalcogenide glasses leads to contamination with REE oxide inclusions and products of their interaction with the silica glass reactor [33]. For deep purification of this type of impurity, a method consisting of chemical transport of REE in a gallium(III) iodide flow has been developed [34]:



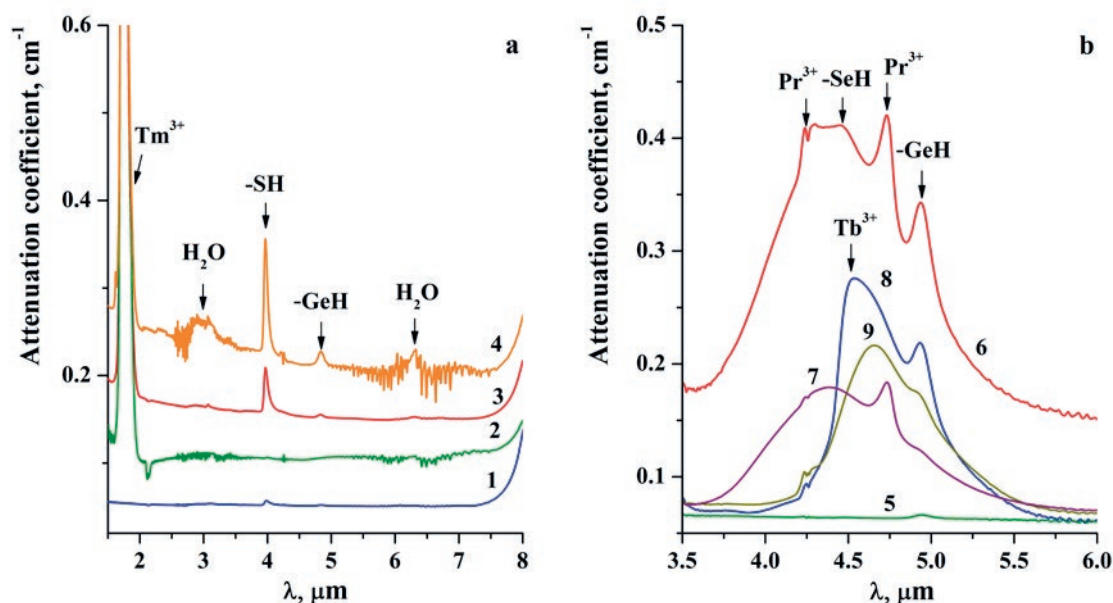
where R – REE. According to the results of thermodynamic modeling of  $\text{GaI}_3 - \text{R} - \text{R}_2\text{O}_3$  sys-

tems, the effective chemical transport of REE takes place at reactor temperatures above 650 °C and  $\Delta T > 250$  °C. The equilibrium partition coefficient for oxygen impurity under these conditions is in the order of  $n \times 10^3$ . The formation of complex iodides may also facilitate chemical transport:



The volatility of such complexes is significantly higher than that of the simple iodides of the corresponding REE [35]. It has been found experimentally that the average rate of chemical transport increases by two orders of magnitude at preliminary alloying of REE with gallium. This may be due to the additional amount of GaI by reaction (12), which promotes the formation of complex iodides. This approach enables the simultaneous loading of REE and gallium into the batch reactor.

The  $\text{Ga}_5\text{Ge}_{20}\text{Sb}_{10}\text{Se}_{65}$  composition was chosen as a base glass for REE doping. This glass has high crystallization stability, which is a critical property for preparing low-loss optical fibers. The glasses



**Fig. 4.** Absorption spectra of  $\text{Ga}_5\text{Ge}_{36}\text{S}_{59}$  glasses doped with 1400 ppm(wt) Tm (a) and  $\text{Ga}_5\text{Ge}_{36}\text{Se}_{59}$  glasses doped with 760 ppm(wt) Pr or Tb, prepared using different methods of REE purification (b). 1 – undoped sample; 2 – vacuum alloying of Tm and Ga; 3 – treatment of Tm in sulfur vapor (the technique is proposed in [33]); 4 – without Tm purification; 5 – undoped sample; 6 – without Pr purification; 7 – vacuum alloying of Pr and Ga; 8 – treatment of Tb in selenium vapor; 9 – vacuum alloying of Tb and Ga [32]



were doped with Ce, Pr, Nd, Tb, Dy in the range of 0.05–1 wt. %. The developed process included the following main steps: 1) preparation of Ge – Sb – Se batch by passing selenium vapor over a mixture of germanium and antimony; 2) double distillation of the batch; 3) alloying of gallium with REE; 4) chemical transport of REE and gallium in the flow of gallium(III) iodide into the reactor; 5) loading of Ge – Sb – Se batch by distillation into the reactor with gallium and REE; 6) melting of  $\text{Ga}_5\text{Ge}_{20}\text{Sb}_{10}\text{Se}_{65}$  + REE batch, quenching of the melt, glass annealing and slow cooling.

It has been shown that at chemical transport loading of rare earth metals, some impurities (REE oxides,  $\text{SiO}_2$ ,  $\text{Al}_2\text{O}_3$ ,  $\text{Ga}_2\text{O}_3$ ,  $\text{TiO}_2$ ,  $\text{Ta}_2\text{O}_5$ , REE oxofluorides), chemically inert to gallium iodide vapors, remain in the initial ampoule. Metal impurities (iron, manganese, titanium, aluminum, tin, etc.), capable of forming stable and volatile at temperatures of 300–700 °C simple and complex iodides, are transported together with the REE iodides; tungsten and molybdenum impurities do not completely transform into iodides and are partially transported. In the process of REE loading they are purified from impurities of fluorine, hydrogen, oxygen, some metals, and heterogeneous inclusions.

The glass samples doped up to 1 wt % REEs were prepared with reproducibly low content of hydrogen impurity in the form of SeH-groups not more than 1.5 ppm(at.); metals in total < 1 ppm(wt.); micron-sized inclusions

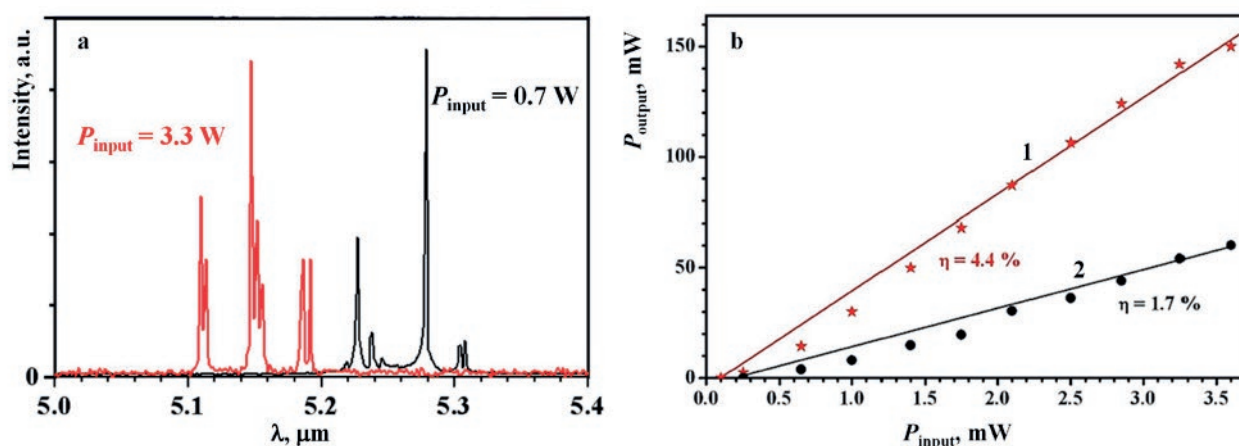
<  $10^2$  pcs/cm<sup>3</sup> and submicron particles – at the level not exceeding the background scattering of the glass. Optical losses in the optical fiber with the 20 μm diameter  $\text{Ga}_5\text{Ge}_{20}\text{Sb}_{10}\text{Se}_{65}$  + 1130 ppm(wt) Tb core glass and  $\text{Ge}_{12}\text{As}_{20}\text{Sb}_5\text{S}_{63}$  clad glass were 1.8 dB/m at a wavelength of 1.56 μm [6]. This is significantly lower than the values measured in 230 μm diameter unclad optical fibers doped with 500 ppm(wt)  $\text{PrCl}_3$  or  $\text{PrI}_3$  prepared by the conventional method in [36] (25–75 dB/m).

Fig. 5 shows the spectrum of laser generation in the optical fiber drawn from  $\text{Ga}_5\text{Ge}_{20}\text{Sb}_{10}\text{Se}_{65}$  + 1130 ppm(wt) Tb glass [7]. The 53 cm long fiber was pumped with a thulium laser ( $\lambda = 1.98$  μm). The maximum output power was 150 mW. The possibility of achieving laser generation in the 5 μm region in doped chalcogenide glasses with practically significant properties correlates with the presence of micron heterogeneous inclusions and optical losses due to these inclusions. Significant characteristics of laser generation have so far been achieved only in samples prepared using the developed method of REE loading, in which the content of micron inclusions does not exceed <  $10^2$  pcs/cm<sup>3</sup>.

The limitation of the developed method of REE loading is due to the high reactivity of their iodides towards silica glass [37]:



In this reaction, REE iodides act as transporters for silica(IV), which enters the chalcogenide



**Fig. 5.** Laser generation spectra of the optic fiber fabricated from the 1130 ppm(wt) Tb-doped  $\text{Ga}_5\text{Ge}_{20}\text{Sb}_{10}\text{Se}_{65}$  core glass and the  $\text{Ge}_{12}\text{As}_{20}\text{Sb}_5\text{S}_{63}$  cladding glass (a); the dependence of the output power of generation  $P_{\text{output}}$  on the pump power  $P_{\text{input}}$  (b). Curves b1 and b2 refer to optical schemes with the use of an attached mirror and without it respectively. Parameter  $\eta$  is the slope efficiency [7]

batch. Heterogeneous  $\text{SiO}_2$  inclusions appear to be the main source of excessive optical losses in fibers based on doped chalcogenide glasses. To improve the laser properties of chalcogenide optical fibers, it is necessary to further reduce the content of this impurity.

### 3. Application of REE for binding oxygen impurities

Due to the disadvantages of aluminum and magnesium mentioned in [18], a search was initiated for alternative getters to prepare especially pure chalcogenide glasses with a low content of oxygen impurities. It was found that along with an increase in the intensity of the absorption bands of hydrogen-containing impurities, the addition of REE leads to a significant increase in the transparency of the glasses in the absorption regions of germanium, tellurium and gallium oxides. The results of thermodynamic modeling predict a high ability of REE to reduce oxides of chalcogenide glass components, which increases in the series  $(\text{Al}) \rightarrow \text{Eu} \rightarrow \text{Ce} \rightarrow \text{La} \rightarrow \text{Pm} \rightarrow \text{Pr} \rightarrow \text{Nd} \rightarrow \text{Sm} \rightarrow \text{Yb} \rightarrow \text{Gd} \rightarrow \text{Dy} \rightarrow \text{Tb} \rightarrow \text{Tm} \rightarrow \text{Lu} \rightarrow \text{Ho} \rightarrow \text{Er} \rightarrow \text{Y}$  [38].

To experimentally confirm the efficiency of REEs as oxygen impurity getters, a series of glasses with the  $\text{Ga}_{10}\text{Ge}_{15}\text{Te}_{75}$  + 1000 ppm (wt) REE composition were prepared [38]. The absorption spectra of the prepared samples are shown in Figure 6. The  $\text{Ge}_{20}\text{Te}_{80}$  glass spectrum shows

intense absorption bands of  $\text{Te-O}$  (13.6  $\mu\text{m}$ ) and  $\text{Ge-O}$  (12.6 and 8.0  $\mu\text{m}$ ). In the spectrum of the  $\text{Ga}_{10}\text{Ge}_{15}\text{Te}_{75}$  sample without the addition of the getter, the intensity of these bands decreases by a factor of 30–50. Intense  $\text{Ga-O}$  bands appear in the 15–20  $\mu\text{m}$  region and a low intensity band in the 10  $\mu\text{m}$  region, which may correspond to  $\text{Ga-OH}$  impurity [22]. Consequently, gallium is quite effective in reducing germanium and tellurium oxides and improving the transparency of telluride glasses in the 8–15  $\mu\text{m}$  region. The addition of 1000 ppm(wt) of aluminum and REE to  $\text{Ga}_{10}\text{Ge}_{15}\text{Te}_{75}$  glasses results in a significant decrease in the intensity ( $< 5 \cdot 10^{-4} \text{ cm}^{-1}$ ) of the  $\text{Ga-O}$ ,  $\text{Ga-OH}$  and  $\text{Ge-O}$  absorption bands due to the greater reducing power of these elements compared to gallium. This corresponds to a reduction in the impurity content of the gallium(III) oxide by 3 orders of magnitude. Absorption bands of the corresponding oxides appear in the spectra of glasses doped with Al, Pr, Sm, La and Eu [39]. When distilling the glass-forming melt, a significant decrease in the intensity of these bands can be expected due to the non-volatility of the oxides. However, the absence of absorption bands in the initial samples is preferable, as incomplete removal of oxides during distillation may occur. In the spectrum of the Eu-doped sample, the intensity of the oxide band is the highest among the REEs studied and the  $\text{Ga-O}$  absorption bands are present. This

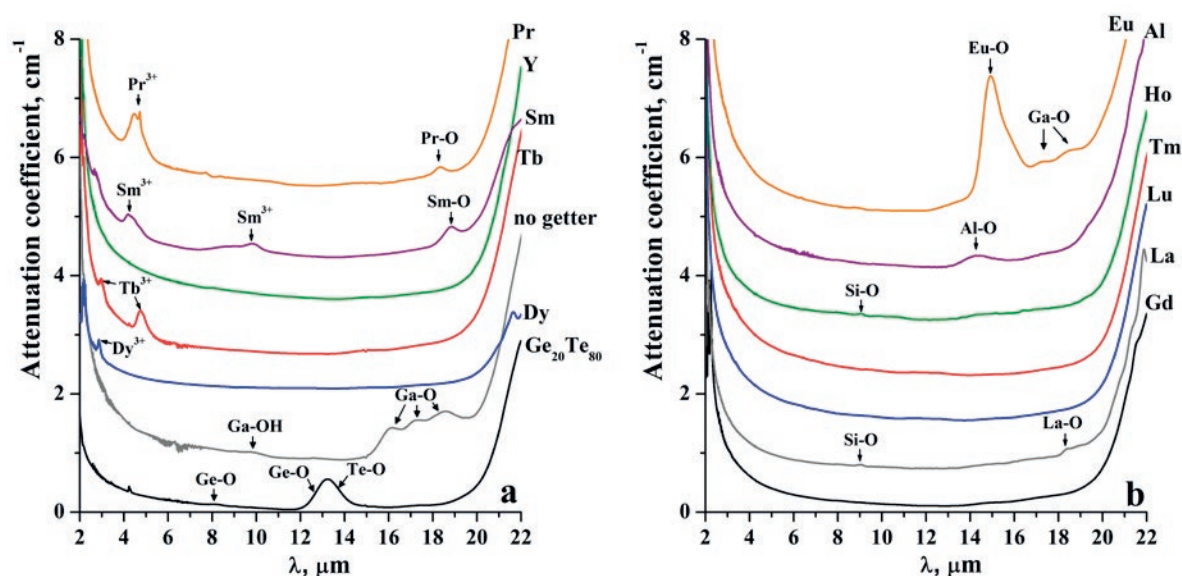


Fig. 6. Absorption spectra of  $\text{Ga}_{10}\text{Ge}_{15}\text{Te}_{75}$  glasses with the addition of 1000 ppm(wt) of getter [38]

is due to the tendency of europium to oxidize rapidly in the air and to have the lowest reducing power among the REEs according to the results of thermodynamic modeling.

The spectra of glasses doped with Dy, Tb, Sm and Pr show absorption bands due to electronic transitions [40]. In the studied samples of  $\text{Ga}_{10}\text{Ge}_{15}\text{Te}_{75}$  glasses in the spectral range of 2–20  $\mu\text{m}$ , there are no intense absorption bands when doped with Y, Gd and Lu. These getters seem to be the most suitable for preparing especially pure telluride glasses with low oxygen impurity content. Ho and Tm can also be included in this series as their absorption bands as electronic transitions are in the short wavelength region ( $< 2 \mu\text{m}$ ) and practically do not appear in the spectrum of the telluride glass. However, these bands will be present in the spectra of sulfide and selenide glasses.

Among 11 REEs investigated for their ability to bind oxygen impurities in chalcogenide glasses, the following groups can be distinguished:

- 1) give no absorption bands due to electron transitions and oxide impurities – Y, Gd, Lu;
- 2) give absorption bands due to electronic transitions but no oxide bands – Tm, Dy, Tb and Ho;
- 3) give oxide absorption bands – Eu, Sm, Pr, La.

The advantages of REE groups 1) and 2) in comparison with aluminum, which is conventionally used as a getter, are:

- high efficiency in the reduction of gallium, germanium and tellurium oxides;
- more complete removal at distillation of chalcogenide glass melt;
- absence of intense absorption bands from oxides in the glass transparency region;
- lower etching capacity of the silica-glass surface compared to aluminum.

These REEs are recommended as getters for preparing especially pure glasses with extremely low oxygen impurity content. For example, the efficiency of Dy as a getter for preparing especially pure glasses of the Ge – As – Sb – S system has been shown in [41].

The disadvantage of REEs as oxygen getters compared to aluminum is rapid oxidation when stored in the air. Aluminum in contact with oxygen and moisture is covered with a thin but dense protective film which prevents further

oxidation. REEs, mainly La, Pr, Ce, Nd, Eu and Sm, oxidize quite rapidly to form oxides, hydroxides, carbonates and hydrocarbonates. Oxidation penetrates deep into the metal volume, so the application of these REEs requires special sample preparation. To a lesser extent, oxidation in air is characteristic of Y, Gd and Lu.

#### 4. Conclusions

The chemical transport method is highly efficient in preparing especially pure chalcogenide glasses with extremely low content of limiting impurities. This is due to the fundamental reasons that the separation factor in this deep purification method is determined by the ratios of equilibrium constants or rates of chemical reactions involving the main substance and impurities. By selecting a suitable transport agent and optimizing the process conditions, it is possible to achieve high values of the separation factor and ensure a reduction of the impurity content by several orders of magnitude in a single stage.

A major advantage of chemical transport is that it is not only a method of deep purification, but also of vacuum loading of the batch components into the reactor. This eliminates subsequent interaction of the purified materials with the air atmosphere until the finished glass is removed from the reactor.

*P*-element iodides are the optimal, but not the only transport agents for deep purification of chalcogenide batch components. There are several fundamental and technological reasons for this. Firstly, iodides exhibit less chemical activity against silica-glass at elevated temperatures than other halides. Secondly, residual iodines (typically less than 0.1 at.%) do not adversely affect the target properties of the glasses. As noted in the first part of the review [18], small additions of iodide increase the crystallization stability of the glasses, the overall level and range of transparency, and promote the dissolution of REE. Thirdly, iodides are easily synthesized under laboratory conditions without the use of highly toxic reagents. Along with gallium(III) iodide, germanium(IV) iodide can be used for the chemical transport of batch components, particularly in the preparation of gallium-free glasses.

A further improvement of the developed methods for preparing especially pure



chalcogenide glasses may be the multiple purification of the batch components with chemical transport. In this case, the efficiency of impurity removal compared to a single process increases in  $\alpha^{n-1}$  time, where  $n$  – the number of stages. Another direction is to extend the range of batch components that can be purified and loaded with chemical transport. Silver iodide is one of such components. The addition of AgI significantly increases the crystallization stability of telluride glasses and makes it possible to fabricate optical fibers from them [10, 42].

The most significant result presented in the review is the achievement of mid- IR laser generation on REEs in chalcogenide glasses, which was previously not possible. This result is an example of a solution to a classic problem in the chemistry of high-purity substances – increasing the purity of materials led to the discovery of a new functional property in them, which was not manifest due to the high impurity content for this property. This brings chalcogenide glasses into the class of laser materials [43] and greatly expands their practical applications.

### Author contributions

A. P. Velmuzhov – research concept, methodology development, conducting research, text writing, final conclusions. M. V. Sukhanov – research concept, methodology development, conducting research, editing. E. A. Tyurina – methodology development, conducting research, editing. V.S. Shiryayev – research concept, conducting research, editing.

### Conflict of interests

The authors declare that they have no known competing financial interests or personal relationships that could have influenced the work reported in this paper.

### References

1. Heo J., Chung W. J., Rare-earth-doped chalcogenide glass for lasers and amplifiers. In: *Chalcogenide glasses: preparation, properties and applications*. J.-L. Adam, X. Zhang (eds.). Oxford Cambridge Philadelphia New Delhi: Woodhead publishing series in electronic and optical materials; 2014;44: 347–380. <https://doi.org/10.1533/9780857093561.2.347>
2. Jackson S. D., Jain R. K. Fiber-based sources of coherent MIR radiation: key advances and future prospects. *Optics Express*. 2020;28(21): 30964–31017. <https://doi.org/10.1364/OE.400003>
3. Sojka L., Tang Z., Zhu H., ... Sujecki S. Study of mid-infrared laser action in chalcogenide rare earth doped glass with Dy<sup>3+</sup>, Pr<sup>3+</sup> and Tb<sup>3+</sup>. *Optical Materials Express*. 2012;2(11): 1632–1640. <https://doi.org/10.1364/OME.2.001632>
4. Sujecki S., Sojka L., Beres-Pawlik E., ... Seddon A. B. Numerical modelling of Tb<sup>3+</sup> doped selenide-chalcogenide multimode fibre based spontaneous emission sources. *Optical and Quantum Electronics*. 2018;50: 416. <https://doi.org/10.1007/s11082-017-1255-5>
5. Churbanov M. F., Denker B. I., Galagan B. I., ... Velmuzhov A. P. First demonstration of ~ 5  $\mu$ m laser action in terbium-doped selenide glass. *Applied Physics B: Lasers and Optics*. 2020;126(7): 117. <https://doi.org/10.1007/s00340-020-07473-w>
6. Denker B. I., Galagan B. I., Koltashev V. V., ... Velmuzhov A. P. Continuous Tb-doped fiber laser emitting at ~5.25  $\mu$ m. *Optics and Laser Technology*. 2022;154: 108355. <https://doi.org/10.1016/j.optlastec.2022.108355>
7. Koltashev V. V., Denker B. I., Galagan B. I., ... Plotnichenko V. G. 150 mW Tb<sup>3+</sup> doped chalcogenide glass fiber laser emitting at  $\lambda > 5 \mu$ m. *Optics & Laser Technology*. 2023;161: 109233. <https://doi.org/10.1016/j.optlastec.2023.109233>
8. Shiryayev V. S., Sukhanov M. V., Velmuzhov A. P., ... Plotnichenko V. G. Core-clad terbium doped chalcogenide glass fiber with laser action at 5.38  $\mu$ m. *Journal of Non-Crystalline Solids*. 2021;567: 120939. <https://doi.org/10.1016/j.jnoncrysol.2021.120939>
9. Le Coq D., Cui S., Boussard-Plédel C., Masselin P., Bychkov E., Bureau B. Telluride glasses with far-infrared transmission up to 35  $\mu$ m. *Optical Materials*. 2017;72: 809–812. <https://doi.org/10.1016/j.optmat.2017.07.038>
10. Cui S., Boussard-Plédel C., Lucas J., Bureau B. Te-based glass fiber for far-infrared biochemical sensing up to 16  $\mu$ m. *Optics Express*. 2014;22(18): 21253. <https://doi.org/10.1364/OE.22.021253>
11. Chatwin C. R. Carbon dioxide laser. In: *Encyclopedia of modern optics*. 2005: 289–400. <https://doi.org/10.1016/B0-12-369395-0/00845-9>
12. Wilhelm A. A., Boussard-Plédel C., Coulombier Q., Lucas J., Bureau B., Lucas P. Development of far-infrared-transmitting Te based glasses suitable for carbon dioxide detection and space optics. *Advanced Materials*. 2007;19: 3796–3800. <https://doi.org/10.1002/adma.200700823>
13. Bureau B., Maurugeon S., Charpentier F., Adam J.-L., Boussard-Plédel C., Zhang X.-H. Chalcogenide glass fibers for infrared sensing and space optics. *Fiber and Integrated Optics*. 2009; 28: 65–80. <https://doi.org/10.1080/01468030802272542>
14. Zhang S., Zhang X., Barillot M., ... Parent G. Purification of Te<sub>75</sub>Ga<sub>10</sub>Ge<sub>15</sub> glass for far infrared transmitting optics for space application. *Optical Materials*. 2010;32: 1055–1059. <https://doi.org/10.1016/j.optmat.2010.02.030>
15. Speiser R., Johnston H. L. Vapor pressures of inorganic substances. IX. Gallium. 1953;75(6): 1469–1470. <https://doi.org/10.1021/ja01102a057>
16. Habermann C. E., Daane A. H. Vapor pressures of the rare-earth metals. *The Journal of Chemical Physics*. 1964;41: 2818–2827. <https://doi.org/10.1063/1.1726358>

17. Churbanov M. F., Shiryayev V. S. Preparation of high-purity chalcogenide glasses. In: *Chalcogenide glasses: preparation, properties and applications*. J.-L. Adam, X. Zhang (eds.). J.-L. Adam, X. Zhang (eds.). Oxford Cambridge Philadelphia New Delhi: Woodhead publishing series in electronic and optical materials; 2014;44: 3–35. <https://doi.org/10.1533/9780857093561.1.3>
18. Velmuzhov A. P., Sukhanov M. V., Tyurina E. A., Shiryayev V. S. Advanced methods for preparing especially pure glasses based on germanium and gallium chalcogenides. Part 1. Synthesis via volatile and low-melting compounds. Review. *Condensed Matter and Interphases*. 2025;27(1): 16–28. <https://doi.org/10.17308/kcmf.2025.27/12482>
19. Schäfer H. *Chemical transport reactions*. New York, London: Academic Press; 1964. 174 p.
20. Devyatykh G. G., Elliev Yu. E. *Introduction to the theory of deep purification of substances\**. Moscow: Nauka Publ.; 1981. 320 p. (In Russ.)
21. He Y., Wang X., Nie Q., ... Dai S. Optical properties of Ge–Te–Ga doping Al and AlCl<sub>3</sub> far infrared transmitting chalcogenide glasses. *Infrared Physics & Technology*. 2013;58: 1–4. <https://doi.org/10.1016/j.infrared.2012.12.038>
22. Taş A. C., Majewski P. J., Aldinger F. Synthesis of gallium oxide hydroxide crystals in aqueous solutions with or without urea and their calcination behavior. *Journal of the American Ceramic Society*. 2002;85(6): 1421–1429. <https://doi.org/10.1111/j.1151-2916.2002.tb00291.x>
23. IVTANTHERMO: Thermodynamic database and software for PC, version 3.0\* [Electronic resource]. Moscow: THERMOCENTER RAS; 1992–2005. (In Russ.)
24. Shiryayev V. S., Velmuzhov A. P., Tang Z.Q., Churbanov M.F., Seddon A.B. Preparation of high purity glasses in the Ga–Ge–As–Se system. *Optical Materials*. 2014;37: 18–23. <https://doi.org/10.1016/j.optmat.2014.04.021>
25. Velmuzhov A. P., Sukhanov M. V., Anoshina D. E., ... Shiryayev V. S. Preparation of high purity glasses based on germanium and gallium tellurides using chemical transport. *Journal of Non-Crystalline Solids*. 2022;585: 121529. <https://doi.org/10.1016/j.jnoncrsol.2022.121529>
26. Sukhanov M. V., Velmuzhov A. P., Tyurina E. A., Blagin R. D. *Method for producing extra-pure chalcogenide glasses containing gallium*. RF Patent: No. 2770494. Publ. 18.04.2022, Bull. No. 11. Available at: <https://patenton.ru/patent/RU2770494C1.pdf>
27. Velmuzhov A. P., Tyurina E. A., Sukhanov M. V., ... Shiryayev V.S. Distillation with separate condensation of components as a new way to prepare especially pure Ge<sub>x</sub>Te<sub>100-x</sub> glasses with precisely desired composition. *Separation and Purification Technology*. 2023;324: 124532. <https://doi.org/10.1016/j.seppur.2023.124532>
28. Velmuzhov A. P., Sukhanov M. V., Shiryayev V. S., Plekhovich A. D. Preparation of high-purity germanium telluride based glasses with low oxygen impurity content. *Journal of Non-Crystalline Solids*. 2021;553: 120480. <https://doi.org/10.1016/j.jnoncrsol.2020.120480>
29. Sukhanov M. V., Velmuzhov A. P., Otopkova P. A., ... Shiryayev V. S. Rare earth elements as a source of impurities in doped chalcogenide glasses. *Journal of Non-Crystalline Solids*. 2022;593: 121793. <https://doi.org/10.1016/j.jnoncrsol.2022.121793>
30. Mikheeva V. I., Kost M. E. The hydrides of the rare-earth metals. *Russian Chemical Reviews*. 1960;29(1): 55–73. <https://doi.org/10.1070/RC1960v029n01ABEH001216>
31. Seddon A. B., Tang Z., Furniss D., Sujecki S., Benson T. M. Progress in rare-earth-doped mid-infrared fiber lasers. *Optics Express*. 2010;18(25): 26704. <https://doi.org/10.1364/OE.18.026704>
32. Velmuzhov A. P., Sukhanov M. V., Plotnichenko V. G., Plekhovich A. D., Shiryayev V. S., Churbanov M. F. Preparation of REE-doped Ge-based chalcogenide glasses with low hydrogen impurity content. *Journal of Non-Crystalline Solids*. 2019;525: 119669. <https://doi.org/10.1016/j.jnoncrsol.2019.119669>
33. Sukhanov M. V., Velmuzhov A. P., Kotereva T. V., Skripachev I. V., Churbanov M. F. New approach for preparation of high-purity sulfide-germanium glasses doped with praseodymium. *Optical Materials*. 2019;9(8): 3204–3214. <https://doi.org/10.1364/OME.9.003204>
34. Sukhanov M. V., Velmuzhov A. P., Ketkova L. A., ... Sverchkov S. E. Method for preparing high-purity REE-doped chalcogenide glasses for bulk and fiber lasers operating at ~ 5 μm region. *Journal of Non-Crystalline Solids*. 2023;608: 122256. <https://doi.org/10.1016/j.jnoncrsol.2023.122256>
35. Boghosian S., Papatheodoros G. N. Halide vapors and vapor complex. *Handbook on the physics and chemistry of rare earths*. 1996;23: 435–496. [https://doi.org/10.1016/S0168-1273\(96\)23008-9](https://doi.org/10.1016/S0168-1273(96)23008-9)
36. Tang Z., Sojka L., Furniss D., ... Seddon A. B. Comparative study of praseodymium additives in active selenide chalcogenide optical fibers. *Optical Materials Express*. 2018;8: 3910–3926. <https://doi.org/10.1364/OME.8.003910>
37. Van Erk W. Transport processes in metal halide gas discharge lamps. *Pure and Applied Chemistry*. 2000;72(11): 2159–2166. <https://doi.org/10.1351/pac200072112159>
38. Velmuzhov A. P., Sukhanov M. V., Tyurina E. A., Evdokimov I. I., Kurganova A. E., Shiryayev V. S. Rare-earth metals as effective getters for purification of germanium telluride glasses from oxygen impurities. *Journal of Non-Crystalline Solids*. 2023;603: 122112. <https://doi.org/10.1016/j.jnoncrsol.2022.122112>
39. Baun W., McDevitt N. T. Infrared absorption spectra of rare-earth oxides in the Region 800 to 240 cm<sup>-1</sup>. *Journal of the American Ceramic Society*. 1963;46(6): 294. <https://doi.org/10.1111/j.1151-2916.1963.tb11729.x>
40. Liu G. Electronic energy level structure. In: *Spectroscopic Properties of Rare Earths in Optical Materials*. R. Hull, J. Parisi, R. M. Osgood, H. Warlimont, G. Liu, B. Jacquier (eds.). Berlin, Germany: Springer Verlag; 2005;83: 1–94. [https://doi.org/10.1007/3-540-28209-2\\_7](https://doi.org/10.1007/3-540-28209-2_7)
41. Karaksina E. V., Blagin R. D., Sukhanov M. V., ... Shiryayev V. S. Preparation and properties of especially pure Ge–Sb–As–S glasses for IR optics. *Journal of Non-Crystalline Solids*. 2024;642: 123158. <https://doi.org/10.1016/j.jnoncrsol.2024.123158>
42. Shiryayev V. S., Velmuzhov A. P., Churbanov M. F., ... Plotnichenko V. G. Preparation and investigation of high purity Ge–Te–AgI glasses for optical application. *Journal of Non-Crystalline Solids*. 2013; 377: 1–7. <https://doi.org/10.1016/j.jnoncrsol.2013.03.039>
43. Sukhanov M. V., Velmuzhov A. P., Snopatin G. E., ... Sverchkov S. E. Chalcogenide glasses doped with rare-earth

elements – established laser materials in the 5–6  $\mu\text{m}$  range. *High-purity substances. Preparation, analysis, application: Abstracts of the XVII All-Russian Conference, June 7–9, 2022, Nizhny Novgorod\**. Nizhny Novgorod: IAP RAS, 2022. p. 147. (In Russ.)

*\* Translated by author of the article*

### Information about the authors

Alexander P. Velmuzhov, Cand. Sci. (Chem.), Senior Research Fellow at the Laboratory of High-Purity Chalcogenide Glasses for Mid-IR Photonics, G. G. Devyatykh Institute of Chemistry of High-Purity Substances of the Russian Academy of Science (Nizhny Novgorod, Russian Federation).

<https://orcid.org/0000-0002-8739-3868>

[velmuzhov.ichps@mail.ru](mailto:velmuzhov.ichps@mail.ru)

Maxim V. Sukhanov, Cand. Sci. (Chem.), Senior Research Fellow at the Laboratory of High-Purity Chalcogenide Glasses for Mid-IR Photonics, G. G. Devyatykh Institute of Chemistry of High-Purity Substances of the Russian Academy of Science (Nizhny Novgorod, Russian Federation).

<https://orcid.org/0000-0003-0525-6286>

[sukhanov@ihps-nnov.ru](mailto:sukhanov@ihps-nnov.ru)

Elizaveta A. Tyurina, Cand. Sci. (Chem.), Junior Research Fellow at the Laboratory of High-Purity Chalcogenide Glasses for Mid-IR Photonics, G. G. Devyatykh Institute of Chemistry of High-Purity Substances of the Russian Academy of Science (Nizhny Novgorod, Russian Federation).

<https://orcid.org/0000-0002-6107-9862>

[tyurina.ichps@mail.ru](mailto:tyurina.ichps@mail.ru)

Vladimir S. Shiryaev, Dr. Sci. (Chem.), Deputy Director for Research, G. G. Devyatykh Institute of Chemistry of High-Purity Substances of the Russian Academy of Science (Nizhny Novgorod, Russian Federation).

<https://orcid.org/0000-0002-1726-7313>

[shiryaev@ihps-nnov.ru](mailto:shiryaev@ihps-nnov.ru)

*Received 15.08.2024; approved after reviewing 26.08.2024; accepted for publication 16.09.2024; published online 25.06.2025.*





## Original articles

Research article

<https://doi.org/10.17308/kcmf.2025.27/12764>

## On the mechanism of recrystallization of bismuth chalcogenides during photonic treatment with incoherent radiation

E. K. Belonogov<sup>1,2</sup>, S. B. Kushev<sup>1</sup>✉, D. V. Serikov<sup>3</sup>, S. A. Soldatenko<sup>1</sup>, T. L. Turaeva<sup>1</sup>

<sup>1</sup>Voronezh State Technical University,  
84 20-letiya Oktyabrya st., Voronezh 394006, Russian Federation

<sup>2</sup>Voronezh State University,  
1 Universitetskaya pl., Voronezh 394018, Russian Federation

<sup>3</sup>Voronezh Communications Design Bureau,  
16B Krasnodonskaya st., Voronezh 394019, Russian Federation

### Abstract

**Purpose:** The aim of this work is to reveal the nature and systematize the mechanisms of gradient structure formation in the surface layer of bismuth chalcogenide during photon treatment with incoherent radiation from xenon lamps.

**Experimental:** Semiconductor thermoelectric branches based on  $\text{Bi}_2\text{Te}_3\text{--Bi}_2\text{Se}_3$  solid solutions have been investigated by transmission electron microscopy, X-ray diffractometry, and photometry methods. The nature of nanostructuring and formation of gradient layer in the surface region of  $\text{Bi}_2\text{Te}_{3-x}\text{Se}_x$  thermoelectric at photon treatment by incoherent radiation of xenon lamps is considered.

**Conclusions:** It is shown that these processes can be caused by a sequence of independent processes: growth of free electron concentration, decrease of defect formation threshold, localization in skin layer of high temperature gradient, generation and propagation of sonic phonons, collecting and secondary recrystallization, formation of nanocrystalline phase in Bi-Te-Se system.

**Keywords:** Photon treatment, Recrystallization, Electron microscopic micrograph, X-ray diffractometry, Nanostructured layer, Lattice defects, Bismuth chalcogenides

**For citation:** Belonogov E. K., Kushchev S. B., Serikov D. V., Soldatenko S. A., Turaeva T. L. On the mechanism of recrystallization of bismuth chalcogenides during photonic treatment with incoherent radiation. *Condensed Matter and Interphases*. 2025;27(2): 203–210. <https://doi.org/10.17308/kcmf.2025.27/12764>

**Для цитирования:** Белоногов Е. К., Кушев С. Б., Сериков Д. В., Солдатенко С. А., Тураева Т. Л. О механизме рекристаллизации халькогенидов висмута при фотонной обработке некогерентным излучением. *Конденсированные среды и межфазные границы*. 2025;27(2): 203–210. <https://doi.org/10.17308/kcmf.2025.27/12764>

✉ Sergey B. Kushev, e-mail: [kushev\\_sb@mail.ru](mailto:kushev_sb@mail.ru)

© Belonogov E. K., Kushchev S. B., Serikov D. V., Soldatenko S. A., Turaeva T. L., 2025



The content is available under Creative Commons Attribution 4.0 License.

## 1. Introduction

Increasing the efficiency of thermoelectric devices along with the search for new materials includes the development of new technologies for the realization of metal-semiconductor switching interconnection. Previously, the authors of this article have conducted a series of studies of the effect of pulsed photon treatment (PT) by radiation of powerful xenon lamps on the mechanical properties of semiconductor thermoelectric branches (based on solid solutions  $\text{Bi}_2\text{Te}_3\text{--Bi}_2\text{Se}_3$ ) and adhesion of interconnect layers [1], electrical properties [2], thermal conductivity and Q-factor of thermoelectric branches [3]. These studies have shown the principal possibility and efficiency of using the PT method in the development of thermoelectric devices. It was shown in [4] that the energy effect of PT stimulates local recrystallization of the surface layer, which leads to the formation at a depth of  $\sim 500$  nm of an area characterized by a gradient dispersion of the crystal structure, namely, adjacent large and nanoscale crystallites and, as a consequence, to changes in the electrical properties, thermal conductivity and thermoelectric Q of semiconductor materials.

The authors of papers [5–7] have shown that the effect of PT compared to conventional thermal treatment is manifested in the acceleration of diffusion processes [5], increase in the dispersity of the formed structures [6], and decrease in the temperature thresholds of phase formation [7]. Possible mechanisms of acceleration at photon activation of metal diffusion processes in semiconductors, synthesis of silicides and recrystallization in metal films have been considered in papers [8–10]. However, as shown in the review [11], the current mechanisms of activation of processes due to their complexity and stages in each specific case are not the same and require individual consideration taking into account the athermic and thermal nature. On the examples of synthesis of thin films of metals, silicides, carbides, nitrides and oxides, the authors considered the effect of PT, manifested in the excitation of the electronic subsystem (for the crystallization of amorphous materials), the rupture of interatomic bonds, the formation of vacancies, recrystallization. Such studies of massive multicomponent semiconductor systems

have not been carried out, and the mechanism of the influence of PT on the structure of the surface region of the semiconductor material  $\text{Bi}_2\text{Te}_{3-x}\text{Se}_x$  still awaits its detailed characterization.

The aim of this work is to reveal the nature and systematize the mechanisms of gradient structure formation in the surface layer of bismuth chalcogenide at PT by incoherent radiation of xenon lamps.

## 2. Experimental part

Initial samples of  $\text{Bi}_2\text{Te}_{3-x}\text{Se}_x$  ( $x \sim 1$ ) for research were obtained by the method of cold and subsequent hot pressing in steel molds from the powder of material of corresponding composition with dispersity of  $0.063 \div 1$  mm.

PT of plates was performed alternately from both sides by powerful radiation of xenon lamps (spectral range  $\lambda = 0.2 \div 1.2$   $\mu\text{m}$ ) in argon atmosphere on the UOLP-1M installation with radiation doses  $E_1 = 125 \div 175$   $\text{J}/\text{cm}^2$ , which corresponded to the processing time  $1 \div 1.4$  s.

To investigate the wavelength dependence of the reflection coefficient for  $\text{Bi}_2\text{Te}_{3-x}\text{Se}_x$  samples, rectangular samples of  $10 \times 10 \times 0.5$   $\text{mm}^3$  with larger faces normal to the briquette pressing axis (z-cut) and parallel to the briquette pressing axis (x-cut) were used. Reflection spectra of unpolarized radiation were recorded on a Lambda 650 spectrophotometer with a URA module in the wavelength range  $0.190 \div 0.9$   $\mu\text{m}$  with a resolution of  $\pm 0.15$  nm at a temperature of 300 K, the angle of incidence of radiation on the sample did not exceed  $8^\circ$ .

## 3. Results and their discussion

Previously, we found [4] that the energy effect of PT at  $E_1 \sim 175$   $\text{J}/\text{cm}^2$  stimulates local recrystallization of the surface layer with the formation in the surface region of the solid solution  $\text{Bi}_2\text{Te}_{3-x}\text{Se}_x$  (n-type) gradient region at a depth of  $\sim 500$  nm and more (Fig.1). ), in which large crystallites of  $0.5 \div 3$  microns in size border the surface nanostructured layer with a high density of defects (nanopores, nanocracks, inclusions) and crystallite size  $\sim 15 \div 30$  nm.

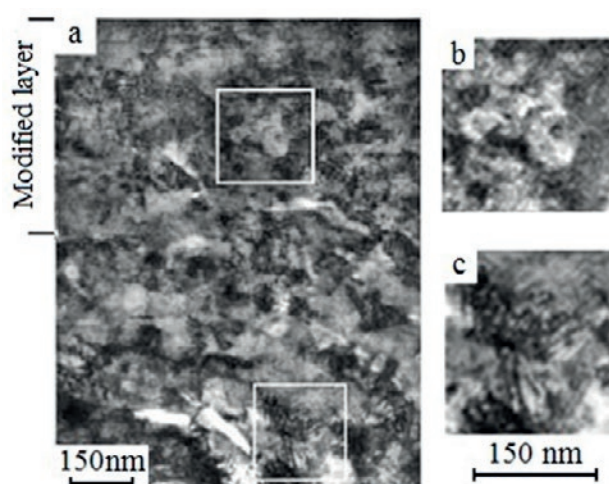
The modified layer contains a large number of pores and inclusions (Fig. 1a), the average density of which is  $\sim 2 \cdot 10^{10}$   $\text{cm}^{-2}$ . Crystallites are morphologically isotropic (average size

$\sim 40\div 60$  nm) and practically do not contain linear defects (dislocations).

The material in the sample volume (starting from a depth of  $1\text{ }\mu\text{m}$ ) has a large-block structure (Fig. 1b), the crystallite size is  $0.5\div 3\text{ }\mu\text{m}$ . This grain structure is characterized by the presence of large lamellar inclusions and cracks ranging in size from  $50\text{ nm}$  to  $1\text{ }\mu\text{m}$ , as well as small globular defects up to  $50\text{ nm}$ . Some large crystallites contain a network of dislocations with a linear density of  $\sim 1\text{--}10^6\text{ cm}^{-2}$ .

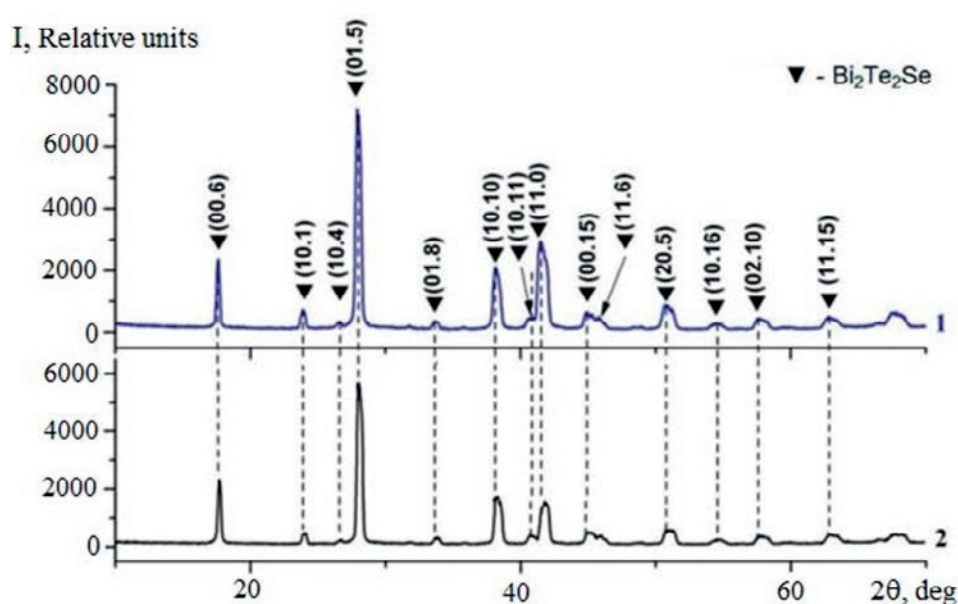
No change in the phase composition of the samples after PT was detected, as evidenced by X-ray diffractometry studies (Fig. 2). Thus, when the surface of bismuth telluride is irradiated with high-energy radiation from xenon lamps for a very short period of time ( $t = 1.4\text{ s}$ ), accelerated recrystallization occurs in the surface layer of the material with the formation of a gradient nanocrystalline structure without changing the phase composition.

According to [12] the emission spectrum of xenon lamps INP-16/250 is incoherent, covers the wavelength range of  $0.2\text{--}1.2\text{ }\mu\text{m}$  and has two maxima near  $0.4$  and  $0.9\text{ }\mu\text{m}$  (Fig. 3). This spectrum was obtained at minimum values of radiation power. With increasing power of xenon lamps, the plasma temperature increases with increasing fraction of ultraviolet radiation and decreasing fraction of infrared radiation [13].



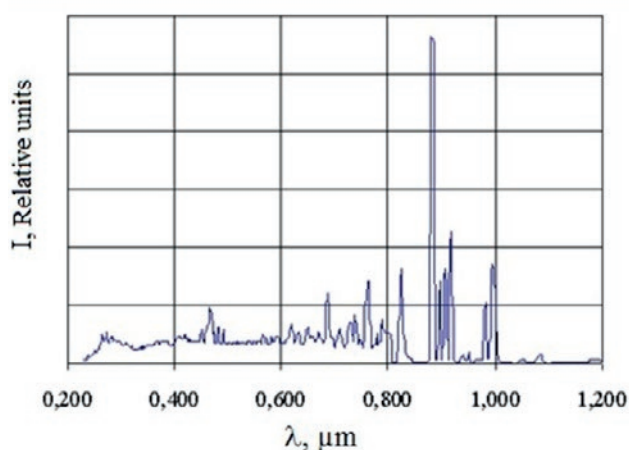
**Fig. 1.** TEM micrograph of a cross section of a  $\text{Bi}_2\text{Te}_{3-x}\text{Se}_x$  sample after PT in argon at  $E_t \sim 175\text{ J/cm}^2$  [4]

According to paper [14], the concentration of free electrons in bismuth telluride is  $n = (2.0\div 2.25)\cdot 10^{20}\text{ cm}^{-3}$ . The concentration of free electrons increases at the PT surface of  $\text{Bi}_2\text{Te}_3$  due to the internal photoeffect. The maximum intensity of electromagnetic radiation from xenon lamps in the infrared range of  $0.8\div 1.0\text{ }\mu\text{m}$  corresponds to the energy interval of photons  $(2.0\div 2.5)\cdot 10^{-19}\text{ J}$  ( $1.4\div 1.6\text{ eV}$ ). At the irradiation dose with  $E_t = 125\text{ J/cm}^2$  delivered to the sample in  $1.4\text{ s}$ , the photon flux is more than  $3\cdot 10^{20}\text{ cm}^{-2}\cdot\text{s}^{-1}$ .



**Fig. 2.** X-ray diffractograms from the surface of the studied samples before (1) and after PT in Ar with  $E_t \sim 125\text{ J/cm}^2$  (2) [4]





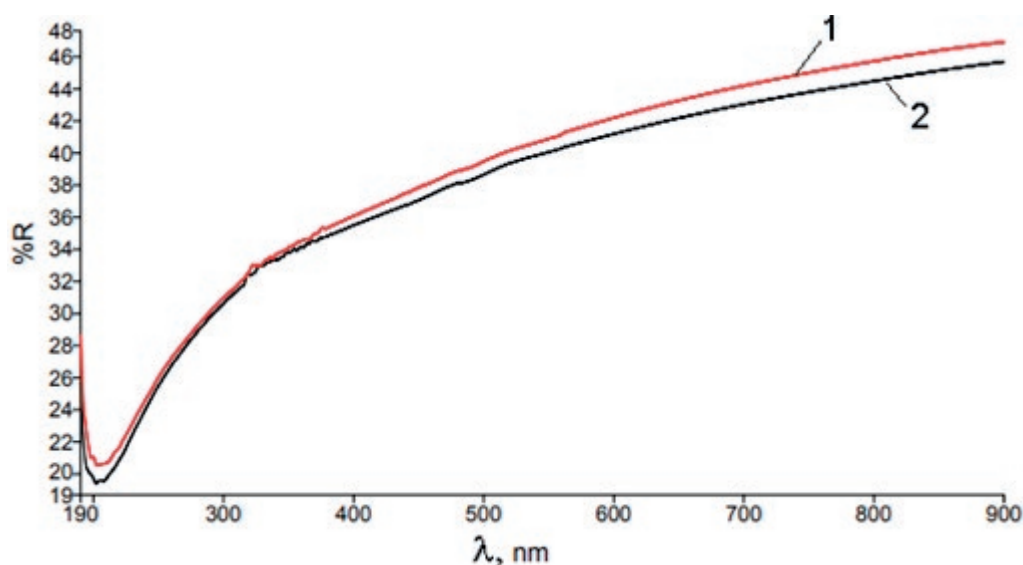
**Fig. 3.** Spectral distribution of the emission intensity of xenon lamps INP 16/250 [12]

The band gap of bismuth telluride is  $0.15 \div 0.17$  eV [15], so the photon energy of xenon lamps is sufficient to activate electronic conduction in the surface layer of the material, the thickness of which is equal to the thickness of the skin layer for the infrared range in  $\text{Bi}_2\text{Te}_3$ . Thus, the concentration of electrons in the surface layer of bismuth telluride at the moment of PT is comparable to the concentration of free electrons in the metal. The free electrons in the metal in the process of scattering electromagnetic waves form a reflected wave of high intensity, allowing a small fraction of the radiation in. As a rule, in the infrared and visible parts of the spectrum the reflection coefficient is larger than in the ultraviolet range [16].

Fig.4 shows the reflection spectra of the surfaces of z- and x-sections of the original  $\text{Bi}_2\text{Te}_{3-x}\text{Se}_x$  samples. As can be seen from the figure, for both samples in the spectrum there are no maxima or minima, indicating polarization or absorption of radiation by the crystal in this region of the spectrum. The curves are monotonic and similar to the dependences observed for metals in the corresponding wavelength range [16]. The reflection coefficient is  $20 \div 28$  and  $42 \div 48$  % in the ultraviolet and infrared ranges, respectively. A slight difference in the reflectivity of z- and x-cut samples indicates the lowest roughness of the briquette faces, which are cut perpendicular to the pressing axis. The obtained results are in agreement with the data of [17, 18], in which the lumen studies of thin films of  $\text{Bi}_2\text{Te}_3$  and  $\text{Bi}_2\text{Te}_{2.7}\text{Se}_{0.3}$  with a thickness of  $\sim 100$  nm in the wavelength range of  $0.2 \div 1.1$   $\mu\text{m}$  showed low transmittance. Thus, the transmittance ratio for  $\text{Bi}_2\text{Te}_3$  was not more than 15% and for  $\text{Bi}_2\text{Te}_{2.7}\text{Se}_{0.3}$  not more than 3 %.

It can be assumed that for the investigated  $\text{Bi}_2\text{Te}_{3-x}\text{Se}_x$  samples the skin effect, i.e. exponential decrease of the absorbed energy at removal from the surface, will be manifested in the process of PT. The skin-layer thickness in bismuth telluride for a given emission spectrum can be estimated by the known approximation  $\delta = \frac{1}{\sqrt{\pi\nu\mu\mu_0\sigma}}$ , where

$\nu$  – emission frequency,  $\mu_0$  – magnetic constant;



**Fig. 4.** Reflection coefficient spectra of  $\text{Bi}_2\text{Te}_{3-x}\text{Se}_x$  crystals: curve 1 - z-cut, curve 2 - x-cut

$\mu$  – relative magnetic permeability;  $\sigma$  – specific electrical conductivity [19, 20].

Based on the obtained data, Fig. 5 shows the dependence of the skin layer thickness for  $\text{Bi}_2\text{Te}_3$  on the wavelength and photon energy of PT. The skin layer thickness does not exceed 90 nm for the whole radiation spectrum.

Also, for comparison, we evaluated the radiation absorption depth  $\delta$  in polycrystalline bismuth telluride films for the wavelength range  $0.2 \div 1.4 \mu\text{m}$  using in calculations the optical parameters of the material [21, 22]:  $\delta = 2/\alpha$ , where  $\alpha = 4\pi k/\lambda_0$  is the attenuation coefficient,  $k$  is the extinction coefficient [22],  $\lambda_0$  is the wavelength of the incident radiation. The results are presented in Fig. 6.

Comparison of the skin-layer thickness determined from the electrical and optical characteristics in the wavelength range  $0.4 \div 1.2 \mu\text{m}$  with the results described above allows us to conclude that the entire radiation energy is absorbed in the  $\text{Bi}_2\text{Te}_{3-x}\text{Se}_x$  surface layer with a thickness not exceeding 60 nm. Electron-photon interaction takes place in the whole range of xenon lamps, so several mechanisms of acceleration of the recrystallization process of the surface layer are possible. First, energy absorption in a small surface layer leads to surface heating, which initiates active propagation of acoustic phonons in the surface region. Second, a pulsed multiple increase in the number of charge carriers (exclusively in the surface region of the material)

will lead to a concentration gradient and diffusion of charge carriers from the surface region into the material volume. These factors will lead to an intense interaction between electrons and acoustic phonons in a skin layer no thicker than 60 nm. As a result of electron-phonon interaction, the concentration of defects, primarily vacancies, increases sharply in the surface region of the material, which accelerates the recrystallization process.

Due to the gradient nature of the energy impact at PT, the collecting recrystallization within the skin layer is very difficult, and secondary recrystallization is possible both within the skin layer and in the volume of the material, which leads to the formation of a gradient grain structure at the surface of the material. Activation of secondary recrystallization in the surface layer of bismuth telluride is due to the nonequilibrium concentration of vacancies that actively diffuse from the skin layer.

The photon energies of xenon lamps are sufficient for the formation and migration of tellurium vacancies ( $1.41 \div 1.18$  and  $0.94 \div 1.17$  eV, respectively [15]). Consequently, for an absorption coefficient  $\mu = 2.1 \cdot 10^7 \text{ m}^{-1}$  ( $\lambda \approx 0.55 \mu\text{m}$ ) [23] at a skin-layer depth of 50 nm, the intensity of absorbed light energy ( $I = 0.62 - I_0 \exp(-\mu h) \approx 0.2I_0$ ) is up to 20% of the incident at PT, which corresponds to the number of absorbed quanta of light  $\approx 6 \cdot 10^{19}$ . The same layer of irradiated material contains about  $3.3 \cdot 10^{16}$  atoms, so the fraction of atoms in the excited state can be extremely large. It was shown in papers [24–25] that laser irradiation

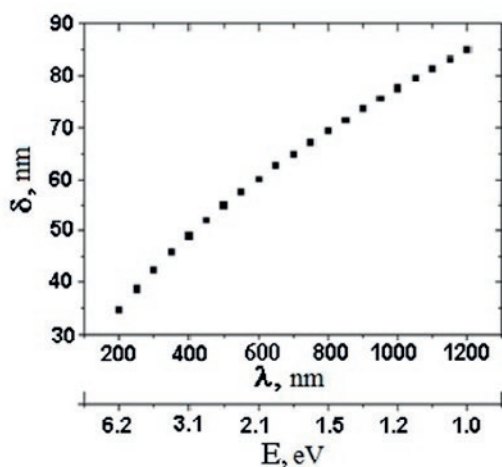


Fig. 5. Graph of dependence of skin layer thickness on the wavelength / photon energy of incident radiation

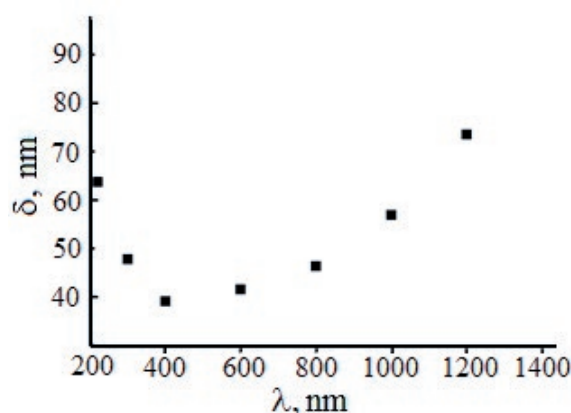


Fig. 6. Dependence of absorption depth for polycrystalline films of bismuth telluride on the wavelength of incident radiation

of metal films initiates a high concentration of nonequilibrium vacancies (up to  $10^{-4}$ ). Taking into account practically equal values of vacancy formation energies in metals and bismuth telluride  $1.2 \div 1.4$  eV [26] and  $1.18 \div 1.41$  eV [15], respectively, we can assume for bismuth telluride the vacancy concentration of  $\sim 10^{-4}$ .

The nature of the PT effect can be analyzed in the framework of the theory of excitation of the electronic subsystem of the crystal by high-energy quanta of light [27]. The skin effect limits light penetration to depths on the order of wavelength. The absorbed energy excites surface electronic states relaxing as a result of electron-phonon interaction mainly by the radiationless mechanism. The probability of such a transition

in the Bickson–Jortner model [28] is  $P = e^{-\frac{2\pi}{\hbar} v_{\text{eff}}^2 \rho_{\text{eff}}}$ , where  $v_{\text{eff}}^2$  – some effective matrix element of the electron-phonon interaction, and  $\rho_{\text{eff}}$  – the effective density of electronic states. Excited surface centers propagate hypersonic waves into the sample volume. Emerging phonons of resonance frequencies, determined by elastic parameters and crystal symmetry, have amplitude of oscillations significantly higher than thermal ones. The high energy of vibrating atoms allows them to initiate phase transformations and leads to structural rearrangements. Since the hypersonic velocity is three orders of magnitude greater than the thermal field propagation velocity, powerful hypersonic waves lead to the formation of point crystal defects, which do not occur during heat treatment, or occur at higher temperatures. This photon activation mechanism

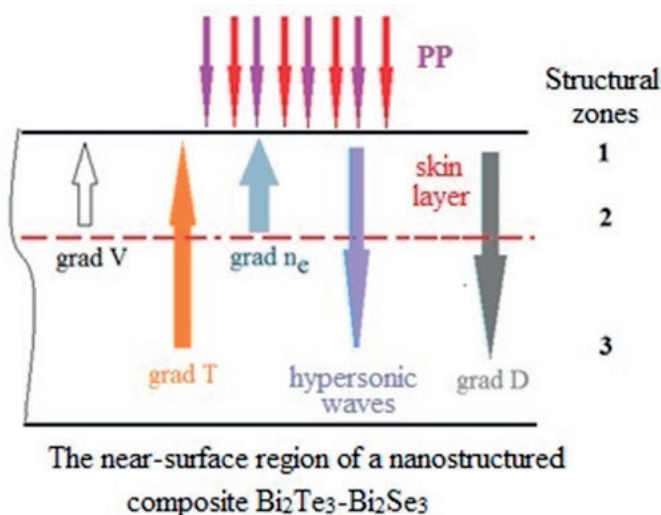
explains the acceleration of the recrystallization process in metal thin films at PT [11].

It can be seen that the formation of the gradient structure in the surface layer ( $\sim 500$  nm) during the PT of  $\text{Bi}_2\text{Te}_{3-x}\text{Se}_x$  plates can be caused by the complex interaction of the processes simultaneously occurring during PT: amorphization, formation of nanocrystalline phase, growth of free electron concentration, generation of nonequilibrium vacancies under the action of hypersonic phonons, flux from the skin layer of point defects, growth of material plasticity, secondary recrystallization initiated by sonic phonons and temperature gradient [29].

A significant increase in the sample surface temperature to  $0.4 \div 1.0 T_{\text{PL}}$  at PT [29] precludes amorphization of the surface region of  $\text{Bi}_2\text{Te}_{3-x}\text{Se}_x$  plates. The diffractograms from  $\text{Bi}_2\text{Te}_3$ – $\text{Bi}_2\text{Se}_3$  plates after PT show no peaks (Fig. 2), indicating the formation of new phases. Consequently, the processes of phase transformations, formation of superstructures, and spinoidal decomposition can be considered unlikely in the PT process.

Fig. 7 schematically presents an illustration of the processes assisting phase and structural transformations in the PT process.

A conventional division into structural zones near the surface of  $\text{Bi}_2\text{Te}_{3-x}\text{Se}_x$  plates can be proposed: 1) the most defective region preserving nanocrystalline phases after PT; 2) the region of structural rearrangement of the material by hypersonic phonons; 3) the region of secondary recrystallization initiated by sonic phonons, a high concentration of mobile point defects



**Fig. 7.** Schematic illustration of the processes assisting structural transformations at the surface of  $\text{Bi}_2\text{Te}_{3-x}\text{Se}_x$  plates during the PT process:  $V$  – local vacancy concentration;  $n_e$  – concentration of free electrons;  $T$  – local temperature;  $D$  – average crystallite size; 1, 2, 3 – conditional zones differing in dispersion of the crystal structure



coming from the skin layer. These zones can significantly overlap each other, however, the gradient principle remains and forms a gradient grain structure, where the most dispersed crystallites are located near the surface of the material, and the largest ones - in the depth.

#### 4. Conclusion

Thus, the nature of nanostructuring and formation of gradient layer in the surface layer of bismuth telluride at PT by incoherent radiation of xenon lamps is caused by a sequence of independent processes:

- growth of free electrons concentration;
- decrease of defect formation threshold;
- localization of a large temperature gradient in the skin layer;
- generation and propagation of sonic phonons;
- secondary recrystallization;
- formation of nanocrystalline phase in the Bi-Te-Se system.

As a result of PT by incoherent radiation of xenon lamps, a surface layer with a gradient of the average crystallite size  $\text{grad } D$  is formed. At the free surface the value of  $\text{grad } D$  in the direction of the volume of bismuth telluride reaches the maximum value. High rate of energy impact of broadband radiation of gas-discharge lamps causes nanostructuring of the surface region, changes in structural and morphological parameters and physicochemical properties of the massive semiconductor material  $\text{Bi}_2\text{Te}_{3-x}\text{Se}_x$ . Determining factors of photon activation of structural transformations: internal photoeffect, decrease of defect formation threshold.

#### Contribution of the authors

The authors contributed equally to this article.

#### Conflict of interests

The authors declare that they have no known competing financial interests or personal relationships that could have influenced the work reported in this paper.

#### References

1. Belonogov E. K., Dybov V. A., Kostyuchenko A. V., Kushchev S. B., Serikov D. V., Soldatenko S. A. The effect of pulsed photonic treatment on the mechanical properties of semiconductor thermoelectric branches (based on  $\text{Bi}_2\text{Te}_3$ – $\text{Bi}_2\text{Se}_3$  solid solutions) and adhesion of the switching layers. *Journal of Surface Investigation: X-ray, Synchrotron and Neutron Techniques*. 2019;5: 17–24. <https://doi.org/10.1134/S0207352819050056>
2. Grebennikov A. A., Bocharov A. I., Kushchev S. B., ... Safonov I. A. Effect of pulsed photon treatment on electrophysical and thermal properties of  $n$ -type solid solution on the base of  $\text{Bi}_2\text{Te}_3$ – $\text{Bi}_2\text{Se}_3$ . I. Electrophysical characteristics. *Physics and Chemistry of Materials Treatment*. 2019;5: 14–20. <https://doi.org/10.30791/0015-3214-2019-5-14-20>
3. Grebennikov A. A., Bocharov A. I., Kushchev S. B., ... Safonov I. A. Effect of pulsed photon treatment on electrophysical and thermal properties of  $n$ -type solid solution on the base of  $\text{Bi}_2\text{Te}_3$ – $\text{Bi}_2\text{Se}_3$ . II. Thermal conductivity and thermoelectric figure of merit. *Physics and Chemistry of Materials Treatment*. 2019;6: 22–27. <https://doi.org/10.30791/0015-3214-2019-6-22-27>
4. Belonogov E. K., Kushev S. B., Sumets M. P., ... Turaeva T. L. The effect of photonic processing on increasing the thermoelectric Q-factor of a solid solution  $\text{Bi}_2\text{Te}_3$ – $\text{Bi}_2\text{Se}_3$ . *Inorganic Materials: Applied Research*. 2023;14(5): 595–603. <https://doi.org/10.1134/s2075113323030061>
5. Kapustin Yu. A., Kolokolnikov B. M., Sveshnikov A. A. Photostimulated gold diffusion during pulsed photon processing\*. *Semiconductors*. 1990;24(2): 318–322. Available at: <http://journals.ioffe.ru/articles/viewPDF/22840>
6. Vavilova V. V., Kovneristyi Yu. K., Palii N. A., Timofeev V. N., Ievlev V. M., Isaenko A. P. Effects of thermal annealing and pulsed photon processing on the relaxation and crystallization of amorphous Fe-P-Si alloys. *Inorganic Materials*. 2004;40(2): 152–160. <https://doi.org/10.1023/B:INMA.0000016090.36608.2f>
7. Ievlev V. M., Soldatenko S. A., Kushchev S. B., Gorozhankin Yu. V., Vakhtel V. M. Effect of photon activation during the synthesis of silicide films in the heterosystem (111) Si-Ni-Pt. *Condensed Matter and Interphases*. 2007;9(3): 216–227. (In Russ., abstract in Eng.). Available at: [https://elibrary.ru/download/elibrary\\_9596050\\_91117226.pdf](https://elibrary.ru/download/elibrary_9596050_91117226.pdf)
8. Belyavskij V. I., Kapustin Yu. A., Sviridov V. V. Subthreshold defect formation during high-power pulse processing of silicon\*. *Semiconductors*. 1991;25(7): 1204–1208. (In Russ.). Available at: <http://journals.ioffe.ru/articles/viewPDF/23492>
9. Kushchev S. B. *Study of the phase composition and substructure of silicides formed during pulsed photon processing of metal films on silicon by incoherent radiation\**. Doct. phys. math. sci. diss. Abstr. Voronezh: 2000. 35 p. (In Russ.). Available at: <https://viewer.rsl.ru/ru/rsl01000244921?page=1&rotate=0&theme=white>
10. Ievlev V. M., Latyshev A. N., Selivanov V. N., Turaeva T. L., Sinel'nikov A. A. Effect of photon irradiation on the process of recrystallization of thin metallic films. *Physics of Metals and Metallography*. 2007;103(1): 58–63. <https://doi.org/10.1134/s0031918x07010073>
11. Ievlev V. M. Activation of solid-phase processes by radiation of gas-discharge lamps. *Russian Chemical Reviews*. 2013;82(9): 815–834. <https://doi.org/10.1070/rc2013v082n09abeh004357>
12. Serbin O. V. *Synthesis of nanodispersed films of lead titanate and tungsten carbide using pulsed photon processing*. Cand. phys. math. sci. diss. Voronezh: 2003. 119 p. (In Russ.). Available at: <https://www.dissercat.com/content/sintez->

nanodispersnykh-plenok-titanata-svintsa-i-karbida-volframa-metodom-impulsnoi-fotonnoi

13. Marshak I. S. *Pulsed light sources\**. Moscow – Leningrad: Gosenergoizdat Publ.; 1963. 336 p. (In Russ.)

14. Veis A. N., Zhitinskaya M. K., Lukyanova L. N., Kutasov V. A. Peculiarities of bismuth telluride energy spectrum from optical measurements data. *SPbPU Journal – Physics and Mathematics*. 2013;3(177): 29–41. (In Russ.). Available at: <https://physmath.spbstu.ru/userfiles/files/articles/2013/3/03.pdf>

15. Fleurial J. P., Gailiard L., Triboulet R., Scherrer H., Scherrer S. Thermal properties of high quality single crystals of bismuth telluride – part I: Experimental characterization. *Journal of Physics and Chemistry of Solids*. 1988;49(10): 1237–1247. [https://doi.org/10.1016/0022-3697\(88\)90182-5](https://doi.org/10.1016/0022-3697(88)90182-5)

16. Gurevich M. M. *Photometry (theory, methods and instruments)\**. Leningrad: Energoatomizdat Publ.; 1983. 272 p. (In Russ.)

17. Saberi Y., Sajjadi S. A., Mansouri H. Comparison of thermoelectric properties of  $\text{Bi}_2\text{Te}_3$  and  $\text{Bi}_2\text{Se}_{0.5}\text{Te}_{2.5}$  thin film materials synthesized by hydrothermal process and thermal evaporation. *Ceramics International*. 2021;47: 11547–11559. <https://doi.org/10.1016/j.ceramint.2020.12.285>

18. Adam A. M., Tolan M., Refaat A. A., Nafady A., Petkov P., Ataalla M. Optical properties of thin  $\text{Bi}_2\text{Te}_3$  films synthesized by different techniques. *Superlattices and Microstructures*. 2021;155: 106909. <https://doi.org/10.1016/j.spmi.2021.106909>

19. Newell D. B., Tiesinga E. The International System of Units (SI). *National Institute of Standards and Technology Special Publication 330*. 2019: 122. <https://doi.org/10.6028/NIST.SP.330-2019>

20. Ivanov O., Yaprntsev M., Lyubushkin R., Soklakova O. Enhancement of thermoelectric efficiency in  $\text{Bi}_2\text{Te}_3$  via rare earth element doping. *Scripta Materialia*. 2018;146: 91–94. <https://doi.org/10.1016/j.scriptamat.2017.11.031>

21. Carterb M. J., El-Desoukyc A., Matthieu A. A., Philippe B., LeBlanca S. Pulsed laser melting of bismuth telluride thermoelectric materials. *Journal of Manufacturing Processes*. 2019;43: 35–46. <https://doi.org/10.1016/j.jmapro.2019.04.021>

22. Zimmer A., Stchakovsky M., Stein N., Johann L., Eypert C., Boulanger C. Optical constants of electroplated  $\text{Bi}_2\text{Te}_3$  films by Mueller matrix spectroscopic ellipsometry. *Thin Solid Films*. 2008;516(10): 2922–2927. <https://doi.org/10.1016/j.tsf.2007.06.011>

23. Srinivasan R., McReynolds K., Gothard N. W., Spowart J. E. Texture development during deformation processing of the *n*-type bismuth telluride alloy  $\text{Bi}_2\text{Se}_{0.5}\text{Te}_{2.5}$ . *Materials Science and Engineering: A*. 2013;588(A): 376–387. <https://doi.org/10.1016/j.msea.2013.09.044>

24. Markevich M. I., Tochizki I. I., Chaplanov A. M. On the kinetics of redistribution of vacancies in f.c.c. metals films under high rate heating. *Thin Solid Films*. 1989;168(3): 363–368. [https://doi.org/10.1016/0040-6090\(89\)90020-5](https://doi.org/10.1016/0040-6090(89)90020-5)

25. Markevich M. I., Chaplanov A. M. Structural transformations in thin metal films under pulsed laser irradiation. *Proceedings of the National Academy of Sciences*

of Belarus. *Physical-technical series (Vestsi Natsyyanal'nai akademii navuk Belarusi. Seryya fizika-tekhnichnykh navuk)*. 2016;1: 28–35. (In Russ.) Available at: <https://vestift.belnauka.by/jour/article/view/151/152>

26. Honeycomb R. *Plastic deformation of metals\**. Moscow: Mir; 1972. 408 p. (In Russ.)

27. Vavilova V. V., Ievlev V. M., Isaenko A. P., ... Selivanov V. N. Hypersonic mechanism of photon activation of solid-phase processes\*. In: *The effect of electromagnetic fields on the plasticity and strength of materials. Materials of the 5th international conference, February 14–15, 2003*. Voronezh: VSTU Publ.; 2003. p. 31–33. (In Russ.)

28. Medvedev E. S., Osherov V. I. *Theory of non-radiative transitions in polyatomic molecules\**. Moscow: Nauka Publ.; 1983. 280 p. (In Russ.)

29. Belonogov E. K., Dybov V. A., Kostyuchenko A. V., ... Soldatenko S. A. Modification of the surface of thermoelectric branches based on a  $\text{Bi}_2\text{Te}_3$ – $\text{Bi}_2\text{Se}_3$  solid solution by pulse photon treatment method. *Condensed Matter and Interphases*. 2017;19(4): 479–488. (In Russ., abstract in Eng.). Available at: [https://elibrary.ru/download/elibrary\\_32322272\\_25557687.pdf](https://elibrary.ru/download/elibrary_32322272_25557687.pdf)

\* Translated by author of the article

## Information about the authors

Belonogov Evgeniy Konstantinovich, Dr. Sci. (Phys.-Math.), Associate Professor, Professor at the Department of Physics, Voronezh State Technical University (Voronezh, Russian Federation).

<https://orcid.org/0000-0002-0216-0986>  
ekbelonogov@mail.ru

Kushchev Sergey Borisovich, Dr. Sci. (Phys.-Math.), Professor, Professor at the Department of Physics, Voronezh State Technical University (Voronezh, Russian Federation). <https://orcid.org/0000-0003-1263-1806>  
kushev\_sb@mail.ru

Serikov Dmitry Vladimirovich, Cand. Sci. (Phys.-Math.), Research Engineer, Voronezh Design Bureau of Communications (Voronezh, Russian Federation). <https://orcid.org/0000-0002-0464-3500>  
dmitriy.tut@mail.ru

Soldatenko Sergey Anatolievich, Cand. Sci. (Phys.-Math.), Research Fellow, Associated Professor at the Department of Physics, Voronezh State Technical University (Voronezh, Russian Federation).

<https://orcid.org/0000-0002-3927-2738>  
cossack408@mail.ru

Turaeva Tatyana Leonidovna, Cand. Sci. (Phys.-Math.), Associate Professor, Head of the Department of Physics, Voronezh State Technical University (Voronezh, Russian Federation).

<https://orcid.org/0000-0002-6126-1605>  
tlturaeva@mail.ru

Received 10.01.2025; approved after reviewing 13.02.2025; accepted for publication 17.02.2025; published online 25.06.2025.



## Original articles

Research article

<https://doi.org/10.17308/kcmf.2025.27/12765>

## Investigation of the possibility of ice film 0 formation on the dielectric surface in a microwave resonator

G. S. Bordonskiy<sup>1</sup>✉, V. A. Kazantsev<sup>1</sup>, A. K. Kozlov<sup>1</sup>

Federal State Budgetary Scientific Institution Institute of Natural Resources, Ecology and Cryology  
of the Siberian Branch of the Russian Academy of Sciences,  
16a Nedorezova st., Chita 672002, Russian Federation

### Abstract

**Purpose:** The possibility of detecting ice 0 by deposition of water vapor on quartz glass dielectric plates placed in the cavity of a microwave rectangular resonator near the frequency of 2.8 GHz is investigated.

**Experimental:** Measurements of the characteristics of the resonator filled with air at atmospheric pressure in the temperature range from 5 to –140 °C have been performed. Variations of the transmittance power of the resonator at the resonance frequency and its quality factor of fit were found with their characteristic change at a temperature of –23 °C. This temperature corresponds to the formation of ice 0 from supercooled water. It is assumed that in the experiment, films of ice 0 are detected in the response of the resonator to the temperature change in the investigated interval.

**Conclusions:** This result is of interest due to the possible influence of water vapor condensation on the functioning of a variety of technical devices in terrestrial conditions when ice 0 is formed.

**Keywords:** Ice 0, Conductive films, Microwave range, Resonator measurements

**For citation:** Bordonskiy G. S., Kazantsev V. A., Kozlov A. K. Investigation of the possibility of ice film 0 formation on the dielectric surface in a microwave resonator. *Condensed Matter and Interphases*. 2025;27(2): 211–216. <https://doi.org/10.17308/kcmf.2025.27/12765>

**Для цитирования:** Бордонский Г. С., Казанцев В. А., Козлов А. К. Исследование возможности образования пленки льда 0 на поверхности диэлектрика в микроволновом резонаторе. *Конденсированные среды и межфазные границы*. 2025;27(2): 211–216. <https://doi.org/10.17308/kcmf.2025.27/12765>

✉ Georgy S. Bordonskiy, e-mail: [lgc255@mail.ru](mailto:lgc255@mail.ru)

© Bordonskiy G. S., Kazantsev V. A., Kozlov A. K., 2025



The content is available under Creative Commons Attribution 4.0 License.



## 1. Introduction

The papers [1–3] reported the discovery by computer modeling of a crystalline modification of ice called ice 0. This ice is a ferroelectric, contains 12 water molecules in the unit cell, and forms at a pressure of 0.1 MPa at temperatures below  $-23\text{ }^{\circ}\text{C}$ . Ice 0 is considered a transitional form from deeply supercooled water to hexagonal ice Ih. In papers [3, 4], such an ice phase was registered during measurements of the extinction of laser radiation in the visible range when radiation was transmitted through plates made of various dielectrics with a layer of nanometer-thick ice condensed from water vapor. The plates consisted of glass, mica, Ih ice and sodium chloride crystals.

The special property of the ferroelectric to form strongly conducting thin, on the order of nanometer, layers at the dielectric boundary was utilized in the experimental studies [5,6]. These layers created a significant absorption (and reflection) of external electromagnetic radiation from the ice film 0 deposited on the dielectric substrate. If the plates with the investigated ice were heated above  $-23\text{ }^{\circ}\text{C}$ , the extinction effect abruptly disappeared, which served as evidence for the formation of ice 0 on the surface. The electrodynamic model of the structure was presented in the form of island films of ice covered with a layer of high conductivity, in which a resonance of surface plasmon modes appeared [7, 8]. These modes in the case of irregularly shaped conductive particles of nanometer dimensions create scattering and absorption in a wide frequency interval extending from the optical to the radio range. The upper frequency of this interval is determined by the plasma frequency of charge carriers with a sharp maximum of the effect, which is located at the Frelich frequency. At this frequency, for a conducting layer  $\varepsilon' = -2$  ( $\varepsilon'$  is the real part of the relative complex dielectric constant). For example, theory and extinction measurements for small aluminum ellipsoids have shown that the extinction changes by about 5 orders of magnitude as the wavelength increases from its maximum ( $\sim 0.5\text{ }\mu\text{m}$ ) to 1 mm [7]. For spherical particles, the same change is much larger and amounts to 9 orders of magnitude. Thus, it can be expected that extinction should be manifested

during the formation of inhomogeneous ice film 0 not only in the optical, but also in the microwave range. It should be noted that in recent years, studies of nanostructures made of water and ice that exhibit unusual physical and chemical properties have been initiated [9].

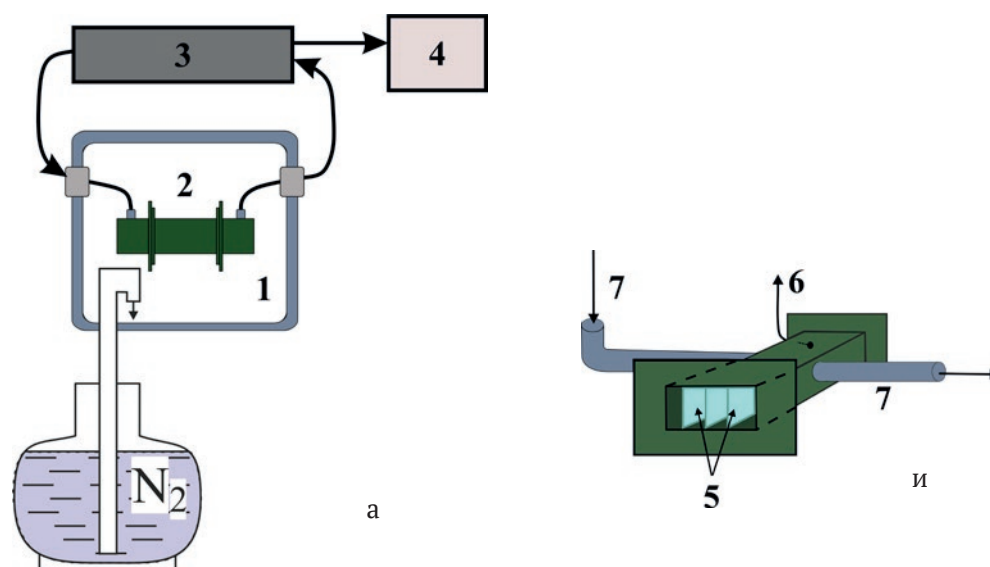
The purpose of this work was to measure the response of a microwave resonator to a dielectric plate with ice deposited on it in order to establish the possibility of detecting ice 0 when it forms in a cold atmosphere and to determine the degree of influence of such layers on the characteristics of the resonator at microwave frequencies. The detection of this effect is of interest for the development of electromagnetic non-contact techniques for studying the characteristics of boundary layers between ice 0 and various media.

## 2. Experimental

The scheme of the setup for the study is presented in Fig. 1.

In the experiment, we cooled a rectangular resonator with thin quartz glass plates installed in it. The natural frequency of the resonator is about 2.8 GHz; its linear dimensions are  $72\times 34\times 77\text{ mm}$ ; the resonator material is copper (the quality factor of the loaded resonator at room temperature is  $\sim 550$ ). The thickness of quartz glass plates was 0.19 mm, their dimensions were  $24\times 24\text{ mm}$ , and their number was 13 pcs. After cooling by cold nitrogen vapor to the minimum temperature, the resonator, in some cases, was pumped with a certain volume of air to introduce an additional amount of water vapor into the cavity. The minimum temperature in the cooling chamber was  $-140\text{ }^{\circ}\text{C}$ .

Measurement of the characteristics of the resonator: its Q-factor ( $Q$ ) and values of the resonant frequency ( $f_p$ ) were performed in the mode of slow heating of the refrigerating chamber. The average heating rate of the resonator was  $\sim 1\text{ }^{\circ}\text{C}/\text{min}$ . Heating was carried out when the supply of cold nitrogen vapor was stopped and the temperature in the laboratory room was stable. During this process, water vapor in the resonator condensed on the surface of quartz plates and walls of the resonator to form a thin layer of ice. In the absence of air supply to the resonator, as well as the relative humidity of air  $\sim 15\text{ }\%$  at the initial temperature of  $20\text{ }^{\circ}\text{C}$ , the maximum



**Fig. 1.** a) Scheme of the installation for searching for ice films 0 during its formation in a microwave resonator: 1 – refrigerator, 2 – resonator, 3 – scalar analyzer of radio frequency circuits P4-18, 4 – data collection system; b) scheme of the resonator type  $H_{101}$ , where 5 – thin plates of quartz glass, 6 – thermocouple outlet, 7 – air pumping tubes

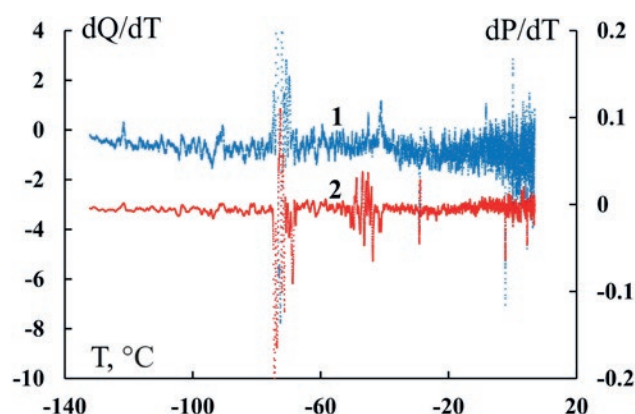
possible calculated thickness of the ice film was  $\sim 100$  nm. Since the plates were cooled through the walls of the resonator, the largest mass of water condensed on them. Therefore, pumping a certain volume of air through the resonator was also used in the experiments. The mass of the incoming water vapor and the formed volume of ice, as well as the known values of the dielectric permittivity of ice Ih show that their amount for the case of hexagonal ice cannot noticeably change the characteristics of the resonator.

From measurements of the resonant response of the resonator, we found  $f_p$ , the bandwidth of its passband at the level of 0.5 dB ( $\Delta f_p$ ), the passband power at the resonant frequency ( $P$ );  $Q$  ( $Q = f_p / \Delta f_p$ ) was determined by calculation. One measurement was performed for a time of  $\sim 1$  s. The total time of measurements was  $\sim 3$  hours. Accuracy of absolute measurements of air temperature in the chamber:  $\sim 1$  °C, amplitude of the transmitted power  $\sim 0.05$  dB, Q-factor  $\sim 3$ . We also calculated the derivative of the measured quantities by temperature ( $T$ ):  $dP/dT$  and  $dQ/dT$ .

### 3. Measurement results

The results of measurements of  $dQ/dT$  and  $dP/dT$  as a function of temperature during heating of the resonator from  $-140$  °C are shown in Fig. 2. In this experiment, the deposition of gases from the primary filled and isolated from the atmosphere

volume of the resonator cavity was used. The initial value of air temperature was  $20$  °C and its relative humidity ( $W$ )  $\sim 15$  %. The derivatives were found for a slow heating process, which was carried out when the cooling device was switched off. This was done to obtain smooth dependences on temperature and time, since during cooling there were possible some irregularities in the temperature increment, worsening the accuracy of measurements. This procedure also allowed us to obtain a larger value of the thickness of the deposited ice layer in the temperature range of



**Fig. 2.** The dependence of the derivatives of Q-factor (1) and power (2) of the resonator transmission at the resonant frequency on temperature. Averaging the derivative over 50 points. The total number of measured points is  $\sim 10^4$ . ( $dP/dT$  – in relative units)

interest (below  $-20^{\circ}\text{C}$ ). Vapor condensation at the beginning of the experiment occurred at about  $-5^{\circ}\text{C}$ . The exact value of the saturated vapor pressure for ice 0 is unknown, but this ice could not have formed at temperatures above  $-23^{\circ}\text{C}$ .

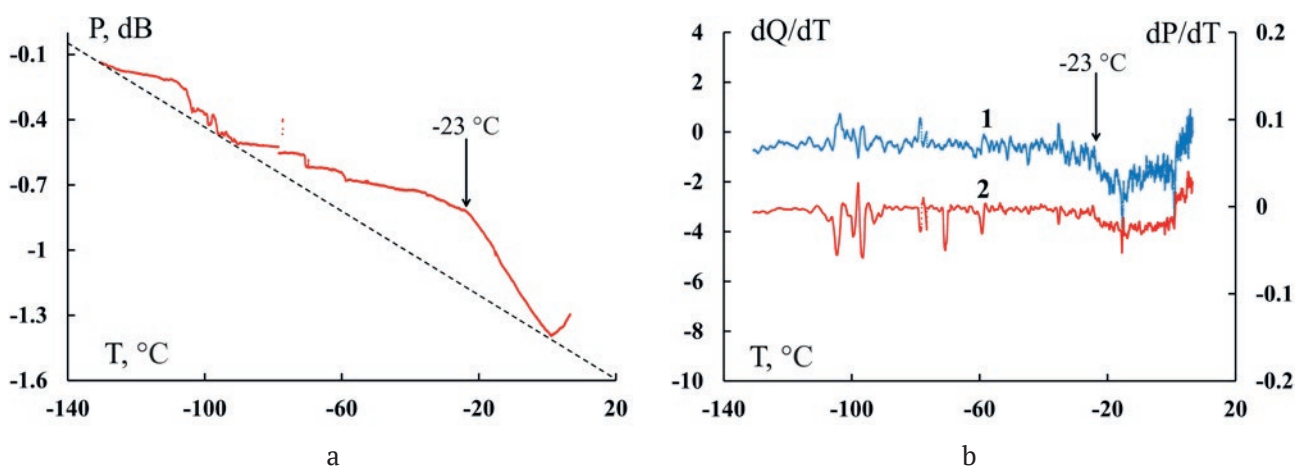
The total surface area of the metal and 13 quartz glass plates used in the experiment allowed us to obtain the maximum possible ice thickness at a water vapor mass of  $5.5 \times 10^{-4}$  g of about tens of nanometers with its uniform distribution on the surface of the plates.

Since, as noted above, it was expected that thinner films were deposited on the quartz plates than on the metal of the resonator walls, the experiments also included an additional air supply to the cavity. Fig. 3 shows the data for this case. At a relative humidity of 16 % (air temperature  $20^{\circ}\text{C}$ ), 3 liters of air were injected into the cavity using a compressor for a time of 1.5 min. The addition of water vapor was 0.0083 g. Additional water vapor was introduced at a temperature in the resonator of about  $-150^{\circ}\text{C}$ . The maximum calculated thickness of the ice layer on the surface was 900 nm. The calculations were performed for the known values of the mass of water vapor, the area of quartz plates and the walls of the resonator. The real value of this layer on the plates is significantly lower, since some vapors could condense in the supply tube and also escape from the waveguide cavity before settling on the plates.

To compare the data in the analysis, we measured the parameters of the resonator with plates when it was filled with nitrogen. In this case, a uniform variation of the transmittance power with temperature was observed. The approximation of  $P(T)$  for the case of no gases in the resonator is shown in Fig. 3a with a dashed line.

#### 4. Results and discussion

When performing the experiments, it was assumed that the formed ice layer 0 creates a conductive layer of nanometer thickness at the dielectric boundary [3, 4]. This will lead to a sufficiently pronounced effect of changing the goodness of the resonator and, consequently, the transmittance power even in the low-frequency region of the microwave range. In this case, the absorption effect is associated with an increase in the loss factor due to the resonance of surface plasmons in island conducting films. The thickness of about 10 nm is necessary for the occurrence of such a state of the films [7]. Therefore, it is sufficient to deposit on the surface of quartz plates layers of ice 0 with a thickness of  $\sim 10\ldots 100$  nm for appreciable changes in the Q-factor. Since it is difficult to obtain ice 0 in the experiment, we used a technique with initial cooling of the whole system (vapor and substrate), in which some initial vapor deposition in the form



**Fig. 3.** a) The dependence of the power transmission through the resonator on the temperature when it is heated after purging the resonator with air with an initial humidity of 16% (at an initial temperature of  $20^{\circ}\text{C}$ ). Power in decibels from the conditional level. The dashed line is the same for the case of approximating the absence of gases in the resonator; b) The dependence of the derivatives of  $Q$  (1) and power (2) of the resonator transmission at the resonant frequency on the temperature after purging the resonator with air with an initial humidity of 16 % (at an initial temperature of  $20^{\circ}\text{C}$ ). Averaging the derivative over 100 points. The total number of measured points is  $\sim 104$ . ( $dP/dT$  – in relative units)



of ice Ih in the temperature range from  $-5^{\circ}\text{C}$  and below was possible. However, ice 0 can also form on the surface of ice Ih, which was shown in our earlier experiment [10]. It can also be formed in the volume of ice Ih in the form of individual clusters, which was shown in [11].

Examination of the results of Fig. 2, which correspond to an ice layer on  $\sim 10$  nm quartz glasses, reveals two features in the region slightly below  $-78^{\circ}\text{C}$  and in the  $-45^{\circ}\text{C}$  region. No clear traces associated with ice 0 are observed in this experiment. In Fig. 3, where films on the order of one hundred nanometers thick were deposited, in contrast, the temperature of  $-23^{\circ}\text{C}$  clearly stands out, where an extremum of increasing  $P$  compared to the calibration value was observed (dashed line for the case of no gases in the resonator). In addition, a power jump was observed at  $-78^{\circ}\text{C}$  and some increase in the  $-110^{\circ}\text{C}$  region.

The deviations of the plots from the mean value near  $-78^{\circ}\text{C}$  can be related to the solid-gas phase transition process for carbon dioxide, which is also in air and appears in the mixture with ice. The phase transition of solid carbon dioxide into gas and leads to some fluctuations of values in a small temperature range. These temperature values appear more sharply in the plots of the  $dQ/dT$  and  $dP/dT$  derivatives, Fig. 3b. This figure shows a sharp change in the slope of the derivative plots as the temperature rises above  $-23^{\circ}\text{C}$ , which corresponds to the transition of ferroelectric ice 0 to hexagonal ice Ih with the disappearance of conductive films of nanometer thickness at the boundaries of ice 0 with other dielectrics.

It is interesting to note the appearance of the resonator response for the case presented in Fig. 3, at a temperature of  $-105^{\circ}\text{C}$  (approximately  $-95$  to  $-115^{\circ}\text{C}$ ). Such a feature was also observed in the extinction plots of laser radiation when passing through ice films deposited on a dielectric, previously found in [3, 4], which, however, was not investigated.

It also turned out that in the subsequent work [12], in the study of flexoelectric phenomena – charge formation in areas with anisotropy of mechanical strain, a phase transition near  $-110^{\circ}\text{C}$  was detected in ice. It was concluded that electric polarization induced by strain anisotropy can be an effective method to detect phase transitions

in surface layers; especially for ferroelectric. Our results support this conclusion.

It is worth mentioning the physical features of thin layers during gas condensation which were utilized in the technique of the performed measurements. The most important one is the detection of highly conductive layers several nanometers thick. According to papers [5, 6], such layers arise at the contacts of dielectric and ferroelectric. Consequently, using the proposed technique it is possible to detect both ultra-thin (nanometer) and thicker (micron) layers of ferroelectric materials. The temperature dependences of the resonator response determine the ferroelectric phase transition.

The phase transition near  $-105^{\circ}\text{C}$  can be associated with the formation of ice XI. This ice is formed at temperatures below  $-200^{\circ}\text{C}$ , but its nuclei remain when the samples are heated to a temperature of  $\sim -120^{\circ}\text{C}$ , as presented in the paper [13]. Since the concentration of ice XI is small at high temperatures, it has not been previously recorded by standard methods of matter structure measurements. Another important feature manifested in the method we used is the increase in the goodness of the resonator, i.e., the decrease in its losses, during the formation of ferroelectric ices. This can be explained by plasmon effects during the growth of nanometer island films and the emergence of highly conductive contact films. Such phenomena associated with increasing electromagnetic fields are studied in plasmonics and are associated with resonances of plasmonic modes [7, 14]. An example is giant Raman scattering, when the amplification of scattered fields by groups of molecules near specially fabricated structures can increase  $10^{10}$  times [8]. The details of this phenomenon require a special study. For example, in the paper [15] they investigated the effect of percolation transition on ultra-thin island metal films and found significant changes in the resonance of surface plasmon-polaritons and, consequently, in their electrophysical properties.

#### 4. Conclusions

It is shown that the emergence of a conducting layer of nanometer thickness on the dielectric surface is a consequence of the formation of a film of ferroelectric ice 0 on it. The occurrence of

resonance of plasmon modes in the microwave range in ice films deposited in the resonator was confirmed by the change of its parameters.

In the performed experiment with a microwave resonator near the resonant frequency of 2.8 GHz, in the temperature range of 5...–140 °C, filled with quartz plates, the changes in the transmitted power at the resonant frequency and its goodness of fit were observed. The measurements revealed characteristic changes of these parameters at a temperature of –23 °C, which corresponds to the value at which the ferroelectric ice 0 is formed.

The used microwave technique for recording the formation of ferroelectric films during gas condensation is applicable to the study of the characteristics of superfine layers when their electrical conductivity changes.

### Contribution of the authors

The authors contributed equally to this article.

### Conflict of interests

The authors declare that they have no known competing financial interests or personal relationships that could have influenced the work reported in this paper.

### References

1. Russo J., Romano F., Tanaka H. New metastable form of ice and its role in the homogeneous crystallization of water. *Nature Materials*. 2014;13(7): 733–793. <https://doi.org/10.1038/nmat3977>
2. Quigley D., Alfè D., Slater B. Communication: on the stability of ice 0, ice i, and Ih. *The Journal of Chemical Physics*. 2014;141(16): 161102. <https://doi.org/10.1063/1.4900772>
3. Bordonskiy G. S., Orlov A. O. Signatures of the appearance of ice 0 in wetted nanoporous media at electromagnetic measurements. *JETP Letters*. 2017;105(8): 492–496. <https://doi.org/10.1134/S0021364017080021>
4. Bordonskiy G. S., Gurulev A. A., Orlov A. O. Transmittance of electromagnetic radiation of the visible range by a thin film of ice 0 condensed on a dielectric substrate. *JETP Letters*. 2020;111(5): 278–281. <https://doi.org/10.1134/S0021364020050070>
5. Korobeynikov S. M., Drozhzhin A. P., Furin G. G., Charalambakos V. P., Agoris D. P., Surface conductivity in liquid-solid interface due to image force. *Proceedings of 2002 IEEE 14th International Conference on Dielectric Liquids*; 2002. 02CH37319. <https://doi.org/10.1109/icdl.2002.1022745>
6. Korobeynikov S. M., Melekhov A. V., Soloveitchik Y. G., Royak M. E., Agoris D. P., Pyrgioti E. Surface conductivity at the interface between ceramics and transformer oil. *Journal of Physics D: Applied Physics*. 2005;38(6): 915–921. <https://doi.org/10.1088/0022-3727/38/6/021>
7. Bohren C. F., Huffman D. R. *Absorption and scattering of light by small particles*. Wiley; 1983. 530 p.
8. Mayer S. A. *Plasmonics: Fundamentals and Applications*. Springer; 2007. 223 p.
9. Bordonskiy G. S., Gurulev A. A. Regarding physical and chemical transformations with the involvement of water near –45 °C. *Condensed Matter and Interphases*. 2019;21(4): 478–489. <https://doi.org/10.17308/kcmf.2019.21/2359>
10. Bordonskiy G. S., Gurulev A. A., Orlov A. O. Electromagnetic features of structures made of Ih ice covered with ice 0. *Proc. SPIE 12780, 29th International Symposium on Atmospheric and Ocean Optics: Atmospheric Physics*, 17 October 2023, 127800D. <https://doi.org/10.1117/12.2688621>
11. Leoni F., Shi R., Tanaka H., Russo J. Crystalline clusters in mW water: stability, growth, and grain boundaries. *The Journal of Chemical Physics*. 2019;151(4): 044505. <https://doi.org/10.1063/1.5100812>
12. Wen X., Ma Q., Shen S., Catalan G. Flexoelectricity and surface phase transition in natural ice. *arXiv*. 2022;2212.00323v1: 1/14. <https://doi.org/10.48550/arXiv.2212.00323>
13. Arakawa M., Kagi H., Fernandez-Baca J. A., Chakoumakos B. C., Fukazawa H. The existence of memory effect on hydrogen ordering in ice: The effect makes ice attractive. *Geophysical Research Letters*. 2011;38(16): L16101. <https://doi.org/10.1029/2011gl048217>
14. Gajduk A. E. *Multiresonance polarization systems based on metasurfaces*. Cand. phys.-math. sci. diss. Abstr. Novosibirsk: 2021. 19 p. (In Russ.). Available at: [https://www.isp.nsc.ru/autoreferat/gayduk\\_autoreferat.pdf](https://www.isp.nsc.ru/autoreferat/gayduk_autoreferat.pdf)
15. Tomilina O. A., Berzhansky V. N., Tomilin S. V. The Influence of the Percolation transition on the electric conductive and optical properties of ultrathin metallic films. *Physics of the Solid State*. 2020;62: 700–707. <https://doi.org/10.1134/S1063783420040228>

### Information about the authors

Georgy S. Bordonskiy, Dr. Sci. (Phys.–Math.), Professor, Chief Researcher at the Laboratory of Geophysics of Cryogenesis, Institute of Natural Resources, Ecology and Cryology SB RAS (Chita, Russian Federation).

<https://orcid.org/0000-0002-0009-0822>  
lgc255@mail.ru

Vyacheslav A. Kazantsev, postgraduate student, Junior Researcher at the Laboratory of Geophysics of Cryogenesis, Institute of Natural Resources, Ecology and Cryology SB RAS (Chita, Russian Federation).

<https://orcid.org/0000-0001-7539-1796>  
lgc255@mail.ru

Alexey K. Kozlov, postgraduate student, Junior Researcher at the Laboratory of Geophysics of Cryogenesis, Institute of Natural Resources, Ecology and Cryology SB RAS (Chita, Russian Federation).

<https://orcid.org/0000-0002-8413-6049>  
lgc255@mail.ru

Received 12.03.2024; approved after reviewing 24.05.2024; accepted for publication 17.06.2024; published online 25.06.2025.



## Original articles

Research article

<https://doi.org/10.17308/kcmf.2025.27/12863>

## Self-assembly of cationic polymers in mixed polymer-lipid monolayers at the liquid-air interface

D. M. Kamorin<sup>1,2</sup>, A. S. Simagin<sup>1,2</sup>, O. A. Kazantsev<sup>1</sup>, A. I. Slivkin<sup>3</sup>, O. G. Zamyshlyayeva<sup>1,2</sup>,  
A. A. Emasheva<sup>2</sup>, N. B. Melnikova<sup>1,2</sup>✉

<sup>1</sup>Nizhny Novgorod State Technical University n.a. R. E. Alekseev,  
24 Minina ul., Nizhny Novgorod 603155, Russian Federation

<sup>2</sup>Lobachevsky National Research State University of Nizhny Novgorod,  
23 Gagarin pr., Nizhny Novgorod 603022, Russian Federation

<sup>3</sup>Voronezh State University,  
1 Universitetskaya pl., Voronezh 394018, Russian Federation

### Abstract

**Purpose:** The self-assembly of cationic polymers at the liquid-air interface is the most important process for the design of new targeted drug delivery systems, including lipid-polymer hybrid nanoparticles.

We studied the self-assembly of cationic pH-sensitive polymers at the liquid-air interface in mixed Langmuir polymer-lipid monolayers of cholesterol with Lipoid S100.

**Experimental:** We used synthetic approaches to the synthesis of ionene polymer and studied its physicochemical properties by NMR, IR, HPLC, and gel permeation chromatography. The surface behavior and states of polymer monolayers and their mixtures with lipids (compressibility and molecular area) at the liquid-air interface were examined using the Langmuir-Blodgett technique. The resulting lipoplexes were studied by dynamic light scattering (average weight diameter and zeta potential).

**Conclusions:** High stability of lipid-polymer nanoparticles was achieved for compositions of mixed monolayers with the compressibility modulus ( $C_s^{-1}$ ) of at least 50 mN/m. In this case, the particle sizes were in the range from 32 to 73 nm and the zeta potential values for non-quaternized cationic polymers were strongly negative (from –15 to –45 mV), while for the ionene polymers they were significantly positive (from +8 to +49 mV).

**Keywords:** Self-assembly at interfaces, Polymer-lipid nanoparticles, Langmuir monolayers, Ionene polymers

**Funding:** The study was supported by the Russian Science Foundation (grant No. 22-73-10220).

**For citation:** Kamorin D. M., Simagin A. S., Kazantsev O. A., Slivkin A. I., Zamyshlyayeva O. G., Emasheva A. A., Melnikova N. B. Self-assembly of cationic polymers in mixed polymer-lipid monolayers at the liquid-air interface. *Condensed Matter and Interphases*. 2025;27(2): 217–225. <https://doi.org/10.17308/kcmf.2025.27/12863>

**Для цитирования:** Каморин Д. М., Симагин А. С., Казанцев О. А., Сливкин А. И., Замышляева О. Г., Емашева А. А., Мельникова Н. Б. Самоорганизация катионных полимеров в смешанных монослоях с липидами на межфазной границе раздела «жидкость-воздух». *Конденсированные среды и межфазные границы*. 2025;27(2): 217–225. <https://doi.org/10.17308/kcmf.2025.27/12863>

✉ Nina B. Melnikova, e-mail: [melnikovnb@gmail.com](mailto:melnikovnb@gmail.com)

© Kamorin D. M., Simagin A. S., Kazantsev O. A., Semenov V. N., Slivkin A. I., Zamyshlyayeva O. G., Emasheva A. A., Melnikova N. B., 2025



The content is available under Creative Commons Attribution 4.0 License.



## 1. Introduction

Self-assembly at the liquid-air interface plays a crucial role in designing new systems for targeted drug delivery. Lipid-polymer hybrid nanoparticles (lipoplexes), which combine the advantages of liposomes and polymerosomes and compensate for their disadvantages, are of greatest interest for the delivery of various drugs, including nucleic acids [1, 2].

The important requirement for polymers chosen as platforms is not only their low toxicity, amphiphilicity, ability to form micelles, Langmuir monolayers, and thin films at various interfaces, but also their cationic charge. Cationic polymers, especially those containing ionene units with a high positive charge, combined with lipids, are especially attractive for developing lipid-polymer nano-systems at the liquid-air interface enhancing the efficiency of drug delivery to the cell nucleus. Several studies have shown that cationic pH-sensitive methyl methacrylate copolymers (Eudragit) when combined with lipids, such as cholesterol, lecithin or their derivatives, effectively deliver nucleic acids to target cells with minimal cytotoxicity via polymeric nanoparticles [3, 4, 5]. Controlled incorporation of ionene chains of a given length into methacrylic amides or esters, such as methoxy[oligo(propylene glycol)-co-oligo(ethylene glycol)-methacrylate-co-N-[3-(dimethylamino)propyl]methacrylamide)

and their methyl iodide-quaternized analogs, is of particular interest not only due to their strong bactericidal, antioxidant, and fungicidal properties but also due to their ability to self-assemble at interfaces. All polymers were found to form stable mixed monolayers with lipids (cholesterol, dihexadecyl phosphate) at various interfaces.

Ionene polymers containing ammonium groups represent a unique class of cationic polymers since they are characterized by a very high density of their ionic sites and controllable charge densities along their skeletal chains [6-9]. In addition, the synthesis of ionene polymers is usually relatively simple.

In this work, we investigated the self-assembly at the water-air interface of three cationic pH-sensitive polymers (Fig. 1): 1) methyl methacrylate-butyl methacrylate-dimethylaminoethyl methacrylate (MMA-BMA-DMAEM), similar to Eudragit 100; 2) ionene macromonomer – PK-Im; 3) homopolymer ionene macromonomer PK-Im – PK-Ip, each combined with a mixture of lipids. The study focused on: 1) the surface behavior of the polymers in mixed polymer-lipid monolayers composed of cholesterol and Lipoid S100 as model lipids; 2) the colloidal-chemical properties of hybrid polymer-lipid nanoparticles produced by precipitation.

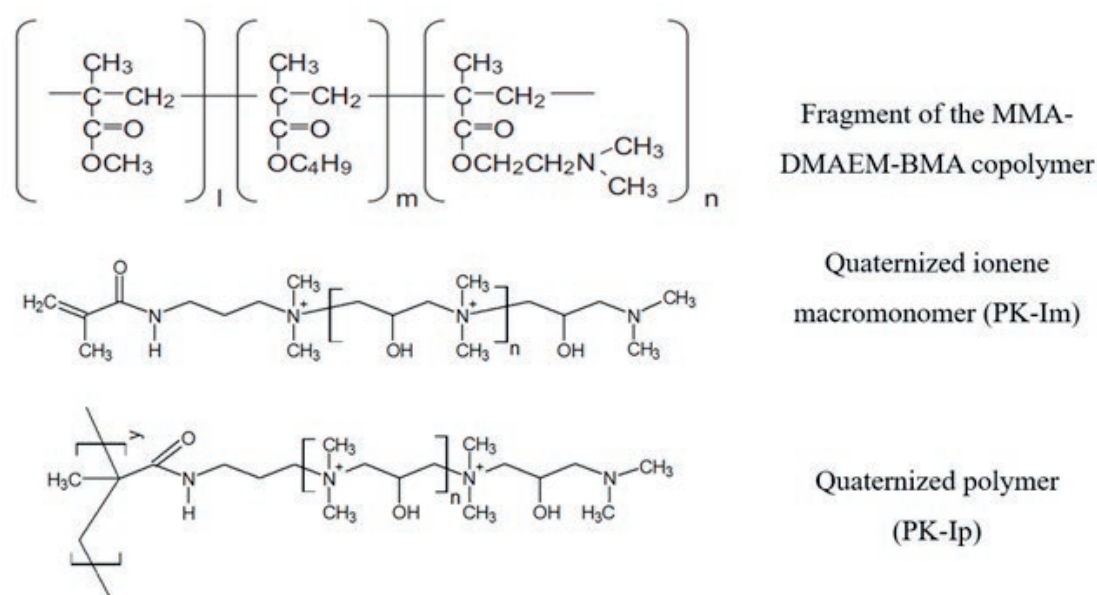


Fig. 1. General formulas of cationic pH-sensitive polymers

## 2. Experimental

### 2.1. Materials and methods

Dimethylaminopropyl methacrylamide (DMAPMA) and 1,3-bisdimethylaminopropan-2-ol (BDAP) were purchased from Sigma-Aldrich. Epichlorohydrin (ECH) and initiator 2,2'-azobisisobutyronitrile (AIBN) were purchased from Acros Organics.

Solvents, i.e. acetone, hexane, chloroform, methanol, and DMSO, were purchased from Acros Organics. Deionized water was produced using a Chromatek deionizer, Russia, Dzerzhinsk, with an electrical conductivity of less than 0.1  $\mu\text{Ohm/cm}$ . A statistical copolymer (MMA-BMA-DMAEM) with MW = 89,000 was obtained by radical polymerization in toluene at 60 °C using AIBN as the initiator. The reaction proceeded to high conversion, with a monomer feed ratio of 1:1:2.

### 2.2. Synthesis of PK-Im macromonomer

The macromonomer was synthesized by polycondensation of epichlorohydrin (ECH) and 1,3-bisdimethylaminopropan-2-ol (BDAP) in the presence of dimethylaminopropyl methacrylamide (DMAPMA) in water with stirring at 25 °C in a reactor with a reflux condenser. Epichlorohydrin was added to a mixture of amines in water under stirring and cooling for 30 min, then the reaction mixture was kept at room temperature. The ratio of ECH:BDAP:DMAPMA was 3.5:3:1 with a total reagent content of 40% by weight. After 6 hours of synthesis, the conversion of the initial monomer was 60%, and after 24 hours it reached 74%. The macromonomer was precipitated with acetone. IR spectrum (Shimadzu, Japan) was as follows: in the region of O-H stretching vibrations it was 3,500–3,400  $\text{cm}^{-1}$  (broad and intense band), in the region of carbonyl group stretching vibrations it was 1,730–1,668  $\text{cm}^{-1}$ , and in the region of C-H bond stretching vibrations of the hydrocarbon skeleton it was 3,000–2,800  $\text{cm}^{-1}$ . The  $^1\text{H}$  NMR spectrum of the ionic macromonomer (Agilent DD2 NMR 400WB, USA; tetramethylsilane standard, DMSO- $\text{D}_6$  solvent) showed the following signals ( $\delta$ , ppm):  $-\text{CH}_3$  in different positions designated by letters at 1.7 (m), 2.49 (q), and 3.25–3.26 (d, e); the vinyl group  $=\text{CH}_2$  (a) at 5.25–5.32 and 5.52–5.75;  $-\text{CH}_2-$  at 3.18–3.25 (g, h) and 3.48–3.52 (c, d); and  $>\text{CH}-$  at 4.16–4.20. The molecular weight of the macromonomer ( $^1\text{H}$  NMR) was 642 g/mol,

which corresponded to 4 atoms of quaternary ammonium in the monomer.

### 2.3. Synthesis of PK-Im ionene polymer

Polymerization of PK-Im ionene macromonomer was carried out in a stirred reactor in a nitrogen flow in DMSO at a monomer concentration of 20% by weight. The reaction was carried out at 70 °C with 1% by weight of AIBN as the initiator, achieving a conversion of 89.9%. The resulting polymer was precipitated in acetonitrile. The homopolymer had  $M_w = 13,900$ ,  $M_n = 6,300$ , and polydispersity = 2.2 (HPLC chromatograph Chromos ZhK-301, Russia; column Agilent PL aguagel-OH, aqueous eluent with 0.1 M  $\text{Na}_2\text{SO}_4$ , polyethylene glycol standards).

### 2.4. Study of monolayers in the aqueous subphase

Polymer self-assembly into monolayers was studied by recording surface pressure isotherms  $\pi = f(A)$  using a Wilhelmy plate method with a KSVmini device (Finland). Deionized water was used as an aqueous subphase. The polymer with a concentration of 1 mg/ml (10  $\mu\text{l}$ ) and lipid solutions (Lipoid S100 or cholesterol) in chloroform with a concentration of 1 mg/ml (5–20  $\mu\text{l}$ ) were added dropwise to the aqueous subphase using a chromatographic syringe. Each new portion was added after the previous one had completely spread. The introduction of portions “drop by drop” promotes the formation of stable Langmuir monolayers. The solvent evaporation time was 30 minutes, the monolayer compression rate was 10 mm/min. The electrical conductivity of deionized water (Chromatek deionizer, Russia) was less than 0.1  $\mu\text{Ohm/cm}$ . To prepare mixed polymer-lipid monolayers, lipid was first applied to the surface of the aqueous subphase and after 30-minute evaporation of the solvent, the polymer solution was applied dropwise.

### 2.5. Lipoplex studies

Zeta potential was determined by dynamic light scattering (DLS) on a NanobrookOmni instrument (Brookhaven Instruments Corporation, USA). For analysis, 1 mg of the sample was dispersed in 25 ml of deionized water (or a buffer solution with pH = 7.4), ultrasonicated for 5 min, and filtered through a polyethersulfone filter with a pore size of 0.8  $\mu\text{m}$ . Average hydrodynamic diameter

was obtained by using polymodal analysis of the correlation function ( $25 \pm 0.1$  °C, angle 90 ° in the range from 0.1 to 5,000 nm in 1 cm polystyrene cuvettes).

## 2.6. Methods for the preparation of nanoparticles with an ionene homopolymer

Weighed portions of Lipoid S100 and cholesterol were placed in a round-bottomed flask and dissolved in 10 ml of chloroform. The solvent was removed on a rotary evaporator for 1 hour. Then the sample was left in air for 10 minutes to remove residual solvent. A weighed portion of an ionene polymer was dissolved in 10 ml of water. The lipid film was hydrated with the resulting solution. The resulting suspension was treated in an ultrasonic bath for 30 min.

## 3. Results and discussion

### 3.1. Mixed cholesterol and Lipoid S100 Langmuir monolayers

Fig. 2 shows the compression isotherms of mixed lipid monolayers on pure water at different molar ratios. The molecular area  $A_0$  (the area occupied by one lipid molecule in a monolayer) for Lipoid S100 was  $1.4 \text{ nm}^2$ . This differed significantly from the value for egg lecithin (1-oleoyl-2-palmitoyl-phosphatidylcholine),  $0.56 \pm 0.2 \text{ nm}^2$  [10]. The molecular area of cholesterol was  $0.38 \text{ nm}^2$ , which was almost identical to the results of previous studies [11].

The elasticity of the resulting lipid film, a potential shell for lipoplexes, and its mechanical properties were calculated using the compressibility modulus ( $C_s^{-1}$ ) by the formula:

$$C_s^{-1} = -A_0(d\pi/dA)_{p,T} \quad (1),$$

where  $A_0$  is the area occupied by one molecule in a monolayer at a surface pressure of  $\pi$  and  $d\pi/dA$  is the gradient or rate of changes in the surface pressure during the spread of the surface film. The compressibility modulus of cholesterol on the subphase of pure water with pH 5.0–6.0 is about 700 mN/m [11], however, the analysis of the obtained data showed that cholesterol monolayers can be unstable at the “water-air” interface and can have two phase states upon compression: the first at about  $\pi = 10 \text{ mN/m}$  and the second at about  $\pi = 30 \text{ mN/m}$  on the aqueous subphase under the analyzed conditions (compression rate,

pH, and the temperature of the experiment). The compression conditions for the monolayers were selected in such a way as to make it possible to obtain mixed polymer-lipid films in the future. Fig. 2 demonstrates improved elasticity of mixed lipid monolayers as the Lipoid S100 proportion increases: the maximum compressibility modulus (elasticity) increases in the following series of Lipoid S100 to cholesterol ratios:  $1:1 < 3:1 < 5:1 < 7:1$ .

Thus, based on the study of elasticity (by compressibility modulus) of lipid monolayers, it follows that the basic lipid support can be a mixture of non-ionizing lipid cholesterol with ionizing phosphatidylcholine-containing lipids (conventionally called “lecithin”), while the main requirement for a stable phase state of the monolayers is Lipoid S100 : cholesterol ratio of 5:1 or 7:1.

### 3.2. Study of cationic polymers self-assembly in homogeneous and mixed polymer-lipid Langmuir monolayers

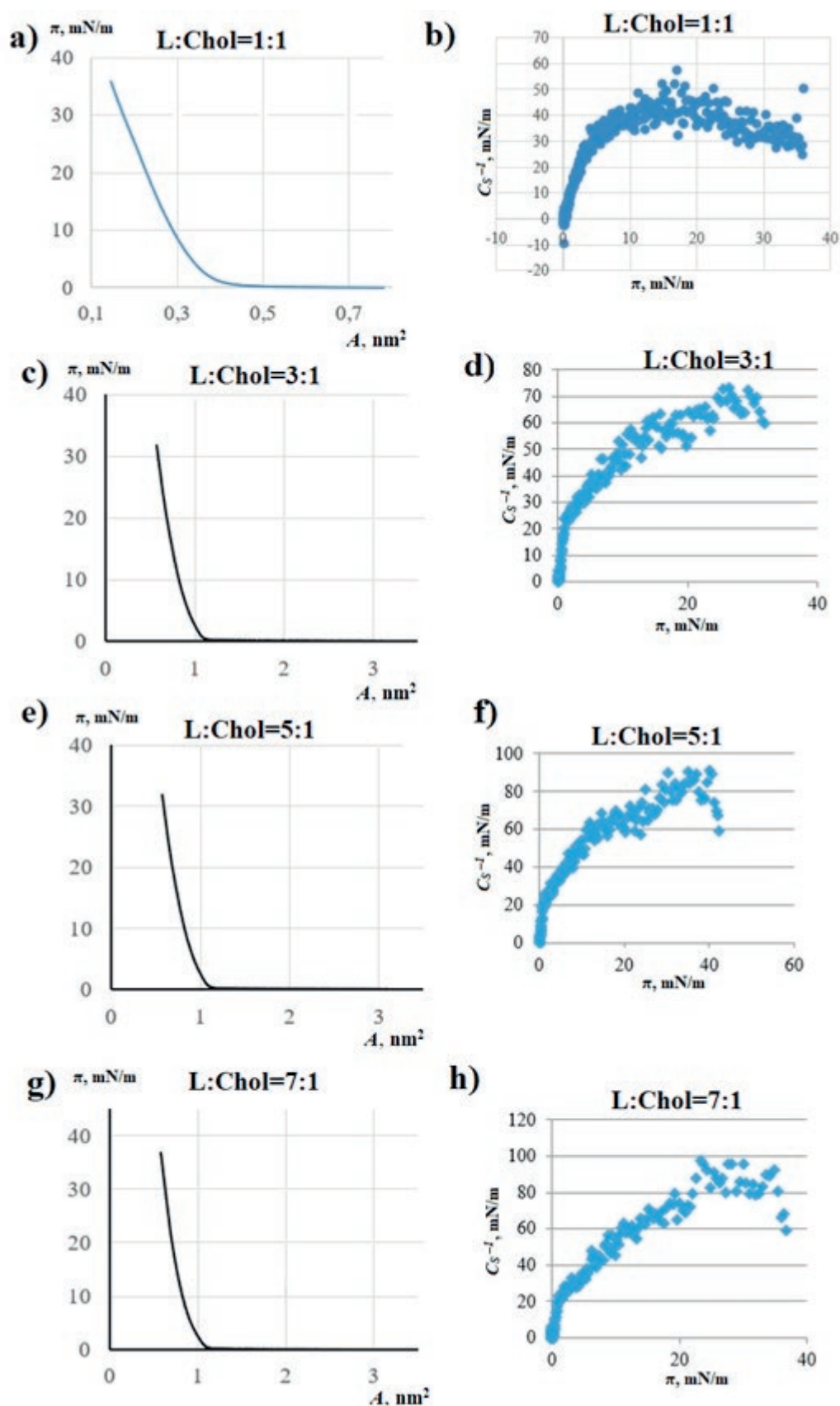
The primary and essential requirement for the formation of hybrid polymer-lipid nanoparticles is the formation of stable mixed “polymer-lipid” monolayers at the “water-air” interface.

The state of the surface film of the copolymer (MMA-BMA-DMAEM) depended on the conditions of its formation (volume of the applied polymer solution, compression rate). The molecular area changed from  $260 \text{ nm}^2$  to  $180 \text{ nm}^2$  with increasing copolymer concentration, while the compressibility modulus remained unchanged at about 45 mN/m, which is characteristic of liquid-condensed films whose elasticity is close to that of lecithin's. Fig. 3 shows a typical compression isotherm and the compressibility modulus of the polymer (MMA-BMA-DMAEM) monolayer on water at the maximum copolymer concentration.

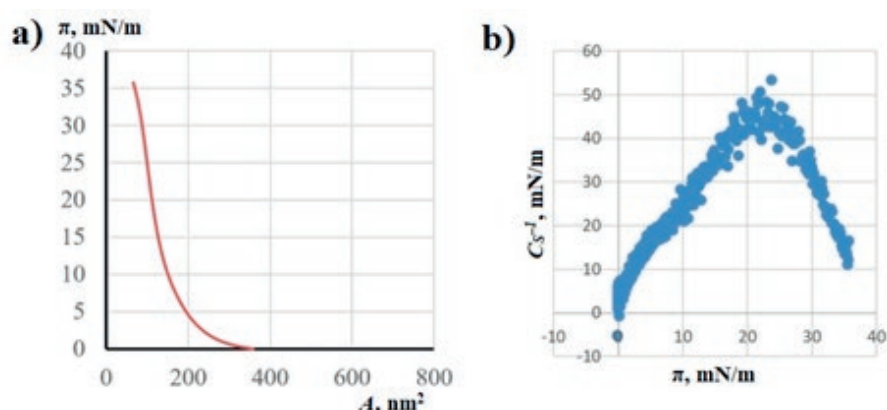
In contrast, PK-Im and PK-Ip ionene cationic polymers did not form stable monolayers on the water surface. However, all studied polymers formed stable mixed Langmuir monolayers with cholesterol and Lipoid S100. Fig. 4 shows the compression isotherms and hysteresis curves of mixed monolayers of ionene polymers and Lipoid S100 (a, c) and cholesterol (b, d).

The degree of hysteresis was estimated by the formula  $\Delta A_0 = A_0 - A'_0$ , where  $A'_0$  is the limiting area of the lipid under tension in the mixed

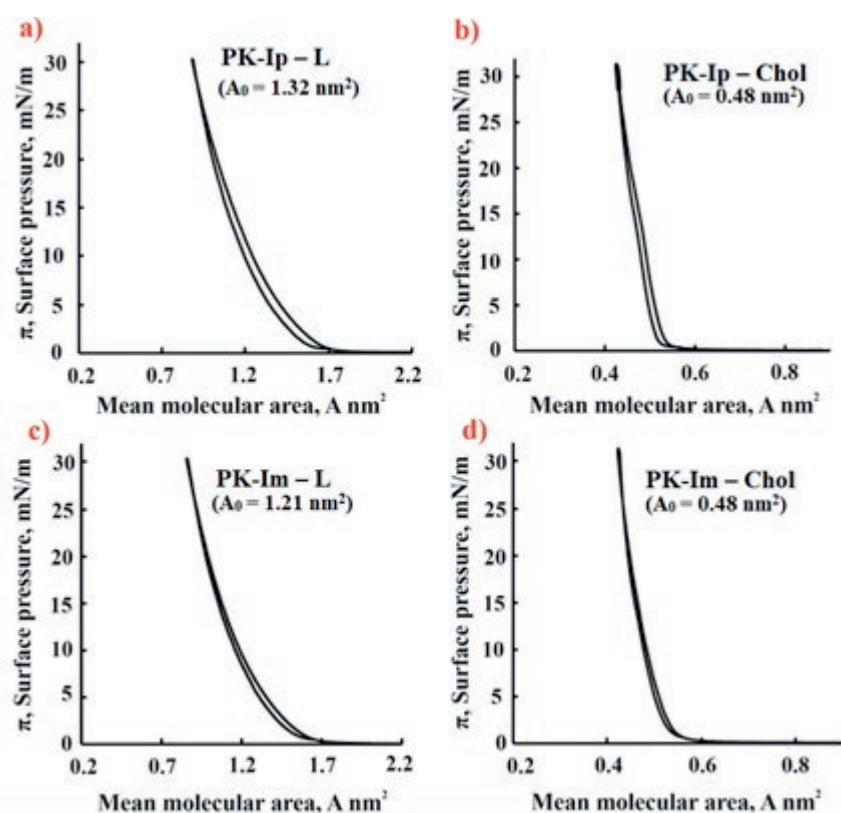




**Fig. 2.** Compression isotherms and compressibility moduli of mixed lipid monolayers with Lipoid S100 (L) – cholesterol (Chol) ratios of (1:1 – a, b; 3:1 – c, d; 5:1 – e, f; 7:1 – g, h)



**Fig. 3.** Compression isotherm and compressibility modulus of monolayers of the MMA-BMA-DMAEM copolymer



**Fig. 4.** Hysteresis curves of mixed monolayers of PK-Ip ionene polymer with Lipoid S100 (a), PK-Ip ionene polymer with cholesterol (b), PK-Im ionene macromonomer with Lipoid S100 (c), and PK-Im ionene macromonomer with cholesterol (d)

monolayers. The minimum hysteresis of the compression-tension curves of mixed monolayers was as follows: PK-Ip – Lipoid S100 ( $\Delta A_0 = 0.07 \text{ nm}^2$ ); PK-Im – Lipoid S100 ( $\Delta A_0 = 0.01 \text{ nm}^2$ ); PK-Ip – cholesterol ( $\Delta A_0 = 0.01 \text{ nm}^2$ ); and PK-Im – cholesterol ( $\Delta A_0 = 0.01 \text{ nm}^2$ ). These data indicate stable and similar states of all examined monolayers, and that polymer and monomer monolayers had the same structure. Table 1 summarizes the characteristics of mixed

“copolymer (MMA-BMA-DMAEM) – lipid” Langmuir monolayers. The data indicate that stable mixed monolayers form when the Lipoid S100 : cholesterol ratio did not exceed 3:1. Further increasing the Lipoid S100 proportion beyond this point did not enhance monolayer stability.

### 3.3. Colloidal-chemical properties of the studied lipoplexes

One of the problems of the formation of hybrid polymer-lipid nanoparticles (or lipoplexes)

**Table 1.** Properties of mixed monolayers of copolymer on lecithin and on a mixture of lipids (calculated by lipids)

Monolayer	L:Chol	$V_{\text{polymer}}, \mu\text{l}$	$A_0, \text{nm}^2$	Compressibility	
				$C_s^{-1}, \text{mN/m}$	$\pi, \text{mN/m}$
L	1:0	–	1.40 (L)	56	28
L–P	1:0	5	1.90 (L)	61	23
L–P	1:0	10	2.30 (L)	60 32	19 39
Chol	0:1	–	0.48 (Chol)	228	31
Chol–P	0:1	5	0.84 (Chol)	71 46	22 41
Chol–P	0:1	10	1.04 (Chol)	55 40	20 42
Chol–L	1:1	–	0.34 (Chol)	45	16
Chol–L–P	1:1	5	0.57 (Chol)	50	21
Chol–L–P	1:1	10	0.65 (Chol)	51 24	15 39
L–Chol	3:1	–	0.95 (L)	70	30
L–Chol–P	3:1	5	1.68 (L)	55	25
L–Chol–P	3:1	10	2.43 (L)	58	18
L–Chol	5:1	–	0.95 (L)	67 87	17 36
L–Chol–P	5:1	5	1.54 (L)	65	26
L–Chol–P	5:1	10	2.54 (L)	60 22	17 37
L–Chol	7:1	–	0.85 (L)	90	30
L–Chol–P	7:1	5	1.90 (L)	57 28	23 43
L–Chol–P	7:1	10	2.50 (L)	58 22	17 37

\* L – Lipoid S100, Chol – cholesterol, P – copolymer (MMA-BMA-DMAEM)

is their tendency to aggregate resulting in instability. Accordingly, determining the size of nanoparticles, particularly their hydrodynamic radius can be used to monitor the stability of nanoparticles. Additionally, the size of lipoplex particles (from 100 to 200 nm) affects their surface charges. The assessment of the zeta potential prior to the formation of stealth lipoplexes can also be used as a standard method of analysis. The inclusion of hydrophilic polymers (commonly modified polyethylene glycols) in the aqueous phase intended to ensure “stealth” properties during the second stage of lipoplex formation significantly changes the surface charge. As a

rule, without modified PEGs, hybrid polymer-lipid nanoparticles have a high positive or negative charge, which determines their stability. After PEGylation, the particles tend to acquire an insignificant charge. In this regard, when developing technologies for producing lipoplexes, the charge of the particles is controlled before and after PEGylation. Table 2 shows the zeta potential values of poly(MMA-BMA-DMAEM)-lipid nanoparticles in water. Negative zeta potential values characterize the stability of the system consisting of the main components of the future nanocontainer and the small size of the nanoparticles.



**Table 2.** Colloidal properties of the obtained nanoparticles poly(MMA-BMA-DMAEM)-Lipid

N	L, mg	Chol, mg	P *, mg	Zeta potential, mV	Size, nm
1	200	50	200	-36.95±1.02	51
2	16	4	200	-27.68±4.06	73
3	10	10	200	-44.93±2.41	38
4	200	50	200	-34.95±1.54	49
5	10	10	200	-39.02±1.43	41
6	26.5	13.5	200	-49.68±3.96	32
7	132.8	67.2	40	-39.81±2.42	41
8	186	94	40	-53.69±1.79	31
9**	132.8	67.2	40	-15.23±1.23	73

Notes: \* P = poly(MMA-BMA-DMAEM) copolymer (Mw. 89000); L – Lipoid S100, \*\* Liposome formation medium – phosphate buffer solution, pH 7.4

The zeta potential value decreased when the lipid-polymer film was dispersed in a phosphate buffer solution (pH 7.4). Since the obtained polymer is pH-sensitive and dissolves at pH 5, it is expected to dissolve at endosomal acidic pH, so it is preferable to form the nanocontainer core at pH 8 or higher. The charge sign of the hybrid lipid-polymer particles also affects their stability and distribution in the body. For example, liposomes containing dioleoyloxytrimethylammonium propane, which carry a positive charge, enhance the accumulation of antitumor drugs in the abdominal cavity of test animals. This effect is achieved due to the delayed release of the active substance and the resistance of these nanoparticles to macrophages. We have shown that nanoparticles based on an ionene polymer make it possible to obtain nanoparticles with a high positive charge (Table 3), which is a good indicator for predicting the stability of these particles.

#### 4. Conclusion

In this work, we have shown that a number of polymers, such as poly(MMA-BMA-DMAEM) copolymer and ionene polymers (PK-Im and PK-Ip), combined with lipids (Lipoid S100 and

cholesterol) form genuine mixed layers that are most stable at various surface pressures. This stability is particularly pronounced at Lipoid S100: cholesterol molar ratio of 3:1, indicating a stable surface film under these conditions. In addition to the molecular area and collapse pressure, the compressibility modulus ( $C_s^{-1}$ ) can be used as a stability control parameter with a minimum value of 50 mN/m. Nanoparticles of the MMA-BMA-DMAEM-lipid composition exhibited a strong negative charge (from -15 to -45 mV) and had small sizes in ranging from 32 to 73 nm. An alternative composition of stable lipid-polymer nanoparticles was a combination of lipids with positively charged ionene polymers, forming nanoparticles with a high zeta potential (from +8 to +49 mV).

Thus, we have proposed a method for predicting the compatibility and miscibility of the main components in hybrid lipid-polymer nanoparticles and demonstrated it using the (MMA-BMA-DMAEM) copolymer, ionene polymer (PK-Ip), Lipoid S100 lecithin, and cholesterol. This approach employs Langmuir monolayer technique and a method for preparation of lipid-polymer nanoparticles.

**Table 3.** Properties of nanoparticles with ionene polymer PK-Ip\*

N	Lipoid, mg	Chol, mg	Ionene, mg	L:Chol	Lipids:ionene	Zeta potential, mV
1	8	32	40	1:4	1:1	+48.89±0.91
2	3	32	10	1:4	4:1	+26.25±2.92
3	20	20	10	1:1	4:1	+24.55±1.16
4	10	10	200	1:1	1:10	+8.02±1.55

Notes: \* Lipids are dissolved in 10 ml of chloroform; ionene – in 10 ml of water

## Contribution of the authors

The authors contributed equally to this article.

## Conflict of interests

The authors declare that they have no known competing financial interests or personal relationships that could have influenced the work reported in this paper.

## References

1. Zhou W., Jiang L., Liao S., ... Zhang Y. Vaccines' new era-RNA vaccine. *Viruses*. 2023;15(8): 1760. <https://doi.org/10.3390/v15081760>
2. Wang Y., Zhang R., Tang L., Yang L. Nonviral delivery systems of mRNA vaccines for cancer gene therapy. *Pharmaceutics*. 2022;14(3): 512. <https://doi.org/10.3390/pharmaceutics14030512>
3. Santhanes D., Zhang H., Wilkins A., John Aitken R., Gannon A.L., Liang M. Engineering pH-sensitive dissolution of lipid-polymer nanoparticles by Eudragit integration impacts plasmid DNA (pDNA) transfection. *European Journal of Pharmaceutics and Biopharmaceutics*. 2024;199: 114299. <https://doi.org/10.1016/j.ejpb.2024.114299>
4. Gargouri M., Sapin A., Bouli S., Becuwe P., Merlin J. L., Maincent P. Optimization of a new non-viral vector for transfection: eudragit nanoparticles for the delivery of a DNA plasmid. *Technology in Cancer Research and Treatment*. 2009;8(6): 433–44. <https://doi.org/10.1177/153303460900800605>
5. Doerdelmann G., Kozlova D., Epple M. A pH-sensitive poly(methyl methacrylate) copolymer for efficient drug and gene delivery across the cell membrane. *Journal of Materials Chemistry B*. 2014;2(41): 7123–7131. <https://doi.org/10.1039/C4TB01052C>
6. Tsutsui T. *Developments in ionic polymers. Chapter 4*. A. D. Wilson, H. J. Prosser (eds.). Netherlands: Springer Dordrecht; 1986. p. 163–189. <https://doi.org/10.1007/978-94-009-4187-8>
7. Bara J. E., O'Hara K. E. Recent advances in the design of ionenes: toward convergence with high-performance polymers. *Macromolecular Chemistry and Physics*. 2019;220(13): 1900078. <https://doi.org/10.1002/macp.201900078>
8. Banerjee P., Anas M., Jana S., Mandal T. K. Recent developments in stimuli-responsive poly (ionic liquid) s. *Journal of Polymer Research*. 2020;27: 1–23. <https://doi.org/10.1007/s10965-020-02091-8>
9. Arriaza-Echane C., Velázquez-Tundidor M. V., Angel-López A., ... Coll D. Ionenenes as potential phase change materials with self-healing behavior. *Polymers*. 2023;15(22): 4460. <https://doi.org/10.3390/polym15224460>
10. Gennis R. B. *Biomembranes: molecular structure and function*. New York: Springer-Verlag; 1989. 533 p.
11. Conde M. M., Conde O., Minones J. M. Interactions between polymers and lipid monolayers at the air/water interface: surface behavior of poly(methyl methacrylate)-cholesterol mixed films. *The Journal of Physical Chemistry B*. 2019;114: 10774–10781. <https://doi.org/10.1021/jp103422g>

## Information about the authors

*Denis M. Kamorin*, Cand. Sci. (Chem.), Associate Professor of the Department of Chemical and Food Technologies, Nizhny Novgorod State Technical University n.a. R. E. Alekseev (Nizhny Novgorod, Russian Federation). <https://orcid.org/0000-0002-8712-5062>  
[d.kamorin@mail.ru](mailto:d.kamorin@mail.ru)

*Alexander S. Simagin*, Cand. Sci. (Chem.), Lecturer at the Department of Chemical and Food Technologies, Nizhny Novgorod State Technical University n.a. R. E. Alekseev (Nizhny Novgorod, Russian Federation). <https://orcid.org/0000-0002-6985-2098>  
[alexandr17-2@mail.ru](mailto:alexandr17-2@mail.ru)

*Oleg A. Kazantsev*, Dr. Sci. (Chem.), Professor, Head of the Department of Chemical and Food Technologies, Nizhny Novgorod State Technical University n.a. R. E. Alekseev (Nizhny Novgorod, Russian Federation). <https://orcid.org/0000-0003-1536-3966>  
[kazantsev@dpingtu.ru](mailto:kazantsev@dpingtu.ru)

*Aleksei I. Slivkin*, Dr. Sci. (Pharm.), Full Professor, Head of the Department of Pharmaceutical Technology, Voronezh State University (Voronezh Russian Federation). [slivkin@pharm.vsu.ru](mailto:slivkin@pharm.vsu.ru)  
<https://orcid.org/0000-0001-6934-0837>

*Olga G. Zamyshlyayeva*, Dr. Sci. (Pharm.), Professor at the Department of Macromolecular Compounds and Colloid Chemistry, Lobachevsky State University of Nizhni Novgorod (Nizhny Novgorod, Russian Federation). <https://orcid.org/0000-0002-4331-3125>  
[zam.olga@mail.ru](mailto:zam.olga@mail.ru)

*Anastasia A. Emasheva*, postgraduate student, Junior Research Fellow at the Center for Molecular Biology and Biomedicine, Lobachevsky State University of Nizhni Novgorod (Nizhny Novgorod, Russian Federation). <https://orcid.org/0009-0008-6097-4831>  
[anastasia.emasheva@yandex.ru](mailto:anastasia.emasheva@yandex.ru)

*Nina B. Melnikova*, Dr. Sci. (Chem.), Professor at the Department of Analytical and Medicinal Chemistry, Lobachevsky State University of Nizhni Novgorod (Nizhny Novgorod, Russian Federation). <https://orcid.org/0000-0003-1335-1048>  
[melnikovanb@gmail.com](mailto:melnikovanb@gmail.com)

Received 01.04.2025; approved after reviewing 15.04.2025; accepted for publication 17.04.2025; published online 25.06.2025.

Translated by the author



# Condensed Matter and Interphases

Kondensirovannye Sredy i Mezhfaznye Granitsy  
<https://journals.vsu.ru/kcmf/>

## Original articles

Research article

<https://doi.org/10.17308/kcmf.2025.27/12811>

## The potential corrosion inhibition properties of acetyl benzoic acid derivatives with substituted alkali metals (Na, K, Li): DFT approach

R. O. Kareem<sup>1✉</sup>, O. A. Hamad<sup>2</sup>

<sup>1</sup>Physics Department, College of Science, University of Halabja, Halabja 46018, Iraq

<sup>2</sup>University of Raparin, College of Science, Department of Chemistry, Sulamani 46012, Iraq

### Abstract

**Purpose:** Inhibitors of corrosion shield metals from corroding. Such chemicals may be added to a corrosive environment to either halt or slow down metal corrosion. The molecular structure of 3-acetyl benzoic acid (3ABA)  $C_9H_8O_3$  consists of planar molecules. These molecules aggregate by centrosymmetric hydrogen-bond pairing of ordered carboxyl groups. The novelty of the research and its primary objective was to perform a theoretical computational study on derivatives of 3ABA-M (Metal), where M molecule is modified by adding lithium (Li), sodium (Na), and potassium (K).

**Experimental part:** The study was carried out with the framework of the density functional theory (DFT) at the B3LYP/6-31G+ (d) level in the Gaussian 09W software. It involved geometrical optimization, analyzing spectral properties, electronic transitions, and the energy gap between the Highest Occupied Molecular Orbital (HOMO) and Lowest Unoccupied Molecular Orbital (LUMO). The calculated properties included  $E_{HOMO}$ ,  $E_{LUMO}$ , energy band gap (Egap), ionization energy (IE), electron affinity (EA), absolute electronegativity ( $\chi$ ), global hardness ( $\eta$ ), and global softness (S).

**Conclusions:** The chemical reactivity of the studied molecule was investigated by analyzing its molecular electrostatic potential (MEP) and electron localization function (ELF), using the Multiwfn 3.7 software. Consequently, it was concluded that the large energy gap of 3BAB (5.617 eV) and its high hardness (2.809) correlate with a low refractive index, dielectric constant, and low corrosion inhibition, whereas significant molecular softness of 3ABA-Na (2.88 eV<sup>-1</sup>) is associated with a high refractive index.

**Keywords:** 3-Acetyl Benzoic Acid, Corrosion Inhibition, DFT, Electron Localized Function, Refractive Index

**Acknowledgements:** We express our gratitude to the leaders of Department of physics, college of Science & Halabja University.

**For citation:** Kareem R. O., Hamad O. A. The potential corrosion inhibition properties of acetyl benzoic acid derivatives with substituted alkali metals (Na, K, Li): DFT approach. *Condensed Matter and Interphases*. 2025;27(2): 226–236. <https://doi.org/10.17308/kcmf.2025.27/12811>

**Для цитирования:** Карим Р. О., Хамад О. А. Потенциальные свойства ингибирования коррозии производных ацетилбензойной кислоты с замещенными щелочными металлами (Na, K, Li): DFT подход. *Конденсированные среды и межфазные границы*. 2025;27(2): 226–236. <https://doi.org/10.17308/kcmf.2025.27/12811>

✉ Kareem R. O, e-mail: rebaz.kareem@uoh.edu.iq

© Kareem R. O., Hamad. O. A., 2025



The content is available under Creative Commons Attribution 4.0 License.



## 1. Introduction

Metals can be protected from corrosion by corrosion inhibitors. Introducing such chemicals into a corrosive environment can prevent or slow down metal corrosion. One of the most popular and successful methods for protecting metal surfaces from oxidation or damage is the use of corrosion inhibitors. Every year, substantial amounts of material are lost due to corrosion and the irreversible breakdown of metals and alloys in a variety of sectors [1–4].

The global community has seen the fast spread of infectious illnesses, which pose a significant threat to human health due to the emergence of resistance to existing antimicrobial agents [5, 6]. Extensive research has been conducted on the biological properties of 3-acetylbenzoic acid (3ABA) combined with physiologically active heterocycles. It is highly valuable in the production of heterocyclic compounds and serves as a primary substance in a variety of chemical processes [7]. Due to its powerful antimicrobial capabilities, this molecule has been the focus of considerable research exploring its biological and physiological effects, including antifungal, anti-inflammatory, antibacterial, antimalarial, and anticancer effects. 3ABA is used as a component in hair dyes and as an intermediate agent in the pharmaceutical, cosmetics, agricultural,

and food industries [8]. Due to its ability to effectively interact with molecular targets, the designated chemical has a diverse range of binding interactions, making it potentially valuable in the field of drug development. Fig. 1 shows the 3ABA structure with doped substituted alkali metals, lithium (Li), sodium (Na), and potassium (K).

In the past few decades, there has been a growing interest in predicting and understanding the mechanisms of interaction and adsorption between organic analytes and active substrates, particularly metals. The adsorption orientation and binding sites of 3ABA on metals were determined using Raman and SERS spectroscopy [9,10]. The findings were interpreted using quantum chemical calculations based on density functional theory (DFT) at the B3LYP/LANL2DZ level, while the absorption spectra were analyzed using the IEFPCM method across four distinct solvents. It is essential to perform DFT calculations in order to comprehend the structure of molecules and their properties. In this study, the structure, spectra, and characteristics of physiologically significant molecules were examined using hybrid functionals, including B3LYP and M062X [11,12]. The primary objective of quantum molecular DFT computations is to identify the structure geometry with the lowest

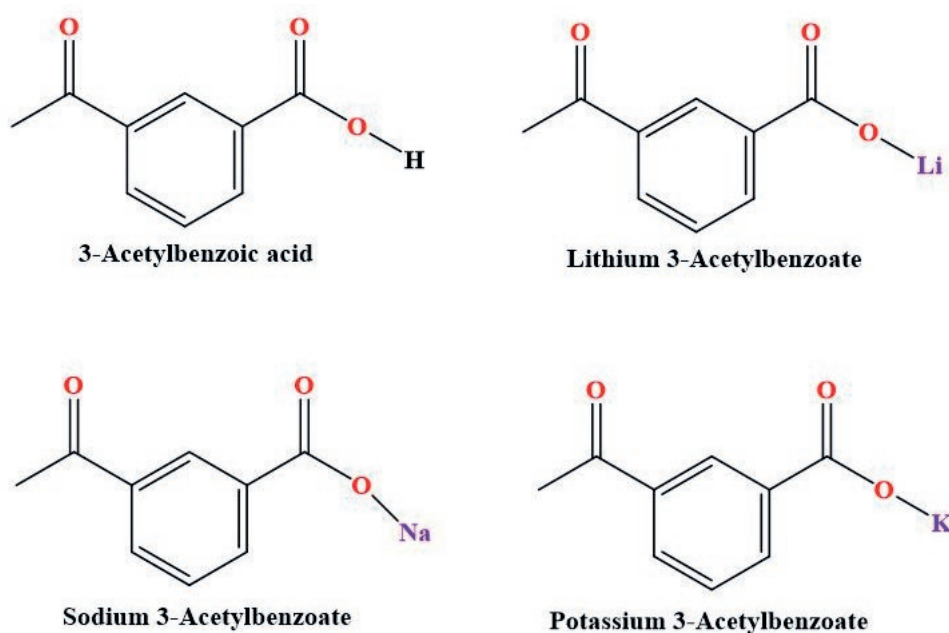


Fig. 1. 3-Acetylbenzoic acid derivative structure using Chemdraw

value of global potential energy surface (PES). The experimental findings were substantiated by molecular optimization and various chemical reactivity calculations, which were used to verify the molecular behavior of the 3ABA. The spectroscopic analysis of 3ABA was used to measure its structural properties, and the results were compared to the calculated values.

The main focus of the current investigation was the structural and electronic characteristics of compounds determined through DFT calculations using the B3LYP functional and the 6-31G+(d) basis set. The acquired data made it possible to estimate the corrosion-inhibiting activity of the 3-acetylbenzoic acid (3ABA) molecule, which was examined using the Gaussian 09W software suite. In this study, zinc was substituted with alkali metals, lithium (Li), sodium (Na), and potassium (K).

## 2. Computational method

The molecular structure of the 3-acetylbenzoic acid (3ABA) molecule was examined using the Gaussian 09W software suite, with zinc substituted by alkali metals, lithium (Li), sodium (Na), and potassium (K). 3ABA molecule was optimized using the DFT method with the B3LYP functional and the 6-31G+(d) basis set [13]. The obtained characteristics included  $E_{\text{HOMO}}$ ,  $E_{\text{LUMO}}$ , energy band gap (Eg), ionization energy (IE), electron affinity (EA), absolute electronegativity ( $\chi$ ), global hardness ( $\eta$ ), and global softness (S). In addition, the molecular electrostatic potential (MEP) on the surfaces was studied [14]. The fundamental optical properties were calculated for every chemical, including work function ( $\Phi$ ), Fermi energy ( $E_f$ ), and optical electronegativity ( $\Delta\chi^*$ ). The electron localization function (ELF) and localized orbital locator (LOL) topologies for the studied compounds were generated using the Multiwfn 3.7 software [15].

## 3. Results and discussion

Quantum chemical calculations, such as the HOMO-LUMO energy analysis, are increasingly used to predict corrosion inhibition efficiency. These calculations show that the inhibitor has the ability to both donate (HOMO) and receive (LUMO) electrons from the metal surface, which affects the formation of protective layers and,

eventually, the efficiency of corrosion inhibition [16, 17].

All theoretical calculations were performed using the Gaussian 09W software package, and the results were subsequently analyzed with Gaussian to evaluate them. The stability of the molecular structure was evaluated by PES scan analysis using the B3LYP level of theory with the 6-31G+(d) basis set. The electronic properties, vibrational characteristics, and optimized structures in both solid and solvation (DMSO) phase were calculated using the DFT-B3LYP method with the 6-31G+(d,p) basis set [18]. The HOMO and LUMO molecular orbitals (MOs) of an organic molecule are closely linked to its chemical and biological activities. The ground-state minimum energies of the optimized molecular structure are shown in Table 1. The energy of a bonded structure, such as an atomic unit, can be negative if the total energy of the system is lower than the sum of the energies of its individual components [19, 20].

The electrostatic potential (ESP) map simultaneously shows the molecular size, shape, and electrostatic potential using color grading, making it a great tool for correlating the chemical structures of biomolecules with their physical characteristics. According to the color coding, areas with a low electron density are shown in blue, areas with a high electron density are shown in red, and sections with no electrical charge are shown in green. The potential values decrease in the order: red < orange < yellow < green < blue. In the 3ABA-Na molecule, the most electronegative areas were located around the oxygen atoms, as shown in Fig. 2, whereas the most electron-rich regions were located in the orange and red regions. The 3ABA-Na molecule had a higher negative potential where the deeper red zones on an electrostatic potential map aligned with areas of high electronegativity. On the other hand, areas of low electronegativity in 3ABA were within lighter blue zones, indicating significantly more positive potential. Fig. 2 shows that the most electron-rich (red and orange) and electronegative (bright) areas of the 3ABA-molecule are centered around the oxygen atoms; while other electron-rich (yellow) areas are at the centers of the cyclopentadienyl rings of ferrocene and the benzene rings, where negatively charged carbon atoms are present [21].

We described the optimized bond lengths and angles for the studied molecule, 3-acetylbenzoic acid, in two distinct phases: gas phase and solvation phase. The experimental data for the studied molecule were then compared with the results from the theoretical optimization of its structure. The studied molecule consists of thirteen carbon atoms, eight hydrogen atoms, and three oxygen atoms (Fig. 2). Bond lengths and bond angles associated with the bonds connected to O1 and O2 in the original structure are notably short. These bonds exhibit the shortest bonds recorded both experimentally and theoretically. The bond angles with the smallest values are C12-O2-H20, C10-C11-H17, and O2-C12-C6 while O1-C10, O3-C12, and O2-C12 are the shortest bonds. C4-C10 and C4-C7-H14 are bond angles with the greatest values, whereas C4-C7-C9 and C10-C11 are the longest bonds [22].

### 3.1. HOMO–LUMO analysis

Molecular electrostatic potential analysis provides a good visualization of the reactivity of molecules identifying sites prone to nucleophilic or electrophilic attack. The studied molecule contains the following components: a benzene ring, a carbonyl group, a carboxyl group, and a methyl group. The electrostatic potentials are shown using various colors. Specifically, a deep red color indicates a negative potential, which implies nucleophilic attack. Conversely, a bright blue color signifies a positive potential, representing an electrophilic attack. Finally, a green color represents a zero potential, indicating a radical attack. As can be seen from the figure, nucleophilic attack in the molecule is most pronounced in the benzene ring attached to the carboxyl group, as well as in the benzene and methyl groups attached to the carbonyl groups. Conversely, the electrophilic attack is observed in the methyl group and benzene ring. Alternatively, the chemical behavior of the 3ABA molecule may be characterized by calculating its HOMO–LUMO energies. These energies are shown in Fig. 3. The HOMO–LUMO energies calculated for 3ABA, 3ABA–Li, 3ABA–Na, and 3ABA–K in the gas system are: –7.12805, –4.89915, –4.71835, and –4.59419 eV and –1.51103, –1.04438, –1.25094, and –1.12211 eV respectively. The band energy gaps for these compounds are: 5.617, 3.855, 3.467,

and 3.472 eV respectively. The studied molecule exhibits a higher electrophilicity index (3.322 eV) and a higher electronegativity (4.320 eV). The results are shown in Table 1 [23]. These values provide strong evidence of the enhanced electronic transition in the studied molecule.

To characterize the molecular structure and determine the optical and electrical properties of molecules, particularly 3ABA and 3ABA–M, the potential energy map, or PEM, is crucial. The values of electronegativity for 3ABA, 3ABA–Li, 3ABA–Na, and 3ABA–K were 4.320, 2.972, 2.985, and 2.858 eV, respectively. Similarly, the values for hardness and softness were 2.809, 1.927, 1.734, and 1.736 eV and 0.178, 0.259, 0.288, and 0.288 eV, respectively. As can be seen from Table 1, this means that 3ABA is more stable and less reactive than 3ABA–M. The blue zone, corresponding to the higher electrophilicity index of 3ABA (4.320 eV), indicates areas with a higher electron density. The potential energy map can also be impacted by other factors, such as electronegativity [24].

In molecular orbital theory, the “EHOMO–ELUMO energy gap” refers to the minimum energy required to excite an electron from the highest occupied molecular orbital to the lowest unoccupied molecular orbital. This energy gap is the key indicator of the substance’s chemical reactivity and stability. The 3ABA, 3ABA–Li, 3ABA–Na, and 3ABA–K compounds had the following HOMO and LUMO values: –7.12805, –4.89915, –4.7183 and –4.59419 eV and –1.51103, –1.04438, –1.25094 and –1.12211 eV respectively.

Thus, it can be concluded that a larger energy band gap indicates a softer molecule, but the opposite is also true: a greater molecular hardness 3ABA (2.809 eV) is associated with a softer molecule, as Table 1 illustrates. These results show that the neutral molecule was impacted by Li, Na, and K elements. A molecular structure with a smaller energy gap, such as the 3ABA–Na compound, exhibits increased flexibility and high polarization, which are directly linked to decreased stability and increased chemical reactivity. This means that it performs better as a corrosion inhibitor. The inhibitory efficiencies of the studied compounds follow the order: 3ABA–Na > 3ABA–K > 3ABA–Li > 3ABA, which aligns well with the theoretical data. These data



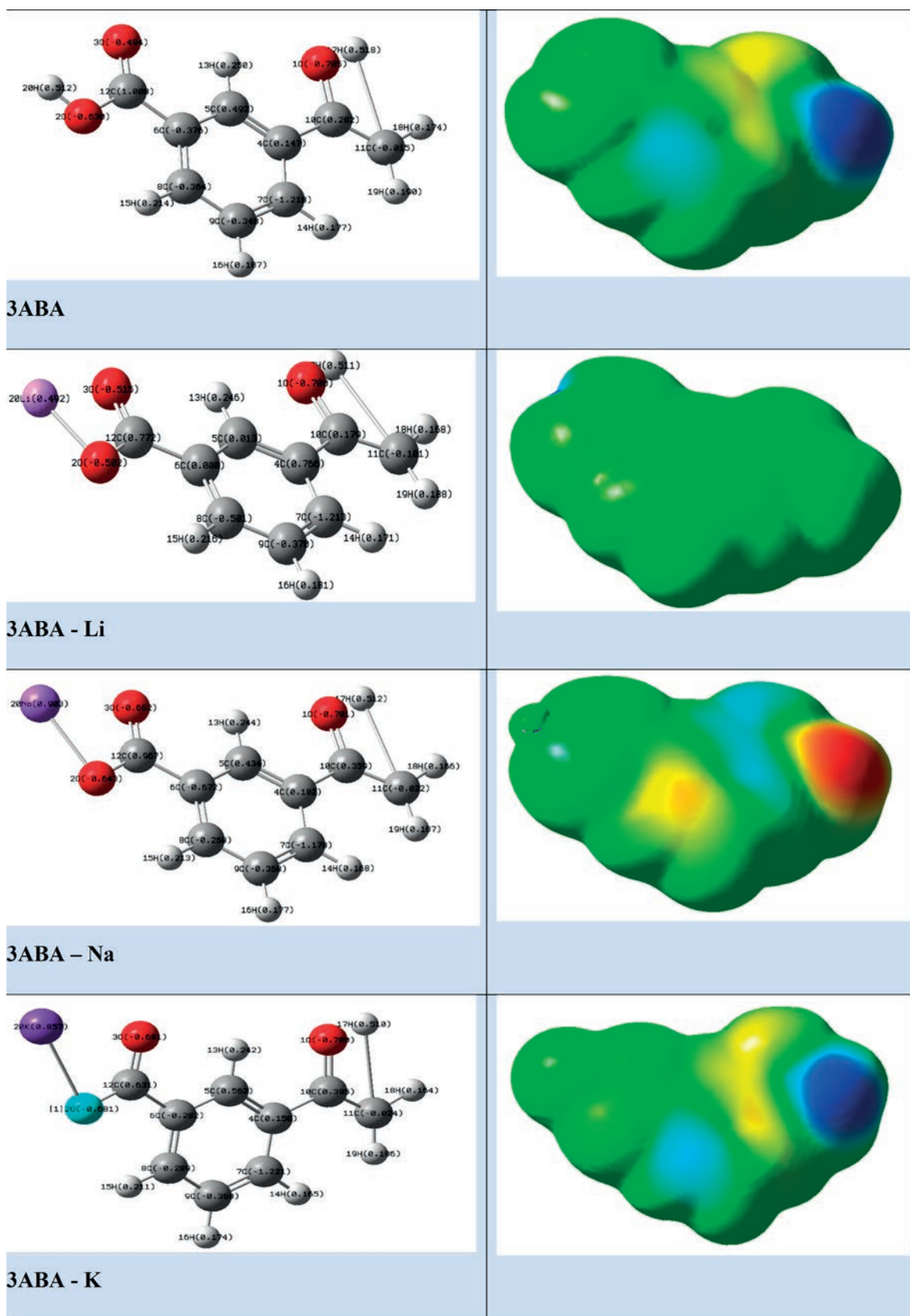


Fig. 2. Left-hand geometry optimization, right hand Electro static potential (ESP) surface

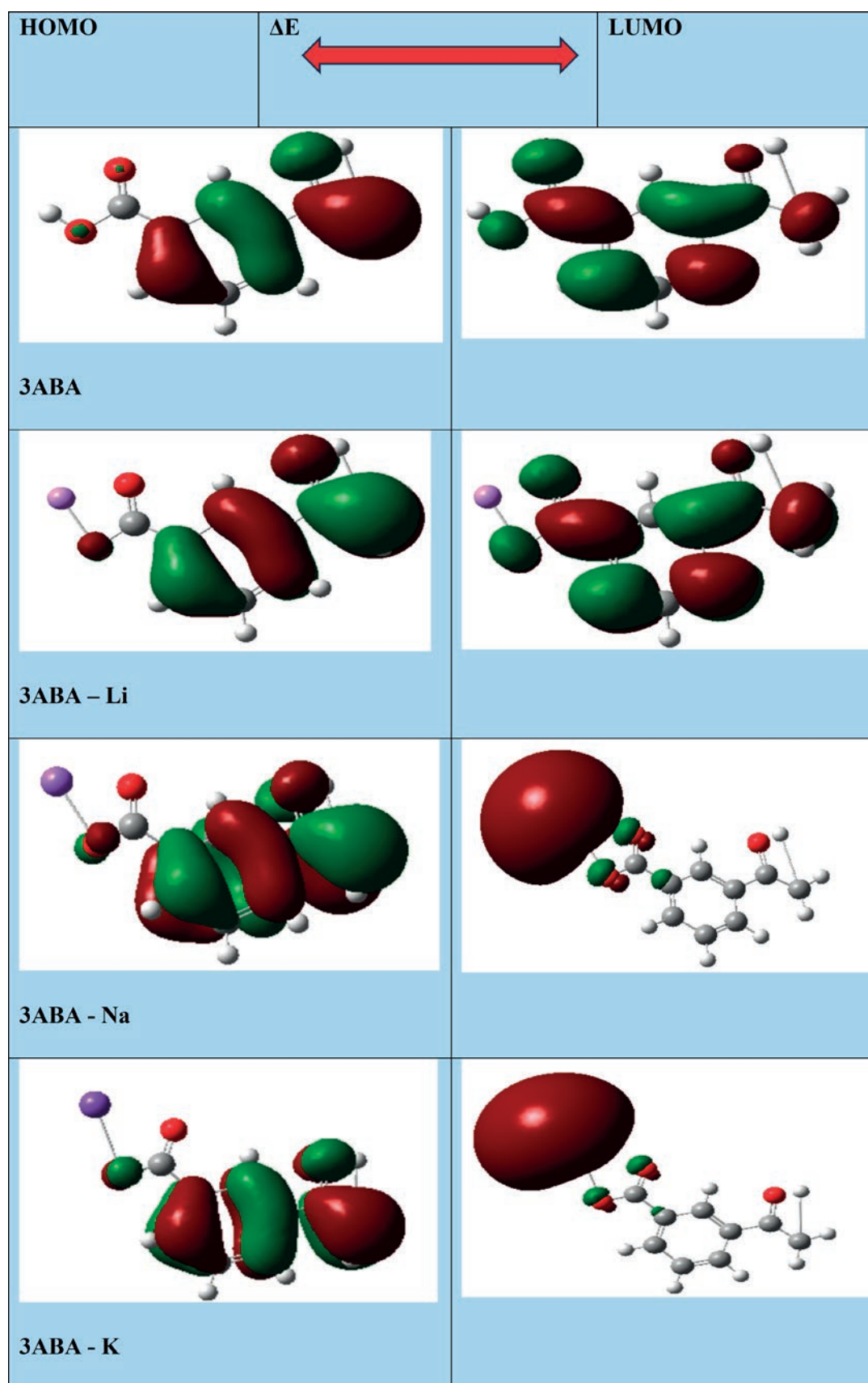


Fig. 3. The FMOS for the title compounds

**Table 1.** Global reactivities calculation

Parameters [25]	3ABA	3ABA - Li	3ABA - Na	3ABA - K
SCF energy (a.u)	-572.98	-508.45	-735.22	-1172.81
HOMO (eV)	-7.12805	-4.89915	-4.71835	-4.59419
LUMO (eV)	-1.51103	-1.04438	-1.25094	-1.12211
IP (eV)	7.128	4.899	4.718	4.594
EA (eV)	1.511	1.044	1.251	1.122
Band gap energy ( $E_g$ ) (eV)	5.617	3.855	3.467	3.472
Hardness ( $\eta$ ) (eV)	2.809	1.927	1.734	1.736
Softness ( $S$ )	0.178	0.259	0.288	0.288
Electronegativity ( $\chi$ ) (eV)	4.320	2.972	2.985	2.858
Chemical potential ( $\mu$ ) (eV)	-4.320	-2.972	-2.985	-2.858
Electrophilicity index ( $\omega$ ) (eV)	3.322	2.291	2.569	2.353
nucleophilicity index	0.301	0.436	0.389	0.425
back-donation	-0.702	-0.482	-0.433	-0.434
charge transfer ( $\Delta N_{max}$ )	1.538	1.542	1.722	1.646
Total Dipole Moment ( $Dy$ )	7.028	5.195	6.328	9.622
Fermi level energy ( $E_f$ ) (eV)	-7.884	-5.421	-5.344	-5.155
work function ( $\Phi$ ) (eV)	7.884	5.421	5.344	5.155
Optical electronegativity ( $\Delta\chi^*$ )	1.505356	1.03314	0.929156	0.930496

suggest that the five extremely electronegative 3ABA molecules (4.320 eV) are ineffective corrosion inhibitors. Fig 4. shows global reactivity correlations for the studied compounds.

The energy gap values, ranked from highest to lowest, are: 3ABA > 3ABA - Li > 3ABA - K > 3ABA - Na. In contrast, the refractive indices follow the opposite order: 3ABA - Na > 3ABA - K > 3ABA - Li > 3ABA. Similarly, the dielectric constants are arranged as 3ABA - Na > 3ABA - K > 3ABA - Li > 3ABA. Data from Tables 1 and 2 show a linear inverse relationship between refractive index and dielectric constant and the HOMO-LUMO energy gap. Consequently, we have revealed that a higher hardness ( $\eta$ ) value corresponds to a lower refractive index and dielectric constant, whereas greater molecular softness ( $S$ ) is associated with higher refractive index.

In summary, a large HOMO and LUMO energy band gap (3ABA), lower refractive index (3ABA), and dielectric constant (3ABA) indicate poor corrosion inhibition performance due to its lower electrical conductivity and reduced reactivity, while a smaller energy band gap for 3ABA - Na is associated with enhanced corrosion inhibition potential (Tables 1 and 2).

### 3.2. Electron localization function (ELF)

In computational chemistry, the electron localization function (ELF) is a valuable tool for visualizing and understanding the distribution of electrons within molecules. ELF provides insights into the electronic structure by indicating the probability of finding electrons localized in specific regions. There is a correlation between the ELF and the likelihood of electrons with the

**Table 2.** Refractive indexes of compounds ( $n$ ), and Dielectric constants of computed ( $\epsilon$ )

Calculated Methods	6-31G (d,p)							
	Refractive indexes ( $n$ )				Dielectric constants of computed ( $\epsilon$ )			
	3ABA	3ABA - Li	3ABA - Na	3ABA - K	3ABA	3ABA - Li	3ABA - Na	3ABA - K
Moss Relation [26]	2.027	2.228	2.287	2.287	4.112	4.964	5.234	5.230
Ravind Revelation [27]	0.601	1.693	1.934	1.931	0.361	2.868	3.741	3.729
Herve Relation [27]	1.799	2.108	2.200	2.199	3.239	4.447	4.843	4.838
Reddy relation [28]	2.327	2.577	2.654	2.653	5.414	6.642	7.045	7.040
Kumar Relation [29]	1.930	2.179	2.255	2.254	3.726	4.749	5.085	5.080
Tripathy Relation [29]	1.889	2.141	2.237	2.236	3.569	4.587	5.007	5.001



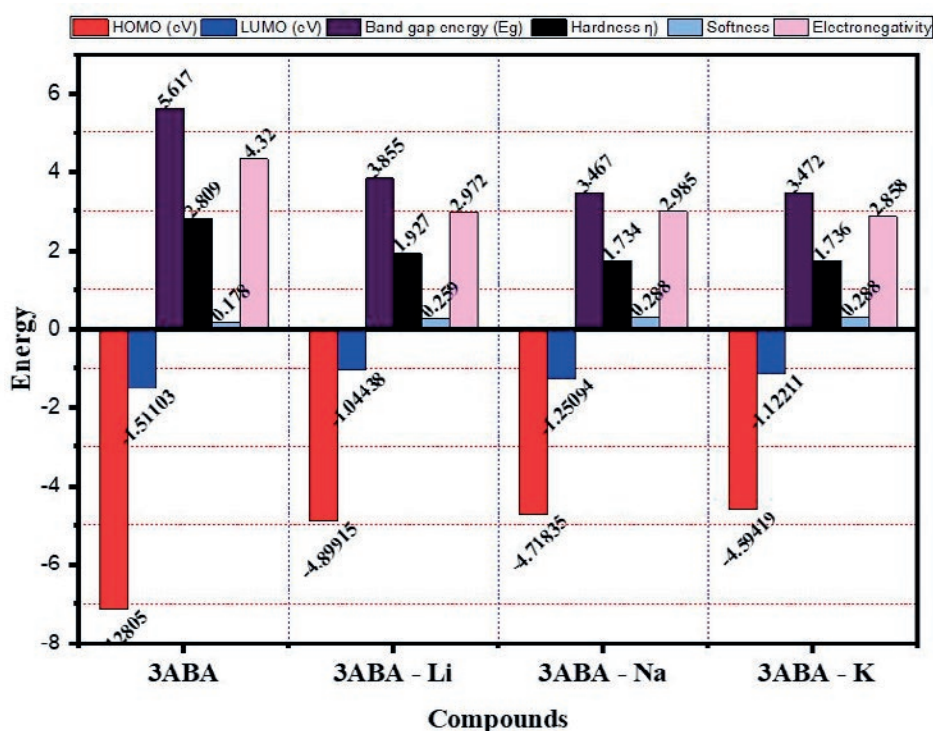


Fig. 4. The global reactivity correlations

same spin being close to each other. This method identifies regions of electron pairing, including bonds, lone pairs, and core electrons. The ELF values range from zero to one, where 0 indicates completely delocalized electrons and 1 stands for highly localized electrons.

Important characteristics: regions near atomic nuclei exhibit high ELF values (close to 1), indicating localized core electrons. In bonding regions, ELF values are intermediate, reflecting the sharing of electron pairs between atoms. High ELF values in areas that are not engaged in bonding correspond to lone pairs.

A related concept, LOL, is concerned with the localization of orbitals rather than electron pairs. Based on the kinetic energy density, LOL helps identify regions with concentrated electron density. LOL provides a complementary perspective to ELF, making it particularly useful for analyzing the kinetic aspects of electron localization.

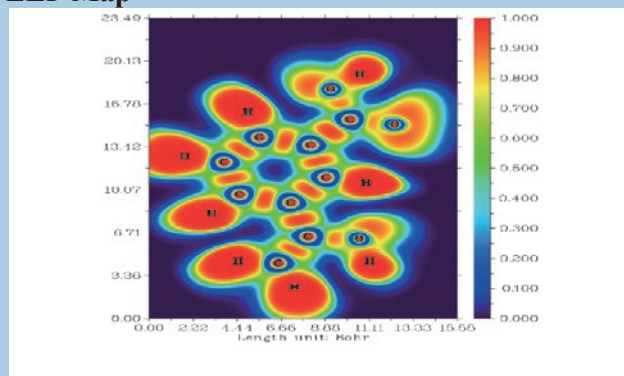
Important characteristics of bonding and non-bonding regions: LOL highlights the probable locations of electrons in both bonding and non-bonding orbitals. It can provide a more accurate view of orbital localization than ELF, especially in complex systems, and can be useful for visualization purposes.

In this study an ELF shaded surface map was used in computational chemistry to show where electrons were located within a molecule. This three-dimensional map enables chemists to better understand bonding patterns, lone pairs, and core electrons. The use of a color scale enhances visualization, clearly highlighting the nature of chemical bonds and interactions. Fig. 5 shows an ELF color-filled map with a color scale ranging from 0.000 to 1.000. The blue surface represents delocalized electrons (below 0.500) around the carbon and oxygen atoms, whereas the red surface indicates highly localized electrons (over 0.500) around the hydrogen atoms. Covalent bond interactions are indicated by the red area between C-C atoms, while the blue areas correspond to electron depletion zones between shells [22].

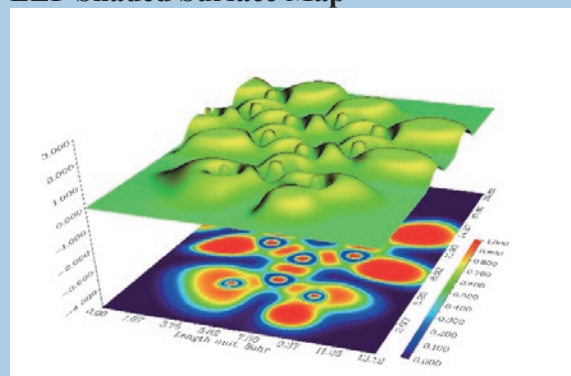
#### 4. Conclusion

In conclusion, our extensive investigation employing Gaussian simulations with DFT approach, using the B3LYP functional and 6-31G+(d) basis set, provided valuable insights into the molecular properties of 3-acetyl benzoic acid (3ABA)  $C_9H_8O_3$ . The primary objective of this research was to theoretical study derivatives

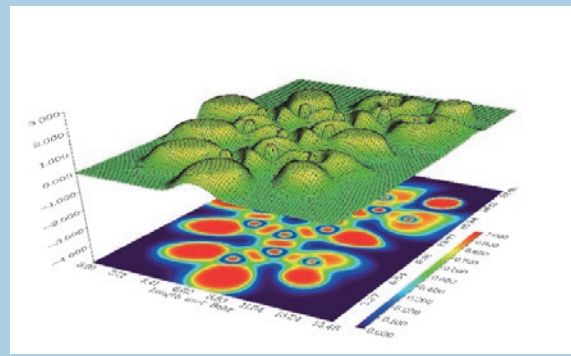
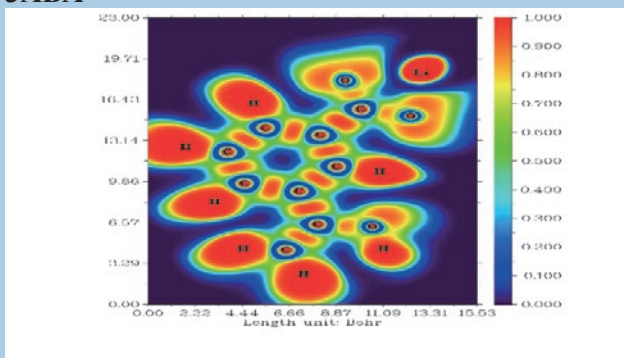
**ELF Map**



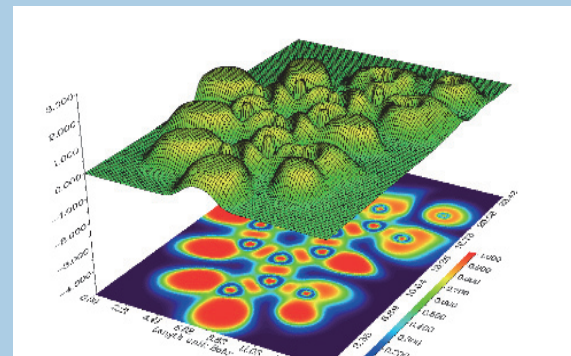
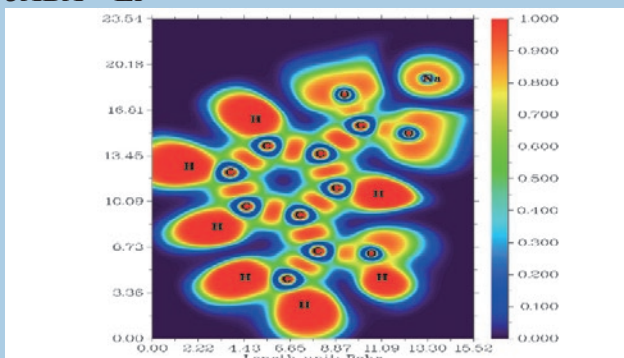
**ELF Shaded Surface Map**



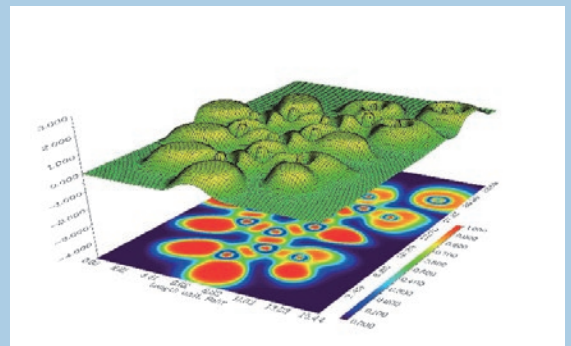
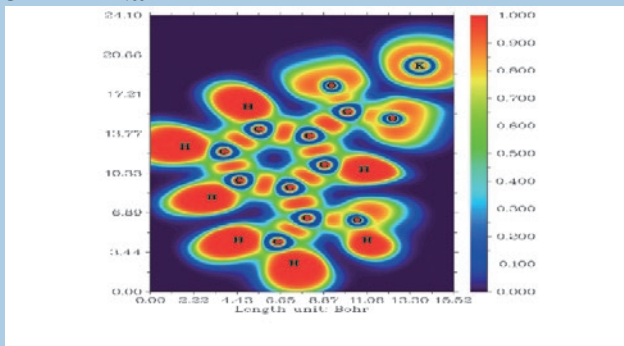
**3ABA**



**3ABA – Li**



**3ABA - Na**



**3ABA - K**

**Fig. 5.** The ELF, and ELF shaded surface map

of 3ABA-M (Metal) where M is represented by lithium (Li), sodium (Na), and potassium (K). The analysis revealed that the most electron-rich (red and orange) and electronegative (bright) areas of the 3ABA molecule are located near the oxygen atoms; while other electron-rich (yellow) areas are found in the center of the cyclopentadienyl rings of ferrocene and benzene rings, where negatively charged carbon atoms are present. A molecular structure with a smaller energy gap, such as the 3ABA - Na compound (3.467 eV), along with lower hardness (1.734 eV) and higher softness (0.288 eV<sup>-1</sup>) has enhanced flexibility and high polarization. These properties are associated with decreased stability and increased chemical reactivity, which contribute to its superior performance as a corrosion inhibitor. Consequently, it can be concluded that a large energy gap in 3ABA (5.617 eV) and a high hardness (2.809 eV) correspond to low refractive index and dielectric constant values, whereas significant molecular softness of 3ABA-Na (2.88 eV<sup>-1</sup>) is associated with a higher refractive index. In the ELF color-filled map, the blue surface represents delocalized electrons (below 0.500) around the carbon and oxygen atoms, whereas the red surface indicates highly localized electrons (over 0.500) around the hydrogen atoms.

*The online version contains supplementary material*

### Contribution of the authors

Kareem R. O. – idea, text writing, scientific editing of the text, and Software; Hamad O. A. – search and analysis of literary data, text writing.

### Conflict of interests

The authors declare that they have no known competing financial interests or personal relationships that could have influenced the work reported in this paper.

### References

1. Verma C., Ebenso E. E., Quraishi M., Hussain C. M. Recent developments in sustainable corrosion inhibitors: design, performance and industrial scale applications. *Materials Advances*. 2021;2(12): 3806–3850. <https://doi.org/10.1039/D0MA00681E>
2. Aslam R., Serdaroglu G., Zehra S., ... Quraishi M. Corrosion inhibition of steel using different families of organic compounds: Past and present progress. *Journal of*

*Molecular Liquids*. 2022;348: 118373. <https://doi.org/10.1016/j.molliq.2021.118373>

3. Verma C., Chauhan D. S., Aslam R., ...Dubey S. Principles and theories of green chemistry for corrosion science and engineering: design and application. *Green Chemistry*. 2024;26(8): 4270–4357. <https://doi.org/10.1039/D3GC05207A>
4. Mazumder M. J. Global impact of corrosion: occurrence, cost and mitigation. *Glob Journal Engineer Science*. 2020;5(4): 1–5. <https://doi.org/10.33552/GJES.2020.05.000618>
5. Pittman C. U., Stahl G. A. Copolymerization of pentachlorophenyl acrylate with vinyl acetate and ethyl acrylate. Polymer-bound fungicides. *Journal of Applied Polymer Science*. 1981;26(7): 2403–2413. <https://doi.org/10.1002/app.1981.070260726>
6. Apostol T.-V., Chifiriuc M. C., Draghici C., ... Barbuceanu S.-F. Synthesis, in silico and in vitro evaluation of antimicrobial and toxicity features of new 4-[(4-chlorophenyl) sulfonyl] benzoic acid derivatives. *Molecules*. 2021;26(16): 5107. <https://doi.org/10.3390/molecules26165107>
7. Park E.-S., Moon W.-S., Song M.-J., Kim M.-N., Chung K.-H., Yoon J.-S. Antimicrobial activity of phenol and benzoic acid derivatives. *International Biodeterioration & Biodegradation*. 2001;47(4): 209–214. [https://doi.org/10.1016/S0964-8305\(01\)00058-0](https://doi.org/10.1016/S0964-8305(01)00058-0)
8. Parc H. W., Park E. H., Yun H. M., Rhim H. Sodium benzoate-mediated cytotoxicity in mammalian cells. *Journal of Food Biochemistry*. 2011;35(4): 1034–1046. <https://doi.org/10.1111/j.1745-4514.2010.00432.x>
9. Thirumurugan P., Matosiuk D., Jozwiak K. Click chemistry for drug development and diverse chemical-biology applications. *Chemical Reviews*. 2013;113(7): 4905–4979. <https://doi.org/10.1021/cr200409f>
10. Ayankojo A. G., Reut J., Nguyen V. B. C., Boroznjak R., Syritski V. Advances in detection of antibiotic pollutants in aqueous media using molecular imprinting technique – a review. *Biosensors*. 2022;12(7): 441. <https://doi.org/10.3390/bios12070441>
11. Maier T. M., Arbuznikov A. V., Kaupp M. Local hybrid functionals: theory, implementation, and performance of an emerging new tool in quantum chemistry and beyond. *WIREs Computational Molecular Science*. 2019;9(1): 1378. <https://doi.org/10.1002/wcms.1378>
12. Ghalla H., Issaoui N., Govindarajan M., Flakus H., Jamroz M., Oujia B. Spectroscopic and molecular structure investigation of 2-furanacrylic acid monomer and dimer using HF and DFT methods. *Journal of Molecular Structure*. 2014;1059: 132–143. <https://doi.org/10.1016/j.molstruc.2013.11.037>
13. Azeez Y. H., Kareem R. O., Qader A. F., Omer R. A., Ahmed L. O. Spectroscopic characteristics, stability, reactivity, and corrosion inhibition of ahpe-dop compounds incorporating (B, Fe, Ga, Ti): a DFT investigation. *Next Materials*. 2024;3: 100184. <https://doi.org/10.1016/j.nxmte.2024.100184>
14. Kareem R. O., Kebiroglu H., Hamad O. A. Investigation of electronic and spectroscopic properties of phosphosilicate glass molecule (BioGlass 45S5) and Ti-BioGlass 45S5 by quantum programming. *Journal of Chemistry Letters*.



2024;4(4): 200–210. <https://doi.org/10.22034/jchemlett.2024.416584.1138>

15. Shukla S., Srivastava A., Kumar P., Tandon P., Maurya R., Singh R. Vibrational spectroscopic, NBO, AIM, and multiwfn study of tectorigenin: a DFT approach. *Journal of Molecular Structure*. 2020;1217: 128443. <https://doi.org/10.1016/j.molstruc.2020.128443>

16. Nadr R. B., Abdulrahman B. S., Azeez Y. H., Omer R. A., Kareem R. O. Quantum chemical calculation for synthesis some thiazolidin-4-one derivatives. *Journal of Molecular Structure*. 2024;1308: 138055. <https://doi.org/10.1016/j.molstruc.2024.138055>

17. Mamand D. M., Azeez Y. H., Qadr H. M. Monte Carlo and DFT calculations on the corrosion inhibition efficiency of some benzimide molecules. *Mongolian Journal of Chemistry*. 2023;24(50): 1–10. <https://doi.org/10.5564/mjc.v24i50.2435>

18. Azeez Y. H., Kareem R. O., Hamad O., ... Kaygılı O. Quantum chemical calculation employed for investigation mesitylene compound. *Journal of Physical Chemistry and Functional Materials*. 2024;7(1): 17–27. <https://doi.org/10.54565/jphcfum.1350445>

19. Issaoui N., Abdessalem K., Ghalla H., Yaghmour S. J., Calvo F., Oujia B. Theoretical investigation of the relative stability of Na+Hen (n = 2–24) clusters: Many-body versus delocalization effects. *The Journal of Chemical Physics*. 2014;141(17). <https://doi.org/10.1063/1.4900873>

20. Gong Y. Structure-property relationships of dyes as applied to dye-sensitized solar cells. 2018. *Repository*. <https://doi.org/10.17863/CAM.22164>

21. Raja M., Muhamed R. R., Muthu S., Suresh M. Synthesis, spectroscopic (FT-IR, FT-Raman, NMR, UV-Visible), NLO, NBO, HOMO-LUMO, Fukui function and molecular docking study of (E)-1-(5-bromo-2-hydroxybenzylidene)semicarbazide. *Journal of Molecular Structure*. 2017;1141: 284–298. <https://doi.org/10.1016/j.molstruc.2017.03.117>

22. Vijayakumari G., Iyandurai N., Raja M., ... Muthu S. Chemical reactivity, solvent effects, spectroscopic (FTIR, Raman, SERS, UV-Visible), Hirshfeld analyses and antimalarial investigation of 3-Acetylbenzoic acid. *Chemical Physics Impact*. 2023;6: 100190. <https://doi.org/10.1016/j.chphi.2023.100190>

23. Mohammed B. A., Kareem R. O., Hamad O. A., Kebiroglu H. The electronic structure and physicochemical characteristics of chlorohydroquinone compounds using density functional theory and Hartree-Fock techniques. *South African Journal Chemistry*. 2024;78: 85–94. <https://doi.org/10.17159/0379-4350/2024/v78a12>

24. Kareem R. O., Hanifi Kebiroğlu M., Hamad O. A. H., Kaygili O., Bulut N. Epinephrine compound: unveiling its optical and thermochemical properties via quantum computation methods. <https://doi.org/10.2139/ssrn.4603446>

25. Hamad O., Kareem R. O., Kaygılı O. Density function theory study of the physicochemical characteristics of 2-nitrophenol. *Journal of Physical Chemistry and Functional Materials*. 2023;6(1): 70–76. <https://doi.org/10.54565/jphcfum.1273771>

26. Moss T. A relationship between the refractive index and the Infra-Red threshold of sensitivity for photoconductors. *Proceedings of the Physical Society Section B*. 1950;63(3): 167. <https://doi.org/10.1088/0370-1301/63/3/302>

27. Ravindra N., Auluck S., Srivastava V. On the penn gap in semiconductors. *Physica Status Solidi (b)*. 1979;93(2): K155–K160. <https://doi.org/10.1002/pssb.2220930257>

28. Reddy R., Gopal K. R., Narasimhulu K., ... Kumar M. R. Interrelationship between structural, optical, electronic and elastic properties of materials. *Journal of Alloys and Compounds*. 2009;473(1-2): 28–35. <https://doi.org/10.1016/j.jallcom.2008.06.037>

29. Kumar V., Singh J. Model for calculating the refractive index of different materials. *NIScPR Online Periodicals Repository*. 2010;48(08): 571–574.

## Information about the authors

*Rebaz Obaid Kareem*, M.Sc in General Physics, Lecturer at the Department of Physics, Faculty of Science, Physics Department, Halabja University (Kurdistan Region, Iraq).

<https://orcid.org/0000-0001-6273-1309>

[rebaz.kareem@uoh.edu.iq](mailto:rebaz.kareem@uoh.edu.iq)

*Othman Abdulrahman Hamad*, PhD in Organic Chemistry, University of Raparin, College of Science, Department of Chemistry (Sulamani, Iraq).

<https://orcid.org/0000-0001-8170-9094>

[osman20f@gmail.com](mailto:osman20f@gmail.com)

Received 03.10.2024; approved after reviewing 13.11.2024; accepted for publication 16.12.2024; published online 25.06.2025.



## Original articles

Research article

<https://doi.org/10.17308/kcmf.2025.27/12822>

## DFT analysis: correlation of epinephrine HOMO-LUMO, refractive index, optical electronegativity, and electrical conductivity with Substituted Halogens (F, Cl, Br)

R. O. Kareem✉

Physics Department, College of Science, University of Halabja,  
Halabja 46018, Iraq

### Abstract

**Purpose:** Epinephrine (EP) may affect lipid and glucose metabolism in addition to haemodynamic parameters, according to a number of studies. This study's primary goal was to provide a theoretical computer analysis of the EP molecule by including halogens like fluorine (F), chlorine (Cl), and bromine (Br): (EP, EP-Br, EP-Cl, and EP-F).

**Experimental part:** The Gaussian program was used to obtain the optimal shape of the EP compound, and the DFT/6-311G (d,p) basis set and B3LYP level of theory were employed. Quantum chemistry properties were then analyzed, including the energy gap ( $E_{\text{HOMO}} - E_{\text{LUMO}}$ ), reduced density gradient (RDG), density of states (DOS), and molecular electrostatic potential (MEP) on surfaces.

**Conclusions:** The results showed that the larger refractive index of the EP-F molecule was associated with a higher value of EP-F ( $0.446 \text{ eV}^{-1}$ ) molecular softness, while the EP molecule exhibited higher hardness ( $\eta$ ) ( $2.296 \text{ eV}$ ) and a smaller refractive index. On the other hand, a smaller bandgap for EP-F ( $4.483 \text{ eV}$ ) indicated reduced chemical stability, increased electron dispersion, a lower work function ( $2.40682 \text{ eV}$ ), and improved electrical conductivity ( $\sigma = 1.249$ ). According to our Electron Localized Function (ELF) topological analysis data, the group of H atoms had a red patch around them, indicating an abundance of delocalized electrons.

**Keywords:** Epinephrine, DFT, Refractive Index, Electron Localized Function (ELF), Electrical Conductivity, Optical Electronegativity

**Acknowledgements:** We express our gratitude to the leaders of Department of physics, college of Science & Halabja University.

**For citation:** Kareem R. O. DFT analysis: correlation of epinephrine HOMO-LUMO, refractive index, optical electronegativity, and electrical conductivity with Substituted Halogens (F, Cl, Br). *Condensed Matter and Interphases*. 2025;27(2): 236–. <https://doi.org/10.17308/kcmf.2025.27/12811>

**Для цитирования:** Карим Р. О. DFT анализ: корреляция HOMO-LUMO молекулы адреналина, показателя преломления, оптической электроотрицательности и электропроводности в результате замещения галогенами (F, Cl, Br). *Конденсированные среды и межфазные границы*. 2025;27(2): 237–250. <https://doi.org/10.17308/kcmf.2025.27/12811>

✉ Kareem R. O, e-mail: rebaz.kareem@uoh.edu.iq

© Kareem R. O., 2025



The content is available under Creative Commons Attribution 4.0 License.

## 1. Introduction

Although both norepinephrine (NEP) and epinephrine (EP) are catecholamines that are chemically similar and play a part in the fight-or-flight response, they are distinct from one another in terms of their receptor selectivity, spectrum of physiological effects, release patterns, and medical uses. Both are organic substances produced by the body's adrenal glands. In healthy individuals, NEP has been demonstrated to have an impact on hemodynamic parameters, lipid and carbohydrate metabolism, and plasma EP increases. On mineral metabolism, EP physiological effects are unknown. There are conflicting reports on how much EP affects blood magnesium levels and large dosages of the hormone have been shown to lower amounts of inorganic phosphorus and calcium [1]. EP is involved in the control of the sympathetic nervous system and the body's response to stress, whereas selenium is more closely linked to enzymatic processes and antioxidant defense [2]. The body releases adrenaline (AD) into the circulation in response to perceived stress or danger. Moreover, it is a component of various emergency medical circumstances, such as cardiac arrest, and is utilized medicinally to treat severe allergic responses. In cases of emergency or rapidly deteriorating circumstances, it can be given by injection [3]. The chemical structure of the powdered form of EP is white to almost white in microcrystalline form, tasteless, and melting point (211–212) °C. The pH of aqueous solutions is somewhat alkaline, numbing, somewhat bitter flavor.

The three -OH and one -NH groups found in the EP molecule are both involved in the formation of hydrogen bonds and are readily exposed to redox processes. The likelihood of an H-bond forming between these four potential bonding places is higher for the -OH group attached to C [5]. Moreover, carboxyl or carbonyl groups might develop as a result of the oxidative sensitivity of the aliphatic OH next to the amino group [6]. It is essential to comprehend the sites of binding and hydrogen bonding interactions of adrenaline [7]. After optimization, all bond lengths that surfaced fall within permissible boundaries [5]. By rotating the three angles from the alcohol groups, -COH, and the dihedral angle

H-C-N-H, the potential energy surface (PES), in which the corresponding lowest energy was for the expanded geometry, was derived [6].

The chemical structure of EP includes halogen atoms, specifically one or two halogen atoms. It's important to note that the addition of halogen atoms, such as chlorine, fluorine, and bromine can influence certain properties of a compound, but in the case of epinephrine, the halide atoms mainly contribute to its structural configuration rather than dramatically altering its chemical or physical properties [8]. Energy in a chemical context can refer to various aspects, including the internal energy of the molecule, its potential energy in a certain environment, or its energy of formation. The presence of halides affects the bond energies within the molecule. The energy required to break or form bonds can be quantified, but these values depend on specific conditions [9].

The EP species' chemical stability demonstrates the results of the quantum chemical calculations. Among other electronic properties, the global hardness and chemical potential were computed. Density Functional Theory (DFT) was utilized to determine the molecular structure of the NEP molecule. In addition, the electronic distribution, energy-related to the structures, and distribution of HOMO and LUMO iso-surfaces are provided [6]. More investigation is required to find out more about the conformational stability of these substances [10]. On the other hand, for computing molecular structure, chemical reaction energies, and energy electronic calculations, DFT is a trustworthy and effective technique [11]. The improved molecular geometries [12]. They found that other factors outside the hydrogen bonding interaction are also responsible for the relative stabilities and activity [7]. An extensively employed approach for determining molecular energies and structural characteristics, as well as for accurately and successfully assessing many molecular properties, is the DFT method. Norepinephrine (NEP) and epinephrine (EP) are both catecholamines with similar chemical structures. The main difference between them is that norepinephrine has a hydrogen atom (H) attached to the nitrogen atom, while epinephrine has a methyl group (-CH<sub>3</sub>) attached to the nitrogen atom. NEP plays a major role in the fight-or-flight response by increasing heart rate,



blood pressure, and blood sugar levels. It not only increases heart rate, but also dilates airways and stimulates glucose release from the liver [13, 14].

The current study is the first theoretical report on the EP molecule, produced by introducing halogens into the ortho position of the benzene ring. Research was conducted mostly with the aim of performing a theoretical and computational analysis of the EP molecule by the inclusion of halogens such fluorine (F), chlorine (Cl), and bromine (Br) to the structure as shown in Fig. 1. Researchers have discovered a number of intriguing correlations between the HOMO-LUMO energy gap, the refractive index ( $n$ ), the dielectric constant ( $\epsilon$ ), the electrical conductivity ( $\sigma$ ), and the optical electronegativity ( $\Delta\chi^*$ ). Additionally, they have discovered the Fermi level energy ( $E_f$ ) and the work function ( $\Phi$ ) of four distinct types of EP molecules. These molecules were created by employing substituted halogens with names such as: EP, EP-Br, EP-Cl, and EP-F.

## 2. Computational studied

The Gaussian 09W software suite was used to look at the structure of the epinephrine (EP) molecule using different halogens, which were named: epinephrine (EP), epinephrine bromine (EP-Br), epinephrine chlorine (EP-Cl), and epinephrine fluorine (EP-F) [15]. A useful way to study molecular structure is through the

density-functional theory (DFT). Based on the B3LYP level of theory, and 6-311G(d, p) basis set, the EP molecule was optimized by using the DFT methodology. The following parameters are often recognized as eigenvalues that represent various energy-related properties:  $E_{\text{HOMO}}$ ,  $E_{\text{LUMO}}$ , the energy band gap ( $E_g$ ), ionization energy (IE), electron affinity (EA), absolute electronegativity ( $\chi$ ), global hardness ( $\eta$ ), global softness ( $S$ ). Also, the reduced density gradient (RDG), the density of state (DOS), and the molecular electrostatic potential (MEP) on surfaces have been investigated. The Multiwfn\_3.7 program is used to create contour maps that illustrate the Electron localized function (ELF) for the title compounds [15–21]. For each chemical, we determine its essential optical characteristics, such as the, the Fermi level energy ( $E_f$ ), and the work function ( $\Phi$ ) [22, 23], refractive index ( $n$ ), the dielectric constant ( $\epsilon$ ), electrical conductivity ( $\sigma$ ), and the optical electronegativity ( $\Delta\chi^*$ ): Moss relation [24], Ravind relation [25], Herve relation [25], Reddy relation [26], Kumar relation [27], Tripathy relation [27].

## 3. Result and Discussion

### 3.1. Geometric optimization and charge distribution

The optimal form was obtained by using the Gaussian software in conjunction with the DFT/

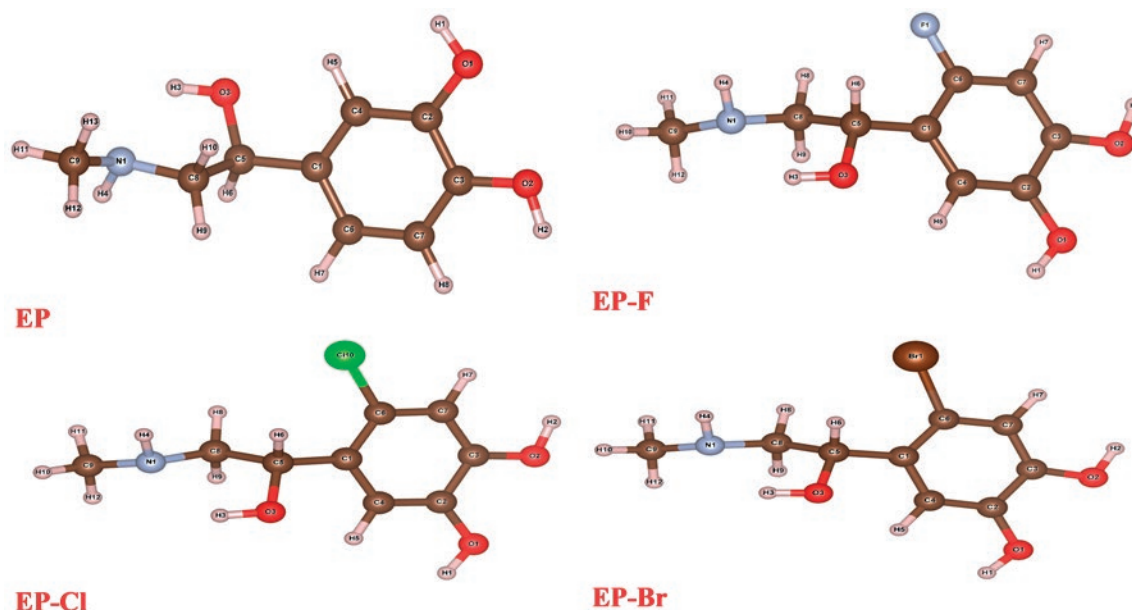


Fig. 1. The title compound's structure

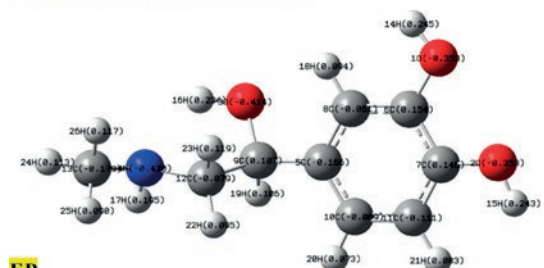
6-311G (d,p) basis sets, which were neutral to the structure of the epinephrine (EP). This is shown in Fig. 1 left hand. The first step of a geometry optimization technique that can be used for this method is to look at the energy that is linked to a certain starting shape of the molecules. There is a clear correlation between the form and type of the molecular orbitals (MOs) of organic chemicals, which are often referred to as HOMO and LUMO, and the chemical and biological functions of these substances [18]. In comparison to other elements such as carbon (C), nitrogen (N), hydrogen (H), halogens like fluorine (F), chlorine (Cl), and bromine (Br), the nitrogen (N) atoms. The N-H groups was investigated to be the most negatively charged: ( $-0.4299$ ,  $-0.4342$ ,  $-0.4336$ , and  $-0.4335$   $e^-$ ) for the EP, EP-Br, EP-Cl, and EP-F molecules. According to the results, the N element with EP has a lower charge ( $4N = -0.4299$   $e^-$ ). This

is because the electronegativity of the hydrogen or ( $H = 2.20$ ) is less than Br, Cl, and F elements. As can be seen on the right-hand side of Fig. 2, the physicochemical characteristics and chemical reactions of the compounds EP, EP-F, EP-Cl, and EP-Br are influenced by the electrostatic potential (ESP) maps and the electron charge densities. It was observed that the charge distribution of all molecules was altered by the presence of halogens like fluorine (F), chlorine (Cl), and bromine (Br). Equation (1) provides a quantitative demonstration of the ESP creation surrounding molecules at a location and a point  $r$  (in atomic units) [28, 29]:

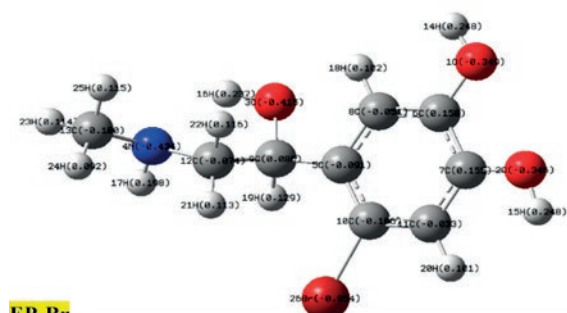
$$V_{(r)} = \sum_A \frac{z_A}{[R_A - r]} - \int \frac{\rho(r)dr}{[r - r]}, \quad (1)$$

where  $\rho(r)$  is the electronic density and  $z_A$  is the nucleus charge at  $R_A$ . The overall charge distribu-

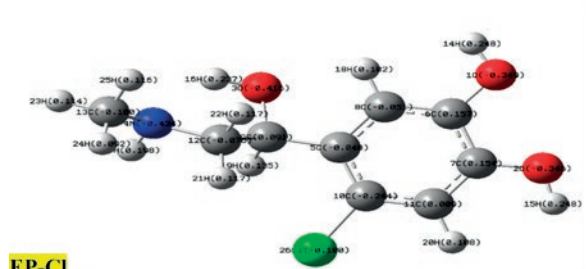
#### Geometric Optimization Shape



EP



EP-Br



EP-Cl

#### Electrostatic Potential or (Charge Density)

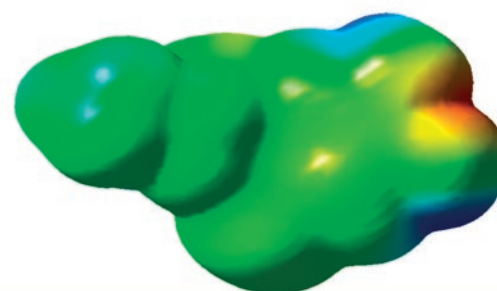
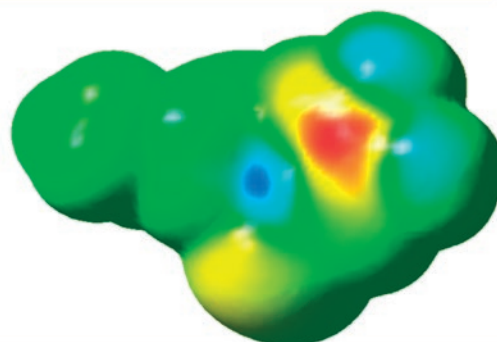
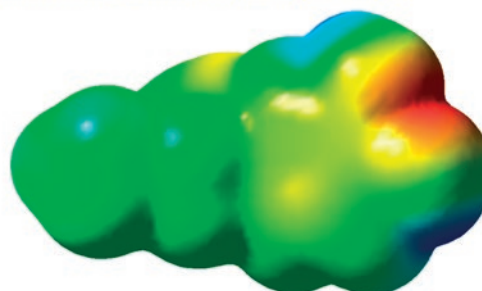


Fig. 2. Left-hand geometry optimization, right hand Electrostatic potential (ESP) surface, DFT approach

tion (electron + nucleus) of the molecule reflects the net electrostatic effect at  $r$ . The potential ( $V$ ) is a function of distance ( $r$ ). Molecular electrostatic potential (MEP) analysis is a powerful tool for studying the boundary of a molecule's charge concentration. Through the use of MEP analysis, the physicochemical characteristics of the system, including chemical reactivity, dipole moment, and partial charges, are linked to the geometry of the system shape [22]. A number of factors are associated with the ESP, including partial charges, electronegativity, the dipolar moment, and the location of chemical processes within the molecular structure. The various color zones that are connected with each molecule are related with varied electronegativity, which are ordered here:  $F = 3.98 > Cl = 3.16 > Br = 2.96 > H = 2.20$  eV. In an electrostatic potential map, areas with a high electronegativity tend to correlate with redder zones, which indicates a more negative potential. On the other hand, areas with a low electronegativity will seem much more positive (bluer) zones. Fig. 2 shows that, according to the EP picture, C-OH had a higher negative charge density and a red zone than other groups. Blue has more positive charge, smaller electron density, and lower proton affinity. When the colors red, yellow, green, and blue are arranged in this way, the potential is increased. The existence of a broad negative zone (green) range is an indication that the molecular structure of norepinephrine (EP, EP-Br, EP-Cl, and EP-F) is particularly reactive with nucleophilic types. This is shown by the fact that the range of the negative zone is vast [29, 30].

### 3.2. Global reactivates analyses

As can be seen in Fig. 3, the energy gap ( $E_g$ ) that exists between the highest occupied molecular orbital (HOMO), and the lowest unoccupied molecular orbital (LUMO) is examined in this section. Additionally, the Frontier molecular orbitals (FMOs) of (EP, EP-Br, EP-Cl, and EP-F) compounds are analyzed as well. FMO analysis is crucial because it reveals the optical properties and electronic behavior of the material. In addition, it provides details on the electrical conductivity of the compound, the distribution of electrons, its stability, and its resistance to sensing. The energy gap ( $E_g$ ) values reveal aspects of charge transport and system reactivity. The complex with the lowest energy gap values has a large electronic distribution from donor to acceptor orbitals, resulting in increased electrical conductivity of title compounds. A smaller bandgap ( $E_g$ )  $E_{\text{HOMO}} - E_{\text{LUMO}}$  is associated with higher electrical conductivity, more electron dispersion, less chemical stability, and more reactivity, according to a review of the literature [12, 17, 22, 31]. The term " $E_{\text{HOMO}} - E_{\text{LUMO}}$  energy gap" is used in the context of molecular orbitals to refer to the minimum amount of energy that is necessary to transfer a molecular orbital from its occupied state to its unoccupied state. It is necessary to investigate, and evaluate both the HOMO and the LUMO aspects of the system in order to acquire an understanding of the electronic structure of the molecular system as well as the mechanism that is responsible for the transfer of potential energy, and chemical stability- reactivity of molecules.

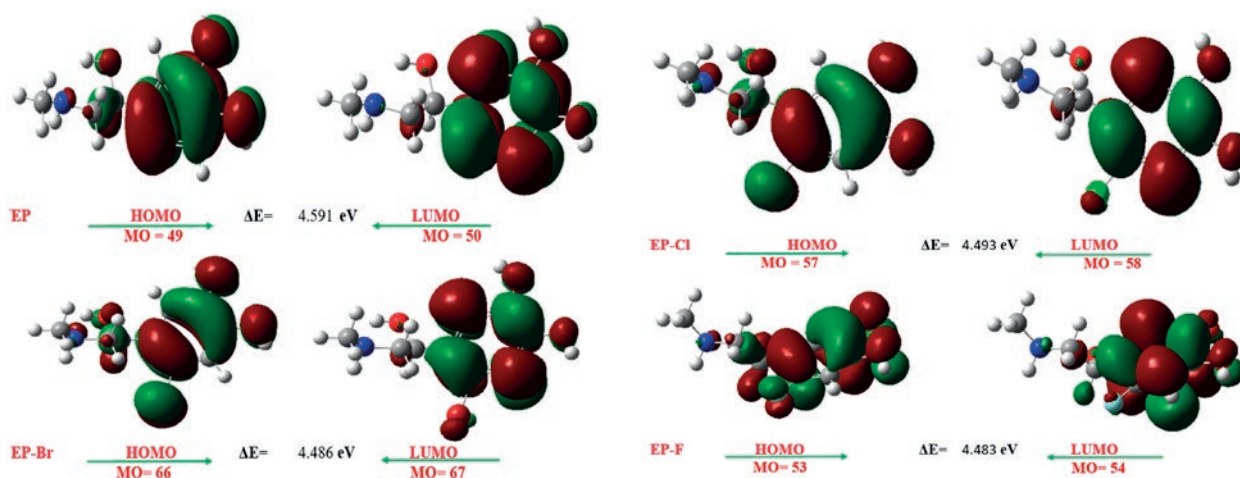


Fig. 3. The Front molecular orbitals (FMOs) diagram according to HOMO-LUMO



An inventory of the HOMO-LUMO energy gap as well as other global reactivities of all compounds can be found in Table 1, which can be seen below. The DFT/ B3LYP level of theory (technique) was used to determine this gap using the basis sets 6-311G (d, p) [16, 17, 32, 33].

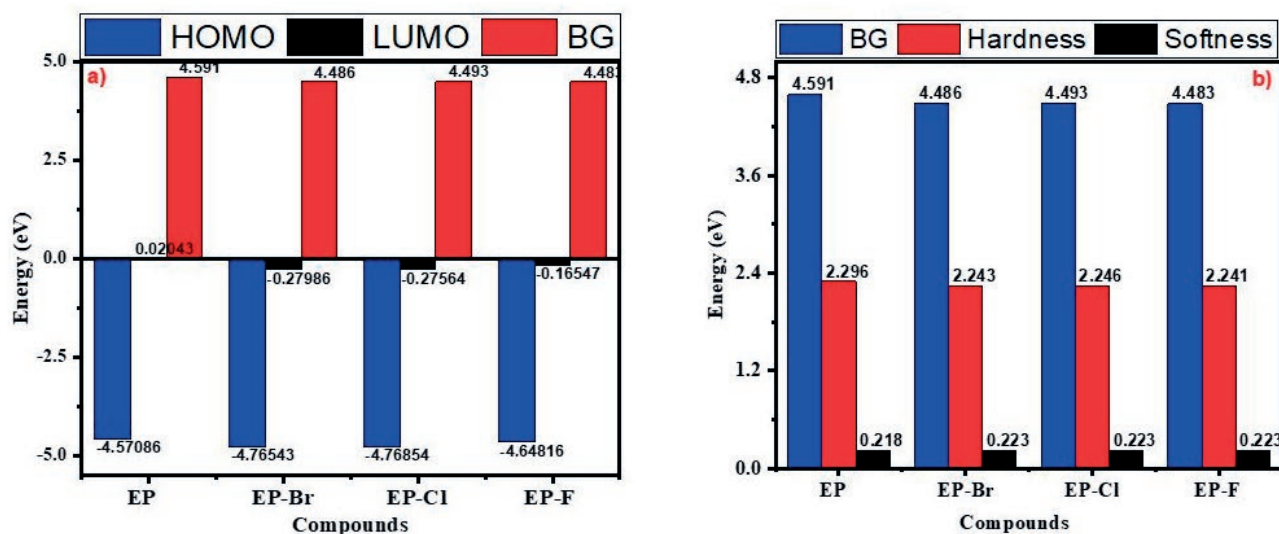
Fig. 4a displays the graph illustrating the variety of correlation between the HOMO, and LUMO of the compounds, as well as the energy gap. The EP-F compound with a lower energy gap of 4.483 eV shows characteristics of high electronic distribution, low chemical stability, high electrical conductivity, and high reactivity. In contrast EP, EP-Br, and EP-Cl have higher energy gaps, resulting in less electronic distribution, high stability, low electrical conductivity, and low reactivity. The EP-F values with the lowest energy gap, which are 4.483 eV, have a significant

electronic dispersion from the donor orbitals to the acceptor orbitals.

According to the literature assessment, systems with higher chemical hardness and ionization potential values imply less reactivity than systems with lower values. Because they can transmit electrons more easily than hard molecules, soft molecules are more reactive. In Table 1, molecular hardnesses are listed from greatest to lowest: EP > EP-Cl > EP-Br > EP-F while molecular softness EP-F > EP-Br > EP-Cl > EP compounds. The PE-F molecule has a softness of  $0.446 \text{ eV}^{-1}$ , which indicates that it is very capable of transferring electrons. According to Fig. 4b, based on this, we may deduce that a larger energy band gap indicates a lower molecular softness, and that the reverse is also true: that a higher molecular hardness is correlated with a

**Table 1.** Calculation of global reactivities parameters DFT/ 6-311 G (d, p)

Parameters Calculation [16, 17, 18, 19, 34, 35, 36]	EP	EP-Br	EP-Cl	EP-F	Recent study DFT/ SSD [17]
HOMO (eV)	-4.57086	-4.76543	-4.76854	-4.64816	-5.698
LUMO (eV)	0.02043	-0.27986	-0.27564	-0.16547	-0.101
IP (eV)	4.571	4.765	4.769	4.648	5.698
EA (eV)	-0.020	0.280	0.276	0.165	0.101
Band gap energy ( $E_g$ ) (eV)	4.591	4.486	4.493	4.483	5.597
Hardness ( $\eta$ ) (eV)	2.296	2.243	2.246	2.241	2.798
Softness (S) ( $\text{eV}^{-1}$ )	0.436	0.445	0.445	0.446	0.357
Electronegativity ( $\chi$ ) (eV)	2.275	2.523	2.522	2.407	2.899
Chemical potential ( $\mu$ ) (eV)	-2.275	-2.523	-2.522	-2.407	–



**Fig. 4.** Displays calculations for Compression HOMO, LUMO, BG, hardness, and softness

lower softness (Fig. 4b). Electronegativity, which is represented by the symbol  $\chi$ , is a measurement that measures the ability of an atom to take an electron. It is possible that EP-Br attracts electrons with a larger degree of attraction force when its electronegativity is high (2.523 eV), since this indicates that the element has a high electronegativity capacity [17, 30, 37, 38]. Based on the current findings, the literature analysis confirms and agrees with the HOMO and LUMO calculation approaches [17].

### 3.3. Optical properties

The optical characteristics of norepinephrine, including its refractive index ( $n$ ), dielectric constant ( $\epsilon$ ), and optical electronegativity ( $\Delta\chi^*$ ), are discussed in this section. The following formula is used to determine the refractive index of the EP, EP-Br, EP-Cl, and EP-F: Moss et al. [24], Ravindra et al. [25], Herve et al. [25], Reddy et al. [26], Kumar et al., and Tripathy et al. [27]. The coefficients of the refractive index that were estimated by using the Moss, Tripathy, Kumar, and Herve equations each have values that are rather close to one another, as can be observed by looking at the information that was collected in Table 2. The association between the refractive index and the energy gap is laid out in Tables 1, 2 are listed from the highest to lowest value: refractive index (EP-F > EP-Br > EP-Cl > EP), while energy gap (EP > EP-Cl > EP-Br > EP-F). From the information shown in Tables 1 and 2, it

is clear that the refractive index of EP Derivatives and the HOMO-LUMO energy gap are inversely connected to one another. The high refractive index corresponds with great molecular softness. The big energy gap is connected with a decreased refractive index. As demonstrated in Tables 2 and 3, the dielectric constant ( $\epsilon$ ) of the EP, EP-Br, EP-Cl, and EP-F increases with increasing optical refractive index values for these elements. According to the data shown in Tables 1, 2, and 3, a higher energy gap is associated with a lower refractive index and a lower dielectric constant [39, 40]. Our findings indicate that high molecular softness ( $S$ ) correlates with a high refractive index, whereas high hardness ( $\eta$ ) correlates with a low refractive index.

### 3.4. Correlation between Fermi energy, and energy gap

The energy gap ( $E_g$ ) values, Fermi level energy ( $E_f$ ), and work function ( $\Phi$ ) values obtained in the present study provide electronic distribution, low chemical stability, high electrical conductivity, and high reactivity. The DFT/B3LYP level of theory (technique) was used to determine this Fermi level energy, and work function 6-311G (d, p) basis sets. Equation (2) provides the formula for calculating the Fermi level energy or ( $E_f$ ), which is the amount of energy that an electron occupies while it is at a temperature of zero degrees Celsius. This energy may be derived from the FMO orbitals. where the work function or ( $\Phi$ )

**Table 2.** Refractive indexes of compounds ( $n$ )

Species	EP	EP-Br	EP-Cl	EP-F
Moss Relation [24]	2.13281938	2.145192	2.144356	2.14555
Ravind Relation [25]	1.23744575	1.302542	1.298202	1.304402
Herve Relation [25]	1.96123086	1.980418	1.979121	1.980974
Reddy Relation [26]	2.45695842	2.472461	2.471413	2.472912
Kumar Relation [27]	2.05995684	2.075377	2.074334	2.075825
Tripathy Relation [27]	2.00701618	2.023146	2.022042	2.02362

**Table 3.** Dielectric constants of computed ( $\epsilon$ )

Species	EP	EP-Br	EP-Cl	NEP-F
Moss Relation [24]	4.548919	4.601847	4.5983	4.6034
Ravind Relation [25]	1.531272	1.696615	1.6853	1.7015
Herve Relation [25]	3.846427	3.922054	3.9169	3.9243
Reddy Relation [26]	6.036645	6.113066	6.1079	6.1153
Kumar Relation [27]	4.243422	4.30719	4.3029	4.3090
Tripathy Relation [27]	4.028114	4.09312	4.0887	4.0950

is the amount of energy that must be expended in order to remove one electron from the Fermi level [41].

$$\text{Fermi level energy } (Ef) = \frac{\text{HOMO} + \text{LUMO}}{2}, \quad (2)$$

$$\Phi = \text{Vel}(+, \infty) - Ef, \quad (3)$$

where the electrostatic potential energy of the electron far from the surface of the material is denoted by  $\text{Vel}(+, \infty)$ , and it is equal to zero. Because of chemical interactions and the transfer of energy levels from the HOMO to the LUMO, substituted halogens such as fluorine (F), chlorine (Cl), and bromine (Br) also impact the  $Ef$  and work function ( $F$ ) values for epinephrine or (EP) compounds. As a result of the fact that the electrostatic potential energy is equal to zero, the work function ( $\Phi$ ) is taken as the negative of the Fermi level energy value. The  $Ef$  is computed by taking the average of the HOMO and LUMO energy values [23]. Using Equation (3), we can determine the relationship that exists between the work function and the Fermi level energy. The variations in the values of the work function also show that there is a transfer of charges between substituted halogens and compounds including epinephrine (EP) [23]. The values of the minimal work function (2.40682) and the Fermi level energy (−2.40682) are experienced by the EP-F compound. According of this, the small energy bandgap ( $Eg$ ) indicates better electrical conductivity, greater electron dispersion, less chemical stability, minimal work

function, and the Fermi level energy as seen in Table 5, and Fig. 5. As a result of this, the small energy bandgap ( $Eg$ ) exhibits characteristics such as improved electrical conductivity, increased electron dispersion, decreased chemical stability, a minimum work function, and the Fermi level energy, as can be shown in Table 5 and Fig. 5.

### 3.5. Electrical conductivity

The process by which electrons travel from the valence band (VB) to the conduction band (CB) is referred to as the electrical conductivity of a substance. The varied electronic properties of the complexes are the cause of the variations in the electrical conductivity of the complexes. Equation (4) is the primary factor in determining the electrical conductivity [42]:

$$\sigma = A T^{\frac{3}{2}} \times \text{EXP}^{\left(\frac{-E}{2KT}\right)}. \quad (4)$$

Where  $\sigma$  is the electrical conductivity,  $A$  is the Richardson constant ( $A = 6 \cdot 10^6$ ,  $T = 298.16$ ), Boltzmann constant ( $K = 8.318 \cdot 10^6$  kJ/mol·K) [43]. The presented equation establishes a connection between the HOMO–LUMO energy gap values and the electrical conductivity of the complexes. As can be seen in Table 6, this data reveals that an increase in the values of the energy gap leads to a decrease in the electrical conductivity of the compounds.

### 3.6. Electron localized function (ELF) topological analysis

Electron localized function (ELF) topology studies are often used to reveal the structure of atomic shells, categorize chemical bonds, and validate charge-shift bonds on the surface of molecules, as well as electron concentrations such as bonding, nonbonding, and lone pair. ELF employs  $\tau(r)$  to detect the additional kinetic energy density induced by Pauli's repulsion principle [44]. The Multiwfn\_3.7 program is used

**Table 4.** Optical electronegativity ( $\Delta\chi^*$ )

Compounds Name	6-311G (d, p)
EP	0.058375
EP-Br	1.202248
EP-Cl	1.204124
EP-F	1.201444

**Table 5.** The work function ( $\Phi$ ), Fermi level energy ( $Ef$ ), and energy gap ( $Eg$ ) correlation

Compounds Name	$Eg$ (eV)	$Ef$ [23] (eV)	$\Phi$ [22, 23] (eV)
EP	4.591	−2.27521	2.27521
EP-Br	4.486	−2.52265	2.52265
EP-Cl	4.493	−2.52209	2.52209
EP-F	4.483	−2.40682	2.40682

**Table 6.** The electrical conductivity ( $\sigma$ ), and energy gap ( $Eg$ ) correlation

Compounds Name	$Eg$ (Ev)	$\sigma$
EP	4.591	122
EP-Br	4.486	1.248
EP-Cl	4.493	1.247
EP-F	4.483	1.249



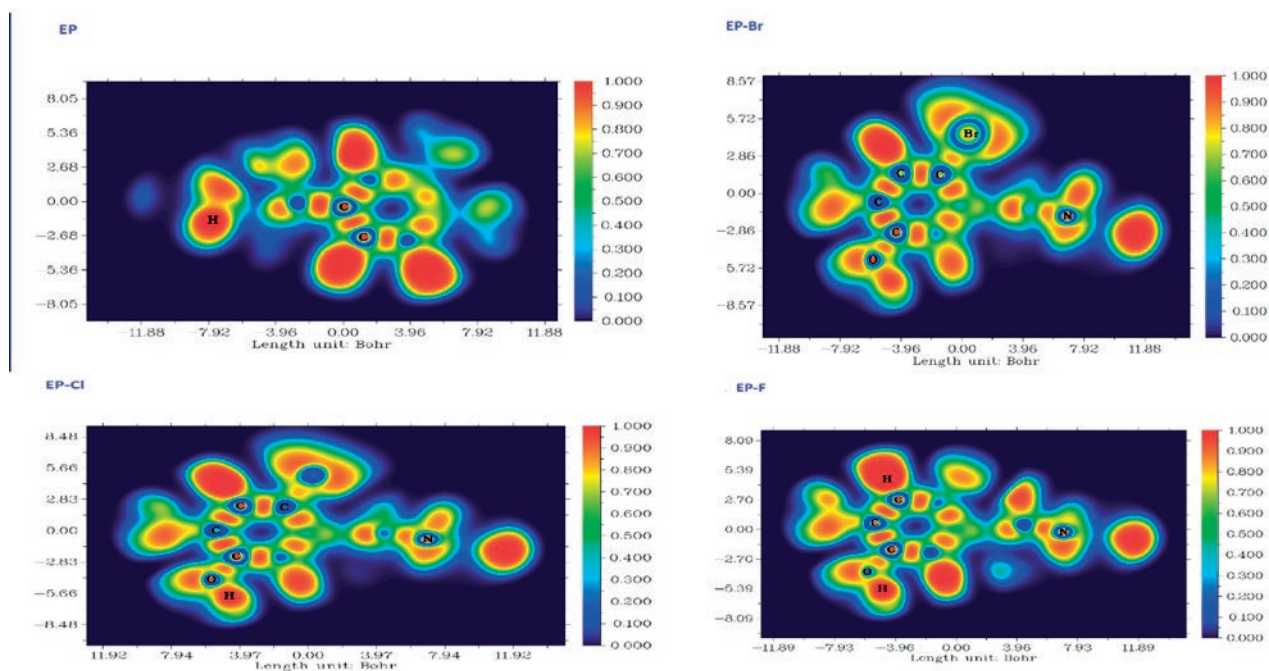


Fig. 5. Electron localized function (ELF) topology

to create contour maps that illustrate the ELF for the title compounds, as seen in Fig. 5 [45].

Fig. 5 depicts ELF color-filled maps ranging from 1.0 to 0.0, illustrated by red and blue colors, respectively. The red color patches surrounding C-C, C-N, and bonds have greater density values, indicating interaction with a confined electron cloud, particularly the hydrogen atoms in terminal carbon. The blue hue area surrounding a few C atoms in compounds indicates delocalized bonding. The group of H atoms has a red area encircling them, which indicates that there are an excessive number of electrons that are considered to be delocalized (Fig. 5) [44, 46].

### 3.7. RDG analyses

The Multiwfn application was applied in order to accomplish the task of making the colorful RDG scatter plots [45], whereas the VMD program was utilized in order to achieve the goal of delivering a graphical representation of the three-dimensional iso surface [47]. Chemical interactions influence the stability of molecular structures. Analyzing reduced density gradient (RDG) calculations may help identify weak interaction or intermolecular forces attraction. The colorful RDG scatter plots were generated using the Multiwfn free software. For the purpose of determining the RDG values, we applied

Equation (5) below according to the electron density  $\rho(r)$ :

$$\text{RDG}(r) = \frac{1|\nabla\rho(r)|}{2(3\pi r^2)^{\frac{1}{3}}\rho^{\frac{4}{3}}(r)} \quad (5)$$

In three-dimensional space,  $r$  stands for the position vector. This vector indicates a particular place in space where several criteria – including electron density and its gradient – are assessed. The low-density gradient reveals regions that contain a limited number of electrons, which are the cause of weak interactions. As part of the isosurface plots, RDG is plotted against the second eigenvalue of the electron density Hessian matrix ( $\lambda_2$ ), and the electron density  $\rho(r)$ . The characteristics of weak interaction may be determined from the isosurface, and these characteristics are dependent on the values of  $\lambda_2$ . The blue zone, which is characterized by negative values, also known as  $\lambda_2(r) \rho(r) < 0$ , is associated with strong interactions, such as hydrogen bonding, and a high electron charge density. As opposed to the green zone, which corresponds to van der Waal interactions that are relatively weak, the red zone, which has positive values  $\lambda_2(r) \rho(r) > 0$ , indicates a strong repulsive interaction and a drop in electron density. The green zone is marked by the sign  $\lambda_2(r) \rho(r) \approx 0$ . The RDG plots

that were anticipated for the test compounds EP, EP-Br, EP-Cl, and EP-F are shown in Fig 6.

### 3.8. Density of state (DOS)

The density of state, often known as DOS, is a crucial metric that provides information on the number of states that exist inside the HOMO-LUMO unit energy interval for a certain chemical system. Its graph is used for the purpose of assessing the type of electron structure in addition to the distribution of molecular orbitals along with the energies linked with their  $E_{\text{HOMO}}$  and  $E_{\text{LUMO}}$  constituents. For the purpose of determining the DOS of the compounds that were investigated, we used the DFT/6-311G (d,p) basis set in this study. Equation (6) allows one to determine the DOS in relation to energy levels [23,48-52]:

$$\text{DOS}(E) = \sum g(E - \varepsilon_i). \quad (6)$$

In this formula,  $E$  represents the total electron energy, ' $g$ ' corresponds to a Gaussian function with a fixed Full Width at Half Maximum (FWHM)

of = 0.3, and  $\varepsilon_i$  signifies the energy associated with the  $i^{\text{th}}$  [53]. It was discovered that the variation in the energy gap ( $E_g$ ): 0.1687, 0.1648, 0.1651, and 0.1647 a.u for the EP, EP-Br, EP-Cl, and EP-F, respectively in Fig. 7. Therefore, it is possible to draw the conclusion that the highest and lowest DOS values in the  $E_g$  were found for compounds containing EP and EP-F compounds. With the presence of substituted halogens in the epinephrine (EP) molecule, it is possible that the density of states (DOS) of the molecule will be altered, as shown in Fig. 7. This is in addition to the peak shifts that occur in the electronic spectra of the molecule. This may be attributed to a number of factors, including the following: shifts in the energy levels of electronic states and the orbitals of molecules.

### 4. Conclusion

In conclusion, our extensive investigation employing Gaussian program simulations with DFT/6-31G(d,p) basis set, and substituted halogens in the molecule of epinephrine (EP)

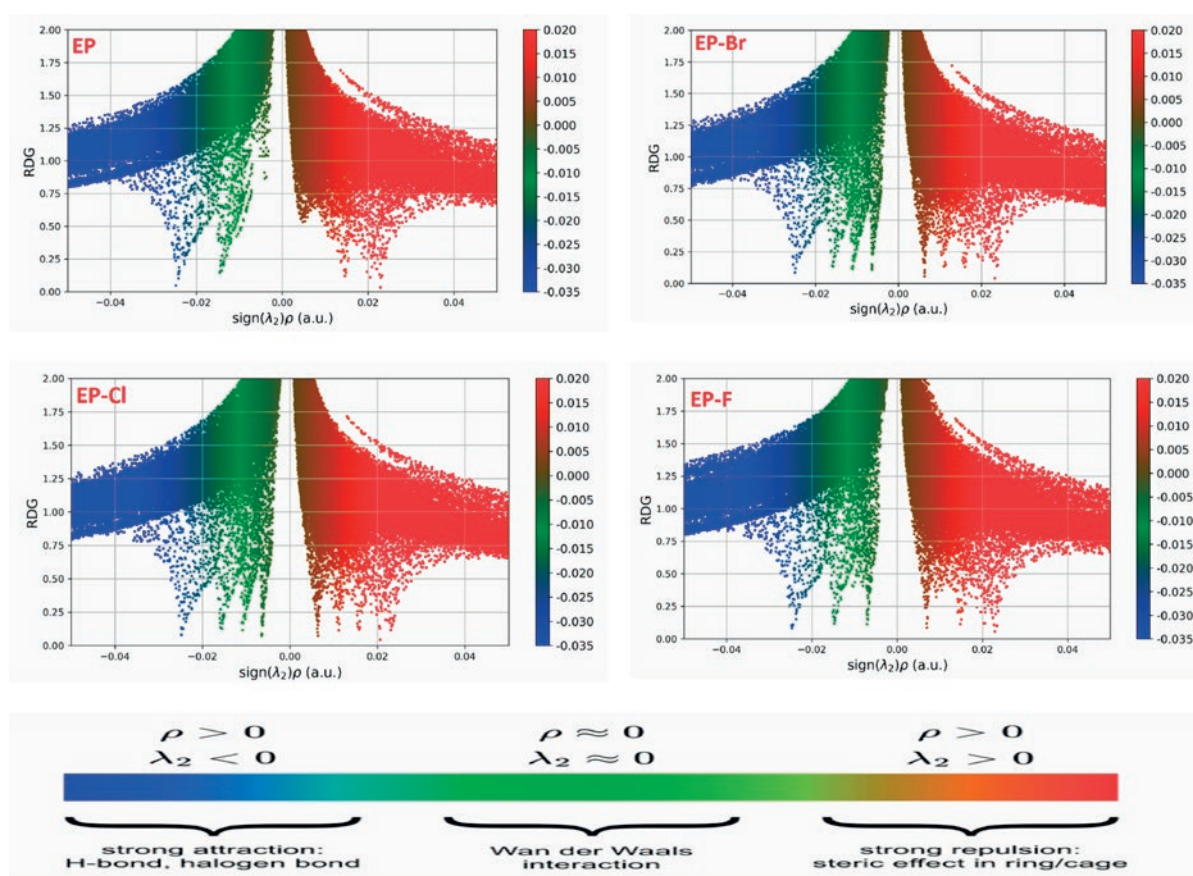


Fig. 6. The RDG scatter

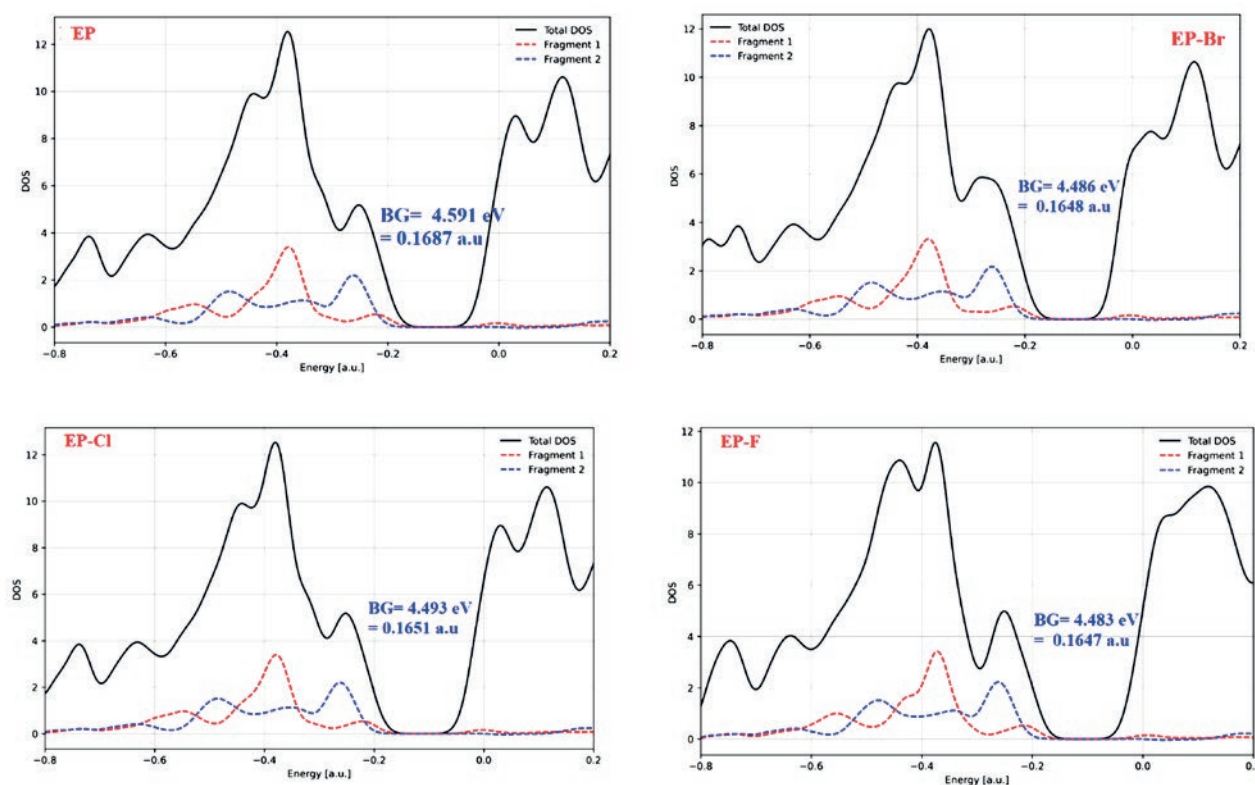


Fig. 7. Total Energy (a.u), the density of state (DOS) using Fragments 1, and 2 DFT/B3LYP/ 6-311G (d,p)

compounds offered crucial insights into their molecular properties. Front molecular orbitals (FMOs), which include HOMO and LUMO as well as other molecular orbitals, provide information about electronic structure, chemical stability, and reactivity. Estimated HOMO-LUMO energy gaps at the B3LYP level of theory (method), The EP-F compound with a smaller energy gap of 4.483 eV has excellent electrical conductivity, reactivity, and electronic distribution, and less chemical stability. Results show that the PE-F molecule has a softness of  $0.446 \text{ eV}^{-1}$ , which indicates that it is very capable of transferring electrons. The optical characteristics of epinephrine, including its refractive index ( $n$ ), dielectric constant ( $\epsilon$ ), and optical electronegativity ( $\Delta\chi^*$ ), are discussed in this section. The correlation between refractive index, and energy gap are listed from the highest to lowest value: refractive index (EP-F > EP-Br > EP-Cl > EP), while energy gap (EP > EP-Cl > EP-Br > EP-F). When the refractive index is high, it means that the molecules are relatively soft, while large hardness ( $\eta$ ) is related to small refractive index. It is associated with a higher energy gap and is associated with a

lower refractive index and a lower dielectric constant. Results from calculations show that a smaller bandgap ( $E_g$ ) implies a higher Fermi level energy, poorer chemical stability, a smaller work function ( $\Phi$ ), and better electrical conductivity. The optical electronegativity ( $\Delta\chi^*$ ) was used to distinguish between different kinds of bonds, and the correlation between lower  $\Delta\chi^*$  values and higher refractive indices demonstrated its connection to the HOMO-LUMO energy gap. The presence of substituted halogens in the molecule of norepinephrine, often referred to as NEP, has the ability to bring about alterations in the energy levels of electronic states, and the orbitals of molecules. This is because the molecule contains halogens that have been replaced. Modifications in the physicochemical properties of the EP molecule, including its stability and reactivity, are also seen. According to our ELF data, the group of H atoms have a red patch surrounding them, indicating that there are too many delocalized electrons.

*The online version contains supplementary material*



## Conflict of interests

The author declares that he has no known competing financial interests or personal relationships that could have influenced the work reported in this paper.

## References

1. Body J.-J., Cryer P. E., Offord K. P., Heath H. Epinephrine is a hypophosphatemic hormone in man. Physiological effects of circulating epinephrine on plasma calcium, magnesium, phosphorus, parathyroid hormone, and calcitonin. *The Journal of Clinical Investigation*. 1983;71(3): 572–578. <https://doi.org/10.1172/JCI110802>
2. Sun Y., Wang Y., Yang Y., Yang M. An electrochemiluminescent sensor for epinephrine detection based on graphitic carbon nitride nanosheet/multi-walled carbon nanotubes nanohybrids. *Chemistry Letters*. 2019;48(3): 215–218. <https://doi.org/10.1246/cl.180893>
3. Sisecioglu M., Gulcin I., Cankaya M., Atasever A., Ozdemir H. The effects of norepinephrine on lactoperoxidase enzyme (LPO). *Scientific Research and Essays*. 2010;5(11): 1351–1356.
4. Kruger L. *Pheroid technology for the transdermal delivery of lidocaine and prilocaine*. North-West University, 2008.
5. Bandyopadhyay P., Karmakar A., Deb J., Sarkar U., Seikh M. M. Non-covalent interactions between epinephrine and nitroaromatic compounds: a DFT study. *Spectrochimica Acta Part A: Molecular and Biomolecular Spectroscopy*. 2020;228: 117827. <https://doi.org/10.1016/j.saa.2019.117827>
6. Gámez-García V., Cortés-Romero C., Palomar-Pardavé M., ... Cuan A. Theoretical study on the chemical stability of adrenalin species. *Revista Mexicana de Física*. 2013;59(1): 135–140.
7. Priya A. M., Azaad B., Biju D. M. A density functional theory investigation on norepinephrine interaction with amino acids and alcohols. *Journal of Molecular Structure*. 2023;1283: 135305. <https://doi.org/10.1016/j.molstruc.2023.135305>
8. Dugas H., Penney C. *Bioorganic chemistry: a chemical approach to enzyme action*. Springer Science & Business Media: 2013.
9. Sanderson R. *Chemical bonds and bonds energy*. Elsevier: 2012; Vol. 21.
10. Silva D. R., Silla J. M., Santos L. A., da Cunha E. F., Freitas M. P. The role of intramolecular interactions on the bioactive conformation of epinephrine. *Molecular Informatics*. 2019;38(6): 1800167. <https://doi.org/10.1002/minf.201800167>
11. Špirtović-Halilović S., Salihović M., Veljović E., Osmanović A., Trifunović S., Završnik D. Chemical reactivity and stability predictions of some coumarins by means of DFT calculations. *Bulletin of the Chemists and Technologists of Bosnia and Herzegovina*. 2014;43: 57–60.
12. Choudhary V., Bhatt A., Dash D., Sharma N. DFT calculations on molecular structures, HOMO–LUMO study, reactivity descriptors and spectral analyses of newly synthesized diorganotin (IV) 2-chloridophenylaceto-hydroxamate complexes. *Journal of Computational Chemistry*. 2019;40(27): 2354–2363. <https://doi.org/10.1002/jcc.26012>
13. Soro D., Ekou L., Koné M. G.-R., Ekou T., Ziao N. DFT study of molecular stability and reactivity on some hydroxamic acids: an approach by Hirshfeld population analysis. *European Journal of Engineering and Technology Research*. 2019;4 (2): 45–49. <https://doi.org/10.24018/ejeng.2019.4.2.1121>
14. Khamooshi F., Doraji-Bonjar S., Akinnawo A. S., Ghaznavi H., Salimi-Khorashad A., Khamooshi M. J. Dark classics in chemical neuroscience: comprehensive study on the biochemical mechanisms and clinical implications of opioid analgesics. *Chemical Methodologies*. 2023;7: 964–993. <https://doi.org/10.48309/chemm.2023.414616.1731>
15. Nasih R. L., Hussin V. K., Hamad O. A., Kareem R. O. Theoretical study chlorohydroquinone molecule with substituted lithium via quantum computation approach. *Chemical Research and Technology*. 2024;1: 73–77. <https://doi.org/10.2234/chemrestec.2024.448968.1009>
16. Hamad O., Kareem R. O., Kaygili O., Materials F. Density function theory study of the physicochemical characteristics of 2-nitrophenol. 2023;6(1): 70–76. *Journal of Physical Chemistry and Functional Materials*. <https://doi.org/10.54565/jphcfum.1273771>
17. Kareem R. O., Kebiroğlu M. H., Hamad O. A., Kaygili O., Bulut N. Epinephrine compound: unveiling its optical and thermochemical properties via quantum computation methods. *Chemical Review and Letters*. 2023;6: 415–427. <https://doi.org/10.22034/CRL.2023.421325.1253>
18. Hussein Y. T., Azeez Y. H. DFT analysis and in silico exploration of drug-likeness, toxicity prediction, bioactivity score, and chemical reactivity properties of the urolithins. *Journal of Biomolecular Structure and Dynamics*. 2023;41(4): 1168–1177. <https://doi.org/10.1080/07391102.2021.2017350>
19. Hussein Y., Yousif A., Ahmed M. I. In silico exploration of pharmacological and molecular descriptor properties of salacinol and its related analogues. *Journal of the Turkish Chemical Society Section A: Chemistry*. 2024;11(1): 279–290. <https://doi.org/10.18596/jotcsa.1246781>
20. Kareem R. O., Kebiroglu H., Hamad O. A. Investigation of electronic and spectroscopic properties of phosphosilicate glass molecule (BioGlass 45S5) and Ti-BioGlass 45S5 by quantum programming. *Journal of Chemistry Letters*. 2024;4(4): 200–210. <https://doi.org/10.22034/jchemlett.2024.416584.1138>
21. Nadr R. B., Abdulrahman B. S., Azeez Y. H., Omer R. A., Kareem R. O. Quantum chemical calculation for synthesis some thiazolidin-4-one derivatives. *Journal of Molecular Structure*. 2024;1308: 138055. <https://doi.org/10.1016/j.molstruc.2024.138055>
22. Javed M., Khan M. U., Hussain R., Ahmed S., Ahamad T. J. R. Deciphering the electrochemical sensing capability of novel Ga<sub>12</sub>As<sub>12</sub> nanocluster towards chemical warfare phosgene gas: insights from DFT. *RSC Advances*. 2023;13(41): 28885–28903. <https://doi.org/10.1039/D3RA05086F>
23. Louis H., Etiese D., Unimuke T. O., ... Nfor E. N. Computational design and molecular modeling of the interaction of nicotinic acid hydrazide nickel-based complexes with H<sub>2</sub>S gas. *RSC Advances*. 2022;12(47): 30365–30380. <https://doi.org/10.1039/D2RA05456F>
24. Moss T. A relationship between the refractive index and the Infra-Red threshold of sensitivity for photoconductors.

*Proceedings of the Physical Society. Section B.* 1950;63(3): 167. <https://doi.org/10.1088/0370-1301/63/3/302>

25. Ravindra N., Auluck S., Srivastava V. On the penn gap in semiconductors. *Physica Status Solidi (b)*. 1979;93(2): K155–K160. <https://doi.org/10.1002/pssb.2220930257>

26. Reddy R., Gopal K. R., Narasimhulu K., ... Kumar M. R. Interrelationship between structural, optical, electronic and elastic properties of materials. *Journal of Alloys and Compounds*. 2009;473(1-2): 28–35. <https://doi.org/10.1016/j.jallcom.2008.06.037>

27. Kumar V., Singh J. Model for calculating the refractive index of different materials. *Indian Journal of Pure & Applied Physics*. 2010;48(08): 571–574. Available at: <https://scispace.com/pdf/model-for-calculating-the-refractive-index-of-different-2gqk94u0ae.pdf>

28. Akintemi E. O., Govender K. K., Singh T. A DFT study of the chemical reactivity properties, spectroscopy and bioactivity scores of bioactive flavonols. *Computational and Theoretical Chemistry*. 2022;1210: 113658. <https://doi.org/10.1016/j.comptc.2022.113658>

29. Omer R. A., Ahmed L. O., Koparir M., Koparir P. Theoretical analysis of the reactivity of chloroquine and hydroxychloroquine. *Indian Journal of Chemistry -Section A (IJCA)*. 2020;59(12). <https://doi.org/10.56042/ijca.v59i12.33714>

30. Rebaz O., Ahmed L., Jwameer H., Koparir P. Structural analysis of epinephrine by combination of density functional theory and Hartree-Fock methods. *El-Cezeri Journal of Science and Engineering*. 2022;9(2): 760–776. <https://doi.org/10.31202/ecjse.1005202>

31. Kucuk C., Yurdakul S., Özdemir N., Erdem B. Structural and spectroscopic characterization, electronic properties, and biological activity of the 4-(3-methoxyphenyl) piperazin-1-ium 4-(3-methoxyphenyl) piperazine-1-carboxylate monohydrate. *Chemical Papers*. 2023;77(5): 2793–2815. <https://doi.org/10.1007/s11696-023-02667-w>

32. Sharma P., Ranjan P., Chakraborty T. Study of TI-based perovskite materials  $\text{TiZrX}_3$  (Z= Ge, Sn, Bi, Sr, X= Cl, Br, I) for application in scintillators: DFT and TD-DFT approach. *Chemical Physics Impact*. 2023;7: 100344. <https://doi.org/10.1016/j.chphi.2023.100344>

33. Shahab H., Husain Y. Theoretical study for chemical reactivity descriptors of tetrathiafulvalene in gas phase and solvent phases based on density functional theory. *Passer Journal of Basic and Applied Sciences*. 2021;3(2): 167–173. <https://doi.org/10.24271/psr.28>

34. Venkatesh G., Sheena Mary Y., Shymamary Y., Palanisamy V., Govindaraju M. Quantum chemical and molecular docking studies of some phenothiazine derivatives. *Journal of Applied Organometallic Chemistry*. 2021;1(3): 148–158. <https://doi.org/10.22034/jaoc.2021.303059.1033>

35. Adole V. A. Computational chemistry approach for the investigation of structural, electronic, chemical and quantum chemical facets of twelve biginelli adducts. *Journal of Applied Organometallic Chemistry*. 2021;1(1): 29–40. <https://doi.org/10.22034/jaoc.2021.278598.1009>

36. Shojiae F. Quantum computations of interactions of most reactive tricyclic antidepressant drug with carbon nanotube, serotonin and norepinephrin. *Chemical Methodologies*. 2020;4(4): 447–466. <https://doi.org/10.33945/SAMI/CHEMM.2020.4.7>

37. Hariharan A., Vadlamudi P. SERS of epinephrine: a computational and experimental study. *Journal of Molecular Structure*. 2021;1246: 131163. <https://doi.org/10.1016/j.molstruc.2021.131163>

38. Yadav T., Sahu R. K., Mukherjee V. Molecular modeling and spectroscopic investigation of a neurotransmitter: epinephrine. *Journal of Molecular Structure*. 2019;1176: 94–109. <https://doi.org/10.1016/j.molstruc.2018.08.077>

39. Reddy R. R., Gopal K. R., Narasimhulu K., ... Ahmed S. Correlation between optical electronegativity and refractive index of ternary chalcopyrites, semiconductors, insulators, oxides and alkali halides. *Optical Materials*. 2008;31(2): 209–212. <https://doi.org/10.1016/j.optmat.2008.03.010>

40. Naccarato F., Ricci F., Suntivich J., Hautier G., Wirtz L., Rignanese G.-M. Designing materials with high refractive index and wide band gap: a first-principles high-throughput study. *APS March Meeting Abstracts*. 2019, p S19.003. <https://doi.org/10.48550/arXiv.1809.01132>

41. Kim C., Kim B., Lee S. M., Jo C., Lee Y. Electronic structures of capped carbon nanotubes under electric fields. *Physical Review B*. 2002;65(16): 165418. <https://doi.org/10.1103/PhysRevB.65.165418>

42. Xu P., Cui L., Gao S., Na N., Ebadi A. A theoretical study on sensing properties of in-doped ZnO nanosheet toward acetylene. *Molecular Physics*. 2022;120(5): e2002957. <https://doi.org/10.1080/002068976.2021.2002957>

43. El-Mageed H. R. A., Ibrahim M. A. A. Elucidating the adsorption and detection of amphetamine drug by pure and doped  $\text{Al}_{12}\text{N}_{12}$  and  $\text{Al}_{12}\text{P}_{12}$  nano-cages, a DFT study. *Journal of Molecular Liquids*. 2021;326: 115297. <https://doi.org/10.1016/j.molliq.2021.115297>

44. Lu T., Chen F. Multiwfn: a multifunctional wavefunction analyzer. *Journal of Computational Chemistry*. 2012;33(5): 580–592. <https://doi.org/10.1002/jcc.22885>

45. Humphrey W., Dalke A., Schulten K. VMD: visual molecular dynamics. *Journal of Molecular Graphics*. 1996;14(1): 33–38. [https://doi.org/10.1016/0263-7855\(96\)00018-5](https://doi.org/10.1016/0263-7855(96)00018-5)

46. Kareem R. O., Kaygili O., Ates T., ... Ercan I. Experimental and theoretical characterization of Bi-based hydroxyapatites doped with Ce. *Ceramics International*. 2022;48(22): 33440–33454. <https://doi.org/10.1016/j.ceramint.2022.07.287>

47. Korkmaz A. A., Ahmed L. O., Kareem R. O., ... Ates B. Theoretical and experimental characterization of Sn-based hydroxyapatites doped with Bi. *Journal of the Australian Ceramic Society*. 2022;58(3): 803–815. <https://doi.org/10.1007/s41779-022-00730-5>

48. İsen F., Kaygili O., Bulut N., ... Ercan F. J., Experimental and theoretical characterization of Dy-doped hydroxyapatites. *Journal of the Australian Ceramic Society*. 2023;59(4): 849–864. <https://doi.org/10.1007/s41779-023-00878-8>

49. Kareem R. O. *Synthesis and characterization of bismuth-based hydroxyapatites doped with cerium*. Thesis for: Masters degree. 2023. Available at: [https://www.researchgate.net/publication/368663130\\_Synthesis\\_and\\_Characterization\\_of\\_Bismuth-Based\\_Hydroxyapatites\\_Doped\\_with](https://www.researchgate.net/publication/368663130_Synthesis_and_Characterization_of_Bismuth-Based_Hydroxyapatites_Doped_with)

50. Bulut N., Kaygili O., Hssain A. H., ... Kareem R. O. Mg-dopant effects on band structures of Zn-based

hydroxyapatites: a theoretical study. *Iranian Journal of Science*. 2023;47(5): 1843–1859. <https://doi.org/10.1007/s40995-023-01531-6>

51. Hamad O. A., Kareem R. O., Azeez Y. H., Kebiroğlu, M. H., Omer R. A., Zebari O. I. H. Quantum computing analysis of naphthalene compound: electronic structure, optical, and thermochemical approaches using DFT and HF.

*Journal of Applied Organometallic Chemistry*. 2024;4(2): 100–118. <https://doi.org/10.48309/jaoc.2024.444132.1167>

### Information about the author

Rebaz Obaid Kareem, M.Sc in General Physics, Lecturer at the Department of Physics, Faculty of Science, Physics Department, Halabja University (Kurdistan Region, Iraq).

<https://orcid.org/0000-0001-6273-1309>

[rebaz.kareem@uoh.edu.iq](mailto:rebaz.kareem@uoh.edu.iq)

Received 06.10.2024; approved after reviewing 15.11.2024; accepted for publication 16.12.2024; published online 25.06.2025.





# Condensed Matter and Interphases

Kondensirovannye Sredy i Mezhfaznye Granitsy  
<https://journals.vsu.ru/kcmf/>

## Original articles

Research article

<https://doi.org/10.17308/kcmf.2025.27/12864>

## Influence of external influences on the activation of domain walls of ferroelectric perovskites

D. V. Kuzenko✉

Scientific Research Institute «Reaktivelectron»,  
17a Bakinskikh Komissarov st., Donetsk 283049, Russian Federation

### Abstract

**Purpose:** The article aims to establish the regularities of the influence of external influences (thermal and electrical) on the activation of domain walls in oxygen-octahedral-type ferroelectric materials with perovskite structure which have a wide application in electronic devices. One of the problems in this case is the stability of domain walls with respect to external influences. With this in mind, the aim of the paper is to determine the activation energy of irreversible motion of domain walls when switching the polarization of a ferroelectric by electric field in a wide temperature range.

**Experimental:** The value of the critical energy  $W_{\max}$  of interaction of ferroelectric domains with an external electric field necessary for irreversible change of the domain structure of a ferroelectric under different thermal conditions is determined. For this purpose, the dielectric hysteresis loops  $P(E)$  of samples obtained at different temperatures were analyzed. Ferroelectric materials with oxygen-octahedral perovskite structure were chosen as objects of study:  $\text{BaZrO}_3/\text{BaTiO}_3$  superlattice,  $\text{Pb}(\text{Zr}_{0.3}\text{Ti}_{0.7})\text{O}_3$ , ceramics  $(\text{Pb}_{0.96}\text{Sr}_{0.04}(\text{Mg}_{1/3}\text{Nb}_{2/3})_{0.275}(\text{Ni}_{1/3}\text{Nb}_{2/3})_{0.1}\text{Ti}_{0.375}\text{Zr}_{0.25}\text{O}_3)$  and ceramics  $\text{Pb}_{0.88}\text{Ba}_{0.06}\text{Sr}_{0.06}(\text{Mg}_{1/3}\text{Nb}_{2/3})_{0.37}\text{Zr}_{0.375}\text{Ti}_{0.255}\text{O}_3$ .

**Conclusions:** Temperature dependences of the critical energy  $W_{\max}$  of interaction of ferroelectric domains with an external electric field necessary for irreversible change of the domain structure of a ferroelectric have been determined. The assumption that the energy  $W_{\max}$  has the meaning of the activation energy of the domain structure of a ferroelectric at switching of polarization by an electric field, necessary for irreversible change of its domain structure, has been substantiated. It is established that the critical energy  $W_{\max}$  decreases linearly with temperature in a wide temperature range below the Curie point. The obtained results have scientific and practical value, since they allow to determine the conditions of stability of the domain structure of a ferroelectric to external influences and expand the possibilities of application of the Sawyer-Tauer method for determination of activation energies of irreversible change of the domain ferroelectric structure.

**Keywords:** Ferroelectric perovskites, Domain walls, Dielectric hysteresis loop, Activation energy, Repolarization, Barium zirconate, Barium titanate, Lead zirconate titanate, Lead magnoniobate

**Funding:** The research is a part of fulfillment of the State assignment of the Ministry of Science and Higher Education of the Russian Federation “Activation mechanisms of phase transitions in ferroelectric materials” (FREU-2023-0001).

**For citation:** Kuzenko D. V. Influence of external influences on the activation of domain walls of ferroelectric perovskites. *Condensed Matter and Interphases*. 2025;27(2): 251–259. <https://doi.org/10.17308/kcmf.2025.27/12864>

**Для цитирования:** Кузенько Д. В. Влияние внешних воздействий на активацию доменных границ сегнетоэлектрических перовскитов. *Конденсированные среды и межфазные границы*. 2025;27(2): 251–259. <https://doi.org/10.17308/kcmf.2025.27/12864>

✉ Danil V. Kuzenko, e-mail: [danil.kuzenko.84@yandex.ru](mailto:danil.kuzenko.84@yandex.ru)

© Kuzenko D. V., 2025



The content is available under Creative Commons Attribution 4.0 License.

## 1. Introduction

For practical applications in electronic engineering and fundamental research in solid state physics and chemistry, of particular interest are ferroelectric perovskites – inorganic crystalline materials whose structure contains internal surfaces of phase interfaces with different direction of the electric polarization vector – domain walls. The presence of domain walls for ferroelectrics determines especially large values of relative dielectric constant ( $10^3$ – $10^4$ ), and also gives a contribution to dielectric losses.

Domain structures can be studied by direct (microscopy) and indirect methods (dielectric spectroscopy). The application of the latter allows us to determine the conditions of stability and activation of its domain structure, as well as to estimate the activation energy of domain walls by the dependences of the complex dielectric constant of a ferroelectric on the magnitude of external influences (temperature, pressure, electric field) [1]. Another method of indirect study of the domain structure is the measurement of dielectric hysteresis loops  $P(E)$  under various external influences (temperature, mechanical, electrical). Determination of domain wall energies is also possible from first principles, which was done by the authors of papers [2] to evaluate the structure and energies of several types of domain walls for two prototypical tetragonal ferroelectric perovskites:  $\text{PbTiO}_3$  и  $\text{BaTiO}_3$ , including charge-neutral  $90^\circ$  domain walls of the Ising and Ising-Bloch types, as well as  $180^\circ$  domain walls of different orientations.

Since real ferroelectrics contain various structure defects, the process of nucleation and motion of domain walls occurs in interaction with the “stopper” system of defects in its crystal structure [3], which affects the mobility of domain walls in their interaction with lattice defects [4]. Although the nucleation and growth of the reverse polarity ferroelectric domain is controlled by the external electric field, this process is also influenced by thermal activation [5]. Thus, the analysis of the temperature evolution of dielectric hysteresis loops allows us to obtain data on the interaction energy of domain and defect structures and the nature of its change with temperature.

Despite the numerous studies of ferroelectric perovskites, even today there are still works on studying the structure of domains, domain walls and defects in these materials, as well as the evolution of these structures under the action of electric fields [6]. It was found that point defects of the crystal lattice, in particular, oxygen vacancies, play a significant role in the stability of the domain structure of perovskites. For the ferroelectric  $\text{BaTiO}_3$ , the activation energy of the motion of such vacancies has a value of 0.91 eV [7].

Dislocations in ferroelectrics also cause the anchoring of domain walls and the nucleation of ferroelectric domains, which significantly affects the electromechanical properties of ferroelectrics. For example, to determine the role of dislocations in ferroelectrics, the driving force of domain walls and their interaction with dislocations have been analyzed by finite element method [8]. It was found that the needle domain originating from the dislocation nucleus causes the domain walls to be anchored, and the interaction of the domain wall with the needle domain leads to a nonlinear dependence of the critical electric field required for the breakthrough of the domain walls through dislocations on the Burgers vector [8].

On this basis, it seems relevant to investigate the influence of external influences on the activation of domain walls of ferroelectrics with perovskite structure. For this purpose, the results of the study of dielectric hysteresis loops  $P(E)$  of several ferroelectric perovskites at different temperatures [9–12] are analyzed and summarized in this work, from which the interaction energies of ferroelectric domains with an external electric field in different temperature and electrical conditions are determined.

## 2. Experimental

To determine the critical energy required to irreversibly change the domain structure of a ferroelectric when its polarization is switched by an electric field, in this paper, based on our previous studies [13, 14], we analyze the dependence of  $W(E)$  obtained from the measured ferroelectric hysteresis data  $P(E)$  according to the formula:

$$W = -P \cdot E, \quad (1)$$

where  $P$  is the polarization value of the ferroelectric corresponding to the electric field  $E$  determined from the dielectric hysteresis loop  $P(E)$ .

The dependences of  $P(E)$  for several ferroelectric materials with perovskite structure in the form of films, ceramics, single crystals, superlattice were obtained at different temperatures. Experimental data presented in papers [9–12] were used for this purpose, namely:

1) Ferroelectric superlattice (multilayer epitaxial layer structure) of barium zirconate/barium titanate  $\text{BaZrO}_3/\text{BaTiO}_3$  (BZ/BT) with comparable unit cell sizes consists of 32 repeating BZ and BT layers with the thickness of individual BZ layers – 6.65 nm, and BT layers – 6.67 nm, deposited by pulsed laser deposition on a single-crystal MgO substrate. To investigate the dielectric hysteresis loops at temperatures of 523, 633, and 658 K, a modified Sawyer–Tauer scheme with conductivity compensation and an external electric field frequency of 10 kHz was used [9].

2) Lead zirconate titanate films of  $\text{Pb}(\text{Zr}_{0.3}\text{Ti}_{0.7})\text{O}_3$  were obtained by sintering and crystallization of the gel-solution precursor at 923 K for 10 min. The polarization hysteresis loops of  $P(E)$  were obtained at an electric field frequency of 100 Hz in the temperature range of 293–343 K [10].

3) Ceramics  $\text{Pb}_{0.88}\text{Ba}_{0.06}\text{Sr}_{0.06}(\text{Mg}_{1/3}\text{Nb}_{2/3})_{0.37}\text{Zr}_{0.375}\text{Ti}_{0.255}\text{O}_3$  (modified lead magnoniobate zirconate titanate PMN-PZT ceramics) were prepared by conventional solid-phase reaction method at a sintering temperature of 1,533 K. Polarization  $P(E)$  hysteresis loops were obtained at a frequency of 1 Hz in the temperature range from 298 to 433 K [11].

4) Ceramic samples of modified lead zirconate titanate ceramics PZT  $(\text{Pb}_{0.96}\text{Sr}_{0.04}(\text{Mg}_{1/3}\text{Nb}_{2/3})_{0.275}(\text{Ni}_{1/3}\text{Nb}_{2/3})_{0.1}\text{Ti}_{0.375}\text{Zr}_{0.25}\text{O}_3)$  were prepared by solid-phase reaction at a sintering temperature of 1,343 K. The polarization hysteresis loops of  $P(E)$  were measured using Sawyer-Tauer scheme in the temperature range from 300 to 433 K at a frequency of 1 Hz [12].

### 3. Results and discussion

The shape of the dielectric hysteresis loop is largely determined by the domain structure of the ferroelectric. And, as noted by Smolensky et

al [15], the change in the direction of spontaneous polarization occurs during polarization switching not by a jump in the whole domain, but by the motion of domain walls. Domain walls are fixed on pinning centers, which in real crystals are various defects of the crystal lattice, with which domain walls interact during their motion [16]. In a weak periodic electric field, the domain walls make reversible oscillations relative to the stationary position. If the electric field exceeds some critical value  $E_{cr}$ , which is less than the coercive field  $E_c$ , the domain walls detach from the stoppers and their motion becomes irreversible. The electric field  $E_{cr}$  is characterized by the fact that its effect on the ferroelectric leads to a change in the shape of individual lines of the X-ray diagram, which is a manifestation of the change in the domain structure of the ferroelectric [13]. The value of the critical field  $E_{cr}$  can also be determined from the  $P(E)$  dependence [14]. For this purpose, it is necessary to determine the field dependence  $W(E)$  of the energy  $W$  from formula (1). In the phenomenological theory of ferroelectrics, expression (1) is the additional energy in the full thermodynamic potential in an external electric field:

$$\Phi = U - T \cdot S + p \cdot V - P \cdot E, \quad (2)$$

where  $U$  is the internal energy,  $T$ ,  $p$ ,  $V$  are thermodynamic parameters (temperature, pressure and volume),  $S$  is the entropy,  $P$  is the polarization of the ferroelectric in the electric field  $E$  [15].

The polarization of ferroelectrics is due to the action of several mechanisms [17], but the main contribution is given by the domain polarization mechanism. Therefore, the contribution of other polarization mechanisms will be neglected in the following.

The polarization switching process can be accompanied either by the growth of existing domains, in which the polarization vector is opposite to the applied field, through the motion of domain walls, or by the nucleation and growth of new domains with the opposite direction of the polarization vector [15]. Under conditions of constant thermodynamic parameters  $T$ ,  $p$ ,  $V$ , the change of the full thermodynamic potential in an external electric field will be caused by the polarization switching processes. In this case,



the spontaneous polarization within each of the domains remains constant, and the main contribution to the macroscopic polarization of the ferroelectric is due to the rearrangement of its domain structure, which largely determines the parameters of the ferroelectric hysteresis. Based on these considerations, the value of  $W$  is predominantly determined by the interaction energy of the ferroelectric domains with the external electric field. On the example of the classical ferroelectric BaTiO<sub>3</sub> (ceramic and monocrystalline), Fig. 1 shows the dependence  $P(E)$  taken from the monograph [18] and the dependence  $W(E)$  obtained in this work. Two maximum points  $W_{\max-}$  and  $W_{\max+}$ , corresponding to the external critical electric fields  $-E_{cr}$  and  $E_{cr}$  are emphasized on the  $W(E)$  dependence. As it was mentioned above, in the critical field  $E_{cr}$ , the domain structure of the ferroelectric undergoes a rearrangement [13, 14]. This means that the energy  $W_{\max}$  is the critical energy of interaction of ferroelectric domains with an external electric field, at which irreversible changes in the domain structure of the ferroelectric begin under external electric influence on it. In this work, the energy dimensionality  $W$  is defined in joules per one mole of matter (J/mole), assuming that the polarization dimensionality  $P$  is C/cm<sup>2</sup> and the electric field strength  $E$  is V/cm. The transition of the energy dimensionality  $W$  from J/cm<sup>3</sup> to J/mole is done by multiplication by the molar volume  $V_m$  ( $V_m = M/\rho$ , where  $M$  is the molar mass, g/mole;  $\rho$

is the density, g/cm<sup>3</sup>).

This paper analyzes the  $W(E)$  dependences obtained from experimental  $P(E)$  dependences of ferroelectric materials with perovskite structure measured at different temperatures [9–12].

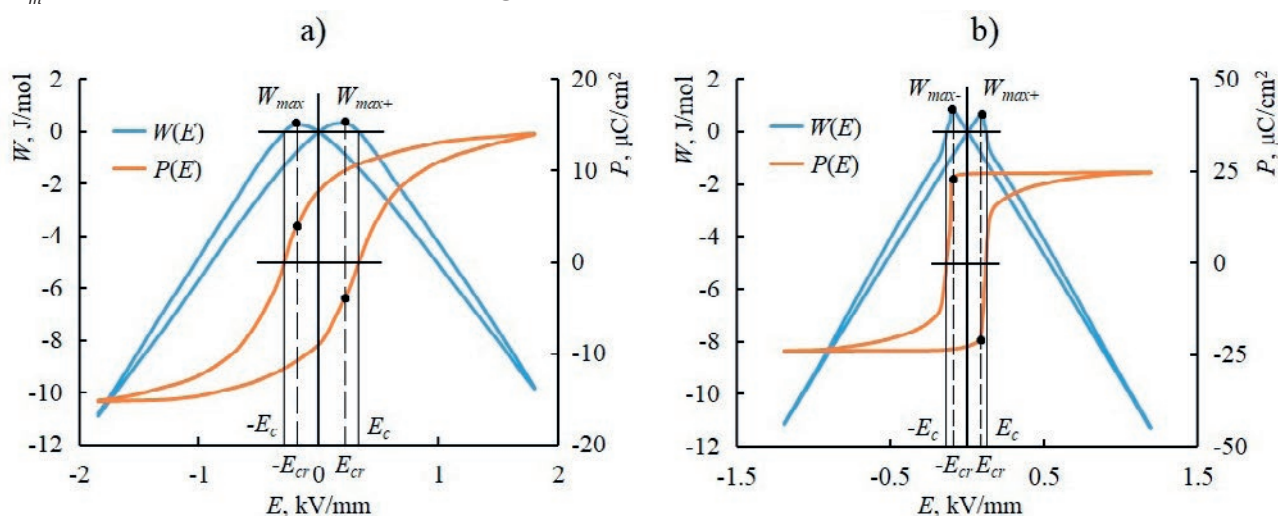
For the ferroelectric superlattice BaZrO<sub>3</sub>/BaTiO<sub>3</sub> [9], the dependences of the interaction energy of the ferroelectric domains with the external electric field  $W(E)$  at temperatures 523, 633, and 658 K are shown in Fig. 2. The dependence  $W_{\max}(T)$  is approximated by a linear dependence at temperatures 20 K below the Curie temperature:

$$W_{\max} = -a_T \cdot T + b_T, \quad (3)$$

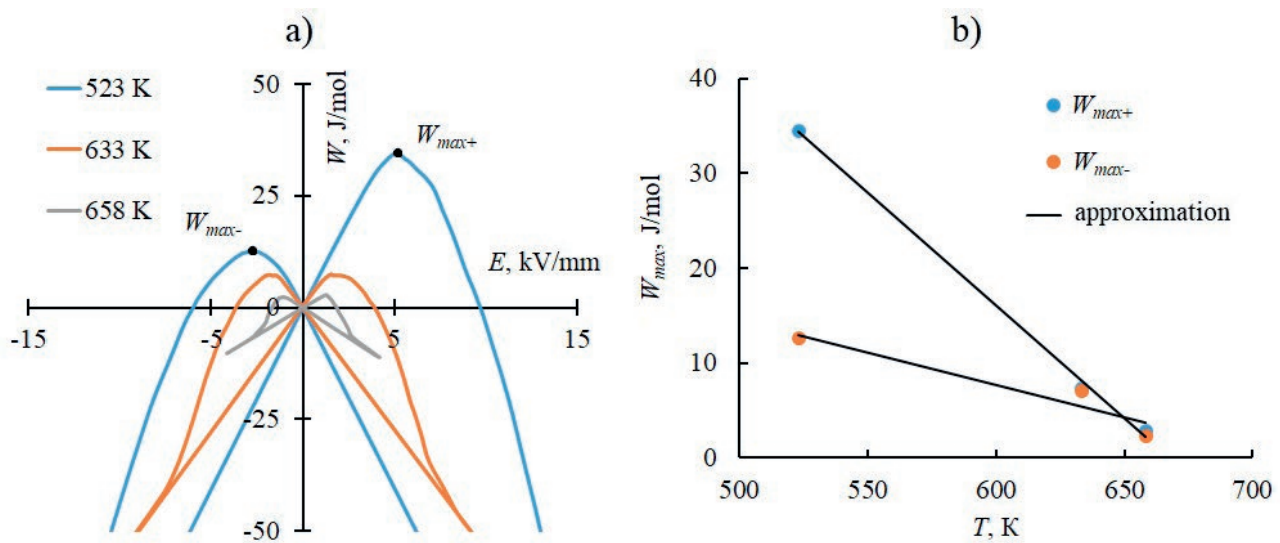
where  $a_T$  and  $b_T$  are coefficients,  $T$  is temperature. For  $W_{\max-}$ :  $a_T \approx 0.07$  J/mole·K,  $b_T \approx 48.6$  J/mole. For  $W_{\max+}$ :  $a_T \approx 0.24$  J/mole·K,  $b_T \approx 158.9$  J/mole.

The reason for the different values of  $W_{\max-}$  and  $W_{\max+}$  at  $T = 523$  K for BaZrO<sub>3</sub>/BaTiO<sub>3</sub> superlattice (Fig. 2b) is the asymmetry of the dielectric hysteresis loop arising due to the presence of an internal electric field in the sample.

Analyzing the dependence of the maximum values of switching currents on the applied field strength, Sidorkin A.S. and co-authors [9] found that the full switching curve has two sections. The initial, so-called “activation” region or the region of “weak” fields, where the specified dependence of the switching current on the applied field is close to exponential, and the subsequent linear region, i.e., the region of “strong” fields, or the



**Fig. 1.** Field dependence of the interaction energy of ferroelectric domains with an external electric field  $W(E)$  and the dielectric hysteresis loop  $P(E)$  of the ferroelectric BaTiO<sub>3</sub> in the form of ceramics (a) and a single crystal (b).  $E_c$  is the coercive field,  $E_{cr}$  is the critical field. From the experimental data  $P(E)$  [18]



**Fig. 2.** Dependences  $W(E)$  of the superlattice BaZrO<sub>3</sub>/BaTiO<sub>3</sub> at different temperatures (a) and the temperature dependences of  $W_{max+}$  и  $W_{max-}$  (b), obtained using experimental data from [9]

region of “sliding”, where the dependence of the maximum switching current is proportional to the field  $i_{max} \approx \mu P E s / d$  ( $P$  – polarization,  $\mu$  – mobility of domain walls,  $s$  – area of the top electrode,  $d$  – thickness of the sample). The boundary between the regions of activation and non-activation switching modes, the so-called  $E_{th}$  threshold or critical field, defined by the switching currents as the field corresponding to the transition of the exponential dependence into a linear one, approximately corresponds to the coercive field defined by the dielectric hysteresis loop [9].

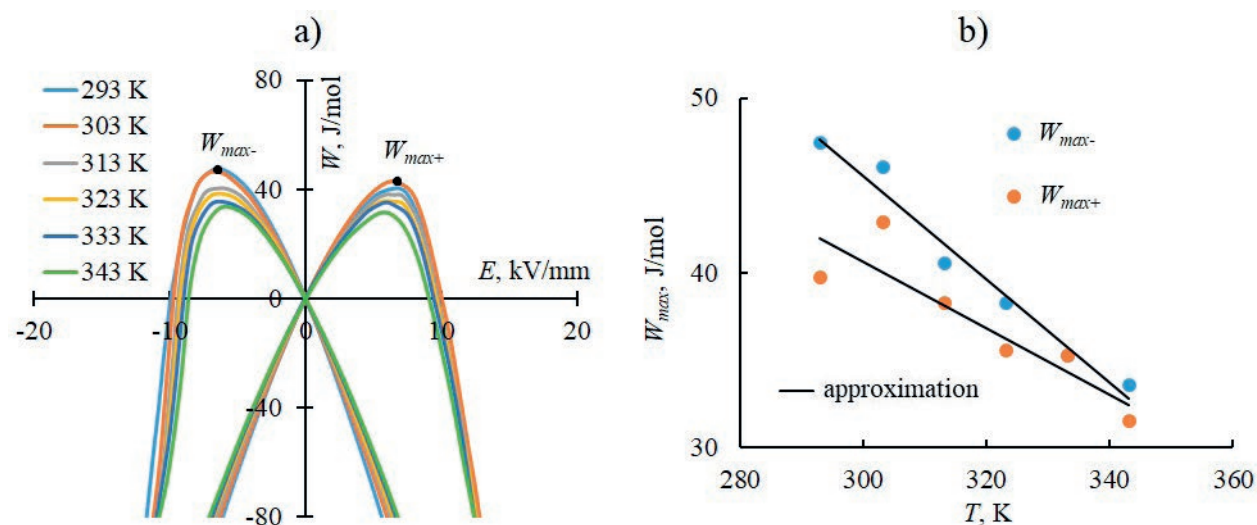
The results of our work suggest that the critical field  $E_{th}$  determined by the authors [9] will correspond to the maximum value of the interaction energy of ferroelectric domains with the external electric field  $W_{max}$  (Fig. 2a) and the corresponding critical field  $E_{cr}$  (Fig. 1). Then the decrease in the linear law (3) of the energy value  $W_{max}$  with increasing temperature  $T$  can be associated with the growth of the domain wall mobility  $\mu$  due to the decrease in the activation energy of the domain wall motion, which is caused by the weakening of the interaction of domain walls with the crystal lattice and defective environment, as well as by the decrease in spontaneous polarization as we approach the Curie temperature  $T_c$ . During polarization switching of the sample, domains of opposite sign are also nucleated, and mainly at

the interfaces (grain boundaries, sample surface). But their subsequent growth is also determined by the mobility of domain walls, which mainly determines the polarization switching process.

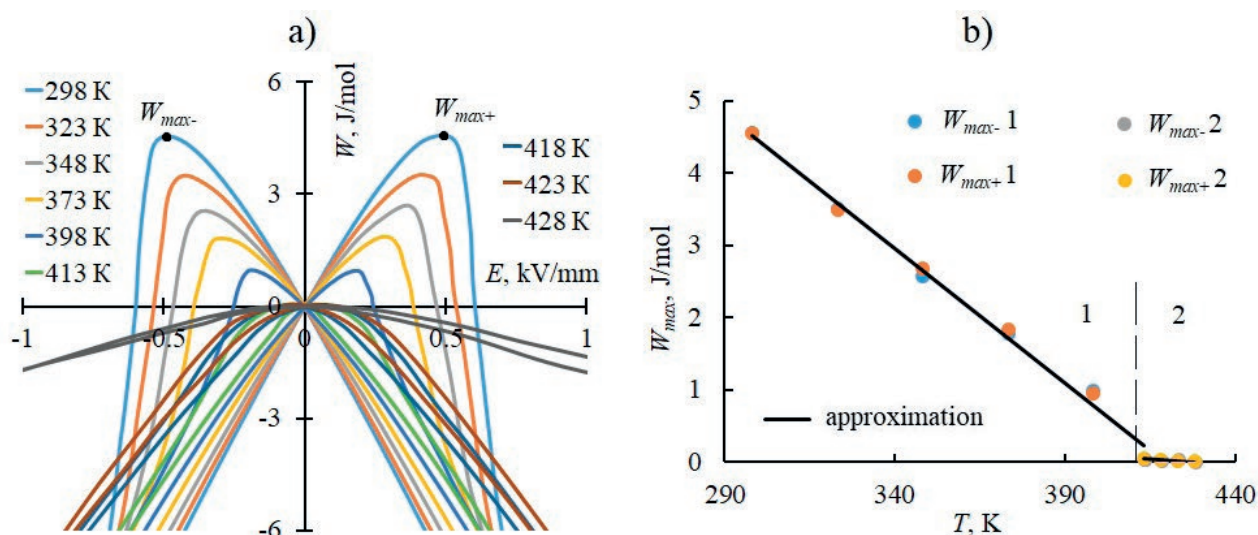
For film samples Pb(Zr<sub>0.3</sub>Ti<sub>0.7</sub>)O<sub>3</sub> [10], the dependences of  $W(E)$  in the temperature range 293–343 K are shown in Fig. 3a. In this case, the dependences  $W_{max+}(T)$  and  $W_{max-}(T)$  presented in Fig. 3b, is also satisfactorily approximated by relation (3). For  $W_{max-}$ :  $a_T \approx 0.29$  J/mole·K,  $b_T \approx 134.9$  J/mole. For  $W_{max+}$ :  $a_T \approx 0.19$  J/mole·K,  $b_T \approx 98.1$  J/mole.

The dependences of  $W(E)$  for ceramics Pb<sub>0.88</sub>Ba<sub>0.06</sub>Sr<sub>0.06</sub>(Mg<sub>1/3</sub>Nb<sub>2/3</sub>)<sub>0.37</sub>Zr<sub>0.375</sub>Ti<sub>0.255</sub>O<sub>3</sub>, plotted according to [11], are shown in Fig. 4a, and the  $W_{max+}(T)$  and  $W_{max-}(T)$  dependences, which practically coincide, are shown in Fig. 4b. Two areas can be distinguished on them. The first one corresponds to the temperature interval 298–409 K; and the second one – 409–433 K. At both sites, the dependences  $W_{max+}(T)$  and  $W_{max-}(T)$  are close to linear and can be approximated by expression (3). The best approximation corresponds to the following parameters. At the first site:  $a_T \approx 0.04$  J/mole·K,  $b_T \approx 15.7$  J/mole. At the second site:  $a_T \approx 0.003$  J/mole·K,  $b_T \approx 1.2$  J/mole.

As can be seen from Fig. 4b, the dependences  $W_{max+}(T)$  and  $W_{max-}(T)$  have two linear sections, the transition between which occurs at a temperature of 409 K. The authors of the paper [11] determined



**Fig. 3.** Dependences  $W(E)$  of thin films of  $\text{Pb}(\text{Zr}_{0.3}\text{Ti}_{0.7})\text{O}_3$  at different temperatures (a) and temperature dependences of  $W_{\max+}$  и  $W_{\max-}$  (b), obtained using experimental data from [10]



**Fig. 4.** Dependences  $W(E)$  of  $\text{Pb}_{0.88}\text{Ba}_{0.06}\text{Sr}_{0.06}(\text{Mg}_{1/3}\text{Nb}_{2/3})_{0.37}\text{Zr}_{0.375}\text{Ti}_{0.255}\text{O}_5$  ceramics at different temperatures (a) and temperature dependences of  $W_{\max+}$  и  $W_{\max-}$  (b), obtained using experimental data from [11]

that starting from this temperature the hysteresis dependence of  $P(E)$  has the form of a double loop. This temperature practically coincides with the temperature  $T_{nr}$  (the lower index “nr” denotes the transition from normal to relaxor ferroelectric state at  $T_{nr} = 409$  K [11]), at which the ferroelectric macrodomains decompose into microdomains – polar microspheres inherent in relaxor ferroelectrics. Such a process is characteristic of relaxor ferroelectrics [19, 20]. The questions of the formation of different types of domain structures in these materials

and the influence of external influences on them are currently an urgent task and require further studies [21, 22].

As noted above, in the temperature region 298–409 K (site 1 in Fig. 4b), the hysteresis dependence of  $P(E)$  has a form inherent to classical ferroelectrics. It can be assumed that below the temperature of 409 K polarization switching in ceramics  $\text{Pb}_{0.88}\text{Ba}_{0.06}\text{Sr}_{0.06}(\text{Mg}_{1/3}\text{Nb}_{2/3})_{0.37}\text{Zr}_{0.375}\text{Ti}_{0.255}\text{O}_5$  occurs according to the laws common to ferroelectrics. Then the value of  $W_{\max}$  will also have the meaning of the interaction energy of ferroelectric domains



with the electric field. At the transition of the investigated sample to the relaxor state in the temperature region 409–433 K (section 2 in Fig. 4b), corresponding to the blurred ferroelectric phase transition of the first kind [15], part of the electric field energy is spent to induce the polar state, as evidenced by the double dielectric hysteresis loops, and the value of  $W_{\max}$  loses the meaning of the interaction energy of ferroelectric domains with the electric field.

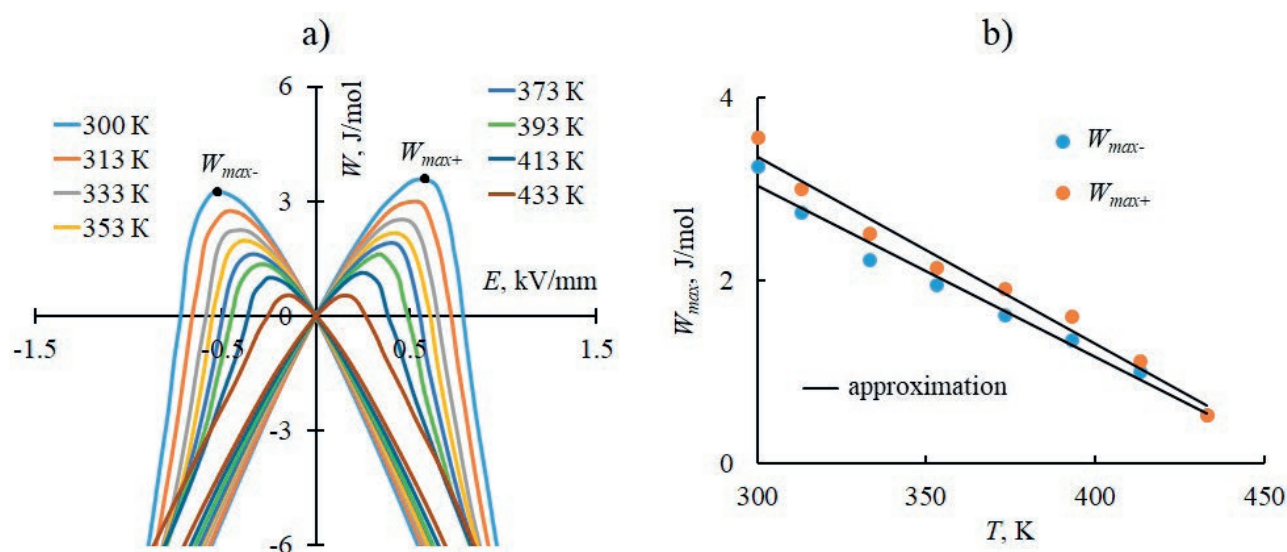
Analysis of  $W_{\max+}(T)$  and  $W_{\max-}(T)$  dependences (Fig. 5) obtained from dielectric hysteresis loops for ceramics  $\text{Pb}_{0.96}\text{Sr}_{0.04}(\text{Mg}_{1/3}\text{Nb}_{2/3})_{0.275}(\text{Ni}_{1/3}\text{Nb}_{2/3})_{0.1}\text{Ti}_{0.375}\text{Zr}_{0.25}\text{O}_3$  [12] showed that they can be satisfactorily approximated by formula (3). For  $W_{\max-}$ :  $a_T \approx 0.019$  J/mole·K,  $b_T \approx 8.7$  J/mole. For  $W_{\max+}$ :  $a_T \approx 0.021$  J/mole·K,  $b_T \approx 9.5$  J/mole.

Analyzing the obtained results, it can be seen that the values of  $W_{\max-}$  and  $W_{\max+}$  for samples of the same composition can both differ from each other (Fig. 2b, Fig. 3b) and practically coincide (Fig. 4b, Fig. 5b). As noted above, for the  $\text{BaZrO}_3/\text{BaTiO}_3$  superlattice such difference is explained by the asymmetry of the dielectric hysteresis loop as a result of the presence of the internal field of interlayer polarization. For  $\text{Pb}(\text{Zr}_{0.3}\text{Ti}_{0.7})\text{O}_3$  thin films, this asymmetry indicates the presence of an internal displacement field [23]. In the case of ceramic bulk samples, however, this asymmetry

is absent (Fig. 4b) or negligible (Fig. 5b).

Another issue that deserves attention is the reason for different values of  $W_{\max}$  and different rates of their decrease  $a_T$  with increasing temperature for different materials. Thus, for  $\text{BaZrO}_3/\text{BaTiO}_3$  superlattice and  $\text{Pb}(\text{Zr}_{0.3}\text{Ti}_{0.7})\text{O}_3$  thin films,  $W_{\max}$  values reach 30–50 J/mole and  $a_T$  values reach 0.2–0.3 J/mole K. At the same time, for the studied samples of modified PZT and PMN-PZT ceramics,  $W_{\max}$  and  $a_T$  have values an order of magnitude smaller:  $W_{\max} = 3\text{--}5$  J/mole and  $a_T = 0.02\text{--}0.03$  J/mole K. Apparently, this is due to the fact that the values of the coercive field for thin-film and bulk samples also differ by an order of magnitude ( $E_c \sim 10$  kV/mm and  $E_c \sim 1$  kV/mm, respectively), while the values of spontaneous polarizations for the four analyzed samples do not differ so significantly and are within the range of values from 20 to 35  $\mu\text{C}/\text{cm}^2$  according to [9–12].

It is worth noting that the growth of the coercive field value with decreasing thickness of the ferroelectric samples is an experimentally established fact [24]. And the reason for this dependence is explained in the model of surface anchoring of domain walls and nucleation near electrodes [25].



**Fig. 5.** Dependences  $W(E)$  of  $\text{Pb}_{0.96}\text{Sr}_{0.04}(\text{Mg}_{1/3}\text{Nb}_{2/3})_{0.275}(\text{Ni}_{1/3}\text{Nb}_{2/3})_{0.1}\text{Ti}_{0.375}\text{Zr}_{0.25}\text{O}_3$  ceramics at different temperatures (a) and temperature dependences of  $W_{\max+}$  and  $W_{\max-}$  (b), obtained using experimental data from [12]

#### 4. Conclusions

Based on the analysis of ferroelectric hysteresis loops  $P(E)$ , the values of critical energies  $W_{\max}$  of interaction of ferroelectric domains with an external electric field at different temperatures have been determined. In the course of the work, a reasonable assumption that the critical energy  $W_{\max}$  has a physical meaning of the activation energy of the domain structure of a ferroelectric at switching polarization by an electric field, necessary for an irreversible change in its domain structure, has been put forward. It was found that in conditions of complete switching of the ferroelectric polarization, the critical energy  $W_{\max}$  decreases according to a nearly linear law with increasing temperature from 300 K to the temperature lying slightly below the Curie point. The obtained results are of scientific and practical value, since they allow us to determine the conditions of stability of the domain structure of a ferroelectric to external conditions and expand the possibilities of application of the Sawyer-Tauer method for determining the activation energies of irreversible changes in the domain ferroelectric structure.

#### Contribution of the author

The author has independently performed all the work on the preparation of this paper.

#### Conflict of interests

The author declares that he has no known competing financial interests or personal relationships that could have influenced the work reported in this paper.

#### References

1. Kuzenko D. V. Temperature-activation mechanism of the temperature dependence of the dielectric constant of ferroelectric ceramics PZT. *Journal of Advanced Dielectrics*. 2022;12(3): 2250010. <https://doi.org/10.1142/S2010135X22500102>
2. Zhang X., Wang B., Ji Y., ... Nan C.-W. First-principles calculations of domain wall energies of prototypical ferroelectric perovskites. *Acta Materialia*. 2023;242: 118351. <https://doi.org/10.1016/j.actamat.2022.118351>
3. Gridnev S. A., Popov I. I. Kinetics of phase transformation at the Curie point of ferroelectric ceramic  $\text{Ba}_{0.8}\text{Sr}_{0.2}\text{TiO}_3$ . *Ferroelectrics*. 2020;561(1): 127–134. <https://doi.org/10.1080/00150193.2020.1736925>
4. Sidorkin A. S., Nesterenko L. P., Sidorkin A. A., Matveev N. N. Effect of sample thickness on the mobility of domain walls in thin ferroelectric films of lead zirconate-titanate and lead titanate. *Bulletin of the Russian Academy of Sciences: Physics*. 2013;77(8): 1038–1040. <https://doi.org/10.3103/s1062873813080388>
5. Durdiev D., Zaiser M., Wendler F., ... Uranagase M. Determining thermal activation parameters for ferroelectric domain nucleation in  $\text{BaTiO}_3$  from molecular dynamics simulations. *Applied Physics Letters*. 2024;124: 132901. <https://doi.org/10.1063/5.0187476>
6. Pramanick A., Prewitt A. D., Forrester J. S., Jones J. L. Domains, domain walls and defects in perovskite ferroelectric oxides: a review of present understanding and recent contributions. *Critical Reviews in Solid State and Materials Sciences*. 2012;37(4): 243–275. <https://doi.org/10.1080/10408436.2012.686891>
7. Warren W. L., Vanheusden K., Dimos D., Pike G. E., Tuttle B. A. Oxygen vacancy motion in perovskite oxides. *Journal of the American Ceramic Society*. 1996;79(2): 536–538. <https://doi.org/10.1111/j.1151-2916.1996.tb08162.x>
8. Zhou X., Liu Z., Xu B.-X. Influence of dislocations on domain walls in perovskite ferroelectrics: phase-field simulation and driving force calculation. *International Journal of Solids and Structures*. 2022;238: 111391. <https://doi.org/10.1016/j.ijsolstr.2021.111391>
9. Sidorkin A. S., Nesterenko L. P., Gagou Y., ... Popravko N. G. Repolarization of ferroelectric superlattices  $\text{BaZrO}_3/\text{BaTiO}_3$ . *Scientific Reports*. 2019;9: 18948. <https://doi.org/10.1038/s41598-019-55475-2>
10. Chen X., Qiao X., Zhang L., ... Geng W. Temperature dependence of ferroelectricity and domain switching behavior in  $\text{Pb}(\text{Zr}_{0.5}\text{Ti}_{0.5})\text{O}_3$  ferroelectric thin films. *Ceramics International*. 2019;45: 18030–18036. <https://doi.org/10.1016/j.ceramint.2019.06.022>
11. Du G., Liang R., Wang L., ... Dong X. Temperature-dependent ferroelectric dynamic hysteresis properties of modified PMN-PZT relaxor ceramics. *Physica Status Solidi – Rapid Research Letters*. 2013;7(6): 438–442. <https://doi.org/10.1002/pssr.201307138>
12. Wen B., Zhang Y., Liu X., Ma L., Wang X. Temperature-dependent ferroelectric hysteresis properties of modified lead zirconate titanate ceramics. *Journal of Materials Science*. 2012;47(10): 4299–4304. <https://doi.org/10.1007/s10853-012-6280-y>
13. Ishchuk V. M., Kuzenko D. V.  $F$ -centers mechanism of long-term relaxation in lead zirconate-titanate based piezoelectric ceramics. 2. After-field relaxation. *Journal of Advanced Dielectrics*. 2016;6(3): 1650019. <https://doi.org/10.1142/S2010135X16500193>
14. Kuzenko D. V., Bazhin A. I., Spiridonov N. A. Energy approach to the dependence of the parameters of ferroelectric ceramics  $(\text{Pb}_{0.95}\text{Sr}_{0.05})(\text{Zr}_x\text{Ti}_{1-x})\text{O}_3$  on a DC electric field. *Ferroelectrics*. 2021;573(1): 76–86. <https://doi.org/10.1080/00150193.2021.1890465>
15. Smolensky G. A., Bokov V. A., Isupov V. A., Krainik N. N., Pasynkov R. E., Shur M. S. *Ferroelectrics and antiferroelectrics*. Leningrad.: Nauka Publ.: 1971. 476 p. (In Russ.)
16. Sidorkin A. S. *Domain structure in ferroelectrics and related materials*. Moscow: Fizmatlit Publ; 2000. 239 p. (In Russ.)
17. Yan H., Inam F., Viola G., ... Reece M. J. The contribution of electrical conductivity, dielectric permittivity and domain switching in ferroelectric hysteresis loops.

*Journal of Advanced Dielectrics*. 2011;1(1): 107–118 <https://doi.org/10.1142/S2010135X11000148>

18. Jaffe B., Cook W. R. Jr., Jaffe H. *Piezoelectric ceramics*. London and New York: Academic Press; 1971. 328 p.

19. Zhang L. L., Huang Y. N. Theory of relaxor-ferroelectricity. *Scientific Reports*. 2020;10: 5060. <https://doi.org/10.1038/s41598-020-61911-5>

20. Carreras-Casas C., García-Zaldívar O., Peláiz-Barranco A., González-Abreu Y., Calderón-Piñar F., Guerra J. D. S. Relaxor ferroelectric behavior: An approach considering both the dipolar and electrical conductivity contributions. *Journal of Advanced Dielectrics*. 2021;11(3): 2140008. <https://doi.org/10.1142/S2010135X21400087>

21. Sun E., Cao W. Relaxor-based ferroelectric single crystals: growth, domain engineering, characterization and applications. *Progress in Materials Science*. 2014;65: 124–210. <https://doi.org/10.1016/j.pmatsci.2014.03.006>

22. Ushakov A. D., Hu Q., Liu X., Xu Z., Wei X., Shur V. Y. Domain structure evolution during alternating current poling and its influence on the piezoelectric properties in [001]-cut rhombohedral PIN-PMN-PT single crystals.

*Applied Physics Letters*. 2021;118(23): 232901. <https://doi.org/10.1063/5.0055127>

23. Misirlioglu I. B., Okatan M. B., Alpay S. P. Asymmetric hysteresis loops and smearing of the dielectric anomaly at the transition temperature due to space charges in ferroelectric thin films. *Journal of Applied Physics*. 2010;108(3): 034105. <https://doi.org/10.1063/1.3457348>

24. Sidorkin A. S., Nesterenko L. P., Ryabtsev S. V., Sidorkin A. A. Frequency dependence of the coercive field and the internal bias field in ferroelectric thin films. *Physics of the Solid State*. 2009;51(7): 1348–1350. <https://doi.org/10.1134/s1063783409070075>

25. Tagantsev A. K. Size effects in polarization switching in ferroelectric thin films. *Integrated Ferroelectrics*. 1997;16: 237–244. <https://doi.org/10.1080/10584589708013046>

### Information about the author

Danil V. Kuzenko, Cand. Sci. (Phys.–Math.), Head of the Functional Materials Department, Federal State Budgetary Scientific Institution «Research Institute «Reaktiv Elektron» (Donetsk, Russian Federation).

<https://orcid.org/0000-0003-3295-9075>

[danil.kuzenko.84@yandex.ru](mailto:danil.kuzenko.84@yandex.ru)

Received 07.08.2024; approved after reviewing 19.02.2025; accepted for publication 17.03.2025; published online 25.06.2025.





## Original articles

Research article

<https://doi.org/10.17308/kcmf.2025.27/12803>

## Modeling of Desloratadine release process from alloys with Polyethylene glycol-6000 by Molecular dynamics method

Y. A. Polkovnikova<sup>✉</sup>, U. A. Tulskeya, V. N. Semyonov, A. I. Slivkin

Voronezh State University,  
1 Universitetskaya pl., Voronezh 394018, Russian Federation

### Abstract

**Purpose:** Desloratadine is a drug with proven antihistaminic activity, is currently presented on the pharmaceutical market only in dosage forms: tablets, solution and syrup. A significant factor limiting the development of new drugs of desloratadine is its low solubility in water. The actual direction of pharmaceutical technology in this regard is research on creation of dosage forms of desloratadine, aimed at increasing its water solubility. Currently, a promising direction in pharmaceutical technology in the development of drug composition is the use of computer modeling. The use of molecular dynamics modeling method is very relevant in the development of solid dispersions of drugs. The aim of this study was to carry out molecular dynamics modeling of desloratadine release from alloys with polyethylene glycol-6000 (desloratadine: polymer ratio 1:1, 1:2, 1:5) into the dissolution medium.

**Experimental:** modeling of desloratadine release from alloys with polyethylene glycol-6000 was carried out by molecular dynamics method (Gromacs 2023 program, Amber 99 force field). The van der Waals interaction energies of desloratadine with polyethylene glycol-6000 and with water were calculated; the fraction of desloratadine molecules that lost the bond with polyethylene glycol-6000. It was found that the average energy of interaction of desloratadine with polyethylene glycol-6000 and with water. Polyethylene glycol-6000 decreases as the content of desloratadine in the alloy decreases. Desloratadine in the alloy, while the interaction energy with water increases.

**Conclusions:** The studies on the release rate of desloratadine from alloys with polyethylene glycol-6000 by molecular dynamics method showed that the highest release rate of desloratadine was achieved at 1:1 ( $5.47 \pm 1.11\%$ ), 1:2 ( $5.39 \pm 0.51\%$ ) ratios and the lowest at 1:5 ( $3.03 \pm 0.00\%$ ). The obtained results indicate the promising use of solid dispersions “desloratadine – polyethylene glycol-6000” (1:1 ratio).

**Keywords:** Modeling, release, Desloratadine, Polyethylene glycol-6000, Molecular dynamics

**Funding:** The research was funded by the Russian Science Foundation grant No. 24-25-20015, <https://rscf.ru/project/24-25-20015/>.

**For citation:** Polkovnikova Yu. A., Tulskeya U., Semyonov V. N., Slivkin A. I. Modeling of Desloratadine release process from alloys with Polyethylene glycol-6000 by Molecular dynamics method. *Condensed Matter and Interphases*. 2025;27(2): 260–266. <https://doi.org/10.17308/kcmf.2025.27/12803>

**Для цитирования:** Полковникова Ю. А., Тульская У. А., Семенов В. Н., Сливкин А. И. Моделирование процесса высвобождения дезлоратадина из сплавов с полиэтиленгликолем-6000 методом молекулярной динамики. *Конденсированные среды и межфазные границы*. 2025;27(2): 260–266. <https://doi.org/10.17308/kcmf.2025.27/12803>

✉ Yulia A. Polkovnikova, e-mail: [juli-polk@mail.ru](mailto:juli-polk@mail.ru)

© Polkovnikova Yu. A., Tulskeya U., Semyonov V. N., Slivkin A. I., 2025



The content is available under Creative Commons Attribution 4.0 License.

## 1. Introduction

Desloratadine, a histamine H1-receptor antagonist, has a proven safe and effective non-sedative antihistaminic activity and finds use in allergic rhinitis, allergic asthma and urticaria [1, 2]. Desloratadine is available on the pharmaceutical market in the following dosage forms: film-coated tablets, solution and syrup. A significant factor limiting the use of desloratadine is its extremely low solubility in water, which significantly reduces the therapeutic effect of pharmaceutical substances from dosage forms [3, 4].

Several studies have attempted to improve the solubility of Desloratadine by complexing desloratadine with  $\beta$ -cyclodextrin in solution [5].

Currently, various approaches such as salt formation, solubilization with co-solvents, reduction of particle size or preparation of solid dispersions are used to improve the solubility and dissolution rate of poorly water-soluble pharmaceutical substances. A promising and relevant direction in pharmaceutical science is the preparation of solid dispersions [6]. Amorphous solid dispersions are single phase amorphous systems in which drug molecules are molecularly dispersed (dissolved) in a polymer matrix [7]. Obtaining solid dispersions is the most promising method for solubility enhancement because it overcomes the limitations of the above approaches, such as the need to use organic solvents [8].

The class of polymeric carriers widely used in the technology of solid dispersions includes polyethylene glycols (PEG) of different molecular weights [9,10]. In particular, PEG-6000 has been used as a carrier to increase the dissolution rate of poorly water-soluble drugs such as tacrolimus, diclofenac, itraconazole and rofecoxib [11–14]. The conducted literature analysis revealed no information on the use of PEG as carrier polymers to produce solid dispersions with desloratadine in order to increase its water solubility in the creation of dosage forms. Thus, the development of an oral capsulated dosage form with Desloratadine with an increased bioavailability will expand the nomenclature of antihistaminic drugs, which is undoubtedly an urgent task for the development of the modern pharmaceutical market.

A promising direction in pharmaceutical technology is the following obtaining and research of solid dispersions with PEG-6000, including the method of molecular dynamics [15]. The application of molecular modeling, which is important for optimizing formulations and predicting drug release profiles, can provide insight into the interactions between drugs and excipients, including complexation. The aim of this work is to carry out Molecular dynamics simulations of desloratadine release from alloys with PEG-6000 (desloratadine: polymer ratio 1:1, 1:2, 1:5) into dissolution medium.

## 2. Experimental

Modeling of the release of desloratadine from alloys with PEG-6000 was carried out by molecular dynamics method (Gromacs 2023 program [16], Amber 99 force field). Desloratadine molecules, spatial structures of monomers were constructed in HyperChem program. Polymer chains assembly, force field parameterization for the molecules of the components of the simulated systems was carried out using the ParmEd program [17–19].

PEG molecules (Figure 1) with a length of 136 monomers with a molar mass of 6009, as well as desloratadine molecules in the form of cation and  $\text{Cl}^-$  ions were included in the components of the modeled systems (Figure 2).

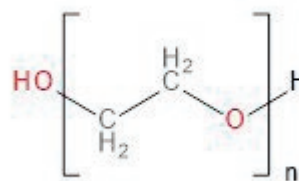
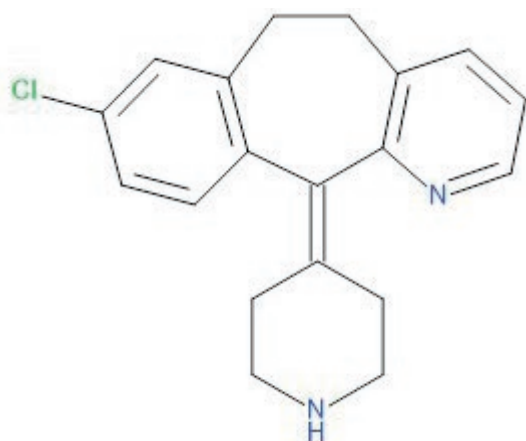


Fig. 1. Structure of the PEG molecule

In the first step of the work, models of desloratadine alloys with PEG-6000 were constructed. Using periodic boundary conditions in all coordinate axes, models of desloratadine alloys with PEG-6000 were prepared by means of molecular dynamics simulations [20, 21].

The van der Waals interaction energy (VDWIE) of desloratadine with PEG-6000 and with water was calculated; the fraction of desloratadine molecules that lost their bond with PEG-6000. A desloratadine molecule was considered to



**Fig. 2.** Chemical structure of the desloratadine molecule

be released into water if it did not bind to the polymer and bound to water.

### 3. Results and discussion

Starting to discuss the results obtained from modeling, it is necessary to present those possible physicochemical interactions that will occur during the absorption and desorption of desloratadine by the polymer. It should be noted that we are dealing with a heterogeneous system in which the polymer in the polymer (polyethylene) matrix contains polar -OH-groups that do not possess ion-exchange properties. Desloratadine reacts as a doubly charged cation upon absorption of PEG-6000. Consequently, the uptake of desloratadine by PEG will be due to the formation of dispersion, induction and hydrogen bonds (with the participation of water molecule as an active reagent). This was the reason for the composition of the modeled systems (Table 1).

The release of desloratadine from the alloy with PEG-6000 1:1 occurs partially, and the formation of associates of desloratadine molecules in the aqueous medium was observed. The percentage of release of desloratadine during the first 20 ns is 8% (Figure 3), while  $\Delta E$  in the interaction energies of

“Desloratadine-PEG-6000” and “Desloratadine - Water” interaction energies reach  $-70$ ;  $-40$  kJ/mol (Fig. 4), and clear transitions of desloratadine to water are observed.

Release rate of desloratadine from the fusion with PEG-6000 at a 1:2 ratio of desloratadine to polymer by mass occurs to a small extent over a simulation time of more than 20 ns. The VDWIE between desloratadine and polymer less than  $-100$  kJ/mol and between desloratadine and water greater than  $-40$  kJ/mol indicate no high involvement of desloratadine in solvent interaction and significant binding to the polymer (Fig. 5).

The percentage of desloratadine release within the first 18 ns is 8 % (Fig. 6), although the  $\Delta E$  in the interaction energies of “Desloratadine-PEG-6000” and “Desloratadine-Water” reaches  $-140$ ;  $-30$  kJ/mol (Fig. 4), and clear desloratadine-to-solvent transitions at distinct time intervals are observed.

At the ratio of desloratadine with PEG-6000 1:5 by mass, the release of desloratadine into the aqueous medium is insignificant (more than 3 %) (Fig. 7). The VDWIE between desloratadine and polymer less than  $-140$  kJ/mol and between desloratadine and water greater than  $-30$  kJ/mol indicate little involvement of desloratadine in interaction with the solvent and strong binding to the polymer (Fig. 8).

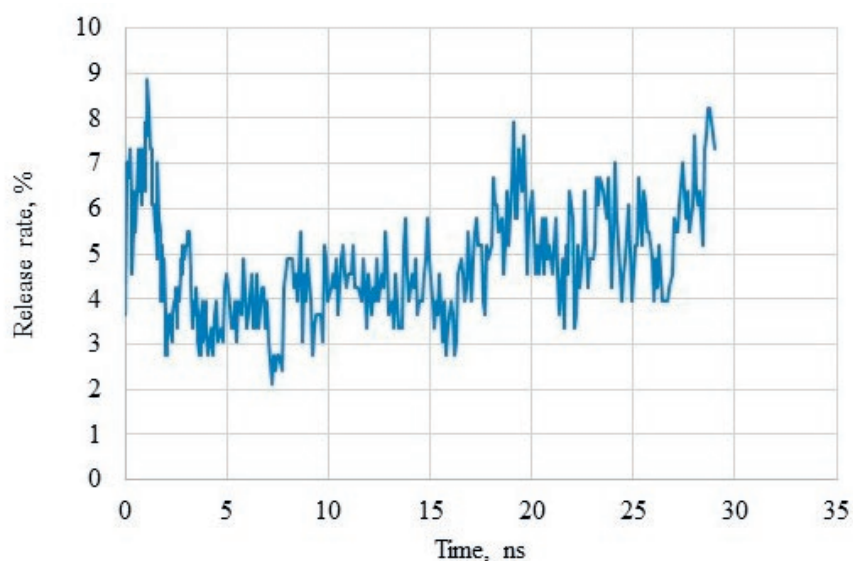
The mean values of VDWIE of desloratadine with PEG-6000 and with water, and the mean values of release rate into water from the fusion with PEG-6000 were calculated (Table 2).

The average interaction energy of desloratadine with polymers decreases as the desloratadine content of the alloy decreases, while the interaction energy with water increases. This trend indicates that the involvement of desloratadine in the solvation and desorption processes decreases as its content in the mixture with the polymer decreases.

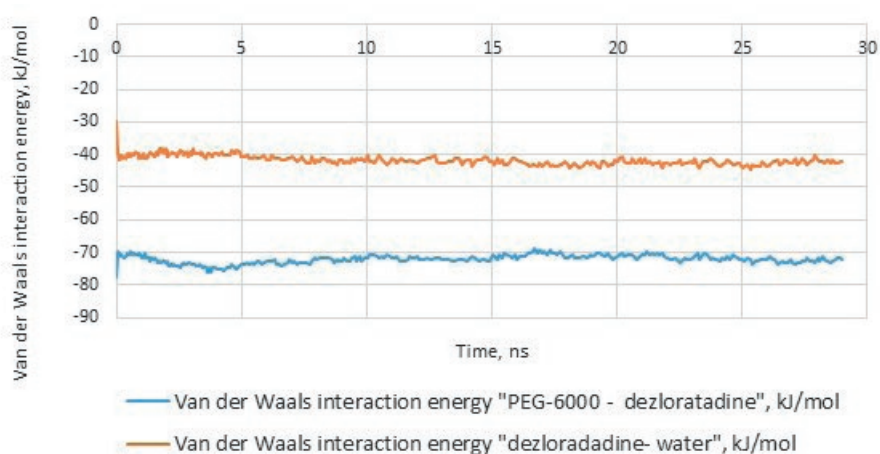
**Table 1.** Amounts of molecules of components of simulated systems

Substance	Desloratadine-PEG-6000 1:1	Desloratadine-PEG-6000 1:2	Desloratadine-PEG-6000 1:5
Desloratadine cation	328	164	66
Cl <sup>-</sup> ion	328	164	66
PEG-6000	17	17	17
Water	20056	20425	20086

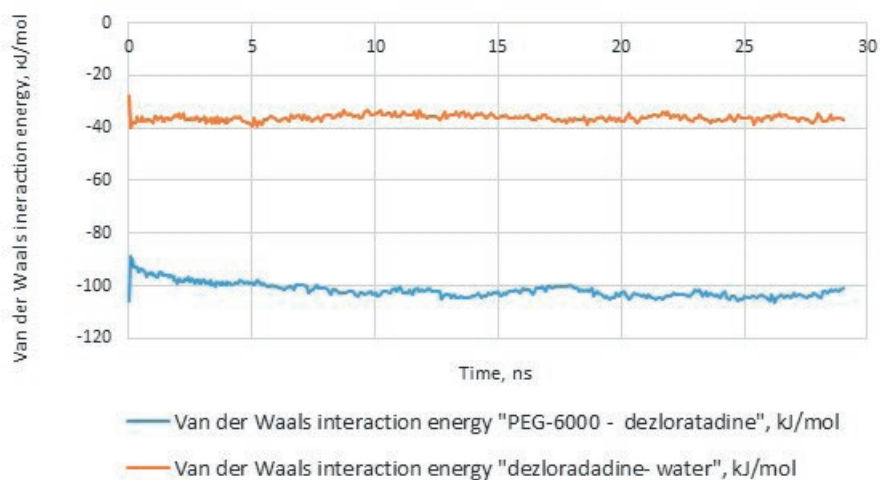




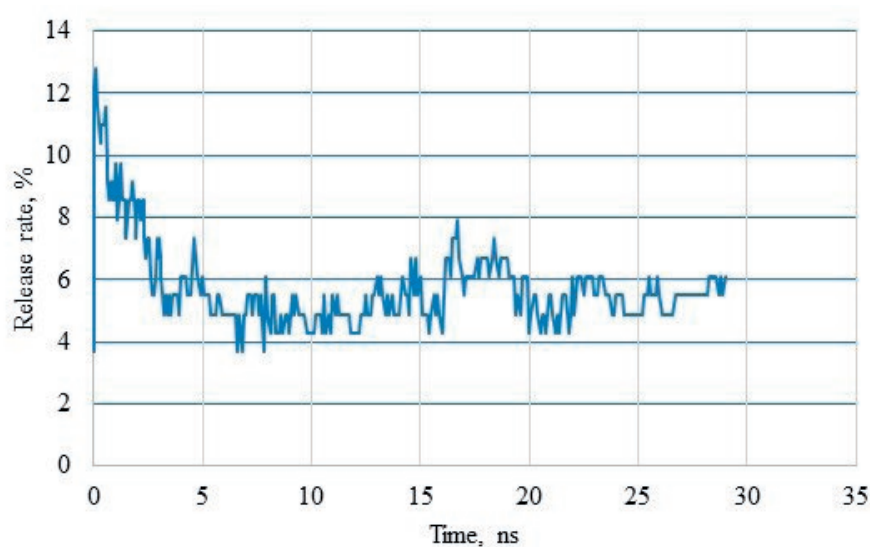
**Fig. 3.** Extent of release of desloratadine molecules not bound to PEG-6000 in water (desloratadine: PEG-6000 1:1)



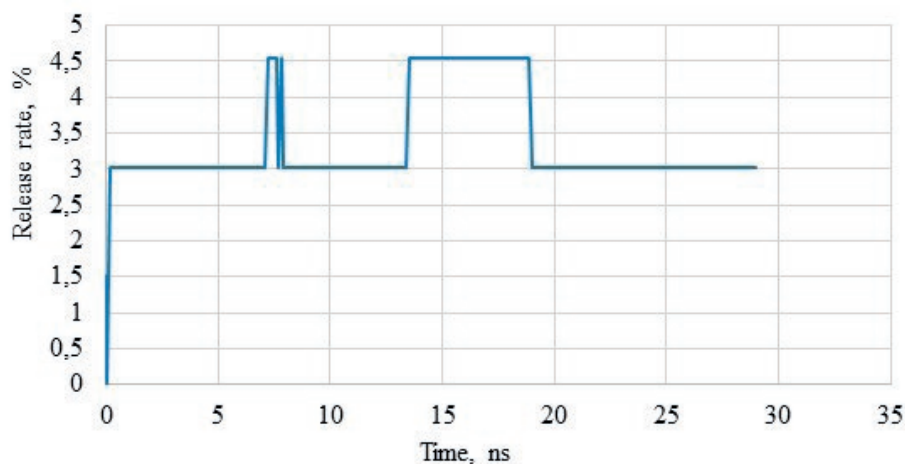
**Fig. 4.** VDWIE of desloratadine with PEG-6000 and with water (desloratadine: PEG-6000 1:1)



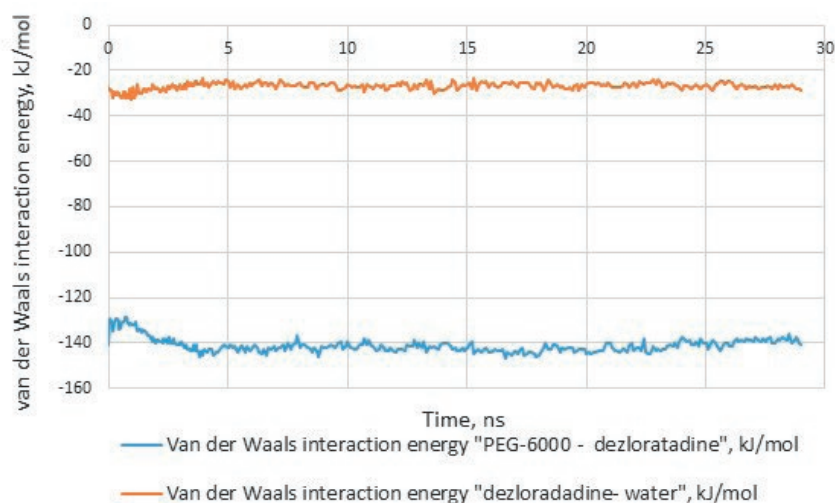
**Fig. 5.** VDWIE of desloratadine with PEG-6000 and with water (desloratadine: PEG-6000 1:2)



**Fig. 6.** Extent of release of desloratadine molecules not bound to PEG-6000 in water (desloratadine: PEG-6000 1:2)



**Fig. 7.** Extent of release of desloratadine molecules not bound to PEG-6000 in water (desloratadine: PEG-6000 1:5)



**Fig. 8.** VDWIE of desloratadine with PEG-6000 and with water (desloratadine: PEG-6000 1:5)

**Table 2.** Release parameters of desloratadine from alloys with PEG-6000

System	Average EVDWI of desloratadine with PEG-6000, kJ/mol	Average EVDWI of desloratadine with solvent, kJ/mol	Average release rate, %
Desloratadine-PEG-6000 1:1	$-72.02 \pm 0.87$	$-42.49 \pm 0.78$	$5.47 \pm 1.11$
Desloratadine-PEG-6000 1:2	$-103.68 \pm 1.09$	$-36.20 \pm 0.96$	$5.39 \pm 0.51$
Desloratadine-PEG-6000 1:5	$-140.38 \pm 2.02$	$-26.68 \pm 1.11$	$3.03 \pm 0.00$

#### 4. Conclusions

The studies of desloratadine release from alloys with PEG-6000 by molecular dynamics method showed that the highest release rate of desloratadine from PEG-6000 into aqueous medium was achieved at a ratio of 1:1, and the lowest at a ratio of 1:5. At ratios of 1:1 and 1:2, the average interaction energy of desloratadine with PEG-6000 per desloratadine molecule was the highest ( $-72.02 \pm 0.87$  kJ/mol) and ( $-103.68 \pm 1.09$  kJ/mol), respectively, while the interaction energy of desloratadine with water was low ( $-42.49 \pm 0.78$  kJ/mol) and ( $-36.20 \pm 0.96$  kJ/mol), respectively, indicating the greatest involvement of desloratadine in the solvation and desorption at this ratio. The results obtained indicate that the use of solid dispersions “Desloratadine – PEG” (1:1 ratio) is promising. The computer modeling data will be subsequently used to establish the value of the computer modeling results characteristics, allowing to obtain solid dispersions of desloratadine with specified biopharmaceutical characteristics.

#### Contribution of the authors

The authors contributed equally to this article.

#### Conflict of interests

The authors declare that they have no known competing financial interests or personal relationships that could have influenced the work reported in this paper.

#### References

1. Popović G., Čakar M., Agbaba D. Acid-base equilibria and solubility of loratadine and desloratadine in water and micellar media. *Journal of Pharmaceutical and Biomedical Analysis*. 2009;49: 42–47. <https://doi.org/10.1016/j.jpba.2008.09.043>
2. DuBuske L. M. Review of desloratadine for the treatment of allergic rhinitis, chronic idiopathic urticaria and allergic inflammatory disorders. *Expert Opinion on Pharmacotherapy*. 2005;6: 2511–2523. <https://doi.org/10.1517/14656566.6.14.2511>
3. *State Pharmacopoeia of the Russian Federation XV* [Electronic edition]. (In Russ.). Available at: <https://pharmacopoeia.regmed.ru/pharmacopoeia/izdanie-15/>
4. Kolašinac N., Kachrimanis K., Homšek I., Grujić B., Đurić Z., Ibrić S. Solubility enhancement of desloratadine by solid dispersion in poloxamers. *International Journal of Pharmaceutics*. 2012;436(1-2): 161–70. <https://doi.org/10.1016/j.ijpharm.2012.06.060>
5. Vasconcelos T., Marques S., das Neves J., Sarmiento B. Amorphous solid dispersions: rational selection of a manufacturing process. *Advanced Drug Delivery Reviews*. 2016;100: 85–101. <https://doi.org/10.1016/j.addr.2016.01.012>
6. Douroumis J. A., Zeitler S. Q. An investigation into the formations of the internal microstructures of solid dispersions prepared by hot melt extrusion. *European Journal of Pharmaceutics and Biopharmaceutics*. 2020;155: 147–161 <https://doi.org/10.1016/j.ejpb.2020.08.018>
7. Barea S. A., Mattos C. B., Cruz A. C., ... Koester L. S. Solid dispersions enhance solubility, dissolution, and permeability of thalidomide. *Drug Development and Industrial Pharmacy*. 2017;43(3): 511–518. <https://doi.org/10.1080/03639045.2016.1268152>
8. Zhai X., Li C., Lenon G. B., Xue C. C. L., Li W. Preparation and characterisation of solid dispersions of tanshinone IIA, cryptotanshinone and total tanshinones. *Asian Journal of Pharmaceutical Sciences*. 2017;12(1): 85–97. <https://doi.org/10.1016/j.ajps.2016.08.004>
9. Bolourchian N., Mahboobian M. M., Dadashzadeh S. The effect of PEG molecular weights on dissolution behavior of simvastatin in solid dispersions. *Iranian Journal of Pharmaceutical Research*. 2013;12: 11–20.
10. Dos Santos K. M., Barbosa R. M., Vargas F. G. A., ... Raffin F. N. Development of solid dispersions of  $\beta$ -lapachone in PEG and PVP by solvent evaporation method. *Drug Development and Industrial Pharmacy*. 2018;44(5): 750–756. <https://doi.org/10.1080/03639045.2017.1411942>
11. Polkovnikova Yu. A., Glizhova T. N., Arutyunova N. V., Sokulskaya N. N. PEG-4000 Increases solubility and dissolution rate of vinpocetin in solid dispersion system *Chimica Techno Acta*. 2022;9(S): 202292S11. <https://doi.org/10.15826/chimtech.2022.9.2.S11>
12. Leonardi D., Barrera M. G., Lamas M. C., Salomón C. J. Development of prednisone: polyethylene glycol 6000 fast-release tablets from solid dispersions: solid-state characterization, dissolution behavior, and formulation parameters. *AAPS PharmSciTech*. 2007;8(4):E108. <https://doi.org/10.1208/pt0804108>



13. Fatmi S., Bournine L., Iguer-Ouada M., Lahiani-Skiba M., Bouchal F., Skiba M. Amorphous solid dispersion studies of camptothecin-cyclodextrin inclusion complexes in PEG 6000. *Acta Polonicae Pharmaceutica – Drug Research*. 2015;72(1): 179–192.
14. Febriyenti F., Rahmi S., Halim A. Study of gliclazide solid dispersion systems using PVP K-30 and PEG 6000 by solvent method. *Journal of Pharmacy And Bioallied Sciences*. 2019;11(3): 262–267. [https://doi.org/10.4103/jpbs.jpbs\\_87\\_18](https://doi.org/10.4103/jpbs.jpbs_87_18)
15. Polkovnikova Yu. A., Slivkin A. I., Belenova A. S. Modeling the process of vinpocetine release from an alloy with PEG-6000 using the molecular dynamics method. *Proceedings of Voronezh State University. Series: Chemistry. Biology. Pharmacy*. 2022; 4: 144–148. (In Russ., abstract in Eng.). Available at: <https://elibrary.ru/item.asp?id=49963564>
16. Abraham M. J., Murtola T., Schulz R., Páll S., Smith J. C., Hess B., Lindahl E. GROMACS: High performance molecular simulations through multi-level parallelism from laptops to supercomputers. *SoftwareX*. 2015;1–2: 19–25. <https://doi.org/10.1016/j.softx.2015.06.001>
17. Han R., Huang T., Liu X., ... Ouyang D. Insight into the dissolution molecular mechanism of ternary solid dispersions by combined experiments and molecular Ssimulations. *AAPS PharmSciTech*. 2019;20(7): 274. <https://doi.org/10.1208/s12249-019-1486-9>
18. Sorin E. J., Pande V. S. Exploring the helix-coil transition via all-atom equilibrium ensemble simulations. *Biophysical Journal*. 2005;88(4): 2472–2493. <https://doi.org/10.1529/biophysj.104.051938>
19. Shirts M. R., Klein C., Swails J. M., ... Zhong E. D. Lessons learned from comparing molecular dynamics engines on the SAMPL5 dataset. *Journal of Computer-Aided Molecular Design*. 2017;31: 147–161. <https://doi.org/10.1007/s10822-016-9977-1>
20. Braga C., Travis K. P. A configurational temperature Nosé-Hoover thermostat. *The Journal of Chemical Physics*. 2005;123(13): 134101. <https://doi.org/10.1063/1.2013227>
21. Shirts M. R., Klein C., Swails J. M., ... Zhong E. D. Lessons learned from comparing molecular dynamics engines on the SAMPL5 dataset. *Journal of Computer-Aided Molecular Design*. 2017;31: 147–161. <https://doi.org/10.1007/s10822-016-9977-1>

### Information about the authors

*Yulia A. Polkovnikova*, Dr. Sci. (Pharmacy), Associate Professor, Associate Professor of the Department of Pharmaceutical Technology and Pharmaceutical Chemistry, Faculty of Pharmacy, Voronezh State University (Voronezh, Russian Federation).

<https://orcid.org/0000-0003-0123-9526>

[juli-polk@mail.ru](mailto:juli-polk@mail.ru)

*Ulyana A. Tulskeya*, resident Faculty of Pharmacy, Voronezh State University (Voronezh, Russian Federation).

<https://orcid.org/0000-0001-5775-9884>

[m.blal1996@gmail.com](mailto:m.blal1996@gmail.com)

*Victor N. Semenov*, Dr. Sci. (Chem.), Professor, Chair of Department of General and Inorganic Chemistry, Voronezh State University (Voronezh, Russian Federation).

<https://orcid.org/0000-0002-4247-5667>

[office@chem.vsu.ru](mailto:office@chem.vsu.ru)

*Alexey I. Slivkin*, Dr. Sci. (Pharmacy), Professor, Head of the Department of Pharmaceutical Chemistry and Pharmaceutical Technology, Faculty of Pharmacy, Voronezh State University (Voronezh, Russian Federation).

<https://orcid.org/0000-0001-6934-0837>

[slivkin@pharm.vsu.ru](mailto:slivkin@pharm.vsu.ru)

Received 02.08.2024; approved after reviewing 09.09.2024; accepted for publication 16.09.2024; published online 25.06.2025.



# Condensed Matter and Interphases

Kondensirovannye Sredy i Mezhfaznye Granitsy  
<https://journals.vsu.ru/kcmf/>

## Original articles

Research article

<https://doi.org/10.17308/kcmf.2025.27/12805>

## Phase diagram of the system $\text{Na}_2\text{SO}_4 - \text{In}_2(\text{SO}_4)_3$ . Comparative analysis of $\text{Na}_2\text{SO}_4 - \text{R}_2(\text{SO}_4)_3$ systems ( $\text{R} = \text{Al}, \text{Ga}, \text{Fe}, \text{In}, \text{Sc}, \text{Yb}$ )

V. Yu. Proydakova<sup>1</sup>, V. V. Voronov<sup>1</sup>, S. V. Kuznetsov<sup>1</sup> ✉, I. N. Nekrylov<sup>2</sup>,  
A. U. Zavrazhnov<sup>2</sup>, P. P. Fedorov<sup>1</sup>

<sup>1</sup>Prokhorov General Physics Institute of the Russian Academy of Sciences,  
38 Vavilova st., Moscow 119991, Russian Federation

<sup>2</sup>Voronezh State University,  
1 Universitetskaya pl., Voronezh 394018, Russian Federation

### Abstract

**Purpose:** The phase diagram of the system of sodium sulfate with indium sulfate has been studied for the first time.

**Experimental:** Thermal and X-ray phase analysis (XRD) techniques, including high-temperature analysis, were used.

**Conclusions:** In the  $\text{Na}_2\text{SO}_4 - \text{In}_2(\text{SO}_4)_3$  system determined a several substances. The  $\text{NaInSO}_4$  compound incongruently melted at 800 °C. The  $\text{Na}_3\text{In}(\text{SO}_4)_3$  compound has polymorphic transformations at 210 and 580 °C, and decomposes in the solid state at 680 °C. The compound containing  $7 \pm 1$  mol. %  $\text{In}_2(\text{SO}_4)_3$  ( $\phi$  phase), changing to the solid solution at 540 °C. The eutectic coordinates are 710 °C, 18 mol. %  $\text{In}_2(\text{SO}_4)_3$ . The solid solution region based on  $\alpha\text{-Na}_2\text{SO}_4$  is  $11 \pm 1$  mol. %  $\text{In}_2(\text{SO}_4)_3$ . The solid solution melting curves show a maximum at 895 °C and 3 mol. %  $\text{In}_2(\text{SO}_4)_3$ . According to XRD data, the  $\text{NaInSO}_4$  compound crystallizes in the structural type of javapaite -  $\text{KFe}(\text{SO}_4)_2$  (monoclinic space group ( $C2/m$ ) with lattice parameters  $a = 8.024 \text{ \AA}$ ,  $b = 5.069 \text{ \AA}$ ,  $c = 7.211 \text{ \AA}$ ,  $\beta = 90.6^\circ$ ), and is isostructural to compounds of similar composition with aluminum, gallium, iron, chromium, vanadium and rhodium sulfates. Low-temperature modification  $\text{Na}_3\text{In}(\text{SO}_4)_3$  crystallizes in trigonal space group ( $R\bar{3}$ ) with lattice parameters  $a = 13.970 \text{ \AA}$ ,  $c = 8.871 \text{ \AA}$ , and is isostructurally similar to similar compounds with sulfates of aluminum, gallium, iron (III), vanadium, rhodium, scandium. X-ray diffraction pattern of the mid-temperature modification  $\text{Na}_3\text{In}(\text{SO}_4)_3$  is indexed in monoclinic space group ( $P21/c$ ) with lattice parameters  $a = 16.187(4) \text{ \AA}$ ,  $b = 13.584(3) \text{ \AA}$ ,  $c = 9.639(2) \text{ \AA}$ ,  $\beta = 91.6^\circ$ . The X-ray diagram of the  $\phi$  phase is indexed in monoclinic space group ( $P21/c$ ) with lattice parameters  $a = 7.836 \text{ \AA}$ ,  $b = 14.845 \text{ \AA}$ ,  $c = 4.57 \text{ \AA}$ ,  $\beta = 91.14^\circ$ .

**Keywords:** Sodium sulfate, Indium sulfate, Aluminum sulfate, Gallium sulfate, Iron sulfate, Scandium sulfate, Ytterbium sulfate, Phase diagrams, Solid solutions, Isomorphism

**For citation:** Proydakova V. Yu., Voronov V. V., Kuznetsov S. V., Nekrylov I. N., Zavrazhnov A. Yu., Fedorov P. P. Phase diagram of the  $\text{Na}_2\text{SO}_4 - \text{In}_2(\text{SO}_4)_3$  system. Comparative analysis of the  $\text{Na}_2\text{SO}_4 - \text{R}_2(\text{SO}_4)_3$  ( $\text{R} = \text{Al}, \text{Ga}, \text{Fe}, \text{In}, \text{Sc}, \text{Yb}$ ). *Condensed Matter and Interphases*. 2025;27(2): 267–277. <https://doi.org/10.17308/kcmf.2025.27/12805>

Для цитирования: Пройдакова В. Ю., Воронов В. В., Кузнецов С. В., Некрылов И. Н., Завражнов А. Ю., Федоров П. П. Фазовая диаграмма системы  $\text{Na}_2\text{SO}_4 - \text{In}_2(\text{SO}_4)_3$ . Сравнительный анализ систем  $\text{Na}_2\text{SO}_4 - \text{R}_2(\text{SO}_4)_3$  ( $\text{R} = \text{Al}, \text{Ga}, \text{Fe}, \text{In}, \text{Sc}, \text{Yb}$ ). *Конденсированные среды и межфазные границы*. 2025;27(2): 267–277. <https://doi.org/10.17308/kcmf.2025.27/12805>

✉ Sergey V. Kuznetsov, e-mail: kuznetzovsv@gmail.com

© Proydakova V. Yu., Voronov V. V., Kuznetsov S. V., Nekrylov I. N., Zavrazhnov A. Yu., Fedorov P. P., 2025



The content is available under Creative Commons Attribution 4.0 License.

## 1. Introduction

An urgent task of chemical materials science is the development of materials with high ionic conductivity that could serve as a substitute for scarce lithium in electrochemical energy sources [1–3]. Sodium ionic conductors, including solid solutions based on high-temperature modification of sodium sulfate, are promising [4–6]. In sulfates, an original mechanism of ionic conductivity enhancement due to rotational dynamics of sulfate ions is realized [7–8].

The investigated phase diagrams of systems with the participation of sodium sulfate indicate the formation of heterovalent solid solutions with the introduction of two-, three- and four-valent cations into the  $\text{Na}_2\text{SO}_4$  lattice, with the formation of cation vacancies that facilitate ionic transport [6, 9–15].

The phase diagrams based on sodium sulfate with sulfates of a number of trivalent metals, namely aluminum [11], iron [12], neodymium, terbium and ytterbium [13], and bismuth [16], have been previously investigated. Preliminary results of our study of the phase diagram of  $\text{Na}_2\text{SO}_4 - \text{Ga}_2(\text{SO}_4)_3$  are published in [15]. In all systems, except  $\text{Na}_2\text{SO}_4 - \text{Bi}_2(\text{SO}_4)_3$ , the formation of solid solutions based on high-temperature modification of sodium sulfate was revealed.

The phase diagram of the  $\text{Na}_2\text{SO}_4 - \text{In}_2(\text{SO}_4)_3$  system has not been studied previously. There is a report on the existence of the compound  $\text{Na}_3\text{In}(\text{SO}_4)_3$  [17]. The aim of this work is to study phase equilibria in the system of indium sulfate with sodium sulfate  $\text{Na}_2\text{SO}_4 - \text{In}_2(\text{SO}_4)_3$  and to carry out a comparative analysis of phase formation in systems of sodium sulfate with trivalent metal sulfates.

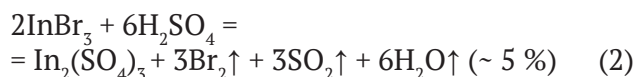
Indium sulfate is characterized by polymorphism [18]. The high-temperature modification  $\text{In}_2(\text{SO}_4)_3$  crystallizes in trigonal space group ( $R\bar{3}$ ) while the low-temperature monoclinic has another space group  $P2_1/n$ .

## 2. Experimental methodology

$\text{Na}_2\text{SO}_4$  with grade “chemical purity” was calcined at 180 °C for four hours to remove crystallization water and placed in the desiccator.

Indium sulfate from LANHIT (purity 99.9 % by metal impurities) was used in this work. In addition, indium (III) sulfate was synthesized

from indium bromide by heating with sulfuric acid dehydrated with thionyl chloride (the water in the sulfuric acid was bound to volatile  $\text{SO}_2$  and  $\text{HCl}$ , which left the liquid phase):

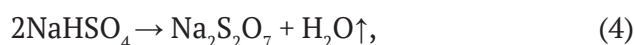


In turn, indium bromide was obtained by direct interaction of metallic indium and dehydrated bromine under heating.

To prepare samples with indium (III) sulfate content of 25 mol. % (compound of  $\text{Na}_3\text{In}(\text{SO}_4)_3$ ), sodium pyrosulfate was mixed with indium oxide in stoichiometric ratios according to Eq.3:



In turn, sodium pyrosulfate was prepared by heating sodium hydrosulfate to 250 °C (4 h):



and indium oxide was synthesized by decomposition of indium nitrate at 250 °C:



Indium (III) nitrate was prepared by dissolving indium metal (In-00) in excess concentrated nitric acid.

Solid-phase synthesis was carried out at 500 °C by sintering of sodium and indium sulfate mixtures in a porcelain mortar. In addition, compositions with low indium sulfate content (< 25 mol. %) was obtained by adding additional amounts of sodium sulfate to the reaction product (3).

Parallel studies have yielded converging results. Indium sulfate preparations are hygroscopic.

Gallium sulfate was obtained by the method described in [19]. In addition, samples in the  $\text{Na}_2\text{SO}_4 - \text{Ga}_2(\text{SO}_4)_3$  and  $\text{Na}_2\text{SO}_4 - \text{Al}_2(\text{SO}_4)_3$  systems were synthesized via ammonium alum, which was precipitated from concentrated sulfate solutions by adding stoichiometric amounts of ammonium sulfate. The thoroughly ground mixtures with sodium sulfate were calcined at 450 °C for 5 h.

Scandium sulfate was obtained from the oxide by interaction with concentrated sulfuric acid at 80 °C.



Thermal analysis (DTA + DTG) was carried out on a Q-1500 D derivatograph. A platinum-rhodium thermocouple, open platinum crucibles were used. Heating and cooling rates in air were 10 deg/min. The weight of the suspensions was 350–400 mg.

In addition, a second DTA technique was used. Samples weighing about 1 g were sealed in Stepanov vessels, which had small holes in the upper part to bleed excess pressure into the atmosphere. Thermographic studies were performed in heating mode at a rate of 4K/min.

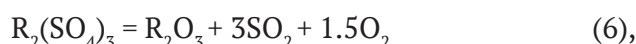
Decoding of thermograms was carried out according to the method [20, 21]. The temperatures of noninvariant transformations were fixed by the onset of effects on the heating curves. Liquidus temperatures were recorded from the onset of effects on the cooling curves, as well as from maxima on the heating curves when an appropriate instrumental correction was introduced (about 10°C). Recording of thermograms was stopped when a noticeable mass loss (due to sulfate decomposition and  $\text{SO}_2$  release) was observed.

X-ray phase analysis (XRD) was performed on a Bruker D8 Discover A25 diffractometer, Da Vinci Design,  $\text{CuK}\alpha$  emission. X-ray diagrams were processed with EVA program version 2.1. Calculation of lattice parameters were carried out using the TOPAS version 4.2 program. The high-

temperature XRD was performed using the HTK 1200N high-temperature chamber manufactured by Anton Paar. The samples were held at each temperature for about 20 min before recording XRD.

### 3. Results and discussion

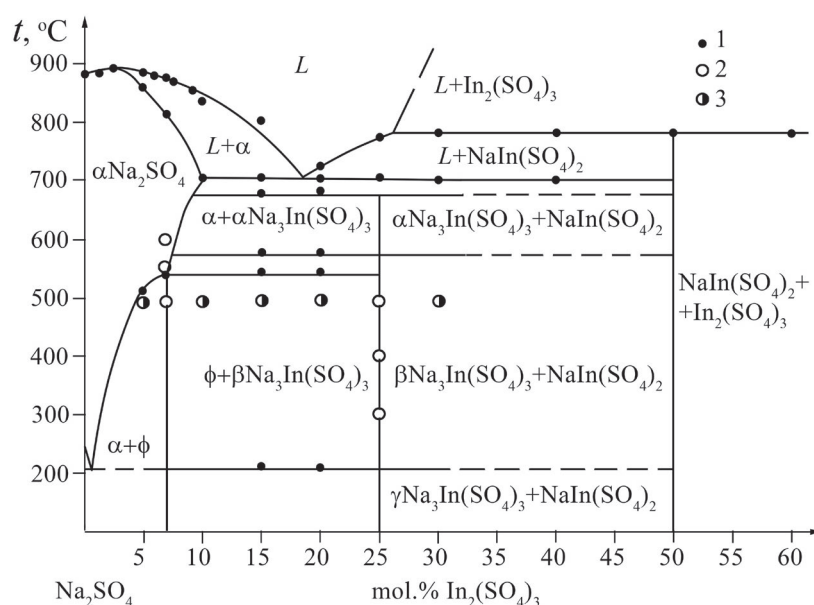
The melting and polymorphic transition temperatures of sodium sulfate are 887 and 240 °C according to our data. Sulfates of trivalent elements decompose by reactions when heated:



that imposes significant limitations on the study of phase equilibria with their participation. In derivatography mode (heating at a rate of 10 deg/min) decomposition of  $\text{Ga}_2(\text{SO}_4)_3$  starts at 680 °C [19].

#### 3.1. $\text{Na}_2\text{SO}_4 - \text{In}_2(\text{SO}_4)_3$ system

In this system (Fig. 1) are formed compounds  $\text{NaInSO}_4$  which melts incongruently at 800 °C,  $\text{Na}_3\text{In}(\text{SO}_4)_3$ , which has polymorphic transformations at 210 and 580 °C and decomposes in the solid state at 680 °C, and a compound containing  $7 \pm 1$  mol. %  $\text{In}_2(\text{SO}_4)_3$  ( $\phi$ -phase), transforming on heating into solid solution based on  $\alpha\text{-Na}_2\text{SO}_4$  ( $\alpha$ -phase). The eutectic coordinates are 710 °C, 18 mol. %  $\text{In}_2(\text{SO}_4)_3$ . The solid solution region based on  $\alpha\text{-Na}_2\text{SO}_4$  is up to  $11 \pm 1$  mol. %  $\text{In}_2(\text{SO}_4)_3$ . The

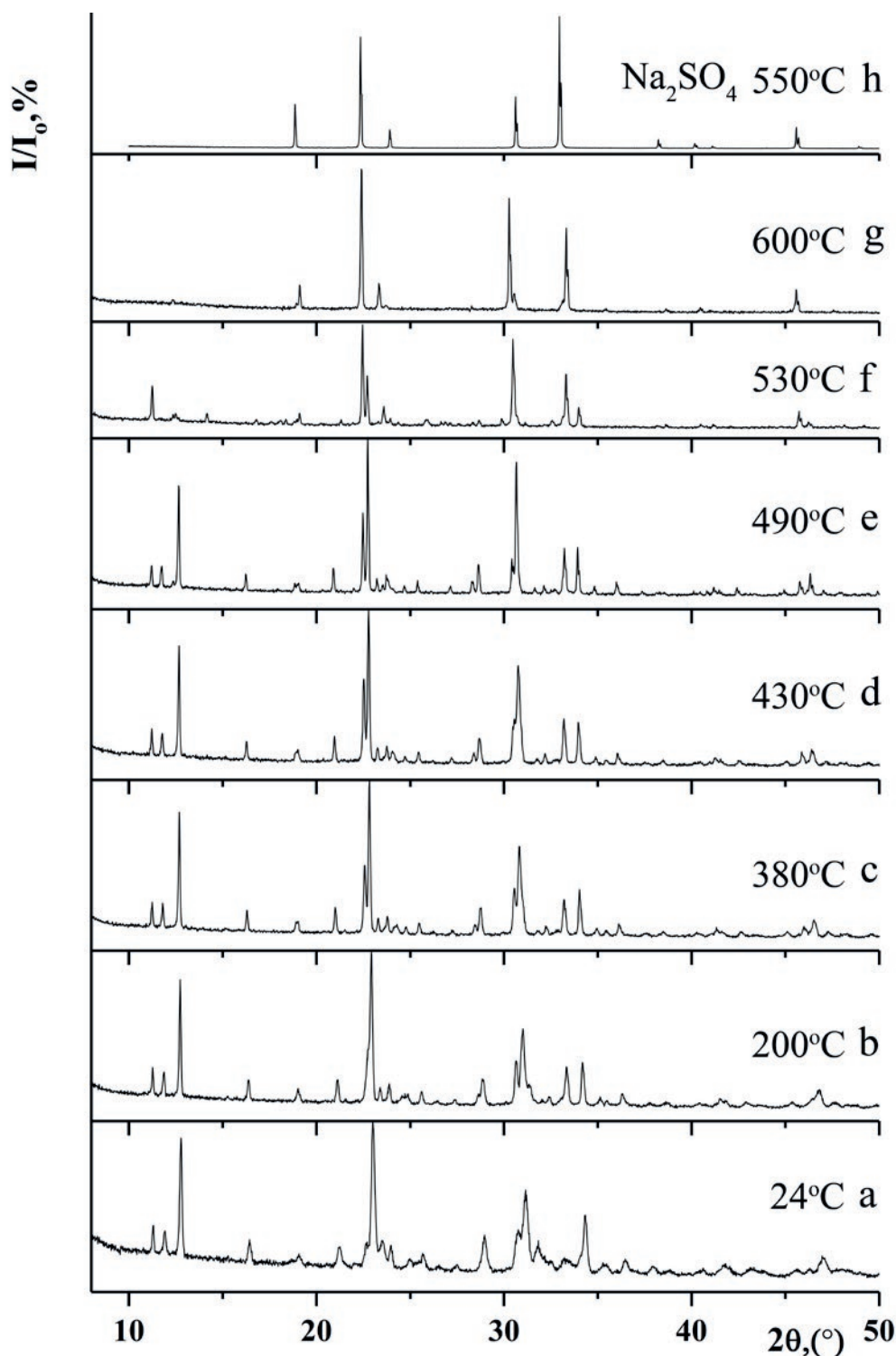


**Fig. 1.** Phase diagram of the system  $\text{Na}_2\text{SO}_4 - \text{In}_2(\text{SO}_4)_3$ . 1 – DTA data; 2 – single-phase samples; 3 – two-phase samples according to XRD data

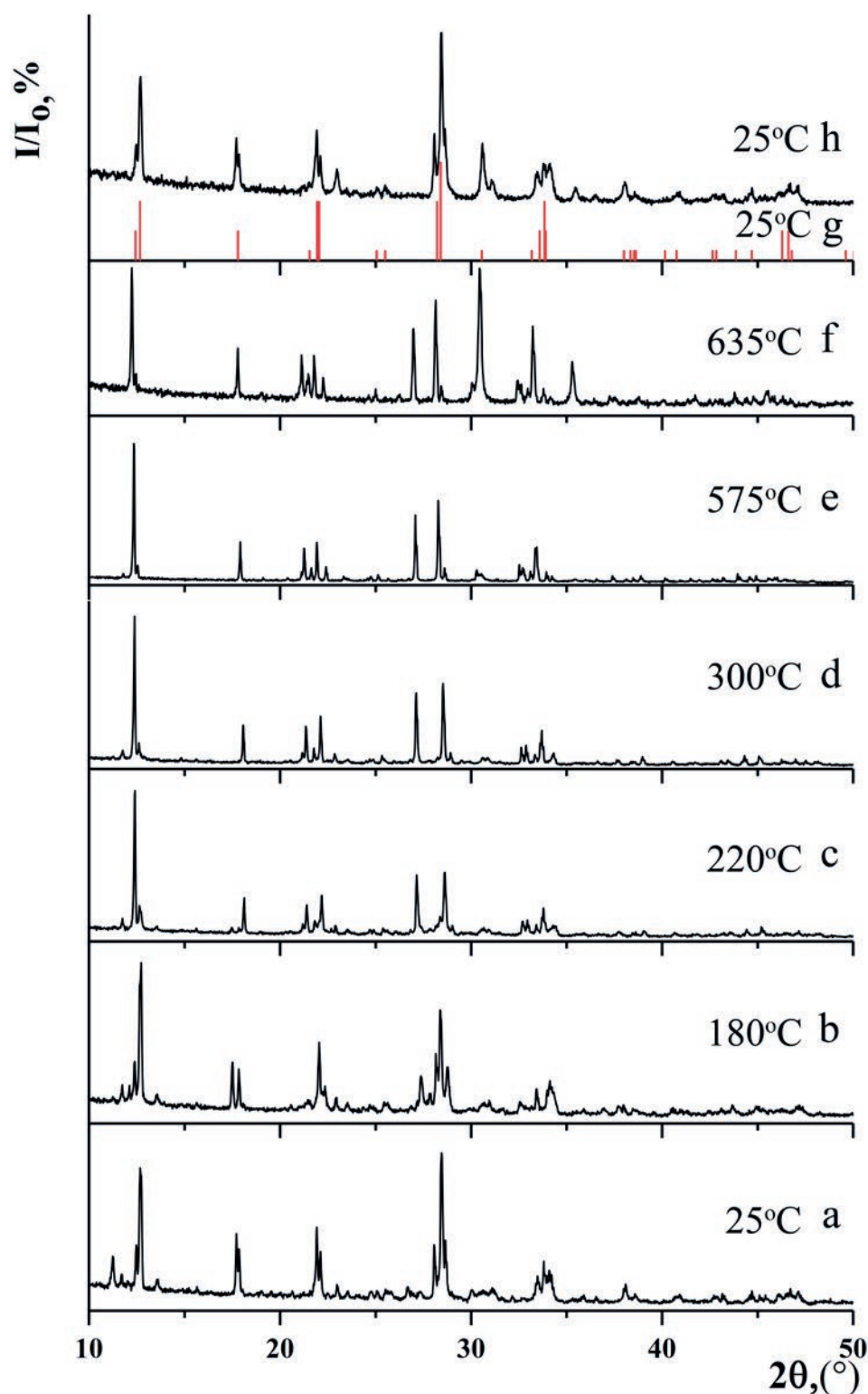
solid solution melting curves show a maximum at 895 °C and 3 mol. %  $\text{In}_2(\text{SO}_4)_3$ .

The  $\text{Na}_3\text{In}(\text{SO}_4)_3$  compound was known [17], while the  $\text{NaInSO}_4$  compound and the  $\phi$ -phase

seem to be described for the first time. X-ray diffraction patterns of the compounds and high-temperature XRD data are presented in Fig. 2, 3 and in the Tables S1-S3 of the electronic application.



**Fig. 2.** High-temperature X-ray phase analysis of the sample 93 %  $\text{Na}_2\text{SO}_4$  - 7 %  $\text{In}_2(\text{SO}_4)_3$ : a – 24 °C; b – 200 °C; c – 380 °C; d – 430 °C; e – 490 °C; f – 530 °C; g – 600 °C; h – 550 °C high-temperature modification of  $\text{Na}_2\text{SO}_4$



**Fig. 3.** High-temperature X-ray phase analysis of a sample of 75 %  $\text{Na}_2\text{SO}_4$  - 25 %  $\text{In}_2(\text{SO}_4)_3$ : a – 25 °C; b – 180 °C; c – 220 °C; d – 300 °C; e – 575 °C; f – 635 °C; g – JCPDS 00-027-1414 ( $\text{Na}_3\text{In}(\text{SO}_4)_3$ ) 25 °C; h – 25 °C

According to XRD data  $\text{NaInSO}_4$  is isostructural to compounds  $\text{NaR}(\text{SO}_4)_4$  ( $\text{R} = \text{Al}, \text{Ga}, \text{V}, \text{Fe}, \text{Rh}, \text{Cr}$ ), the so-called “anhydrous alum” [22-24] (structural type of javapaite –  $\text{KFe}(\text{SO}_4)_2$  [25]), see

Table 1. According to high-temperature XRD, no polymorphic transitions of  $\text{NaInSO}_4$  were recorded up to 300 °C. When heated in air it decomposes starting from 600 °C with  $\text{SO}_2$  emission.



**Table 1.** Lattice parameters of  $\text{NaR}(\text{SO}_4)_2$  compounds, monoclinic space group ( $C2/m$ ),  $Z = 2$  (“anhydrous alum”)

<i>R</i>	<i>a</i> , Å	<i>b</i> , Å	<i>c</i> , Å	$\beta$	Ref.
Al	7.9007	5.003	7.1202	92.87	Our data
Al	7.89	5.10	7.10	92.15	[22]
Ga	7.912	5.095	7.143	92.70	Our data
Ga	7.92	5.10	7.13	92.53	[22]
In	8.024	5.069	7.211	90.60	Our data
Fe	8.02	5.14	7.18	92.20	[22]
Cr	7.956	5.112	7.109	92.20	[22]
V	8.020	5.160	7.135	91.870	[24]
V	8.01	5.16	7.14	91.88	[22]
Rh	7.921	5.127	7.134	92.83	[23]

The low-temperature  $\gamma$ -modification  $\text{Na}_3\text{In}(\text{SO}_4)_3$  is isostructural to the compounds  $\text{Na}_3\text{R}(\text{SO}_4)_3$  ( $R = \text{Al, Ga, V, Fe, Rh}$ ), see Table 2. High-temperature XRD confirmed the polymorphism of  $\text{Na}_3\text{In}(\text{SO}_4)_3$  (Fig. 3). X-ray powder diffraction of the mid-temperature  $\beta$ -modification of  $\text{Na}_3\text{In}(\text{SO}_4)_3$  is indexed in monoclinic space group ( $P21/c$ ) with lattice parameters  $a = 16.187(4)$  Å,  $b = 13.584(3)$  Å,  $c = 9.639(2)$  Å,  $\beta = 91.6^\circ$  (Tab. S2). No analogs were found.

X-ray powder diffraction of the  $\phi$ -phase is indexed in monoclinic space group ( $P21/c$ ) with lattice parameters  $a = 7.836$  Å,  $b = 14.845$  Å,  $c = 4.57$  Å,  $\beta = 91.14^\circ$  (Tab. S3). No analogs were also found. The  $\phi$ -phase on heating changes to a solid solution based on high-temperature modification of sodium sulfate at  $540^\circ\text{C}$ . The transition is captured by both thermography and high-temperature XRD data (Fig. 2).

### 3.1. $\text{Na}_2\text{SO}_4 - \text{R}_2(\text{SO}_4)_3$ systems: a comparative analysis

The compounds  $\text{Na}_3\text{R}(\text{SO}_4)_3$  and  $\text{NaR}\text{SO}_4$  form extended isomorphic series. We synthe-

sized similar compounds with scandium. Crystallographic data are summarized in Tables 1 and 2. Note that the structural types are preserved despite the change of ionic radii of trivalent cations in wide range. The X-ray diffraction patterns of our synthesized compounds in the systems  $\text{Na}_2\text{SO}_4 - \text{R}_2(\text{SO}_4)_3$  ( $R = \text{Al, Ga}$ ) are presented in Fig. 5–7 and in the Tables S4–S7. Previous indexing of X-ray radiographs of  $\text{Na}_3\text{R}(\text{SO}_4)_3$  ( $R = \text{Al, Ga}$ ) in the tetragonal space group was erroneous [15].

There is a great similarity of phase diagrams of  $\text{Na}_2\text{SO}_4 - \text{R}_2(\text{SO}_4)_3$  ( $R = \text{Al, Ga, Fe}$ ) and apparently for systems with vanadium, chromium and rhodium. The phase diagrams of systems with rare-earth element (REE) sulfates look different. Compound with cation ratio 3:1 do not exist, while compound with cation ratio 1:1 have different structure. Indium and apparently scandium are intermediate cases.

Solid solutions based on the high-temperature  $\alpha$ -modification of sodium sulfate revealed in this work are a typical example of heterovalent isomorphism with a variable number of atoms

**Table 2.** Lattice parameters of compounds  $\text{Na}_3\text{R}(\text{SO}_4)_3$ , trigonal space group ( $R\bar{3}$ ),  $Z = 6$ , and ionic radii of  $\text{R}^{3+}$  cations according to Shannon [27], coordination number 6

<i>R</i>	<i>a</i> , Å	<i>c</i> , Å	<i>r</i> , Å	Ref.
Al	13.3516	8.9080	0.535	Our data
Ga	13.413	8.980	0.620	Our data
In ( $\gamma$ )	13.970	8.771	0.800	[17]
In ( $\gamma$ )	13.970	8.871	0.800	Our data
Sc	13.881	8.975	0.870	Our data
Fe	13.415	9.0250	0.69–0.785	JCPDS 39-0243
V	13.43	9.091	0.640	[26]
Rh	13.306	8.604	0.665	[23]

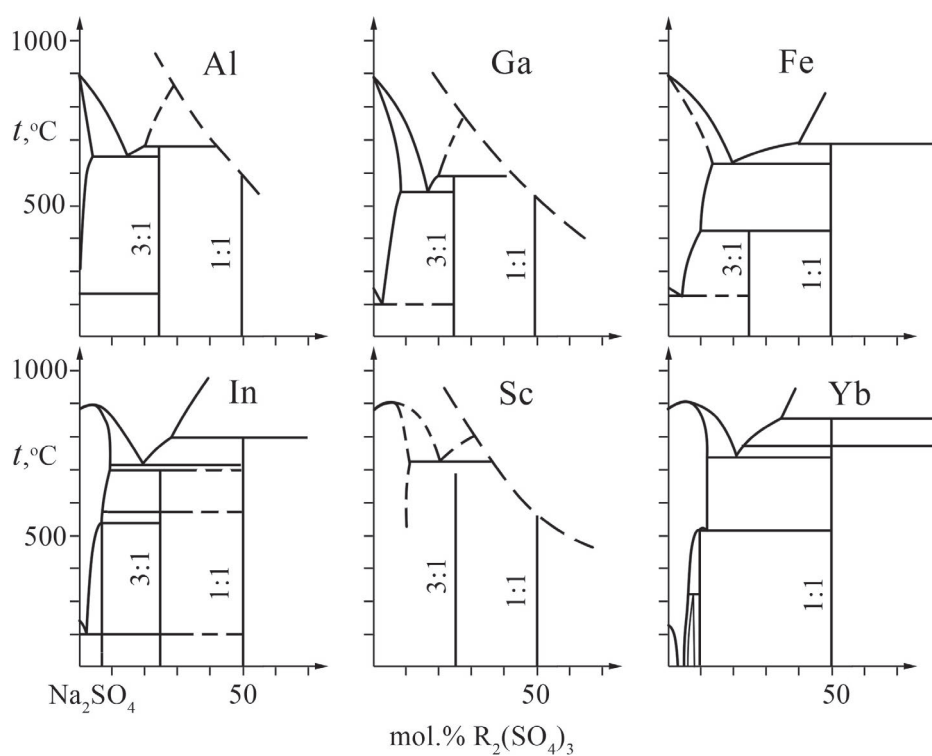


Fig. 4. Scheme of phase equilibria in systems  $\text{Na}_2\text{SO}_4 - \text{R}_2(\text{SO}_4)_3$

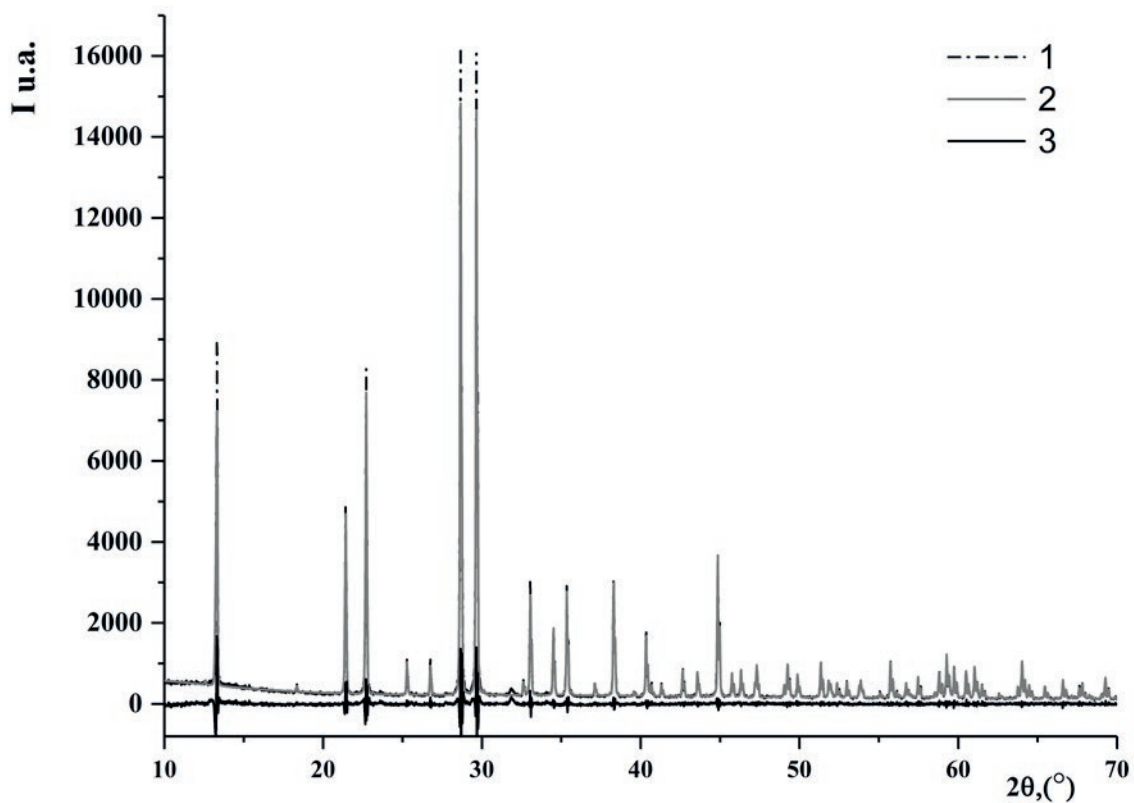
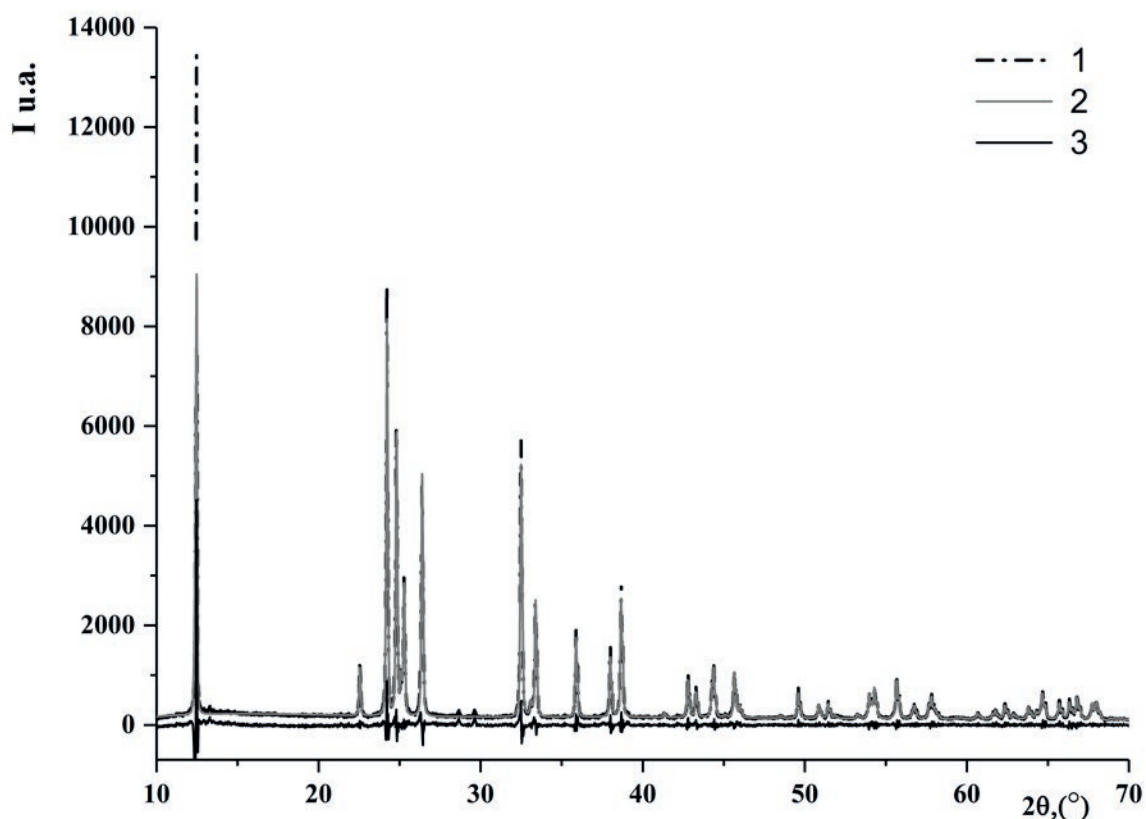
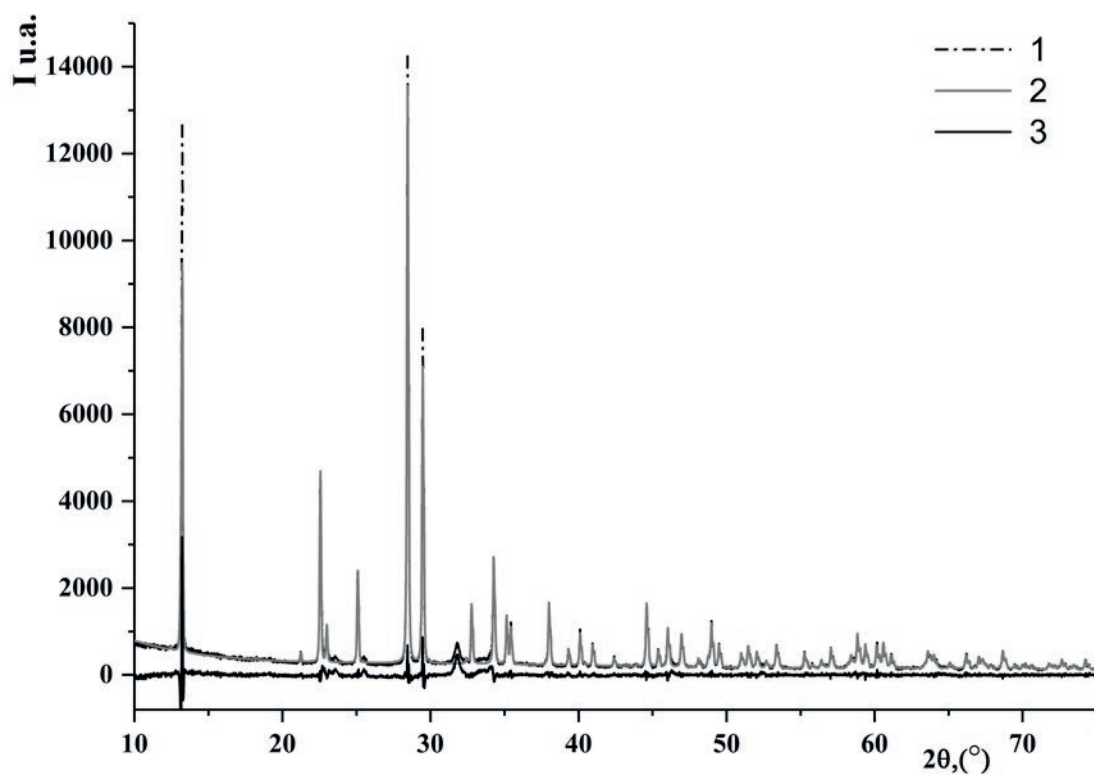


Fig. 5. X-ray diagram of  $\text{Na}_3\text{Al}(\text{SO}_4)_3$ . 1 – experimental X-ray diagram; 2 – calculated X-ray diagram; 3 – difference curve



**Fig. 6.** X-ray diagram of  $\text{NaAl}(\text{SO}_4)_2$ . 1 – experimental X-ray diagram; 2 – calculated X-ray diagram; 3 – difference curve



**Fig. 7.** X-ray diagram  $\text{Na}_3\text{Ga}(\text{SO}_4)_3$ . 1 – experimental X-ray diagram; 2 – calculated X-ray diagram; 3 – difference curve

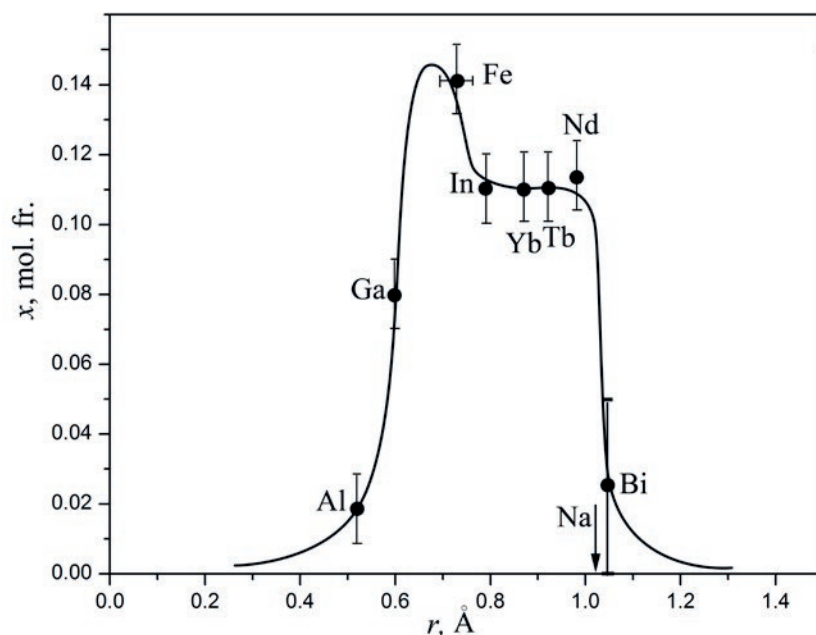


in the unit cell [10, 28]. The formation of such solid solutions involves heterovalent cationic substitutions with the formation of vacancies in the cationic sublattice [6]. The formation of solid solutions of this type correlates with maxima on melting curves [29] and high ionic conductivity of the corresponding materials [10]. In  $\text{Na}_2\text{SO}_4 - \text{R}_2(\text{SO}_4)_3$  systems, in addition to the system with indium sulfate studied in this work, maxima on the melting curves of solid solutions based on  $\text{Na}_2\text{SO}_4$  with  $\text{R}_2(\text{SO}_4)_3$  are formed in systems with  $\text{R} = \text{Nd}, \text{Tb}, \text{Yb}$  [13] and are predicted in the system with scandium sulfate, as well as over the entire lanthanide series.

Fig. 8 shows the dependence of the limiting concentration of solid solutions based on  $\text{Na}_2\text{SO}_4$  with  $\text{R}_2(\text{SO}_4)_3$  on the ionic radius of the trivalent ion for coordination number 6 [27]. For these systems, the coincidence of ionic radii of sodium and isomorphous cations is not an optimal condition for the formation of solid solutions. This is typical for heterovalent solid solutions with a variable number of particles in the unit cell [10]. In the system with bismuth sulfate, where the ionic radii of  $\text{Na}^+$  and  $\text{Bi}^{3+}$  practically coincide, the formation of the corresponding solid solution was not observed at all (the first investigated

point corresponds to the content of 5 mol. %  $\text{Bi}_2(\text{SO}_4)_3$  [16]). It is obvious for  $\text{Na}_2\text{SO}_4 - \text{R}_2(\text{SO}_4)_3$  systems the presence of a two-hump dependence similar to that for solid solutions of divalent metal sulfates in lithium sulfate [30]. Apparently, this character of solubility is associated with the presence of two crystallographic positions in the structure of the high-temperature modification of  $\text{Na}_2\text{SO}_4$ -I [31].

Solid solutions based on high-temperature modification of sodium sulfate are formed in all systems of this group. The thermal effect of the polymorphic transition of sodium sulfate disappears upon addition of gallium sulfate, i.e. stabilization of the structure of hexagonal high-temperature modification of sodium sulfate up to room temperature is observed, which is confirmed by XRD data. The phase diagram of the  $\text{Na}_2\text{SO}_4 - \text{Al}_2(\text{SO}_4)_3$  system [13] is similar to the  $\text{Na}_2\text{SO}_4 - \text{Ga}_2(\text{SO}_4)_3$  system, but the  $\text{Na}_2\text{SO}_4$ -based solid solution region is much smaller (~ 2 mol. % at the eutectic temperature), and the introduction of  $\text{Al}_2(\text{SO}_4)_3$  does not lead to stabilization of the  $\alpha$ - $\text{Na}_2\text{SO}_4$  structure up to room temperature. In the case of indium, the corresponding solid solution is wedged out due to the formation of the  $\phi$ -phase.



**Fig. 8.** Dependence of the limiting concentration of solid solutions based on  $\text{Na}_2\text{SO}_4$  with  $\text{R}_2(\text{SO}_4)_3$  on the ionic radius of the trivalent ion. Data for Al by [11], Ga by [15], Fe by [12], In by this study, Yb, Tb, Nd by [13], Bi by [16]. Ion radii according to [27] for coordination number 6

#### 4. Conclusion

Stabilization to room temperature in the case of REE allowed growing single crystals of stabilized solid solutions doped with neodymium [7] and ytterbium [32]. Solid solution with gallium is the next step.

Indium compounds can be considered as model compounds of corresponding compounds of elements with variable valence (chromium, iron, vanadium) in oxidation degree +3, which can be used as cathode materials in electrochemical devices.

*The online version contains supplementary material*

#### Contribution of the authors

The authors contributed equally to this article.

#### Conflict of interests

The authors declare that they have no known competing financial interests or personal relationships that could have influenced the work reported in this paper.

#### References

- Ivanov-Shchits A. K., Murin I. V. *Solid state ionics*\*. Saint Petersburg: SPbU Publ.; Vol. 1. 2000. Vol. 2. 2010. (In Russ.)
- Yaroslavtsev A. B. Solid electrolytes: main prospects of research and development. *Russian Chemical Reviews*. 2016;85(11): 1255–1276. <https://doi.org/10.1070/rcr4634>
- Skundin A. M., Kulova T. L., Yaroslavtsev A. B. Sodium-ion batteries (a review). *Russian Journal of Electrochemistry*. 2018;54(2): 113–152. <https://doi.org/10.1134/s1023193518020076>
- Heed B., Lunden A., Schroeder K. Sulphate-based solid electrolytes: properties and applications. *Electrochimica Acta*. 1977;22: 705–707. [https://doi.org/10.1016/0013-4686\(77\)80022-4](https://doi.org/10.1016/0013-4686(77)80022-4)
- Lunden A. Enhancement of cation mobility in some sulphate phases due to a paddle wheel mechanism. *Solid State Ionics*. 1998;28-30: 163–167. [https://doi.org/10.1016/s0167-2738\(88\)80026-2](https://doi.org/10.1016/s0167-2738(88)80026-2)
- Eysel W., Hofer H. H., Keester K. L., Hahn Th. Crystal chemistry and structure of  $\text{Na}_2\text{SO}_4(\text{I})$  and its solid solutions. *Acta Crystallographica Section B Structural Science*. 1985;41: 5–11. <https://doi.org/10.1107/s0108768185001501>
- Fedorov P. P., Polkhovskaya T. M., Sobolev B. P., Ivanov-Shits A. K., Sorokin N. I. Growing  $\text{Na}_2\text{SO}_4:\text{Nd}^{3+}$  single crystals and studying its electrical conductivity\*. *Soviet Physics. Crystallography*. 1983;28(3): 598–599. (In Russ.)
- Sorokin N. I., Proydakova V. Yu., Voronov V. V., Kuznetsov S. V., Fedorov P. P. Electrical conductivity of sodium sulfate-based phases. *Inorganic Materials*. 2022;58(8): 806–813. <https://doi.org/10.1134/s0020168522080118>
- Voskresenskaya N. K., Evseeva N. N., Berul S. I., Vereshchetina I. P. *Handbook on the fusibility of systems made of anhydrous inorganic salts*\*. Moscow-Leningrad: USSR Academy of Sciences Publ.; 1961. 846 p. (In Russ.)
- Fedorov P. P. Heterovalent isomorphism and solid solutions with a variable number of ions in the unit cell. *Russian Journal of Inorganic Chemistry*. 2000;45(Suppl. 3): S268–S291. EDN: LGJRLF. Available at: <https://elibrary.ru/lgjrlf>
- Fedorov P. I., Zhang Chi-yuyin. The  $\text{Na}^+, \text{Al}^{3+} // \text{SO}_4^{2-}$  system\*. *Russian Journal of Inorganic Chemistry*. 1966;11(3): 669–671. (In Russ.)
- Bolshakov K. A., Fedorov P. I., Ilyina N. I. Binary systems of sodium sulfate with copper (II) and iron (III) sulfates\*. *Russian Journal of Inorganic Chemistry*. 1963;8(11): 2577–2579. (In Russ.)
- Pokrovsky A. N. *Synthesis, structure and properties of anhydrous double sulfates of lanthanides and elements of group Ia*\*. Dr. chem. sci. diss. Moscow: Moscow State University Publ.; 1981. 327 p. (In Russ.)
- Fedorov P. I., Fedorov P. P. Sodium sulfate - thorium sulfate system. *Russian Journal of Inorganic Chemistry*. 2001;46(9): 1422–1423. Available at: <https://elibrary.ru/item.asp?id=13367703>
- Fedorov P. P., Proydakova V. Yu., Kuznetsov S. V., Voronov V. V. Phase equilibria in systems of gallium sulfate with lithium or sodium sulfate. *Russian Journal of Inorganic Chemistry*. 2017;62(11): 1508–1513. <https://doi.org/10.1134/s0036023617110067>
- Kochubey L. A., Margulis E. V., Vershinina F. I., Vorobyova L. V. The  $\text{Na}_2\text{SO}_4 - \text{Bi}_2(\text{SO}_4)_3$  system\*. *Russian Journal of Inorganic Chemistry*. 1981;26: 2881–2883. (In Russ.)
- Perret R., Tudo J., Jolibois B., Couchot P. Preparation et caracterization cristallographique de quelques sulfates doubles d'indium (III) et de thallium(III),  $\text{M}^{\text{I}}_3\text{M}^{\text{III}}(\text{SO}_4)_3$  ( $\text{M}^{\text{I}} = \text{Na, K, Rb et Cs}$ ). *Journal of the Less Common Metals*. 1974;37(1): 9–12. [https://doi.org/10.1016/0022-5088\(74\)90003-4](https://doi.org/10.1016/0022-5088(74)90003-4)
- Krause M., Gruehn R. Contributions on the thermal behavior of sulphates XVII. Single crystal structure refinements of  $\text{In}_2(\text{SO}_4)_3$  and  $\text{Ga}_2(\text{SO}_4)_3$ . *Zeitschrift für Kristallographie – Crystalline Materials*. 1995;210: 427–431. <https://doi.org/10.1524/zkri.1995.210.6.427>
- Proydakova V. Yu., Kuznetsov S. V., Voronov V. V., Fedorov P. P. Synthesis of gallium sulfate. *Tonkie Khimicheskie Tekhnologii* [Fine Chemical Technologies]. 2017;12(3): 52–57. Available at: <https://elibrary.ru/zbmoyu>
- Fedorov P. I., Fedorov P. P., Drobot D. V. *Physico-chemical analysis of anhydrous salt systems*\*. Moscow: MIHM Publ.; 1987. 90 p. (In Russ.)
- Fedorov P. P., Medvedeva L. V. On thermographic determination of liquidus temperatures\*. *Russian Journal of Inorganic Chemistry*. 1989;34(10): 2674–2677. (In Russ.)
- Perret R., Couchot P. Preparation et caracterisation de quelques “aluns anhydres” de sodium. *Comptes Rendus de Academie des Sciences. Paris*. 1972;C274: 363–369.
- Perret R., Devaux M. Identification cristallographique de quelques composés anhydres du sulfate de rhodium. *Journal of the Less Common Metals*. 1975;42: 43–50. [https://doi.org/10.1016/0022-5088\(75\)90018-1](https://doi.org/10.1016/0022-5088(75)90018-1)
- Ferhmann R., Boghosian S., Papatheodorou G. N., Nielsen K., Berg R.W., Bjerrum N. J. The crystal structure of

$\text{NaV}(\text{SO}_4)_2$ . *Acta Chemica Scandinavica*. 1991;45: 861–964. <https://doi.org/10.3891/acta.chem.scand.45-0961>

25. Graeber E. J., Rozenzweig A. The crystal structure of yavapaiite,  $\text{KFe}(\text{SO}_4)_2$ , and goldichite,  $\text{KFe}(\text{SO}_4)_2 \cdot 4\text{H}_2\text{O}$ . *American Mineralogist*, 1971;56: 1917–1933.

26. Boghosian S., Ferhmann R., Nielsen K., ... Francis G. W. Synthesis and crystal structure of  $\text{Na}_3\text{V}(\text{SO}_4)_3$ . Spectroscopic Characterization of  $\text{Na}_3\text{V}(\text{SO}_4)_3$  and  $\text{NaV}(\text{SO}_4)_2$ . *Acta Chemica Scandinavica*. 1994;48: 724–731. <https://doi.org/10.3891/acta.chem.scand.48-0724>

27. Shannon R. D. Revised effective ionic radii in halides and chalcogenides. *Acta Crystallographica Section A*. 1976;A32: 751–767. <https://doi.org/10.1107/s0567739476001551>

28. Fedorov P. P., Sobolev B. P., Fedorov P. On the influence of ionic radii on the formation of heterovalent solid solutions with a change in the number of atoms in the unit cell. *Soviet Physics. Crystallography*. 1981;26: 291–295.

29. Fedorov P. P., Sobolev B. P. On the conditions of formation of maxima on melting curves of solid solutions in salt systems\*. *Russian Journal of Inorganic Chemistry*. 1979;24(4): 1038–1040. (In Russ.)

30. Fedorov P. P. Concerning the incorporation of divalent cations into the high-temperature modification of  $\text{Li}_2\text{SO}_4$ . *Solid State Ionics* 1996;84: 113–115. [https://doi.org/10.1016/S0167-2738\(96\)83013-X](https://doi.org/10.1016/S0167-2738(96)83013-X)

31. Proydakova V. Yu., Voronov V. V., Pynenkov A. A., ... Fedorov P. P. Sodium sulfate polymorphism. *Russian Journal of Inorganic Chemistry*. 2022;67(7): 970–977. <https://doi.org/10.1134/s0036023622070208>

32. Tsvetkov V. B., Proydakova V. Yu., Kuznetsov S. V., ... Fedorov P. P. Growth of  $\text{Yb} : \text{Na}_2\text{SO}_4$  crystals and study of their spectral – luminescent characteristics. *Quantum Electronics*. 2019;49(11): 1008–1010. <https://doi.org/10.1070/qel17107>

\* Translated by author of the article

## Information about the authors

Vera Yu. Proydakova, Research Fellow, Prokhorov General Physics Institute of the Russian Academy of Sciences (Moscow, Russian Federation).

<https://orcid.org/0000-0001-8017-9175>

[vera.proydakova@gmail.com](mailto:vera.proydakova@gmail.com)

Valery V. Voronov, Cand. Sci. (Phys.–Math.), Leading Researcher, Prokhorov General Physics Institute of the Russian Academy of Sciences (Moscow, Russian Federation).

<https://orcid.org/0000-0001-5029-8560>

[voronov@lst.gpi.ru](mailto:voronov@lst.gpi.ru)

Sergey V. Kuznetsov, Cand. Sci. (Chem.), Head of the Laboratory at the Prokhorov General Physics Institute of the Russian Academy of Science (Moscow, Russian Federation).

<https://orcid.org/0000-0002-7669-1106>

[kouznetzovsv@gmail.com](mailto:kouznetzovsv@gmail.com)

Ivan N. Nekrylov, Department Assistant at the Department of General and Inorganic Chemistry, Voronezh State University (Voronezh, Russian Federation).

<https://orcid.org/0000-0003-4491-4739>

[Icq492164858@gmail.com](mailto:Icq492164858@gmail.com)

Alexander Y. Zavrazhnov, Dr. Sci. (Chem.), Professor at the Department of General and Inorganic Chemistry, Voronezh State University (Voronezh, Russian Federation).

<https://orcid.org/0000-0003-0241-834X>

[alzavr08@rambler.ru](mailto:alzavr08@rambler.ru)

Pavel P. Fedorov, Dr. Sci. (Chem.), Full Professor, Chief Researcher, Prokhorov General Physics Institute of the Russian Academy of Sciences (Moscow, Russian Federation).

<https://orcid.org/0000-0002-2918-3926>

[ppfedorov@yandex.ru](mailto:ppfedorov@yandex.ru)

Received 18.03.2025; approved after reviewing 25.03.2025; accepted for publication 15.04.2025; published online 25.06.2025.



## Original articles

Research article

<https://doi.org/10.17308/kcmf.2025.27/12804>

## Investigation of the transformation of the surface architecture of zinc oxide powders synthesized by grinding during etching with argon ions

I. A. Pronin<sup>1✉</sup>, A. S. Komolov<sup>2</sup>, A. S. Lenshin<sup>3</sup>, N. D. Yakushova<sup>1</sup>, A. A. Karmanov<sup>1</sup>

<sup>1</sup>Penza State University,  
40 Krasnaya st., Penza 440026, Russian Federation

<sup>2</sup>Saint Petersburg State University,  
7-9 Universitetskaya Embankment, Saint Petersburg 199034, Russian Federation

<sup>3</sup>Voronezh State University,  
1 Universitetskaya pl., Voronezh 394018, Russian Federation

### Abstract

**Purpose:** The aim of the work is to study by X-ray photoelectron spectroscopy the transformation of the surface architecture of zinc oxide powders, previously obtained by mechanical milling, during their etching with argon ions.

**Experimental:** The etching was carried out in two steps of 30 s duration each at a current of 1  $\mu$ A. It was found that on the surface of initial powders 45 % of zinc is a part of the crystal lattice of ZnO, and the remaining 55 % exist in the form of hydroxide.

**Conclusions:** The first etching step reduced the fraction of hydroxyl groups on the surface to 1 per 5 zinc cations in the ZnO lattice, and further etching showed the impossibility of deeper purification of the sample from OH-groups. In contrast, the carbon atoms almost completely left the powder surface after the end of the second etching step.

**Keywords:** Zinc oxide, Etching, X-ray photoelectron spectroscopy, Surface

**Funding:** The research was supported by the Russian Science Foundation grant No. 23-29-00844, <https://rscf.ru/project/23-29-00844/>.

**Acknowledgements:** The measurements were partially conducted using the equipment of the Research Park of St. Petersburg State University "Centre for Physical methods of surface investigation".

**For citation:** Pronin I. A., Komolov A. S., Lenshin A. S., Yakushova N. D., Karmanov A. A. Investigation of the transformation of the surface architecture of zinc oxide powders synthesized by grinding during etching with argon ions. *Condensed Matter and Interphases*. 2025;27(2): 278–283. <https://doi.org/10.17308/kcmf.2025.27/12804>

**Для цитирования:** Пронин И. А., Комолов А. С., Леншин А. С., Якушова Н. Д., Карманов А. А. Исследование трансформации поверхностной архитектуры синтезированных размолом порошков оксида цинка при травлении ионами аргона. *Конденсированные среды и межфазные границы*. 2025;27(2): 278–283. <https://doi.org/10.17308/kcmf.2025.27/12804>

✉ Igor A. Pronin, e-mail: [pronin\\_i90@mail.ru](mailto:pronin_i90@mail.ru)

© Pronin I. A., Komolov A. S., Lenshin A. S., Yakushova N. D., Karmanov A. A., 2025



The content is available under Creative Commons Attribution 4.0 License.



## 1. Introduction

Semiconducting metal oxides are materials with applications in gas sensing, catalysis and photocatalysis, transparent conductive coatings, etc. Often the useful properties of this group of materials are determined by their surface condition [1–3]. For example, the sensitivity of tin dioxide to ethanol can be regulated by the ratio of surface Lewisian and Brönsted centers [4]. The efficiency of photocatalysts depends both on the rate of surface recombination of photogenerated charge carriers and on the ability of the semiconductor surface to adsorb water, carbon dioxide, and oxygen particles. In this regard, the study of surface architecture is of great interest. However, the peculiarity of this group of materials is the intensive interaction of the environment with their surface, which complicates the research process without additional sample preparation. In X-ray photoelectron spectroscopy (XPS), Ion etching is usually used as a pre-treatment. The aim of the present work is to investigate the transformation of the surface architecture of zinc oxide by XPS method during argon ion etching. The object of the study was zinc oxide powder, obtained on the basis of commercial (LLC “Vekton”, St. Petersburg, Russia) by grinding in an attritor for 5 h in isopropyl alcohol (grinding process parameters: grinding media material – zirconium dioxide; grinding media diameter – 3 mm; grinding media mass ratio to ZnO mass – 18:1; grinding speed – 400 rpm) [5].

## 2. Experimental

The surface structure of the samples was investigated using a Scanning electron microscope VEGA 3 SBH (TESCAN, Czech Republic) with a reflected electron detector. Crystal structure was determined by Powder diffraction on an automatic X-ray diffractometer DRON-3M (CJSC “Burevestnik”, Russia) with  $\text{CoK}\alpha$ -radiation in the range of  $35^\circ < 2\theta < 85^\circ$ . X-ray photoelectron spectra were measured under ultrahigh vacuum conditions ( $10^{-7}$  Pa) using an Escalab 250Xi spectrometer (Thermo Fisher Scientific Inc., USA) with photon energy  $\text{Al-K}\alpha = 1,486$  eV. The energy scale of the spectrometer was calibrated using the sputter-cleaned Au surface as a reference, so that the binding energy of the Au  $4f_{7/2}$  peak was

set at 84.0 eV. The etching of the sample surface with argon  $\text{Ar}^+$  ions took place at a current of 1  $\mu\text{A}$  for 30 s (mode 1) and 60 s (mode 2), respectively.

## 3. Results and discussion

Fig. 1 shows the diffractogram of the initial sample and a micrograph of its surface.

It can be seen that the ZnO powder is represented by crystallites with a large size variation in the range of 50 nm – 1  $\mu\text{m}$ . Analysis of the diffractogram shows the presence of reflexes (100), (002), (101), (102), (110), (103), (200), (112) and (201) corresponding to the crystal structure of wurtzite [6], other phases were found in the sample. A joint calculation of the sizes of the coherent scattering regions [7] and microstrains of the sample showed that the average crystallite size is ~ 21 nm at strains of ~ 0.575 %, indicating that the material is in a sufficiently stressed state, and the crystallites visualized by scanning electron microscopy are organized from a large number of single crystals.

Fig. 2 presents an overview X-ray photoelectron spectrum of the original zinc oxide sample, indicating the presence of elements corresponding both to the chemical composition of the material (Zn and O) and resulting from contamination of its surface with organic components (C). Low-energy components of the spectrum corresponding to the Valence band ( $\text{Zn}3d$ ,  $\text{Zn}3p$ ,  $\text{Zn}3s$ ), high-energy components of core levels ( $\text{Zn}2p_{3/2}$  and  $\text{Zn}2p_{1/2}$ ), and Auger peaks such as the Zn LMM are reliably identified.

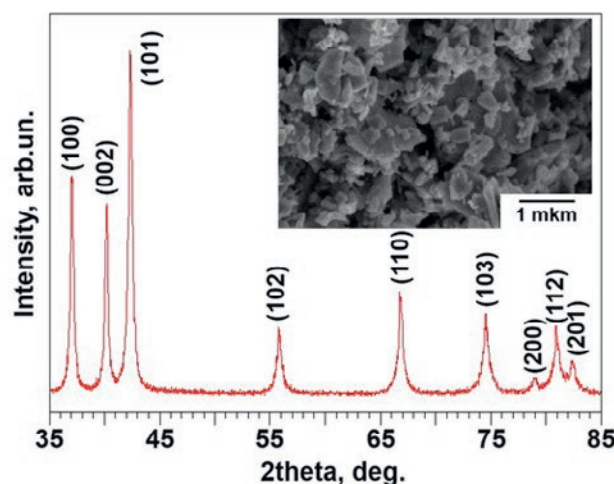
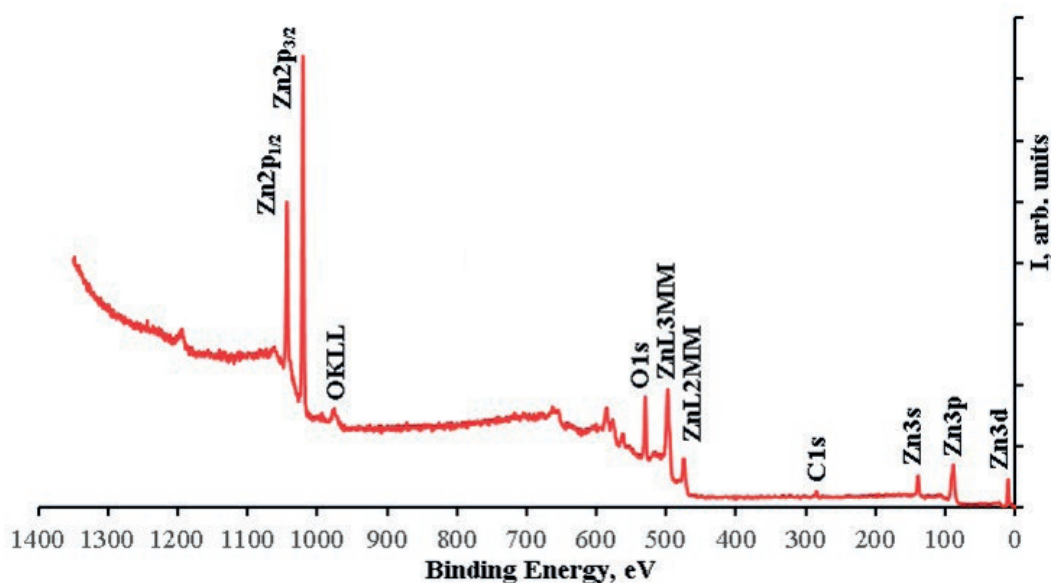


Fig. 1. X-ray diffraction pattern of a sample of zinc oxide powder and micrograph of its surface



**Fig. 2.** Survey X-ray photoelectron spectrum of zinc oxide before argon ion etching

The individual components of the X-ray photoelectron spectra of the original and the sample treated in both modes are shown in Fig. 3, and the Table 1 gives the chemical composition. Consider the characteristics of the initial powder (*curve 1* of Fig. 3). The Zn2p spectrum is represented by a duplet with *BE* binding energies of 1021.08 eV (Zn2p<sub>3/2</sub>) and 1044.50 eV (Zn2p<sub>1/2</sub>). We will use Zn2p<sub>3/2</sub> for further analysis. This curve has a symmetrical appearance and, as a rule, the value of binding energy allows us to attribute it to the zinc cation Zn<sup>2+</sup> in the crystal lattice ZnO. Nevertheless, practice shows that at the same *BE* values it is possible to identify the zinc cation in the Zn(OH)<sub>2</sub> hydroxide molecule, so it is not possible to reliably distinguish between zinc oxide and hydroxide by the XPS method [8]. The spectrum of O1s, on the contrary, is asymmetric and two shapes can be distinguished in it: O(*lat*) with a binding energy of 529.9 eV (corresponding to the oxygen anion O<sup>2-</sup> in the ZnO crystal lattice) and O(*ads*) with a binding energy of 531.30 eV (corresponding to oxygen in molecules adsorbed on the surface: OH-groups, CO<sub>2</sub>, etc.) [9]. The C1s spectrum is also asymmetric

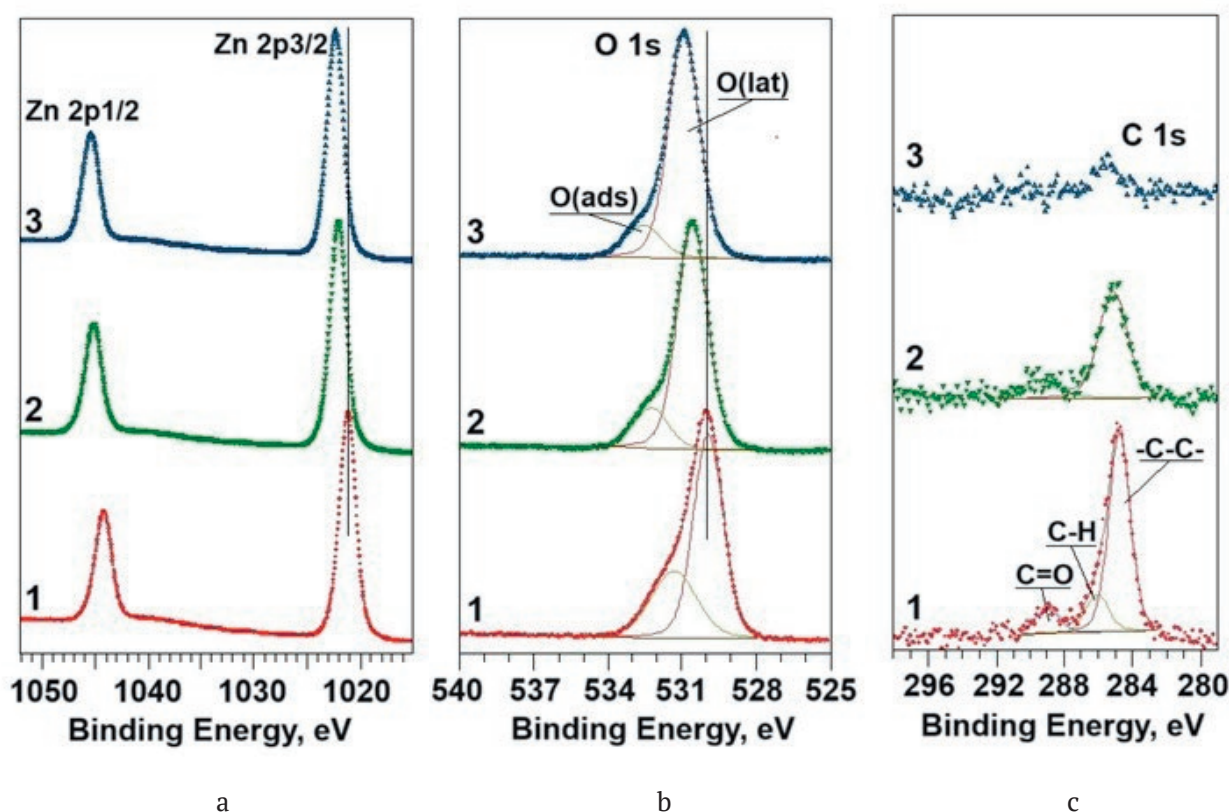
and can be decomposed into three components with Binding energies of 285.00, 286.20, and 289.00 eV: the first corresponds to -C-C- bonds in the graphite structure (which is the Control point of the spectrum); the second corresponds to surface C-H groups; and the third corresponds to C=O groups formed on the powder surface due to chemical adsorption of atmospheric carbon dioxide [10].

Since the atomic fractions of [Zn] and [O(*lat*)] in the original sample are not equal to each other, then, based on the ratio in [Zn(*lat*)] = [O(*lat*)] in zinc oxide, it can be assumed that part of the zinc atoms in the sample does not occupy a position in the crystal lattice, but is probably in the hydroxylated state in the form of Zn(OH)<sub>2</sub>. The calculation shows that only 45% of zinc cations on the unetchable surface can be attributed to ZnO – Table 2.

Let us consider the processes occurring on the sample surface during its etching by argon ions. The Zn(*lat*)/Zn ratio increases in the first etching step from 0.45 to 0.55, with the second step no longer having any effect on the fraction of zinc atoms included in the oxide. Apparently,

**Table 1.** Chemical composition of the surface according to XPS data

Sample	Zn, at. %	O, at. %	C, at. %	O( <i>lat</i> ), at. %	O( <i>ads</i> ), at. %
0	54.00	36.08	9.92	24.08	12.00
1	57.68	38.09	4.23	31.66	6.43
2	60.08	37.44	2.49	32.26	5.18



**Fig. 3.** XPS spectra of Zn2p (a), O1s (b) and C1s (c) (curve 1 – initial sample; curve 2 – etching in mode 1; curve 3 – etching in mode 2)

**Table 2.** Ratios of surface forms according to XPS data

Sample	Zn(lat)/Zn	Zn(lat)/O(ads)	Zn(lat)/C	Zn(lat)/(O(ads)+C)	BE Zn2p3/2, eV
0	0.45	2.03	2.45	1.11	1021.08
1	0.55	4.93	7.50	2.98	1022.08
2	0.54	6.26	13.03	4.23	1022.33

this is primarily due to the desorption of surface hydroxyl groups, which is completed already at the first etching stage, and the second stage practically does not affect this process. The Zn(lat)/O(ads) ratio shows that, if on the initial sample on average 1 oxygen atom in the composition of adsorbed particles corresponded to 2 Zn<sup>2+</sup> cations in the ZnO lattice, then after the first etching step it was already five, and after the second – a little more than six. Together with the fact that the values of Zn(lat)/Zn after the first and second etching steps are almost the same, this indicates that not all O(ads) particles are bound directly to zinc cations in the form of hydroxyl groups. There are other surface forms which, judging from the chemical composition of the sample, contain carbon.

Consider the transformation of the Zn(lat)/C ratio during the etching process. In the original sample, on average, one carbon atom accounts for 2.45 zinc cations; the first etching step increases this number to 7.5 and the second to ~13. This shows that during two etching steps it is possible to remove almost completely carbon from the sample surface both in the form of residues of organic molecules and carbonate-like forms and in the form of graphite. Also the Table 2 shows the ratio Zn(lat)/(O(ads)+C), which characterizes the number of adsorbed particles per Zn<sup>2+</sup> cation in the ZnO lattice. Before etching, Zn(lat) ≈ (O(ads)+C), indicating that the powder surface is heavily contaminated. The first treatment step with argon ions reduced the amount of impurities on the surface to one particle per three



Zn<sup>2+</sup> cations, while the second step reduced the amount of impurities to 4.23.

The increase in the binding energy of Zn2p<sub>3/2</sub> during etching should also be noted (Table. 2). This process is accompanied by an increase in the binding energy of O1s by about the same values, while the binding energy of C1s does not change. This indicates a change in the effective oxidation degree of the zinc cation and a change in the ratio of Zn and O ions occupying regular positions in the nodes of the oxide crystal lattice. This indicates the removal process from the Zn(lat) surface and the formation of vacancies in the zinc V<sub>Zn</sub> sublattice [11]. In connection with this process, the argon ion beam energy corresponding to a current of 1 μA was chosen: at a higher value, not only the adsorbed particles are discharged, but also the surface structure of crystallites is destroyed; a lower value does not allow effective removal of surface hydroxyl groups. Processing times of 30 and 60 s were chosen as typical times, clearly demonstrating the physicochemical processes occurring on the surface.

#### 4. Conclusions

The transformation of surface groups of zinc oxide powders, previously obtained by mechanical milling, during etching with argon ions has been studied by the XPS method. The powders had a wurtzite crystal structure with an average size of coherent scattering regions ~ 20 nm. It was found that on the surface of the original sample only 45 % of zinc atoms were included in the crystal lattice of ZnO, the rest existed in the form of hydroxide. The first etching step increased the proportion of zinc atoms in the oxide lattice to 55 %, but the second step did not change this ratio. Detailed analysis showed that for powder there is a limiting ratio of one hydroxyl group per 5–6 zinc cations in the crystal lattice, and deeper purification from OH-groups by increasing the etching time is difficult. On the contrary, carbon atoms (existing both in the form of graphite and in the composition of organic molecules) and oxygen particles included in the residues of organic groups in combination with carbon are almost completely removed from the surface: after two etching steps, there was only 1 C atom per 13 zinc cations.

#### Contribution of the authors

The authors contributed equally to this article.

#### Conflict of interests

The authors declare that they have no known competing financial interests or personal relationships that could have influenced the work reported in this paper.

#### References

1. Dutta T., Noushin T., Tabassum S., Mishra S. K. Road map of semiconductor metal-oxide-based sensors: a review. *Sensors*. 2023;23(15): 6849. <https://doi.org/10.3390/s23156849>
2. Zaki R. S. R. M., Jusoh R., Chanakaewsomboon I., Setiabudi H. D. Recent advances in metal oxide photocatalysts for photocatalytic degradation of organic pollutants: a review on photocatalysts modification strategies. *Materials Today: Proceedings*. 2023;107: 59–67. <https://doi.org/10.1016/j.matpr.2023.07.102>
3. Lu B., Zhuge F., Zhao Y., ... Lu J. Amorphous oxide semiconductors: from fundamental properties to practical applications. *Current Opinion in Solid State and Materials Science*. 2023;27(4): 101092. <https://doi.org/10.1016/j.cossms.2023.101092>
4. Averin I. A., Pronin I. A., Moshnikov V. A., ... Kuznecova M. V. Analysis catalytic and adsorption properties of d-modifier metal tin dioxide. *Nano- and Mikrosystems Technology*. 2014; 168(7): 47–51. (In Russ., abstract in Eng.). Available at: <https://elibrary.ru/item.asp?edn=sighhn>
5. Pronin I. A., Yakushova N. D., Karmanov A. A., ... Moshnikov V. A. Evolution of acid–base properties of the surface of zinc oxide powders obtained by the method of grinding in an attritor. *Glass Physics and Chemistry*. 2018; 5(44): 464–473. <https://doi.org/10.1134/S1087659618050140>
6. Van Heerden J. L., Swanepoel R. XRD analysis of ZnO thin films prepared by spray pyrolysis. *Thin Solid Films*. 1997;1-2(299): 72–77. [https://doi.org/10.1016/S0040-6090\(96\)09281-4](https://doi.org/10.1016/S0040-6090(96)09281-4)
7. Holzwarth U., Gibson N. The Scherrer equation versus the 'Debye-Scherrer equation'. *Nature Nanotechnology*. 2011;9(6): 534–534. <https://doi.org/10.1038/nnano.2011.145>
8. Marrani A. G., Caprioli F., Boccia A., Zanoni R., Decker F. Electrochemically deposited ZnO films: an XPS study on the evolution of their surface hydroxide and defect composition upon thermal annealing. *Journal of Solid State Electrochemistry*. 2014;18: 505–513. <https://doi.org/10.1007/s10008-013-2281-2>
9. Das J., Pradhan S. K., Sahu D. R., ... Roul B. K. Micro-Raman and XPS studies of pure ZnO ceramics. *Physica B: Condensed Matter*. 2010;10(405): 2492–2497. <https://doi.org/10.1016/j.physb.2010.03.020>
10. Au C. T., Hirsch W., Hirschwald W. Adsorption and interaction of carbon dioxide, formic acid and hydrogen/carbon dioxide mixtures on (1010) zinc oxide surfaces studied by photoelectron spectroscopy (XPS and UPS). *Surface Science*. 1988;3(199): 507–517. [https://doi.org/10.1016/0039-6028\(88\)90918-1](https://doi.org/10.1016/0039-6028(88)90918-1)



11. Pronin I. A., Averin I. A., Karmanov A. A., ... Korotcenkov G. Control over the surface properties of zinc oxide powders via combining mechanical, electron beam, and thermal processing. *Nanomaterials*. 2022;11(12): 1924. <https://doi.org/10.3390/nano12111924>

### Information about the authors

*Igor A. Pronin*, Dr. Sci. (Tech.), Associate Professor, Head of the Department of Nano- and Microelectronics, Penza State University (Penza, Russian Federation).

<https://orcid.org/0000-0003-3037-3601>

[pronin\\_i90@mail.ru](mailto:pronin_i90@mail.ru)

*Aleksey S. Komolov*, Dr. Sci. (Phys.–Math.), Professor, Department of Solid State Electronics, Saint Petersburg State University (Saint Petersburg, Russian Federation).

<https://orcid.org/0000-0003-2942-9823>

[akomolov07@ya.ru](mailto:akomolov07@ya.ru)

*Alexander S. Lenshin*, Dr. Sci. (Phys.–Math.), Senior Researcher, Department of Solid State Physics and Nanostructures, Voronezh State University (Voronezh, Russian Federation).

<https://orcid.org/0000-0002-1939-253X>

[lenshinas@phys.vsu.ru](mailto:lenshinas@phys.vsu.ru)

*Nadezhda D. Yakushova*, Cand. Sci. (Tech.), Associate Professor, Department of Nano- and Microelectronics, Penza State University (Penza, Russian Federation).

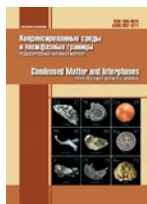
<https://orcid.org/0000-0002-0358-7818>

[yand93@mail.ru](mailto:yand93@mail.ru)

*Andrey A. Karmanov*, Cand. Sci. (Phys.–Math.), Associate Professor, Department of Nano- and Microelectronics, Penza State University (Penza, Russian Federation).

<https://orcid.org/0000-0001-8318-8149>

*Received 02.09.2024; approved after reviewing 30.09.2024; accepted for publication 15.10.2024; published online 25.06.2025.*



## Original articles

Research article

<https://doi.org/10.17308/kcmf.2025.27/12809>

## Analysis of anisotropic heat and thermal diffusivity of thermally expanded graphite

D. A. Prokhorov<sup>1,2✉</sup>, M. G. Rybin<sup>3</sup>, S. M. Zuev<sup>1,2</sup>

<sup>1</sup>MIREA - Russian Technological University,  
78 Vernadsky av., Moscow 119454, Russian Federation

<sup>2</sup>SSC RF FSUE NAMI - State Scientific Center of the Russian Federation Federal State Unitary Enterprise Central Scientific Research Automobile and Automotive Engines Institute,  
2 Avtomotornaya st., Moscow 125438, Russian Federation

<sup>3</sup>RUSGRAFEN LLC,  
15 Biologov av., Moscow Region, Serpukhov urban district, Obolensk settlement 142279, Russian Federation

### Abstract

**Purpose:** This paper aims to look into the anisotropic thermal diffusivity of thermally expanded graphite (TEG) foil using flash method. Its structure is compared with graphene oxide (GO) multilayer foil. Morphology, diffractogram and surface profilometry of TEG and GO produced by two different manufacturing processes are demonstrated. TEG was made of intercalated graphite by thermolysis, and GO was made by microwave-assisted graphite oxide peeling (MEGO).

**Experimental:** The paper studies temperature distribution in the TEG sample as a result of continuous exposure to laser radiation and compares it to those of copper and aluminum samples.

**Conclusions:** It also provides a perspective on possible application of TEG in heat transfer.

**Keywords:** Two-dimensional allotropic modification of carbon, Graphene, Thermally expanded graphite, Anisotropy, Cooling

**For citation:** Prokhorov D. A., Rybin M. G., Zuev S. M. Analysis of anisotropic heat and thermal diffusivity of thermally expanded graphite. *Condensed Matter and Interphases*. 2025;27(2): 284–292. <https://doi.org/10.17308/kcmf.2025.27/12809>

**Для цитирования:** Прохоров Д. А., Рыбин М. Г., Зуев С. М. К анализу анизотропной тепло- и температуропроводности терморасширенного графита. *Конденсированные среды и межфазные границы*. 2025;27(2): 284–292. <https://doi.org/10.17308/kcmf.2025.27/12809>

✉ Dmitry A. Prokhorov, e-mail: [prohorovdmitrii97@yandex.ru](mailto:prohorovdmitrii97@yandex.ru)  
© Prokhorov D. A., Rybin M. G., Zuev S. M., 2025



The content is available under Creative Commons Attribution 4.0 License.

## 1. Introduction

The aim of this research is to measure the anisotropic physical properties of TEG, in particular thermal and thermal diffusivity, and its practical application. The obtained structure of TEG is compared with that of GO, also studied in the frame of this research. Jackie Renteria et al. [1] carried out orthotropy studies on GO and found a significant difference in GO thermal conductivity values of 61 W/m·K in the in-plane direction and 0.09 in the perpendicular (vertical) direction. Further reduction of the oxygen content in GO by high-temperature treatment up to a temperature of plus 1000 °C in theoretical calculations leads to a value of the thermal conductivity coefficient of about 500 W/m·K. Graphene is superior in its thermophysical properties to metals such as copper and aluminum which ensures its applicability in heat dissipation devices like air and liquid cooling radiators.

Mass production of GO is currently carried out by chemical methods such as vapor deposition and subsequent deposition of graphene on the substrate, oxidation of graphite and subsequent reduction from graphene oxide in liquid, application of surfactants (surfactants) in graphite layering, etc. The GO under study was produced by *GRAFENOX LLC* using the modified Hummers' method. [2] The thickness of the GO is about 10 µm.

Mass production of TEG was carried out by *Silur LLC* from intercalated graphite by thermolysis. Natural, clearly crystalline (coarsely flaked) graphite was used as a starting material whose interlayer space was filled with sulfite ions (intercalants) in the presence of sulfuric acid  $H_2SO_4$ . Then the oxidized graphite was heated at a heating rate of at least 600 C°/s to release gaseous decomposition products of  $H_2SO_4$ . During the thermal expansion of the intercalated graphite, there was an increase in the size of graphite crystallites along one direction by more than 300 times. The obtained TEG was rolled into thin films with anisotropy maintenance to thicknesses of 0.3 and 1.5 mm.

The paper also provides a comparison of the side surface morphology of the TEG and GO, in contrast to the work of Teddy Tite et al. [3], where the morphology of graphene nanoplates of 1 to 20 nm frontal surface only was considered which

does not determine the quality of the overlapping graphene layers.

TEG and GO side surface roughness measurements were performed by optical profilometry. Thermal diffusivity was measured by flash method, which measures the temperature increase of the sample as a function of time using a cadmium-mercury-tellurium (MCT) infrared detector.

To obtain diffractograms, the X-ray diffractometric method was used with the same imaging conditions and slits, a Soller slit was installed both on the X-ray tube side and on the detector side.

Practical studies were carried out based on the results of reaching the maximum temperature in copper and aluminum samples, as well as the sample formed after pressing TEG layers. Throughout the experiment, the temperature change of the samples achieved by laser irradiation was continuously recorded by a thermal imager.

It is well known that ultrahigh pressures affect the interatomic distances in the graphene crystal lattice. The relationship between the Grüneisen parameter and thermal conductivity is described by the Leibfried–Schleman formula (1):

$$\chi = \frac{3}{10\pi^3} \frac{k_B^3 M a \theta_D^3}{h^3 \gamma^2 T} \quad (1)$$

where  $\chi$  is the heat transfer coefficient (W/m K),  $\theta_D$  is Debye temperature (K),  $k_B$  is the Boltzmann constant ( $1.381 \cdot 10^{-23}$  J/K),  $M$  is the molecular weight (kg),  $h$  is the Planck's constant ( $6.626 \cdot 10^{-34}$  J/s),  $a$  is the lattice parameter (m),  $T$  – temperature (K),  $\gamma$  – the Grüneisen parameter.

However, it should be noted that the Grüneisen parameter is more appropriately perceived as a combination of acoustic  $\gamma_{ac}$ , elastic  $\gamma_{el}$ , and thermodynamic  $\gamma_{tg}$  factors whose values together give a difference in the readings from 10 to 15 %. Numerical values for these parameters are given in V. N. Belomestnykh et al. paper [4] and are available for calculation by formulas (2–4):

$$\gamma_{ac} = \frac{9}{2} \frac{x^2 - \frac{4}{3}}{x^2 + 2}, \quad (2)$$

where  $\gamma_{ac}$  is Grüneisen acoustic parameter,  $x$  is the parameter characterizing the ratio of propagation

velocity of longitudinal elastic waves to transverse waves.

$$\gamma_{el} = \frac{3}{2} \frac{1+\sigma}{2-3\sigma}, \quad (3)$$

where  $\gamma_{el}$  is the elastic Grüneisen parameter,  $\sigma$  is the Poisson's ratio.

$$\gamma_{tg} = \frac{\alpha V}{\beta_{tg} C_V}, \quad (4)$$

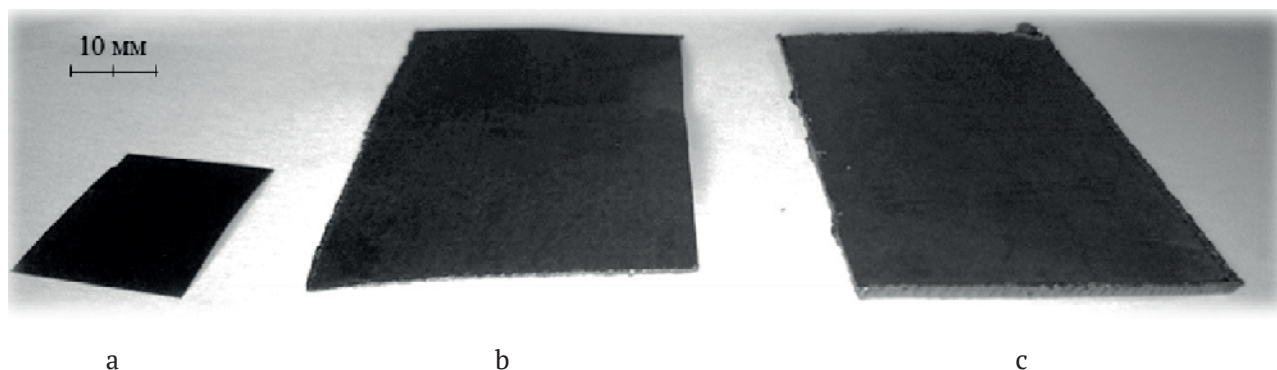
where  $\gamma_{tg}$  is the Grüneisen thermodynamic parameter,  $\alpha$  is the thermal expansion coefficient (1/K),  $\beta_{tg}$  is the volumetric compressibility (1/Pa),  $C_V$  is the specific heat capacity at constant volume (J/K).

In the course of pressing polycrystalline graphene made by chemical reduction of graphite oxide [5], it was found that without taking into account its anisotropic properties, the thermal conductivity coefficient is about 59 W/m K at the pressing pressure up to 44 MPa. Macroscopically, anisotropy is most clearly manifested in single crystals, but can also be observed in polycrystals, for example, the most stable for boron nitride

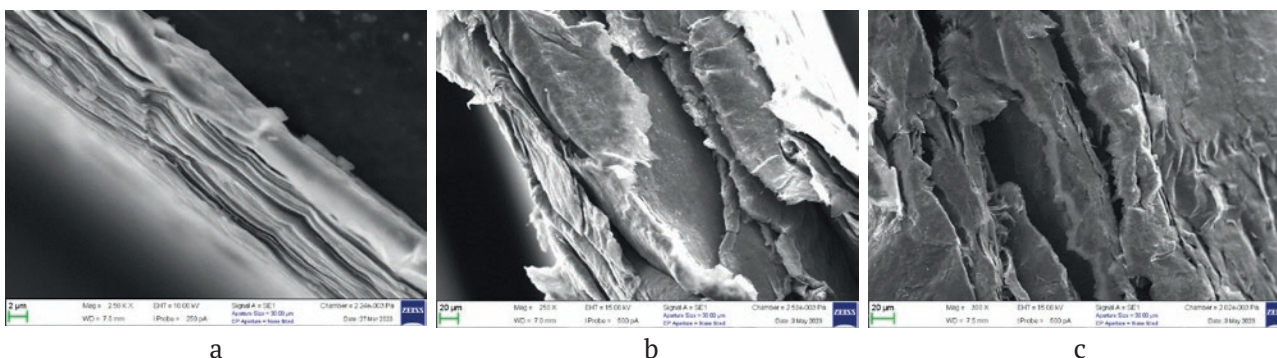
hexagonal crystal lattice (h-BN) has a layered structure with anisotropic thermal conductivity that ranges from 200 to 500 W/m K in the in-plane direction [6] and up to 30 W/m K in the out-of-plane direction [7].

The cross-sectional plane images of the TEG and GO samples shown in Fig. 1 were made by scanning electron microscopy using an AURIGA CrossBeam scanning electron microscope. As can be seen from Fig. 2, the GO sample has a more oriented arrangement of layers which facilitates the study of its anisotropic properties. However, as the sample thickness equals just about 10  $\mu$ m, it is not possible to measure the thermal diffusivity with the flash method, at least with the LFA 467 HyperFlash analyzer. For this reason, further thermal diffusivity measurements including anisotropy were performed for the TEG sample.

For TEG, the thermal diffusivity measurement in the in-plane direction was performed by the flash method on an LFA 467 HyperFlash analyzer at various temperatures. In contrast to the hot guard zone (GHP), heat plates (HFM) or thermally stimulated current (TCT) methods,



**Fig. 1.** TEG and GO samples: a – GO approx. 10  $\mu$ m thick; b – TEG approx. 0.3 mm thick; c – TEG approx. 1.5 mm thick



**Fig. 2.** Lateral surface morphology of TEG and GO samples: a – GO approx. 10  $\mu$ m thick; b – TEG approx. 0.3 mm thick; c – TEG approx. 1.5 mm thick



the flash method (LFA) allows the most accurate measurement of thermal diffusivity of the sample in the range of highest values.

Surface roughness of the samples in the cross-sectional plane was determined by arithmetic mean of absolute values of surface deviations from the reference plane  $Ra$ , RMS value of surface heights (RMS)  $Rq$ , average maximum profile height (average of ten maximums and ten minimums of the surface)  $Rz$  and maximum surface height (distance between maximum and minimum of the surface)  $Rt$ . Surface roughness was created and visualized by optical profilometer WYKO NT 1100 by the non-contact method of optical profilometry.

The diffractograms of the studied samples with a step of 1.2 angular minutes presented in Fig. 3 were obtained by X-ray diffractometric method using X-ray diffractometer DRON-8. On the X-ray tube side, a Soller slit and a 0.5 mm equatorial slit were installed, and on the detector side, a Soller slit, a 0.05 mm equatorial slit, and a nickel beta filter were installed.

For practical studies of temperature distribution in the samples, a unit with a controlled semiconductor laser was assembled whose structure scheme is shown in Fig. 4. The device contains segmental indicators of the current flowing through the semiconductor laser, its voltage, dissipating electric power and temperature in the laser spot. The unit's main control device is a microcontroller with power management technology (picoPower). A USB-

UART interface converter with an integrated clock generator and an initial reset circuit at power-on (Power-On Reset) made on a chip base was used as a linking device between the microcontroller and a personal computer. An analog-to-digital converter was used to measure the amount of current and voltage flowing through the laser. The value of current flowing through the laser was constant and amounted to 1 A at a voltage of 4.6 V. To measure the temperature in the laser spot (sample surface) a Fluke Ti125 thermal imager was used in addition to the thermocouple.

## 2. Experimental

Thermal diffusivity coefficient  $\alpha$  of the TEG sample was measured by placing it a cuvette whose bottom surface was heated by pulses of 0.6 ms with radiant energy of 10 J produced by a xenon lamp. The cuvette made of aluminum was specifically designed for layered samples or composites to measure thermal diffusivity in different directions. Subsequently, the sample diffusivity was extracted from the layered cuvette-sample model using Netzsch Proteus software. This software allows to make certain adjustments following heat loss and changes in the distance from the xenon lamp to the sample inside the measuring chamber. Measurements were performed after the sample was thermostated for 60 minutes at constant temperatures of +25 °C, +100 °C and +150 °C. The time interval  $\tau$  between pulses (shots) was 7 minutes, and there were

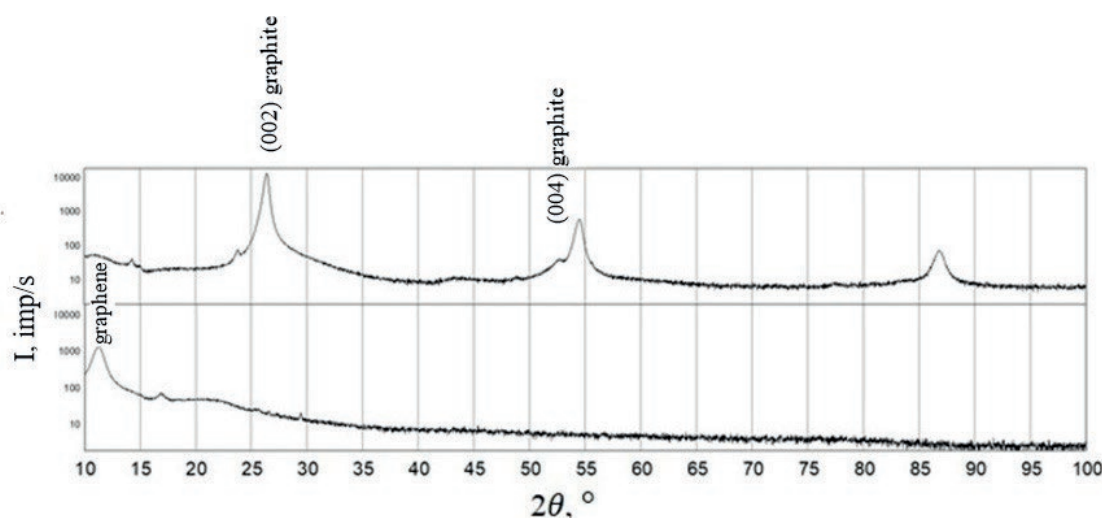


Fig. 3. Diffractograms of TEG and GO samples: top – TEG; bottom – GO

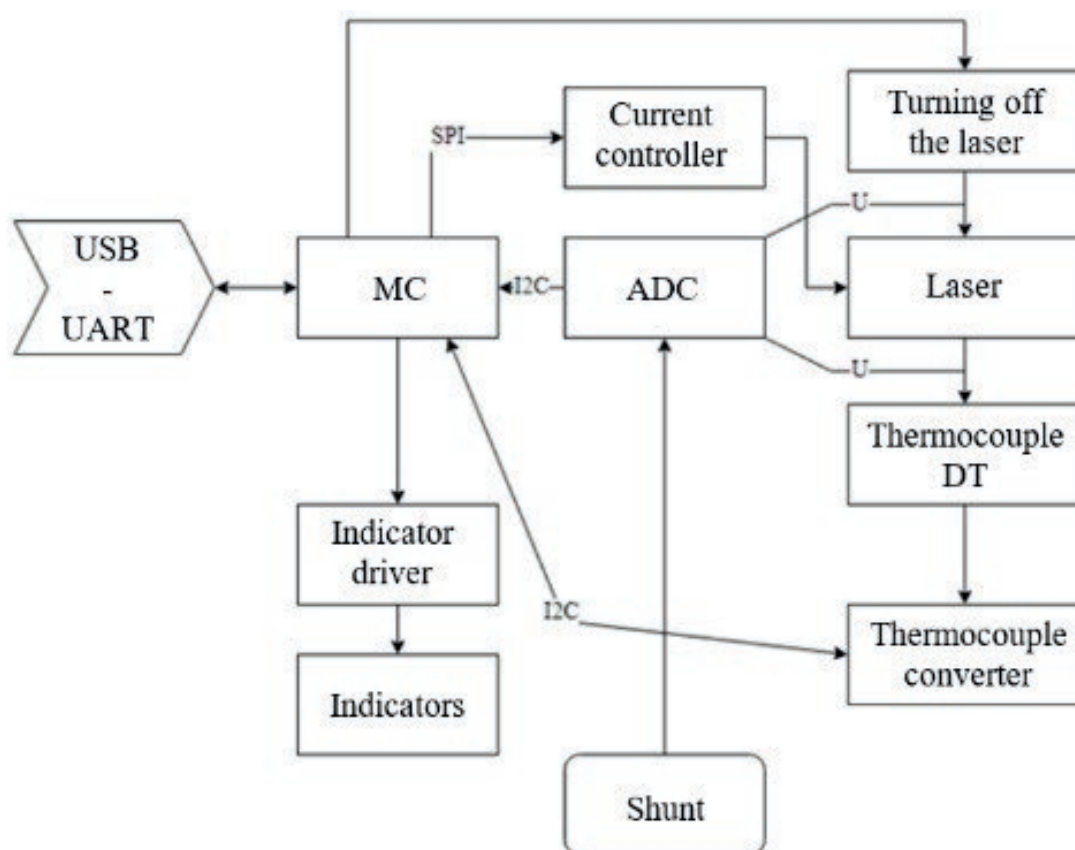


Fig. 4. Structural diagram of controlled semiconductor laser unit

between 10 and 20 of them in order to obtain the average of the measured value. The density of samples  $\rho$  was determined after preliminary thermostatisation of the sample in vacuum by direct measurements of the sample geometric dimensions and its mass. Heat capacity was determined by differential scanning calorimetry using a DSC 204 F1 calorimeter where both the sample and the reference (AXM-5Q graphite) are maintained at an equal and constant temperature. Value of the heat transfer coefficient was calculated using formula 5 under the assumption of a homogeneous system:

$$\chi(T) = \alpha(T) \cdot \rho(T) \cdot C_p(T) \quad (5).$$

Where  $\rho$  is the sample density ( $\text{kg/m}^3$ ),  $\alpha$  is the diffusion coefficient ( $\text{m}^2/\text{s}$ ),  $C_p$  is specific heat capacity at constant pressure ( $\text{J/kg K}$ ).

Based on diffractograms shown in Fig. 3, crystallite sizes of the samples can be roughly estimated using Scherrer equation 6:

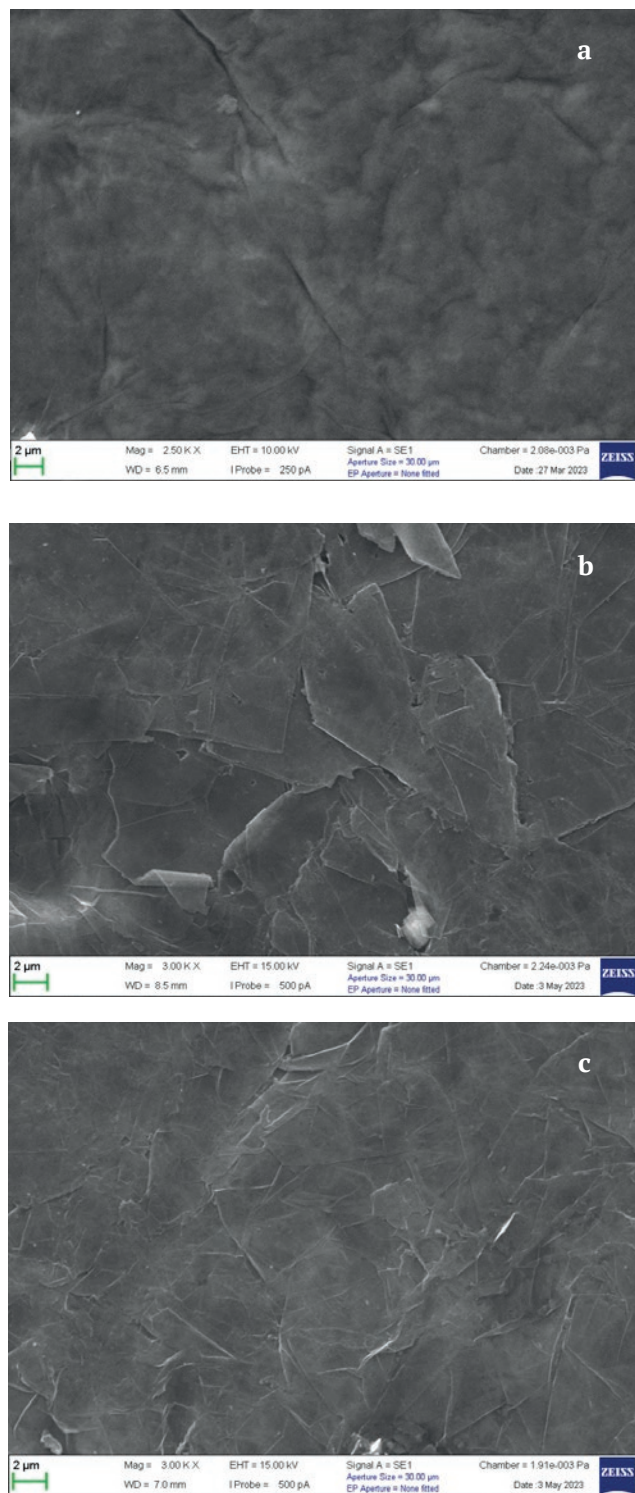
$$d = \frac{k\lambda}{\beta \cos \theta} \quad (6),$$

where  $d$  is the mean size of coherent scattering regions (nm),  $k$  is the sample particle shape factor,  $\lambda$  is the X-ray wavelength (nm),  $\beta$  is half-height reflex width ( $^\circ$ ),  $\theta$  is the diffraction angle ( $^\circ$ ).

Scanning electron microscopy method not only helps to define layer orientation as was shown in Fig. 2, but also to confirm its polycrystalline structure. For samples under study, the morphology of the frontal surface, the characteristic sizes of crystallites obtained by this method were defined (also see Fig. 5).

For practical studies of temperature distribution in the sample, a controlled semiconductor laser was used. The TEG sample was previously compressed under pressure of 300 MPa to a cubic shape with a side of 1.5 cm. The pressing was performed on a hydraulic press by a single impact on 105 layers of the sample which inevitably led to layer compaction and a change in the Grüneisen parameter  $\gamma$  and, consequently, in thermal conductivity coefficient  $\chi$ . The obtained sample shown in Fig. 6 was placed at a distance of 10 cm from the radiation source as shown in

Fig. 7. After 30 seconds of continuous exposure of the sample to laser radiation, the maximum value of its temperature was recorded. A larger value of thermal conductivity coefficient  $\chi$  and



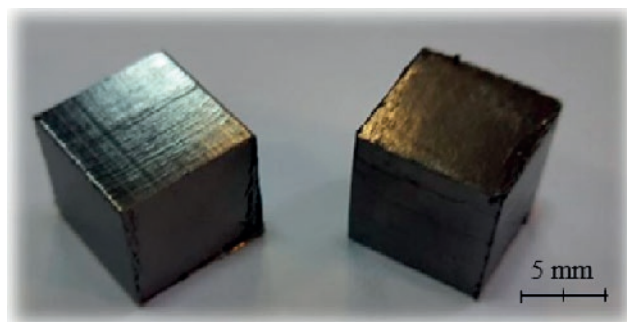
**Fig. 5.** Frontal surface morphology of TEG and GO samples: a – GO approx. 10 μm thick; b – TEG approx. 0.3 mm thick; c – TEG approx. 1.5 mm thick

thermal diffusion  $\alpha$  of the sample resulted in a larger maximum temperature  $T_{\max}$ . To compare the obtained results, two samples of copper and aluminum similar in shape and size were also used.

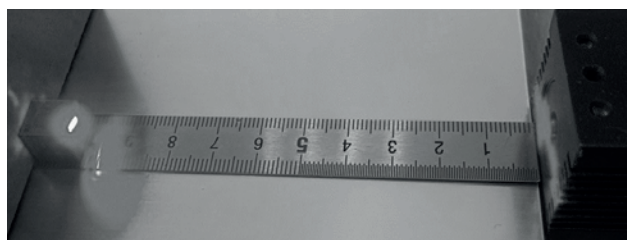
### 3. Results and discussion

Table 1 shows the results of measurements and calculations of physical properties of the TEG sample under study.

A temperature increase in copper, aluminum and silver from + 27 to + 127 °C results in a thermal conductivity coefficient decrease by 2 % [12, p. 70] for copper and by 1.3 % [12, p. 76] for silver, yet in a thermal conductivity coefficient increase by 1 % [12, p. 108] for aluminum. As Table 1 shows, an increase in the TEG temperature at almost similar temperatures (from + 25 °C to + 150 °C) leads to an increase in thermal conductivity by 3 %, but it should be noted that in order to obtain a qualitative dependence of temperature on the TEG thermal conductivity coefficient, it is necessary to increase the number of measurements to several dozens. On average, thermal conductivity of the TEG sample exceeds that of silver by almost one third in the investigated temperature range. It is worth



**Fig. 6.** TEG sample compressed at 300 MPa



**Fig. 7.** Experimental conditions for studying temperature distribution in samples under laser irradiation



**Table 1.** Physical property measurements of TEG sample

$\rho$ , kg/m <sup>3</sup>	$\alpha$ , mm <sup>2</sup> /s	$\chi$ , W/(m·K)	$T$ , °C
990	$116.75 \pm \delta_\alpha$	$622.8 \pm \delta_\chi$	plus 25
	$81.94 \pm \delta_\alpha$	$597.4 \pm \delta_\chi$	plus 100
	$66.37 \pm \delta_\alpha$	$642.6 \pm \delta_\chi$	plus 150

\*  $\delta_\alpha$  – relative error of thermal diffusivity measurement 3 % [8] or  $\pm 8$  % [9].

\*\*  $\delta_\chi$  – relative error of thermal conductivity measurement 4 % [8, 10] or 10.5 % [9, 11], calculated on the basis of the total error according to formula (5) with negligibly small density measurement error (approx. 0.2 %)

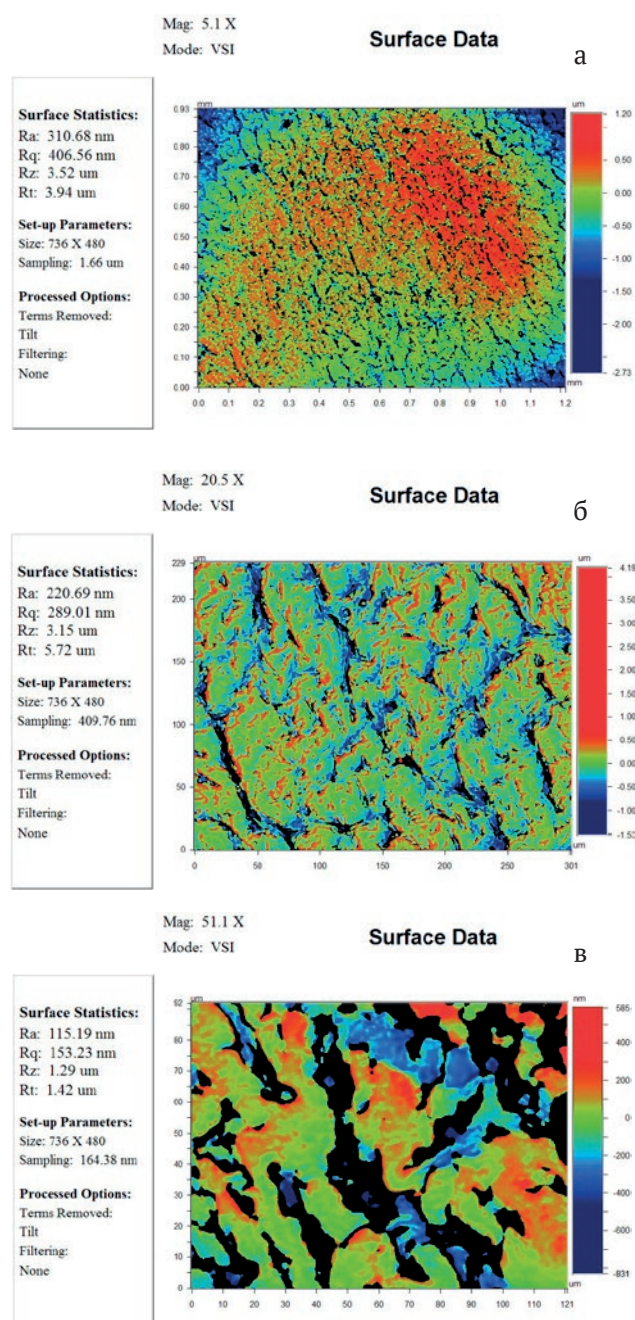
noting that the change in thermal conductivity of TEG in the studied temperature range is more pronounced. When the temperature of copper, aluminum and silver increases from + 27 to + 127 °C their thermal conductivity decreases by 5 % [12, p. 70], 2 % [12, p. 76], and 0.2 % [12, p. 108], respectively, whereas the TEG conductivity decreases by 43 % at almost similar temperatures.

The side surface roughness of the compressed TEG sample whose 2D relief images are shown at various resolutions in Fig. 8, does not require further processing before use in heat transfer.

Measuring the the TEG and GO surface morphology allowed to determine a polycrystalline structure with crystallite interfaces.

Table 2 shows the results of calculations for diffractograms of TEG and GO samples shown in Fig. 3. The TEG sample has a peak near 26.55° (Fig. 3) corresponding to the graphite phase with orientation (002) [14], and a peak near 54.69° with orientation (004). The peaks in the regions of 23° to 25° and 42° to 45° may correspond to both graphite and graphene phases. The diffractogram of the GO sample has one intense peak in the region of angle 11°. Based on earlier studies of graphene diffractograms [15–17], it can be concluded that the diffractogram of the TEG sample corresponds to that of graphite, yet it is impossible to reliably conclude that graphene is absent in it. The diffractogram of the GO sample corresponds to the diffractogram of grapheme without any graphite content.

When studying temperature distribution in the TEG sample compressed under continuous exposure to laser radiation, the thermogram was obtained as shown in Fig. 9. As a result of continuous exposure to laser radiation for 30



**Fig. 8.** Side surface roughness of compressed TEG sample at different resolutions: a – 5.1 X; b – 20.5 X; c – 51.1 X

seconds, the maximum temperature of +31.2 °C was recorded in this sample, while in similar samples of copper and aluminum it was +29.0 °C and +28.4 °C, respectively.

#### 4. Conclusions

Application of anisotropic properties of TEG in the in-plane direction allows to increase thermal conductivity by an order of magnitude

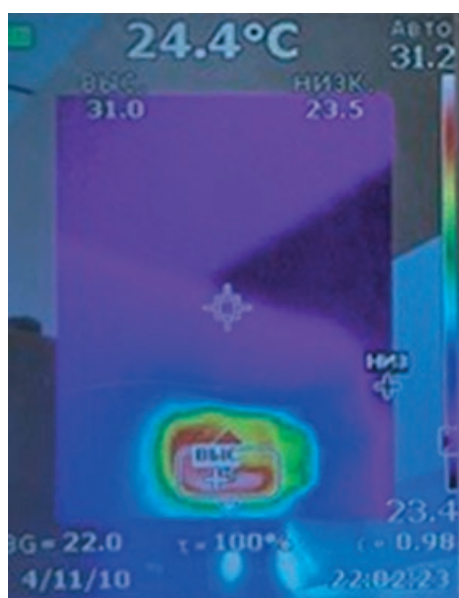


**Table 2.** Results of calculations based on diffraction patterns of the studied samples

Образец	$K$	$a$ , nm	$2\theta$ , °	$\beta$ , °	$d$ , nm
Fig. 2b	0.94	$0.1541 \pm \Delta_\alpha$	$26.41 \pm \Delta_\theta$	0.4356	19.57
Fig. 2a	0.94	$0.1541 \pm \Delta_\alpha$	$11.24 \pm \Delta_\theta$	1.2644	6.59

\*  $\Delta_\alpha$  – absolute measurement error of crystal lattice parameter 0.0001 nm [13].

\*\*  $\Delta_\theta$  – absolute error of diffraction angle measurement 0.01 % [13].

**Fig. 9.** Thermogram of temperature distribution in compressed TEG sample exposed to continuous laser irradiation

which allows for its application as a material replacing copper in heat spreading covers (IHS), simplest cooling radiators, and thermal interfaces (TIM).

Some of the features limiting TEG application include its high conductivity of electric current, and problems in using it for making complex shaped structures.

Although it is impossible to measure thermal diffusivity of the GO sample with the flash method, at least with the LFA 467 HyperFlash analyzer, due to its thickness of about 10  $\mu\text{m}$ , thermophysical properties of this sample may be superior to those of the TEG sample. It is possible to make similar measurements for the GO sample by pressing multiple GO samples at high pressures (up to several GPa).

### Contribution of the authors

The authors contributed equally to this article.

### Conflict of interests

The authors declare that they have no known competing financial interests or personal relationships that could have influenced the work reported in this paper.

### References

1. Renteria J. D., Ramirez S., Malekpour H., ... Balandin A. A. Anisotropy of thermal conductivity of free-standing reduced graphene oxide films annealed at high temperature. *Advanced Functional Materials*. 2015;25(2): 4664. <https://doi.org/10.1002/adfm.201501429>
2. Shulga Y. M., Baskakov S. A., Baskakova Y. V., ... Kovalev I. D. Supercapacitors with graphene oxide separators and reduced graphite oxide electrodes. *Journal of Power Sources*. 2015;279: 722–730. <https://doi.org/10.1016/j.jpowsour.2015.01.032>
3. Tite T., Chiticaru E. A., Burns J. S., Ionita M. Impact of nano-morphology, lattice defects and conductivity on the performance of graphene based electrochemical biosensors. *Journal of Nanobiotechnology*. 2019;17(101): p. 5. <https://doi.org/10.1186/s12951-019-0535-6>
4. Belomestnykh V. N., Tesleva E. P. Poisson's ratio and Gruneisen parameter of solids. *Bulletin of Tomsk Polytechnic University*. 2003;306(5); 8–12. (In Russ., abstract in Eng.). Available at: <https://elibrary.ru/htnczd>
5. Prokhorov D. A., Zuev S. M. Investigation of the characteristics of a graphene-based thermal interface for cooling integrated microcircuits. *Protection of Metals and Physical Chemistry of Surfaces*. 2023;59(2): 155–162. <https://doi.org/10.1134/s2070205123700247>
6. Donghua L., Xiaosong C., Yaping Y., ... Dacheng W. Conformal hexagonal-boron nitride dielectric interface for tungsten diselenide devices with improved mobility and thermal dissipation. *Nature Communications*. 2019;10(1188): 2. <https://doi.org/10.1038/s41467-019-09016-0>
7. Sarkarat M., Lanagan M., Ghosh D., Lottes A., Budd K., Rajagopalan R. Improved thermal conductivity and AC dielectric breakdown strength of silicone rubber/BN composites. *Composites Part C: Open Access*. 2020;2: 100023. <https://doi.org/10.1016/j.jcomc.2020.100023>
8. Light-flash-apparatus LFA 467 HyperFlash-Series methods, techniques, applications for temperature and warmth factors. Netzsch. 0823. Available at: [https://analyzing-testing.netzsch.com/Resources/Persistent/3/6/7/f/367f54b9bc7fc3a5b36f6b41191f5dbaf802ecb7/LFA\\_467\\_HyperFlash\\_en\\_web.pdf](https://analyzing-testing.netzsch.com/Resources/Persistent/3/6/7/f/367f54b9bc7fc3a5b36f6b41191f5dbaf802ecb7/LFA_467_HyperFlash_en_web.pdf)
9. Description of the type of measuring instrument. Thermophysical parameter meters of the LFA 467 HyperFlash modification / GCSI SI FSUE "VNIIM named after

D. I. Mendeleyev<sup>\*</sup>. Certificate of approval of the type of measuring instrument No. 57491-14. 2022. (In Russ.)

10. *Technical Specifications DSC 204 F1 Phoenix* / Netzsch. 0222. Available at: [https://analyzing-testing.netzsch.com/Resources/Persistent/b/8/6/c/b86c2a6637064b1361d580c2bc05367072b194d6/Key\\_Technical\\_Data\\_en\\_DSC\\_204\\_F1\\_Phoenix.pdf](https://analyzing-testing.netzsch.com/Resources/Persistent/b/8/6/c/b86c2a6637064b1361d580c2bc05367072b194d6/Key_Technical_Data_en_DSC_204_F1_Phoenix.pdf)

11. *Description of the measuring instrument type. Differential scanning calorimeters of the DSC 200 F3, DSC 204 F1, DSC 204 HP, DSC 404 C, DSC 404 F1, DSC 404 F3 modifications* / GCSI SI FSUE “VNIIM named after D. I. Mendeleyev<sup>\*</sup>”. Certificate of approval of the type of measuring instruments No. 54912-13. 2023. (In Russ.)

12. Zinoviev V. E. *Thermophysical properties of metals at high temperatures<sup>\*</sup>*. Reference ed., Moscow: Metallurgy Publ.; 1989. p. 384. (In Russ.)

13. *Description of the type of measuring instrument. X-ray diffractometers of the DRON- model 8N and DRON-8T* / GCSI SI FSUE “VNIM named after D. I. Mendelev<sup>\*</sup>”. Certificate of approval of the type of measuring instruments No. 82575-21. 2023. (In Russ.)

14. Fayos J. Possible 3D carbon structures as progressive intermediates in graphite to diamond phase transition. *Journal of Solid State Chemistry*. 1999;148(2): 278–285. <https://doi.org/10.1006/jssc.1999.8448>

15. Siburian R., Sihotang H., Lumban S. R., Supeno M., Simanjuntak C. New route to synthesize graphene nano sheets. *Oriental Journal of Chemistry*. 2018;34(1): 182–187. <https://doi.org/10.13005/ojc/340120>

16. Fentaw T. E., Worku D. A. Controlled synthesis, characterization and reduction of graphene oxide: a convenient method for large scale production. *Egyptian Journal of Basic and Applied Sciences*. 2017;4(1): 74–79. <https://doi.org/10.1016/j.ejbas.2016.11.002>

17. Aftab A., Sadeeq U., Abrar K., ... Qipeng Y. Graphene oxide selenium nanorod composite as a stable electrode material for energy storage devices. *Applied Nanoscience*. 2020;10: 1243–1255. <https://doi.org/10.1007/s13204-019-01204-0>

<sup>\*</sup> Translated by author of the article

## Information about the authors

Dmitriy A. Prokhorov, postgraduate student of the Department of Optical-Electronic Devices and Systems, MIREA - Russian Technological University, Chief Specialist of FSUE “NAMI”, (Moscow, Russian Federation). [prohorovdmitrii97@yandex.ru](mailto:prohorovdmitrii97@yandex.ru)

Maksim G. Rybin, Cand. Sci. (Phys.–Math.), Deputy General Director for Science, Rusgrafen LLC (Moscow Region, Serpukhov Urban District, Obolensk settlement, Russian Federation).

<https://orcid.org/0000-0003-1529-5326>

[rybin@rusgraphene.ru](mailto:rybin@rusgraphene.ru)

Sergei M. Zuev, Cand. Sci. (Phys.–Math.), Associate Professor, Associate Professor of the Department of Optical-Electronic Devices and Systems, MIREA - Russian Technological University, Head of Department of FSUE “NAMI”, (Moscow, Russian Federation).

<https://orcid.org/0000-0001-7033-1882>

[sergei\\_zuev@mail.ru](mailto:sergei_zuev@mail.ru)

Received 04.08.2024; approved after reviewing 30.01.2025; accepted for publication 17.02.2025; published online 25.06.2025.



# Condensed Matter and Interphases

Kondensirovannye Sredy i Mezhfaznye Granitsy  
<https://journals.vsu.ru/kcmf/>

## Original articles

Research article

<https://doi.org/10.17308/kcmf.2025.27/12806>

## Structures for photocatalysis based on ZnO with Ag nanoparticles

D. G. Radaykin✉, V. A. Moshnikov

Saint Petersburg Electrotechnical University “LETI”,  
5F Professor Popov st., Saint Petersburg 197022, Russian Federation

### Abstract

**Purpose:** This paper aims to establish the regularities of the deposited silver influence on the catalytic activity of zinc oxide. Silver nanoparticles make a promising component for improving the catalytic performance of semiconductor materials through the effect of plasmonics.

**Experimental:** The experimental part included synthesis of specimens with different silver content from 0.2 to 2 wt %. SEM images and AFM scans of the powders were obtained to characterize the specimen surface. EDX spectra and elemental mapping were obtained to analyze the composition. As a result, the uniform deposition of silver on the surface of zinc oxide and the agreement of the estimated composition with the obtained were confirmed. Catalyst activity was evaluated by the degree of degradation of the organic dye Rhodamine 6G. The effect of deposited silver on ZnO surface was analyzed.

**Conclusions:** The deposition of 0.2 wt % silver increases the activity by 58 %, while addition of 2 wt % leads to an increase in activity by 92 %. According to the data obtained, a positive effect of deposited silver on the photocatalytic activity of zinc oxide was found. Dependence of activity change on the amount of silver reaches saturation when 2 wt % of silver is reached.

**Keywords:** Zinc oxide, Silver nanoparticles, Photocatalysis, Heterojunction, Ecology

**For citation:** Radaykin D. G., Moshnikov V. A. Structures for photocatalysis based on ZnO with Ag nanoparticles. *Condensed Matter and Interphases*. 2025;27(2): 293–301. <https://doi.org/10.17308/kcmf.2025.27/12806>

**Для цитирования:** Радайкин Д. Г., Мошников В. А. Структуры для фотокатализа на основе ZnO с наночастицами Ag. *Конденсированные среды и межфазные границы*. 2025;27(2): 293–301. <https://doi.org/10.17308/kcmf.2025.27/12806>

✉ Radaykin Dmitry Gennadievich, e-mail: [dima19980219@gmail.com](mailto:dima19980219@gmail.com)

© Radaykin D. G., Moshnikov V. A., 2025



The content is available under Creative Commons Attribution 4.0 License.

## 1. Introduction

Among the global issues humanity is facing, environmental and energy issues are paramount. The consumption of resources and energy, and consequently waste, is increasing at a tremendous rate. Synthetic dyes, antibiotics and plastic microparticles which are toxic substances endangering flora and fauna constitute a significant percentage of the waste discharged. They have a negative effect on aquatic environment reducing the oxygen level, and lead to genetic mutations due to their carcinogenic properties. Therefore, the issue of their neutralization is acute. Various methods to treat wastewater such as biological and physico-chemical treatment are already in use. However, due to the toxicity and complex molecular structure of pollutants, modern and highly efficient treatment methods such as photocatalysis are required.

Due to its ability to operate under green energy conditions, photocatalysis, is one of the key areas in the field of environmental remediation. To date, a significant amount of work has been done on designing and developing photocatalysts for applications such as degradation and transformation of hazardous organic substances, hydrogen generation, and CO<sub>2</sub> and NO<sub>x</sub> reduction [1, 2].

Recombination of electron-hole pairs (excitons) serves as a factor reducing photocatalytic activity. An effective method is to create an interface at the boundary of two materials with different forbidden band widths which allows to obtain a heterojunction and spatially separate photogenerated charges due to internal electric field. This leads to an increase in the exciton lifetime [3]. Different types of heterojunctions such as Schottky barrier [4], *p-n* junction (or isotype) heterojunctions [5], van der Waals [6] and faceted heterojunctions [7] are designed and investigated depending on the specific objectives for their application. Each type has its own advantages and disadvantages, so the proper choice of heterojunction is important. Semiconductor materials, especially metal oxides [8], perovskites [9], chalcogenides [10], as well as hierarchical structures including organometallic frameworks (MOFs) [11], covalent organic frameworks (COFs) [12], and MXenes [13] are widely used in modern nanophotocatalysis.

Nanoarchitectonics is a cutting-edge direction in design of new materials including heterostructures. This concept considers various approaches, such as atomic-molecular design, unconventional growth mechanisms, including oriented splicing and mesocrystal formation, use of colloidal quantum dots to extend the optical sensitivity range of porous hierarchical structures, and sol-gel technologies to obtain new nanostructured materials with desired properties [14–16].

Among semiconductor materials, zinc oxide stands out for its strong oxidizing ability, excellent optoelectronic and catalytic properties, high chemical stability, nontoxicity, and low cost [17, 18]. ZnO nanoparticles, which are generally n-type semiconductors, have a forbidden bandwidth of 3.37 eV and many active catalytic centers. However, the photocatalytic activity of the material is limited by its ability to absorb electromagnetic radiation. Properties of this material are strongly dependent on intrinsic point defects structure. This has led to development of various techniques to modify the surface of ZnO specimens [19–20]. For example, it is possible to change the concentration of oxygen vacancies on the surface of the material, to form new adsorption centers, and change the type of conductivity by mechanical activation, electron beam irradiation, or annealing [21, 22].

Modification of ZnO with metallic elements such as Au, Ag and Cu can lead to an improvement in photocatalytic performance of the material due to change in the zone structure and the plasmon effect. Silver nanoparticles are the most interesting among other metal nanoparticles. They have attracted attention because of their unique electrical conductivity, chemical stability, catalytic and antimicrobial activity [23]. Making ZnO-based composites with addition of Ag leads to changes in the properties of the semiconductor material. They act as a modifier of reaction centers and also as a catalyst for decomposition of pollutants [24]. ZnO islands capture photoinduced charge carriers and enhance light absorption, with both effects accelerating redox reactions and enhancing the photocatalytic efficiency of the material [25–27].

Research papers show that deposition and introduction of precious metal nanoparticles are



promising methods to enhance the photocatalytic activity of the material. Thus, in [28], the co-precipitation method was used to synthesize ZnO specimens containing silver. The flaked specimens were finely dispersed. The activity study was carried out using methyl blue. Addition of silver resulted in an increase in activity from 87.7 to 97.7 % when the silver concentration was increased to 1 wt % with all other conditions of the catalyst activity study being equal. The study [29] used a photo-deposition method to produce zinc oxide with silver nanoparticles on the surface. Presence of silver enhanced specimen performance. It was observed that increasing the amount of silver up to 1 wt % leads to a significant increase in photocatalytic activity, but further increase in the amount of silver leads to a decrease in activity. This is explained by blocking of active centers of zinc oxide.

In the course of this study, ZnO-Ag specimens with different silver mass fraction were obtained by chemical reduction of silver nanoparticles. This is a simple method of obtaining zinc oxide-silver composite.

## 2. Experimental

### 2.1. Synthesis technique

Commercial powder ZnO all-Union State Standard (GOST) 10262-73, *pure* according to chemical classification, was used as the basis of the composite with the content of the parent substance no less than 99 %, and specific surface of 8-10 m<sup>2</sup>/gram.

In order to establish correlation between the composition of ZnO-Ag composite and change in its activity, specimens with different silver mass fraction were synthesized. The composites were obtained by reduction of silver from AgNO<sub>3</sub> salt using NaBH<sub>4</sub> on ZnO surface in presence of polyvinylpyrrolidone stabilizer (PVP) in accordance with the following procedure:

1) ZnO was dispersed in distilled water on an ultrasonic bath for several minutes;

2) AgNO<sub>3</sub> was pre-dissolved in a small amount of distilled water using an ultrasonic bath;

3) the AgNO<sub>3</sub> solution was added to ZnO and stirred vigorously for one hour;

4) to prevent active agglomeration of silver during the reduction, PVP solution was added equimolar to AgNO<sub>3</sub>;

5) the resulting solution was stirred for one hour;

6) NaBH<sub>4</sub> solution equimolar to AgNO<sub>3</sub> was used for silver reduction;

As a result, specimens with different ratios of components were obtained.

## 3. Results and discussion

### 3.1. Characterization of specimen

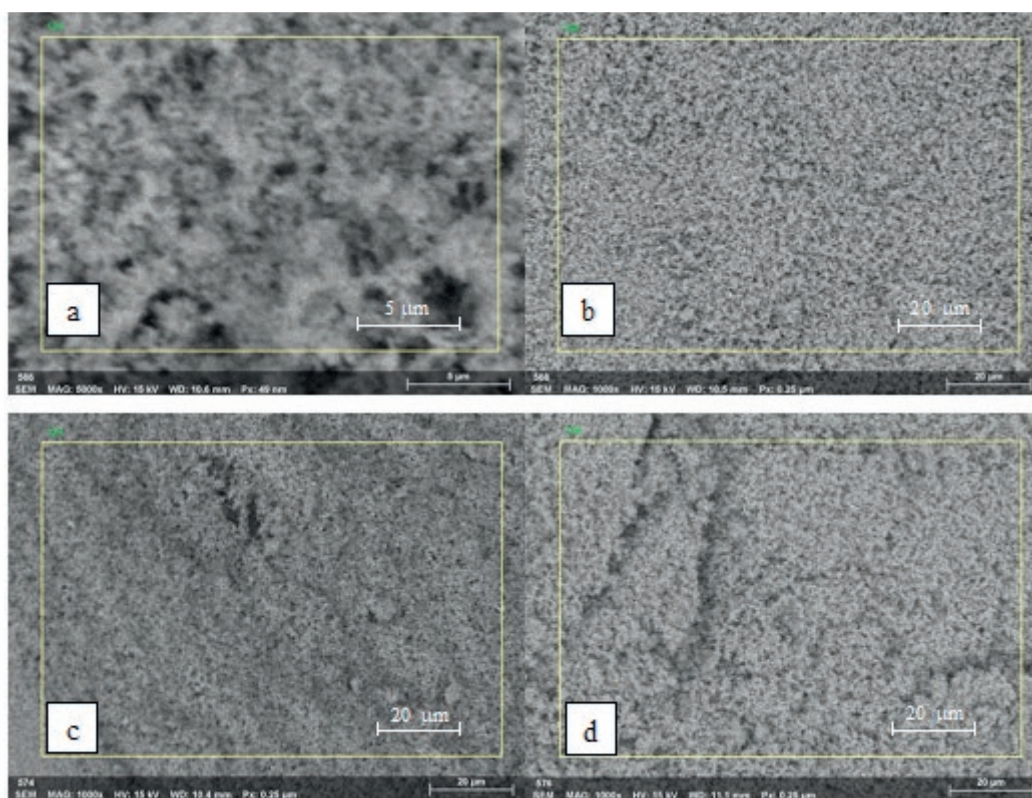
The specimens obtained had different coloration ranging from pale yellow to dark gray. Yellow tint can be considered as an indirect sign of silver nanoparticles recovery on the substrate surface. Table 1 shows external characteristics of the specimens obtained.

Using a Bruker scanning electron microscope, SEM images of the surface of the studied specimens were obtained (see Fig. 1). Primary analysis of the images showed that the substrate used was a finely dispersed powder. According to the obtained image of pure zinc oxide at 5000x magnification, it can be noted that the ZnO particles size was in the submicron range. Analysis of modified specimen images (Fig. 1b-d) allows to draw a similar conclusion about the specimen dispersibility.

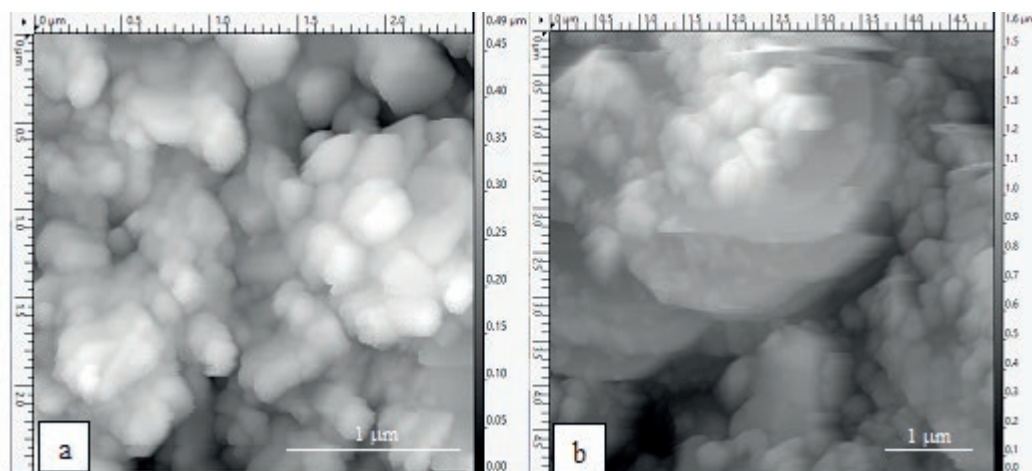
For further information about the surface of the powder catalyst, the surface was scanned using an atomic force microscope (AFM) Ntegra Prima by NT-MDT. Scanning was carried out in semi-contact mode. As a result, surface scans of the ZnO-Ag-2 specimen were obtained (see Fig. 2). Scan analysis allowed to obtain further details about the specimen surface. The powder is comprised of both large formations of more than 1 μm and smaller ones of about 200 nm. The data obtained from these scans do not provide any reliable confirmation of silver nanoparticle deposition on the substrate surface.

**Table 1.** Characteristics of synthesized samples

Sample	Silver content, wt %	Powder color
ZnO	0	White
ZnO-Ag-0.2	0.2	Light yellow
ZnO-Ag-0.5	0.5	Yellow
ZnO-Ag-2	2	Dark grey



**Fig. 1.** SEM images of samples: a) – pure ZnO; b) – ZnO-Ag-0.2; c) – ZnO-Ag-0.5; d) – ZnO-Ag-2

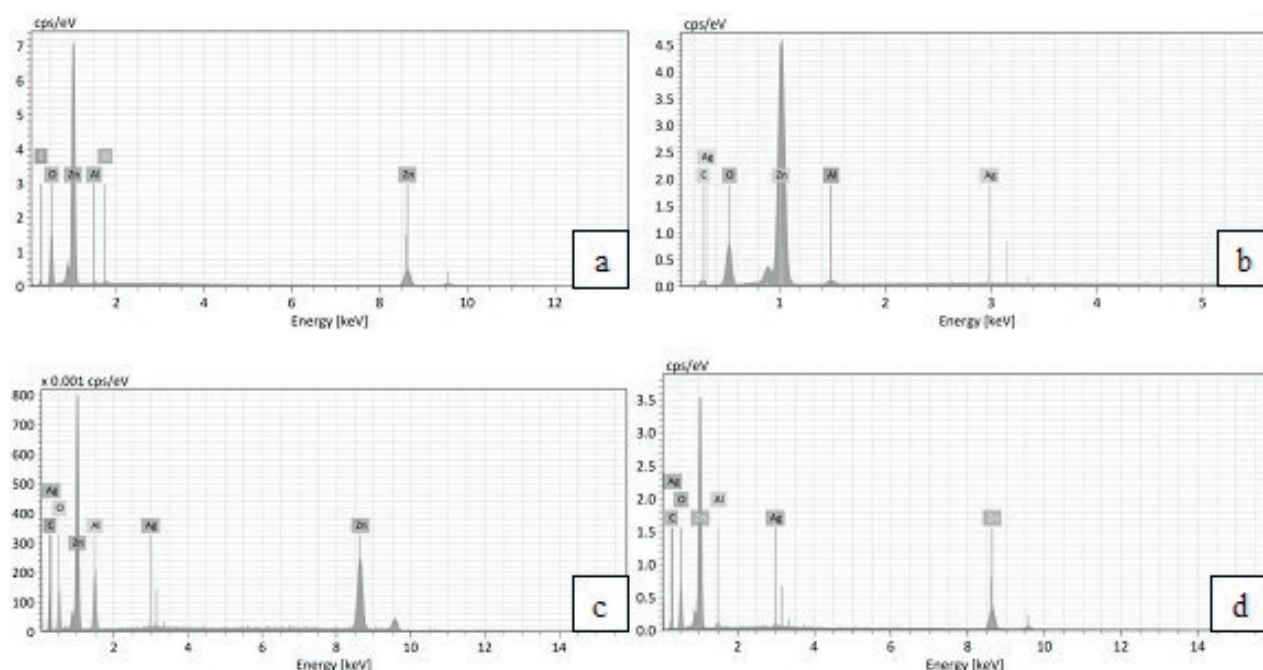


**Fig. 2.** AFM scan of the sample surface ZnO-Ag-2. Scan area a) – 2.5x2.5 mm, b) – 5x5 mm

Energy dispersive analysis (EDX) was performed to confirm the presence of silver on the surface of the synthesized specimens. Local chemical composition was estimated from EDX spectra of the synthesized specimens shown in Fig. 3. In EDX spectrum for pure ZnO specimen (Fig. 3a) the major elements Zn, O are well distinguished, yet C, Al and Si are also present. Presence of carbon, aluminum and silicon is due

to the peculiarities of the substrate on which the specimens were deposited.

The EDX spectrum of ZnO-Ag-0.2 specimen is shown in Fig. 3b. The spectral pattern of the specimen demonstrates that in addition to C and Al impurities, characteristic X-ray lines corresponding to Ag (about 0.25 KeV and 3 KeV) are observed. EDX spectra of the remaining specimens also show the presence of silver



**Fig. 3.** Energy dispersive spectra EDX a) – pure ZnO; b) – ZnO-Ag-0.2; c) – ZnO-Ag-0.5; d) – ZnO-Ag-2

**Table 2.** Percentage of composite elements according to EDX spectra

Sample/element	Zn (wt %)	O (wt %)	Ag (wt %)
ZnO	77	23	–
ZnO-Ag-0.2	86	15	0.13
ZnO-Ag-0.5	86.65	13	0.35
ZnO-Ag-2	80.5	17.12	2.38

in the obtained specimens (Fig. 3c, d). The specimens were quantitatively analyzed based on the obtained spectra. The calculated values of mass percentages of elements are given in Table 2.

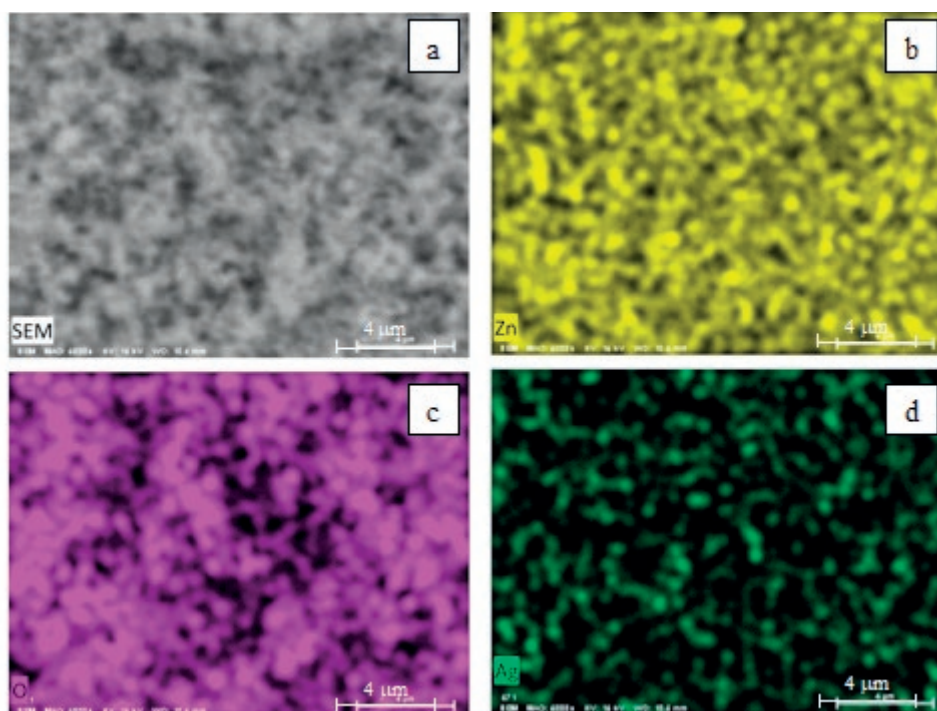
By means of elemental mapping of ZnO-Ag-0.2 specimen it was possible to evaluate the uniformity of Ag nanoparticles recovery (Fig. 4). The obtained elemental map confirms the presence of homogeneously distributed silver on the substrate surface.

According to the obtained mass percentages of the composite elements (Table 2) calculated on the basis of EDX spectra, it can be noted that the composition of the synthesized specimens corresponds to estimated composition. The obtained data allow to reliably identify the relationship between the change in the photocatalytic activity of the composite and the amount of deposited silver.

### 3.2. Evaluation of photocatalytic activity of specimens

Activity of the specimens was evaluated on the basis of photocatalytic decomposition of Rhodamine 6G (R6G). The initial concentration of organic dye was  $21 \pm 0.64$   $\mu\text{mol/liter}$  and the volume of solution was 75 mL. The change in dye concentration was evaluated using a PE 5400UV spectrophotometer. Rhodamine 6G has a pronounced absorption peak (526 nm) and its intensity was taken to calculate the concentration using the Bouguer-Lambert-Bera law. The spectral response of Rhodamine 6G was measured 5 and 10 minutes after the beginning of irradiation of the catalyst with UV light. A UV diode with a wavelength of 365 nm and a power of 4.9 W was taken as an irradiation source. The photocatalytic decomposition was investigated under constant stirring. The mass of the catalyst was  $5.3 \pm 0.2$  mg. The study was carried out at least three times for each of the





**Fig. 4.** Elemental map of ZnO-Ag-0.2: a) – SEM image of the surface; map of element concentrations: b) – Zn; c) – O; d) – Ag

specimens to obtain more accurate data on their activity.

Since the same commercial zinc oxide with the same specific surface area was taken as a basis for synthesized catalysts, the weight activity was used as a comparative characteristic. Table 3 shows the results of calculations.

Analysis of the obtained results showed that the average activity of the composite material exceeds the activity of the initial substrate by 58 % (ZnO-Ag-0.2 specimen). As the amount of deposited silver increases from 0.2 to 2 %, the activity of the composite increases from 58 to 92 %. This dependence has a nonlinear character and begins to reach saturation after 2 wt % of precipitated silver (Fig. 5). According to the obtained dependence, it can be noted that further increase in the amount of silver does

not lead to a significant increase in the activity of the composite material. On the contrary, the probability of undesirable overlapping of active catalytic centers of zinc oxide increases.

To obtain more complete data on synthesized catalysts, the reaction kinetics was studied. The kinetics of photodegradation of dyes is usually described by the Langmuir-Hinshelwood model and approximated by the following kinetic equation:

$$-dC/dt = k_f K_a C / (1 + K_a C),$$

where  $C$  is the current dye concentration at time  $t$ ,  $k_f$  is the rate constant of the process,  $K_a$  is the adsorption equilibrium constant.

At low dye concentration ( $C \ll 1$  mM), the equation simplifies to a pseudo-first-order process rate equation:

**Table 3.** Summary table of the results of the study of the activity of samples

Sample	Weight activity (300 сек), mmol/g·s	Weight activity (600 сек), mmol/g·s	Rate constant, min <sup>-1</sup>
ZnO	0.3447	0.2348	0.0660
ZnO-Ag-0.2	0.5461	0.3330	0.1030
ZnO-Ag-0.5	0.6265	0.3648	0.1350
ZnO-Ag-2	0.6611	0.3945	0.1631



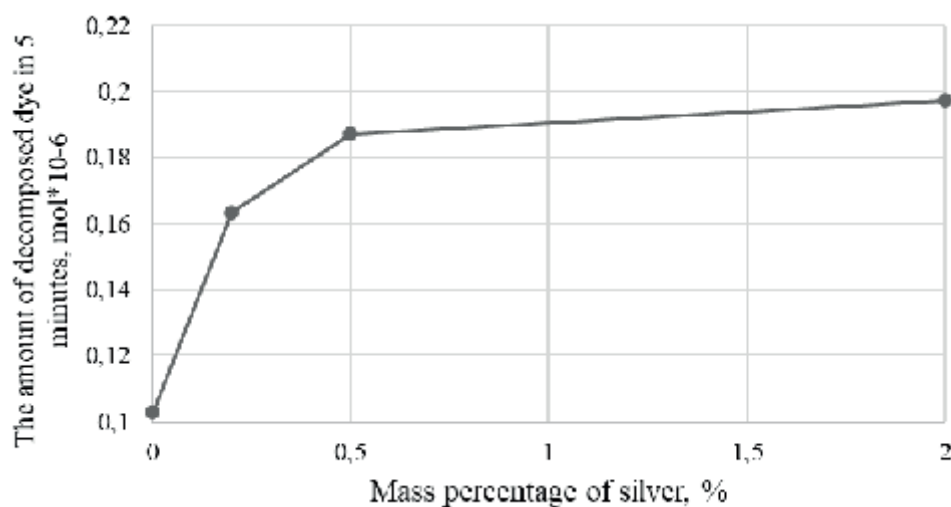


Fig. 5. Graph of the dependence of the composite activity on the silver content

$$\ln(C/C_0) = k_t K_a t = k_{app} t,$$

where  $k_{app}$  is the pseudo-first-order rate constant.

Fig. 6 shows the graph of dependence  $\ln(C/C_0) = f(t)$ , plotted on the basis of experimental data. Using linear approximation, the rate constants for the specimens under study were determined, and the estimated values were recorded in Table 3. Since the rate constant is numerically equal to the reaction rate, the value of the constant allows to evaluate the effect of the catalyst on the rate of the dye photodegradation process. Based on the data obtained, it can be

said that the deposition of 0.2 wt % silver leads to acceleration of the photocatalytic degradation reaction by 56 %, and when 2 wt % is reached, the rate increases by 147 %.

#### 4. Conclusions

In this course of the present research, specimens of composites with different silver content on their surface were synthesized. The amount of silver in the composite was estimated by EDX spectra. The obtained results are compared with the estimated values and allow

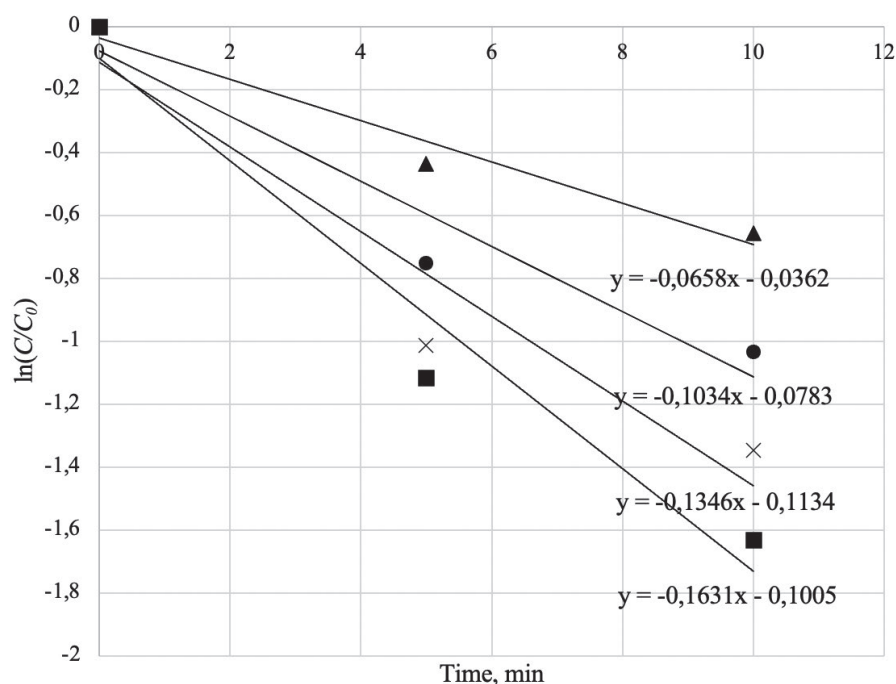


Fig. 6. Dependence graph  $\ln(C/C_0) = f(t)$

to reveal the correlation between the amount of silver and the change in the activity of the composite. To confirm the uniformity of silver recovery, an elemental map of the ZnO-Ag-0.2 specimen was obtained.

Analysis of the activity of composites containing silver showed a positive effect of deposited silver on the properties of zinc oxide. An increase in catalytic activity was observed with an increasing amount of silver. The ZnO-Ag-2 specimen has a weight activity higher by 92 % compared to the original ZnO and increases the rate of photocatalytic degradation by 147 %. According to the available dependence of activity on the amount of silver, it can be noted that 2 wt % is the optimum limiting value at which a significant increase in the activity of the composite occurs.

### Contribution of the authors

D. G. Radaykin responsible for conducting the experiment, writing the review, final conclusions. V. A. Moshnikov responsible for supervising, setting tasks and discussion of results, text editing.

### Conflict of interests

The authors declare that they have no known competing financial interests or personal relationships that could have influenced the work reported in this paper.

### References

1. Tao Y., Ma Z., Wang W. Nickel phosphide clusters sensitized TiO<sub>2</sub> nanotube arrays as highly efficient photoanode for photoelectrocatalytic urea oxidation. *Advanced Functional Materials*. 2023;33(9): 2211169. <https://doi.org/10.1002/adfm.202211169>
2. Li S., Shang H., Tao Y., ... Li H. Hydroxyl radical-mediated efficient photoelectrocatalytic NO oxidation with simultaneous nitrate storage using a flow photoanode reactor. *Angewandte Chemie*. 2023;62: e202305538. <https://doi.org/10.1002/ange.202305538>
3. Wadsworth A., Hamid Z., Kosco J., Gasparini N., McCulloch I. The bulk heterojunction in organic photovoltaic, photodetector, and photocatalytic applications. *Advanced Materials*. 2020;32(38): e2001763. <https://doi.org/10.1002/adma.202001763>
4. Kumari P., Bahadur N., Kong L., O'Dell L. A., Merenda A., Dumeé L. Engineering Schottky-like and heterojunction materials for enhanced photocatalysis performance – a review. *Materials Advances*. 2022: 2309–2323. <https://doi.org/10.1039/D1MA01062J>
5. Sun M., Li F., Zhao F., ... Li D. Ionic liquid-assisted fabrication of metal–organic framework-derived indium oxide/bismuth oxyiodide *p-n* junction photocatalysts for robust photocatalysis against phenolic pollutants. *Journal of Colloid and Interface Science*. 2022;606: 1261–1273. <https://doi.org/10.1016/j.jcis.2021.08.132>
6. Zhou Y., Zhang C., Huang D., ... Qin D. Structure defined 2D Mo<sub>2</sub>C/2Dg-C<sub>3</sub>N<sub>4</sub> Van der Waals heterojunction: oriented charge flow in-plane and separation within the interface to collectively promote photocatalytic degradation of pharmaceutical and personal care products. *Applied Catalysis B: Environmental*. 2022;301: 120749. <https://doi.org/10.1016/j.apcatb.2021.120749>
7. Bao S., Wang Z., Zhang J., Tian B. Facet-heterojunction-based Z-Scheme BiVO<sub>4</sub>/010 microplates decorated with AgBr-Ag nanoparticles for the photocatalytic inactivation of bacteria and the decomposition of organic contaminants. *ACS Applied Nano Materials*. 2020;3: 8604–8617. <https://doi.org/10.1021/acsanm.0c00703>
8. Kannan K., Radhika D., Sadasivuni K. K., Reddy K. R., Raghu A. V. Nanostructured metal oxides and its hybrids for biomedical applications. *Advances in Colloid and Interface Science*. 2019: 102178. <https://doi.org/10.1016/j.cis.2020.102178>
9. Wang J., Liu J., Du Z., Li Z. Recent advances in metal halide perovskite photocatalysts: properties, synthesis and applications. *Journal of Energy Chemistry*. 2021;54: 770–785. <https://doi.org/10.1016/j.jechem.2020.06.024>
10. Wlazlak E., Blachecki A., Bisztyga-Szklarz M., ... Zawal P. Heavy pnictogen chalcogenides: the synthesis, structure and properties of these rediscovered semiconductors. *Chemical Communications*. 2018;54: 12133–12162. <https://doi.org/10.1039/C8CC05149F>
11. Du C., Zhang Z., Yu G., ... Wang S. A review of metal organic framework (MOFs)-based materials for antibiotics removal via adsorption and photocatalysis. *Chemosphere*. 2021;272: 129501. <https://doi.org/10.1016/j.chemosphere.2020.129501>
12. He Z., Goulas J., Parker E., Sun Y., Zhou X., Fei L. Review on covalent organic frameworks and derivatives for electrochemical and photocatalytic CO<sub>2</sub> reduction. *Catalysis Today*. 2023;409: 103–118. <https://doi.org/10.1016/j.cattod.2022.04.021>
13. Solangi N. H., Karri R. R., Mazari S. A., ... Azad A. K. MXene as emerging material for photocatalytic degradation of environmental pollutants. *Coordination Chemistry Reviews*. 2023;477: 214965. <https://doi.org/10.1016/j.ccr.2022.214965>
14. Kozodaev D. A., Muratova E. N., Moshnikov V. A. From nanotechnology to nanoarchitectonics. *Scientific and technical conference of the St. Petersburg Scientific and Technical Association of the Russian Electronic Networks named after A. S. Popov, dedicated to the Day of Radio*. 2024;1(79): 356–358. (In Russ.)
15. Bobkov A. A., Radaykin D. G., Moshnikov V. A. Nanoarchitectonics of porous hierarchical structures for photocatalysis and sensorics. In the collection: *Chemical thermodynamics and kinetics. Collection of scientific papers of the XII International Scientific Conference. Veliky Novgorod*. 2022. p. 69–70. (In Russ.)
16. *Nanoparticles, nanosystems and their application. Catalytic nanosystems*. V. A. Moshnikov, A. I. Maksimov (eds.). St. Petersburg: ETU “LETI” Publ.; 2022. 220 p.
17. Maraeva E., Radaykin D., Bobkov A., ... Moshnikov V. Sorption analysis of composites based on zinc oxide for

catalysis and medical materials science. *Chimica Techno Acta*. 2022;9(4): 20229422. <https://doi.org/10.15826/chimtech.2022.9.4.22>

18. Bobkov A. A., Lashkova N. A., Maximov A. I. Fabrication of oxide heterostructures for promising solar cells of a new generation. *Semiconductors*. 2017;51(1): 61–65. <https://doi.org/10.1134/S1063782617010031>

19. Moshchnikov V. A., Tairov Yu. M., Khamova T. V., Shilova O. A. *Sol-gel technology of micro- and nanocomposites*. St. Petersburg: “Lan” Publ.; 2013. 304 p. (In Russ.)

20. Shomakhov Z. V., Nalimova S. S., Guketlov A. M., Kondratyev V. M., Moshnikov V. A. Control of the properties of adsorption sites in the formation of gas-sensitive structures of mixed oxides. *Izvestiya vysshikh uchebnykh zavedenii. Elektronika*. 2024;29(1): 7–18. (In Russ., abstract in Eng.). <https://doi.org/10.24151/1561-5405-2024-29-1-7-18>

21. Pronin I. A., Plugin I. A., Kolosov D. A. ... Sysoev V. V. Sol-gel derived ZnO film as a gas sensor: Influence of UV processing versus a thermal annealing. *Sensors and Actuators A: Physical*. 2024; 377: 115707. <https://doi.org/10.1016/j.sna.2024.115707>

22. Kareem M. A., Bello I. T., Shittu H. A. Green synthesis of silver nanoparticles (AgNPs) for optical and photocatalytic applications: a review. *OP Conference Series: Materials Science and Engineering*. 2020;805(1): 012020. <https://doi.org/10.1088/1757-899X/805/1/012020>

23. Zhu H., Chen X., Zheng Z. Mechanism of supported gold nanoparticles as photocatalysts under ultraviolet and visible light irradiation. *Chemical Communications*. 2009;48: 7524–7526. <https://doi.org/10.1039/B917052A>

24. Radaykin D. G., Bobkov A. A. Influence of the plasmonic effect of silver nanoparticles on the catalytic activity of zinc oxide. *IV All-Union Congress on Sensorics and Economics “SENSOR MERGER-2023”*. 2023. p. 153–157. (In Russ.)

25. Permyakov N. V., Maraeva E. V., Bobkov A. A., Radaykin D. G., Moshnikov V. A. Study of ZnO-based materials for catalysis and medical materials science. *Nanophysics and nanomaterials, Collection of scientific papers of the International Symposium dedicated to the 110th anniversary of V. B. Aleskovsky and the 115th anniversary of L. A. Sen, St. Petersburg*. 2022.\* (In Russ.). Available at: <https://elibrary.ru/item.asp?id=50737548>

26. Subramanian V. Catalysis with TiO<sub>2</sub>/gold nanocomposites. Effect of metal particle size on the Fermi level equilibration. *Journal of the American Chemical Society*. 2004;126: 4943–4950. <https://doi.org/10.1021/ja0315199>

27. Kareem M. A., Bello I. T., Shittu H. A., Sivaprakash P., Adedokun O., Arumugam S. Synthesis, characterization, and photocatalytic application of silver doped zinc oxide nanoparticles. *Cleaner Materials*. 2022;3(1): 100041. <https://doi.org/10.1016/j.clema.2022.100041>

28. Vaiano V., Matarangola M., Murciab J. J., Rojash H., Navíoc J. A., Hidalgo M. C. Enhanced photocatalytic removal of phenol from aqueous solutions using ZnO modified with Ag. *Applied Catalysis B Environmental*. 2018;225: 197–206. <https://doi.org/10.1016/j.apcatb.2017.11.075>

\* Translated by author of the article

## Information about the authors

Dmitry G. Radaykin, postgraduate student of the Department of Micro- and Nanoelectronics, Saint Petersburg Electrotechnical University “LETI” named after V. I. Ulyanov (Lenin) (Saint Petersburg, Russian Federation).

<https://orcid.org/0000-0002-7125-9744>  
dima19980219@gmail.com

Vyacheslav A. Moshnikov, Dr. Sci. (Phys.–Math.), Professor, Department of Micro- and Nanoelectronics, Saint Petersburg Electrotechnical University “LETI” named after V. I. Ulyanov (Lenin) (Saint Petersburg, Russian Federation). <https://orcid.org/0000-0001-6500-5492>

vamoshnikov@mail.ru

Received 10.10.2024; approved after reviewing 30.01.2025; accepted for publication 17.02.2025; published online 25.06.2025.





## Original articles

Research article

<https://doi.org/10.17308/kcmf.2025.27/12807>

## Structural and optical properties of Mg-doped ZnO films obtained by spray pyrolysis

E. S. Rembeza<sup>1✉</sup>, S. Z. Zaynobidinov<sup>2</sup>, M. B. Rasulova<sup>2,3</sup>

<sup>1</sup>Voronezh State University,  
1 Universitetskaya pl., Voronezh 394018, Russian Federation

<sup>2</sup>Andijan State University,  
129 Universitet st., Andijan city 170100, Republic of Uzbekistan

<sup>3</sup>Andijan Mashinasozlik Institute,  
56 Baburshok st., Andijan city 170119, Republic of Uzbekistan

### Abstract

**Purpose:** The paper aims to determine the optimal technological conditions for preparing metal oxide films by spray pyrolysis, as well as to study their structural and optical parameters. Zinc oxide thin films have an important combination of properties for practical application including transparency in the visible range of electromagnetic radiation and low electrical resistance which is provided by a large value of the bandgap width and by obtaining non-stoichiometric compositions or by introducing appropriate alloying elements. The possibility of practical application of ZnO thin films also depends on their optical and electrical properties.

**Methods:** Thin films of unalloyed zinc oxide as well as ZnO films doped with magnesium with different percentages from 1 to 15 at. % were prepared by spray pyrolysis. Structural and optical properties of magnesium-doped zinc oxide thin films were studied. Through X-ray diffraction analysis it was found that all films are polycrystalline with hexagonal wurtzite structure and crystallographic orientation (002) aligned or oriented along the plane of the substrate.

**Conclusions:** Studies of optical properties by UV-visible spectrophotometry showed that transmittance of magnesium-doped zinc oxide thin films increased from 70 to about 85 %, and the bandgap width increased from 3.20 to 3.42 eV. These properties of magnesium-doped ZnO thin films demonstrate their high potential for efficient use in many optoelectronic devices and instruments such as solar cells, gas sensors, allow their use as photocatalysts, etc.

**Keywords:** ZnO thin films, Mg doping, Spray pyrolysis method, Structural properties, Optical properties

**For citation:** Rembeza E. S., Zainobiddinov S. Z., Rasulova M. B. Structural and optical properties of Mg-doped ZnO films obtained by spray pyrolysis. *Condensed Matter and Interfaces*. 2025;27(2): 302–307. <https://doi.org/10.17308/kcmf.2025.27/12807>

**Для цитирования:** Рембеза Е. С., Зайнобиддинов С. З., Расулова М. Б. Структурные и оптические свойства пленок ZnO, легированного Mg, полученных методом спрей-пиролиза. *Конденсированные среды и межфазные границы*. 2025;27(2): 302–307. <https://doi.org/10.17308/kcmf.2025.27/12807>

✉ Ekaterina S. Rembeza, e-mail: [rembeza@phys.vsu.ru](mailto:rembeza@phys.vsu.ru)

© Rembeza E. S., Zainobiddinov S. Z., Rasulova M. B., 2025



The content is available under Creative Commons Attribution 4.0 License.

## 1. Introduction

Recently, there has been growing interest in metal oxides since thin film coatings of metal oxides are a group of the most demanded materials in modern micro- and nanoelectronics. Among them, zinc oxide (ZnO) is one of the most high-potential materials used for application of transparent electrically conductive contacts, gas sensors and piezoelectric transducers production.

ZnO is one of the most important semiconductor materials. Due to alternate placement of zinc and oxygen in the unit cell of the crystal lattice, it has the structure of wurtzite belonging to hexagonal crystal lattice and space group  $P6_3mc$ . Application of ZnO thin films in optoelectronic devices such as solar cells is possible due to high binding energy of excitons (60 meV) [1,2,3]. Zinc oxide ZnO with its good optoelectronic properties is often used as a transparent conducting oxide (TCO) electrode in photovoltaic devices and in planar displays. TCOs are materials that have high visible light transparency ( $> 80\%$ ) and low resistivity ( $< 10^{-3}$  Ohm cm) [4,5].

Morphological, structural, optical, electrical and photodetection properties of ZnO have been studied well enough, yet influence of doping with various impurities is still insufficiently investigated. The parameters of undoped ZnO thin films are often unstable due to changes in surface conductivity by chemisorption and oxygen adsorption. Doping is an effective way to influence the surface states, electrical conductivity, formation of energy levels and concentration of charge carriers in a semiconductor. One of the important characteristics is the possibility of changing the bandgap width of ZnO by doping it with group II elements such as Be, Mg, Ca, Co, Cd and Sr. Studies of doped ZnO have shown that their properties often depend on the method of synthesis. Magnesium doped zinc oxide (MZO) thin films can be synthesized by high frequency sputtering, molecular beam epitaxy, sol-gel method, pulsed laser deposition and chemical vapor deposition [6]. In the course of the present research, the spray pyrolysis method was used since it is not labor-intensive and allows to obtain the materials with required properties through a minimum number of technological operations.

Spray pyrolysis is a method of spraying an aerosol onto a heated substrate. The aerosol is

produced from a pressurized solution of metal salts which vaporizes and, once on the substrate surface, chemically reacts to form the desired properties of the substance. The possibility of moving the nozzle of the atomizer over the substrate provides homogeneous thickness of coatings on the entire surface. The main disadvantages of this method include relatively high temperatures (400 °C for ZnO) impossible to use with flexible polymer substrates [7,8].

The aim of present research is to determine the optimal technological conditions including temperature, pressure, and time for preparation of Mg-doped ZnO films with predetermined properties by spray pyrolysis, as well as to study the structural and optical parameters of the obtained MZO films.

## 2. Methods

To obtain the specimens by spray pyrolysis, zinc acetate dihydrate ( $Zn(CH_3COO)_2 \cdot 2H_2O$ ) was used as the base material, and methanol and diethanolamine (DEA) were used as solvents and stabilizers. First, 5 g of zinc acetate dihydrate was dissolved in 30 mL of methanol, and then diethanolamine was added slowly using a magnetic stirrer to obtain a solution with a molar concentration of 0.75 M. ZnO doping with magnesium was carried out by adding magnesium acetate tetrahydrate  $Mg(CH_3COO)_2 \cdot 4H_2O$  along with zinc acetate to methanol. The ZnO:Mg ratio was 1 at. % for MZO specimen, 1.3 at. % for MZO specimen, 3.5 at. % for MZO specimen, 5.7 at. % for the MZO7 specimen and 15 at. % for the MZO15 specimen. 0.047 g of magnesium acetate tetrahydrate was added to the resulting solution for doping 1 at. % Mg, 0.141 g for doping 3 at. % Mg, 0.234 g for doping 5 at. % Mg, 0.328 g for doping 7 at. % Mg, and 0.705 g for doping 15 at. % Mg. The resulting mixture was stirred for 1 hour at 65 °C, and then for 3 hours at room temperature until a clear and homogeneous solution was obtained.  $Zn_xMg_{1-x}O$  films were deposited by spray pyrolysis on glass substrates aged at 400 °C. The distance between the atomizer and the substrate was 20 cm. The MZO films were sputtered onto the surface of preheated glass at a rate of 2.0 mL/min at an air pressure of 2 bar. Multilayer sputtering of the ZnO film was carried out for 1 min each followed by a break of 30 seconds to

restore the substrate temperature. Thus 20 layers were prepared.

Thickness of the films prepared was determined on an interference microscope MII4. Structural studies of thin films of metal oxides MZO were carried out by X-ray diffraction method on XRD-6100 diffractometer. The X-ray voltage was 40 kV and the current was 30 mA. The scanning range was 8.0–70.0 degrees, the scanning speed was 2 deg/min, and the scanning step was 0.02 degrees. Optical transmission spectra of the investigated films in the range from 200 to 800 nm were obtained on a SPEX SPP-715 M spectrophotometer.

### 3. Results and discussion

Thickness of the films obtained is 344.3 nm for ZnO, and it varies for different doped films. It is 348.4 nm for MZO1, 353.1 nm for MZO3, 357.6 nm for MZO5, 362.2 nm for MZO7, and 380 nm for MZO15. Thus, thickness of the films ranges from 344 to 380 nm.

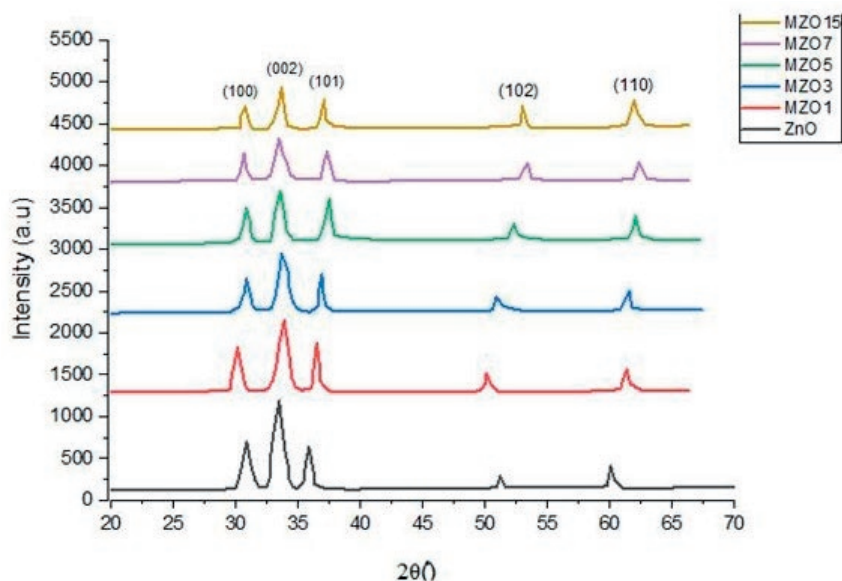
X-ray diffraction patterns of ZnO:Mg thin film with Mg concentration of 1 at. %; 3 at. %; 5 at. %; 7 at. %; 15 at. % are given in Fig.1. The studies showed that all the diffraction maxima of the X-ray diffraction pattern of ZnO film belong to wurtzite structure. As Fig. 1 shows, the intensity of structural line (002) is much stronger than other diffraction lines. This indicates that thin

films have a polycrystalline structure with a predominant *c* index. Fig. 2 shows that structural reflex of the crystallographic direction (002) is shifted toward small angles (from  $2\theta = 34.56^\circ$  to  $2\theta = 34.44^\circ$ ), i.e., toward  $\Delta\theta = 0.12^\circ$  with increasing number of doping Mg atoms in the X-ray diffraction pattern. It was found that the lattice parameters of the magnesium-doped films at room temperature are  $a = b = 0.3265$  nm and  $c = 0.5219$  nm, the *c* parameter increases insignificantly ( $\Delta c = 0.0009$  nm). This, in turn, indicates that  $\text{Mg}^{+2}$  ions are substituted with  $\text{Zn}^{+2}$  in the crystal lattice of the film. In addition, we determined the half-widths (FWHM) of these reflections which first increased (doping with Mg atoms up to 7 at. %) and then decreased (doping with Mg atoms more than 7 at. %).

The obtained results indicate that the ZnO structure does not change upon addition of Mg. Sizes of the formed crystallites (*D*) in ZnO:Mg thin films were calculated according to Scherrer's formula [9]:

$$D = \frac{k\lambda}{\beta \cos\theta}, \quad (1)$$

where,  $\lambda$  is radiation wavelength of 0.154 nm,  $\theta$  is scattering angle (half of the diffraction angle  $2\theta$ ),  $\beta$  is physical line broadening on the diffractogram (width of the reflex at the half of intensity maximum), coefficient  $k \approx 0.91$ .



**Fig. 1.** X-ray images of ZnO and ZnO:Mg thin films with Mg content 1 at. %; 3 at. %; 5 at. %; 7 at. % and 15 at. %

The lattice strain  $\varepsilon$  of Mg-doped ZnO thin films can be estimated through the following expression:

$$\varepsilon = \frac{\beta \cos \theta}{4}. \quad (2)$$

The dislocation density  $\delta$  is calculated as follows:

$$\delta = \frac{1}{D^2}. \quad (3)$$

The estimated values of characteristics of MZO films from the X-ray diffraction data are presented in Table 1. The results showed that with the increasing content of doping impurity Mg in MZO films from 1 to 7 at. %, the full width at half of the maximum value of peaks on X-ray diffraction decreases, i.e. the size of crystallites in the film decreases. This is probably due to the increase in the film deposition rate with increasing Mg doping degree. Consequently, the crystallite size can be controlled by varying the Mg concentration. In fact, higher doping impurity level creates more nucleation centers along with lattice defects and thus leads to a decrease in crystallite size in thin films. The results also showed that the dislocation density increases with increased Mg doping which contributes to an increase in lattice defects along grain boundaries in MZO thin films.

It is known that the peak (002) is related to film deformation. As Figs. 1, 2 show, when Mg is doped at concentrations of 1 at. %, 3 at. %, 5 at. % and 7 at. %, the diffraction peak (002) is at  $2\theta$ : 34.54, 34.50, 34.46 and 34.44 degrees, respectively. Hence, as the concentration of Mg doping impurity increases, the peak (002) gradually shifts towards a higher angle, indicating the increasing strain in the films. Magnesium

doping also affects the intensity of the diffraction peak (002). An increase in the degree of doping leads to a decrease in the intensity of peak (002) compared to the similar peak in the unalloyed ZnO film (see Figs. 1, 2).

Fig. 3 shows the optical transmittance spectra of MZO films at different Mg concentrations. Obviously, with increasing  $\text{Mg}^{2+}$  concentration, the optical transmittance in the visible range increased. ZnO films doped with Mg atoms (from 1 to 15 at. %) have high transmittance from 70 to 85 % in the visible and near-infrared radiation regions. It can be seen that the ZnO film has high transmittance starting from wavelength of 387 nm. The doped MZO film (15 at. % Mg) has a high transmittance of 85 % starting from a wavelength of  $\sim 358$  nm. When doped with Mg, transparency of the MZO film increased by 15 % compared to the undoped ZnO film, and reached its highest value at 15 at. % Mg addition. The transmission spectra of MZO thin films have a

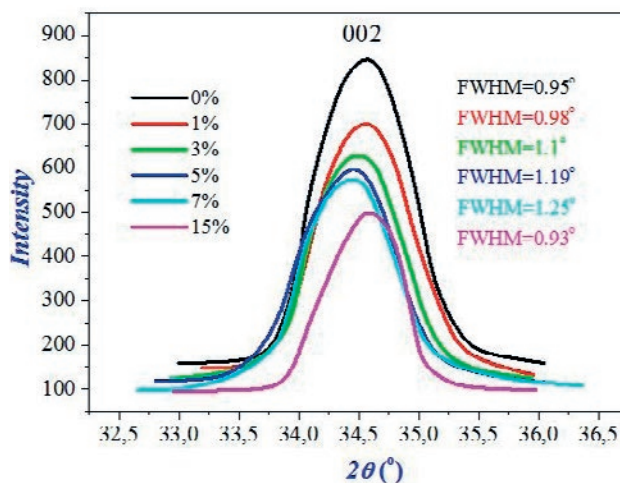
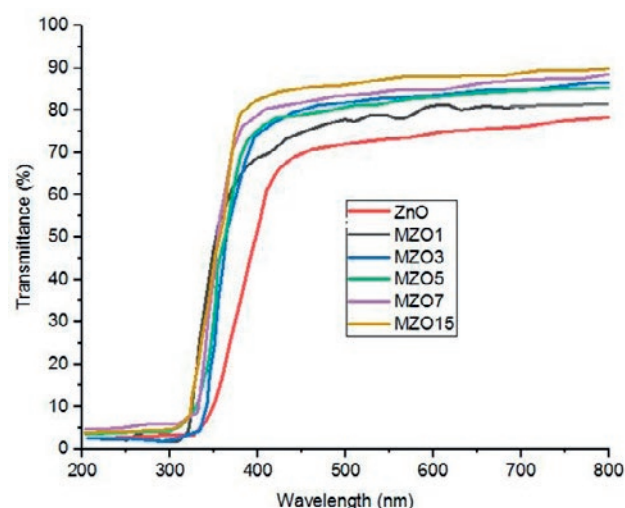


Fig. 2. Shape of reflections (002) of X-ray diffraction patterns of undoped and Mg-doped (from 1 to 15 at. %) ZnO films

Table 1. Characteristics of ZnO:Mg films obtained on the basis of X-ray diffraction data

Sample	Peak position (002) ( $2\theta$ ), degree	Crystallite size $D$ , nm	Lattice deformation $\varepsilon$ , degree	Dislocation density $\delta$ , $\text{nm}^{-1}$
MZO	34.56	92.9	$-1.15 \cdot 10^{-3}$	$1.16 \cdot 10^{-4}$
MZO1	34.54	87.6	$-1.72 \cdot 10^{-3}$	$1.30 \cdot 10^{-4}$
MZO3	34.50	78.5	$-2.7 \cdot 10^{-3}$	$1.62 \cdot 10^{-4}$
MZO5	34.46	73.05	$-3.46 \cdot 10^{-3}$	$1.87 \cdot 10^{-4}$
MZO7	34.44	69.07	$-4.19 \cdot 10^{-3}$	$2.09 \cdot 10^{-4}$
MZO15	34.59	93.02	$-1.154 \cdot 10^{-3}$	$1.15 \cdot 10^{-4}$



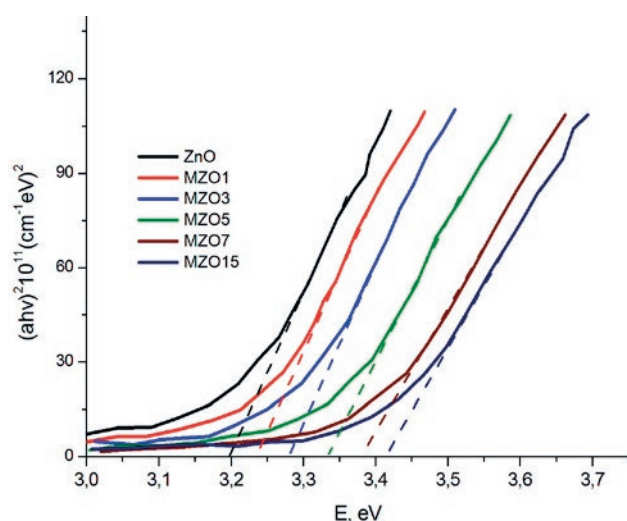


**Fig. 3.** Optical transmission spectra of pure ZnO films and ZnO films with different Mg dopant content

transparency of more than 80 % in the visible and infrared spectral regions. The transparency limit is in the ultraviolet range [10]. The effect of Mg doping on the bandgap width of MZO thin films was studied by the absorption spectra shown in Fig. 4. The bandgap width of unalloyed ZnO thin films and Mg-doped ZnO films was determined by the Tautz method [11] whose value can be estimated through the following expression:

$$\alpha h\nu = B(h\nu - E_g)^2, \quad (4)$$

where  $\alpha$  is the absorption factor,  $h\nu$  is the photon energy calculated on the basis of experimental results of optical transmittance ( $B$ );  $E_g$  is the for-



**Fig. 4.** Optical absorption spectra of pure ZnO films and ZnO films with different Mg dopant content

bidden band width. The absorption factor ( $\alpha$ ) can also be calculated through the following expression from transmittance ( $B$ ):

$$\alpha = \frac{1}{d} \ln \frac{1}{B}, \quad (5)$$

where  $d$  is the layer thickness.

The forbidden band width of ZnO film was 3.20 eV which is the same as in ZnO films prepared by other authors [12]. Fig. 4 shows that after Mg doping, the bandgap width of ZnO gradually increased from 3.20 eV (unalloyed ZnO film) to 3.42 eV (MZO15 film with Mg content of 15 at. %). It is due to defects probably arising as a result of replacement of  $\text{Mg}^{2+}$  ions by  $\text{Zn}^{2+}$  ions in the crystal lattice of MZO film. It is known that the value of  $\text{Mg}^{2+}$  ion radius (0.57 Å) is close to that of  $\text{Zn}^{2+}$  ion radius (0.60 Å); therefore, when doping ZnO films with magnesium, inclusion of  $\text{Mg}^{2+}$  ion in the ZnO lattice is likely [13]. According to the Poling scale, their electronegativities are 1.65 for Zn and 1.31 for Mg. Due to difference in electronegativities of Zn and Mg atoms and ionic radius, formation of new point defects in the structure can cause an increase in the width of the forbidden zone. In addition, the difference in electronegativities of Zn and Mg atoms increases the width of the forbidden zone due to interaction of  $\text{Mg}^{2+}$  and  $\text{O}^{2-}$  ions. It should also be noted that the compound MgO ( $E_g = 7.8$  eV) has a larger bandgap width than ZnO ( $E_g = 3.20$  eV) [14].

#### 4. Conclusions

In the course of the present research, ZnO thin films doped with Mg in various concentrations from 1 to 15 at. % were prepared by spray pyrolysis. Based on the analysis of X-ray diffraction patterns, an obvious growth of MZO films along the plane (002) with hexagonal wurtzite structure was established. With increased Mg concentration, light transmittance of MZO films increases from 70% to 85% in the visible region of the spectrum. The forbidden band width of MZO films increased with increased Mg content in the ZnO structure from 3.20 to 3.42 eV.

Properties of magnesium-doped ZnO thin films prepared can be used in many optoelectronic devices such as solar cells, gas sensors, as photocatalysts, etc.

## Contribution of the authors

E. S. Rembeza responsible for scientific guidance, discussion of final conclusions, scientific editing of the paper. S. Z. Zaynobidinov responsible for scientific guidance, research concept, methodology, discussion of final conclusions. M. B. Rasulova responsible for conducting the research, discussion of final conclusions, writing the review and the text of the paper.

## Conflict of interests

The authors declare that they have no known competing financial interests or personal relationships that could have influenced the work reported in this paper.

## References

1. Rembeza S. I., Rembeza E. S., Svistova T. V., Kosheleva N. N. *Synthesis and properties of metal oxide films*\*. Voronezh: Voronezh State Technical University Publ.; 2017. p. 34–55. (In Russ.)
2. Zaynabidinov S. Z., Yuldashev Sh. U., Boboev A. Y., Yunusaliyev N. Yu. X-ray diffraction and electron microscopic studies of the ZnO(S) metal oxide films obtained by the ultrasonic spray pyrolysis method. *Herald of the Bauman Moscow State Technical University, Series Natural Sciences*. 2024;1(112): 78–92. <https://doi.org/10.18698/1812-3368-2024-1-78-92> (in Russ.)
3. Zainabidinov S. Z., Boboev A. Y., Makhmudov H. A. Synthesis, structure and photoelectric properties of ZnO thin films\*. *Reports of the Academy of Sciences of the Republic of Uzbekistan*. 2021;3: 15–18. (In Russ.)
4. Zinchenko T. O., Pecherskaya E. A. Analysis of materials used for the production of transparent conductive coatings\*. *Information technologies in science and education. Problems and prospects: Proc. V All-Russian Interuniversity Scientific and Practical Conf., March 14, 2018, Penza*. Penza: Penza State University Publ.; 2018. p. 256–258. (In Russ.)
5. Kytin V. G., Kulbachinsky V. A., Glebov D. S., Burova L. I., Kaul A. R., Reukova O. V. The conductivity and magnetic properties of zinc oxide thin films doped with cobalt. *Semiconductors*. 2010;44(2): 155–160. <https://doi.org/10.1134/S1063782610020053>
6. Rouchdi M., Salmani E., Fares B., Hassanai N., Mzard A. Synthesis and characteristics of Mg doped ZnO thin films: Experimental and ab-initio study. *Results in Physics*. 2017;7: 620–627. <https://doi.org/10.1016/j.rinp.2017.01.023>
7. Yuldashev Sh., Zainabidinov S., Yunusaliyev N. Ultrasonic technology for the production and properties of ZnO<S> films\*. *Scientific Bulletin Physical and Mathematical Research*. 2022;2: 60–64. (In Russ.)
8. Rembeza E. S., Yulchiev Sh. Kh., Rasulova M. B. Structure, properties and applications of ZnO metal oxide films\*. *Scientific Bulletin Physical and Mathematical Research*. 2022;2(4): 5–11. (In Russ.)
9. *Advanced X-ray Techniques in Research And Industries*. A. K. Singh (ed.). IOS Press Inc., 2005. 594 p.
10. Rabadanov M. R., Rabadanov R. A. *Process of production of monocrystalline zinc oxide with fast radiation in ultraviolet region of the spectrum*. Patent RF, no. 2202010. Publ. 10.04.2003, bull. no. 10-2 c. Available at: [https://patents.s3.yandex.net/RU2202010C1\\_20030410.pdf](https://patents.s3.yandex.net/RU2202010C1_20030410.pdf)
11. Tauc J. *The Optical Properties of Solids*. New York: Academic Press; 1966. 448 p.
12. Srikant V., Clarke D. R. On the optical band gap of zinc oxide. *Journal of Applied Physics*. 1998;83(10): 5447–5451. <https://doi.org/10.1063/1.367375>
13. Çağlar M., Wu J., Li K., Caglar Y., Ilican S., Xue D. F. Mg<sub>x</sub>Zn<sub>1-x</sub>O films fabricated by sol-gel spin coating. *Materials Research Bulletin*. 2010;45: 284–287. <https://doi.org/10.1016/j.materresbull.2009.12.025>
14. Heo S., Cho E., Hyung-Ik L., ... Choi B. D. Band gap and defect states of MgO thin films investigated using reflection electron energy loss spectroscopy. *AIP Advances*. 2015;5(7): 077167. <https://doi.org/10.1063/1.4927547>

\*Translated by author of the article

## Information about the authors

Ekaterina S. Rembeza, Dr. Sci. (Phys.-Math.), Professor at the Department of General Physics, Voronezh State University (Voronezh, Russian Federation).

<https://orcid.org/0000-0003-0811-0979>  
rembeza@phys.vsu.ru

Sirojiddin Z. Zaynobiddinov, Dr. Sci. (Phys.-Math.), Professor, Academician of the Academy of Sciences of the Republic of Uzbekistan (Andijan, Republic of Uzbekistan).

<https://orcid.org/0000-0003-2943-5844>  
prof\_sirojiddin@mail.ru

Markhabo B. Rasulova, Doctoral student of the Andijan Engineering Institute (Andijan, Republic of Uzbekistan).

Received 25.04.2024; approved after reviewing 02.12.2024; accepted for publication 16.12.2024; published online 25.06.2025.



## Original articles

Research article

<https://doi.org/10.17308/kcmf.2025.27/12810>

## Diffraction studies of the PA MBE grown of GaN layers on silicon substrates without their nitridation and an intermediate AlN nucleation layers

P. V. Seredin<sup>1</sup>✉, O. K. Kosheleva<sup>1</sup>, D. L. Goloshchapov<sup>1</sup>, N. S. Builov<sup>1</sup>, Ya. A. Peshkov<sup>1</sup>, A. M. Mizerov<sup>2</sup>, S. N. Timoshnev<sup>2</sup>, M. S. Sobolev<sup>2</sup>, Sh. Sh. Sharofidinov<sup>3</sup>

<sup>1</sup>Voronezh State University,  
Universitetskaya pl. 1, Voronezh 394018, Russian Federation

<sup>2</sup>Alferov University,  
8 ul. Khlopina, Bld. 3, letter A, Saint Petersburg 194021, Russian Federation

<sup>3</sup>Ioffe Physical Technical Institute, Russian Academy of Sciences,  
26 Politekhnikeskaya st., Saint Petersburg 194021, Russian Federation

### Abstract

**Purpose:** The paper describes structural features of the growth of GaN layers synthesized by plasma-assisted molecular beam epitaxy on silicon substrates without substrate nitridation and without the formation of an aluminum-containing interlayer.

**Experimental:** High-resolution X-ray diffraction was used to show that the proposed method can be used to grow strain-free GaN films.

It was found that in GaN layers grown directly on the Si substrate after its surface passivation by Ga atoms, the value of residual strain was at 300 MPa, while the use of indium atoms as a surfactant during the growth of the GaN layer resulted in a higher residual strain.

**Conclusions:** The obtained results are important for understanding the viability of the proposed approach for the formation of GaN layers directly integrated with Si without substrate nitridation and the formation of an aluminum-containing buffer. This method opens new opportunities for designing AlInN-based optoelectronic devices.

**Keywords:** Plasma-assisted molecular beam epitaxy, GaN layers, Silicon substrate, X-ray diffraction, Strain-free GaN films

**Funding:** The study was carried out within the framework of the grant of the Ministry of Education and Science of the Russian Federation (project No. FZGU-2023-0006). PA MBE synthesis of the samples was carried out as a part of the grant provided by the Ministry of Science and Higher Education of the Russian Federation (grant No. FSRM-2023-0006).

**Acknowledgements:** The research was carried out using the equipment of the Laboratory of Gallium Nitride and Silicon Electronics of Voronezh State University and the Research Institute of Electronic Technology.

**For citation:** Seredin P. V., Kosheleva O. K., Goloshchapov D. L., Builov N. S., Peshkov Y. A., Mizerov A. M., Timoshnev S. N., Sobolev M. S., Sharofidinov Sh. Sh. Diffraction studies of the PA MBE grown of GaN layers on silicon substrates without their nitridation and an intermediate AlN nucleation layer. *Condensed Matter and Interphases*. 2025;27(2): 308–315. <https://doi.org/10.17308/kcmf.2025.27/12810>

**Для цитирования:** Середин П. В., Кошелева О. К., Голощапов Д. Л., Буйлов Н. С., Пешков А. Я., Мизеров А. М., Тимошнев С. Н., Соболев М. С., Шарофидинов Ш. Ш. Дифрактометрические исследования особенностей формирования слоев GaN на подложках кремния методом МПЭ ПА без использования процедуры нитридации подложки и промежуточного AlN зародышевого слоя. *Конденсированные среды и межфазные границы*. 2025;27(2): 000-000. <https://doi.org/10.17308/kcmf.2025.27/12810>

✉ Pavel V. Seredin, e-mail: [paul@phys.vsu.ru](mailto:paul@phys.vsu.ru)

© Seredin P. V., Kosheleva O. K., Goloshchapov D. L., Builov N. S., Peshkov Y. A., Mizerov A. M., Timoshnev S. N., Sobolev M. S., Sharofidinov Sh. Sh., 2025



The content is available under Creative Commons Attribution 4.0 License.



## 1. Introduction

AlIIN semiconductors, with GaN being the most prominent example, have excellent electrophysical and optical properties that make them ideal for their use in high-power, high-frequency electronic devices [1,2]. However, there are still some unresolved problems related to the growth of high quality AlIIN layers on silicon substrates, which are most affordable for the production of microelectronic devices. These problems are associated with significant differences in the parameters of crystal lattices and thermal expansion coefficients [3].

Over the past decades, many methods have been proposed to reduce number of defects in the operating area [4, 5], with the most prominent of them being the use of Al transition and buffer layers. However, methods for optimizing AlIIN growth conditions vary depending on the used substrate. Interestingly, several studies have demonstrated that optical and electronic devices can be manufactured without intermediate layers like AlN or AlGaIn.

In our previous work concerned with the study of the initial stages of plasma-assisted molecular beam epitaxy (PA MBE) of GaN layers on Si(111) substrates, it was demonstrated that the smoothest surfaces of GaN layers on Si(111) substrates can be obtained either without pre-epitaxial substrate nitridation or after high-temperature nitridation ( $T_N = 850\text{ }^{\circ}\text{C}$ ) [6]. Therefore, it is extremely important to study the mechanisms of nitride growth in the region of the epitaxial layer/substrate hetero-interface, which would effectively reduce the elastic stresses to a level where microcracks and defects are not formed in the operating area. Thus, this paper describes the results of diffractometric studies of the peculiarities of PA MBE growth of GaN layers on silicon substrates without substrate nitridation and the formation of an intermediate AlN nucleation layer under Ga-enriched conditions and with additional In flow intended in order to increase the surface mobility of adatoms.

## 2. Materials and methods

In the study, the GaN epitaxial layers were grown by PA MBE technique on a Veeco Gen 200 setup, which allows simultaneously using up to 4

four-inch plates (or one substrate with a diameter of up to 200 mm) during the growth process [6]. Undoped GaN layers were grown on semi-insulating Si(111) substrates ( $R > 10,000\text{ Ohm/cm}$ ) that had been treated using the Shiraki method.

The PA MBE synthesis of GaN layers consisted of two stages. First, a low-temperature LT-GaN nucleation layer with a thickness of  $\sim 10\text{ nm}$  was grown. Then (second stage), the main GaN layer was grown, which for A-type samples was synthesized at  $T_p = 720\text{ }^{\circ}\text{C}$ , while for B-type samples, the main GaN layer was under a similar nitrogen flow, but at a lower temperature of  $T_p = 700\text{ }^{\circ}\text{C}$ , with the addition of indium flow intended to increase the surface mobility of the adatoms and consequently achieve a smoother GaN surface.

Reflection high-energy electron diffraction (RHEED) was used for in-situ observation of the nucleation and changes in the surface morphology of the GaN/Si(111) layers. It was found that the onset of the growth was accompanied by a decrease in the intensity of the initial RHEED pattern of the substrate followed by the formation of misoriented LT-GaN grains ("polycrystalline" RHEED pattern) characteristic of nucleation. At the beginning of the main GaN layer growth, there was a gradual formation of a "dot" RHEED pattern, characteristic of the growth of a continuous layer with a developed surface morphology. Further growth of the main GaN layer was accompanied by a transition from a "dot" to "linear" RHEED pattern, indicating a transition from nanocolumnar to two-dimensional growth.

Fig. 1 schematically shows the technological profiles of the grown samples.

High-resolution X-ray diffraction data were obtained at 305 K using a DRON-8T diffractometer. The  $2\theta$ - $\omega$  scans and  $\omega$  rocking curves (XRC) were taken using  $\text{CuK}_{\alpha}$  radiation with an angular reproducibility of  $\pm 0.0001^{\circ}$ . High resolution was achieved with the help of a Ge(220) $\times$ 4 Bartels monochromator and a 0.05 mm slit installed in front of the detector.

Processing and analysis of experimental diffractometric data (smoothing, fitting, baseline removal, determination of centers of maximum) were performed using the Fityk, OriginPro software packages (OriginLab Corporation) [7].



### 3. Results and discussion

Fig. 2 shows the X-ray diffraction results for GaN/Si (111) heterostructures. Only two reflections were observed in the  $2\theta$ - $\omega$  scans. The first one (less intense) was a reflection from (111) plane of the silicon substrate, and the second, (0002), was a reflection from the GaN plane, respectively. No other reflections were detected, indicating that the grown GaN layer was in a monocrystalline state and had a hexagonal lattice with wurtzite structure.

To determine the crystalline quality of the epitaxial films, symmetric and asymmetric

X-ray  $2\theta$ - $\omega$  scans and high-resolution  $\omega$  rocking curves were obtained for the (0002) and  $(10\bar{1}2)$  planes. The results are shown in Fig. 3. It can be seen that the Bragg angle of the maxima of the symmetric and asymmetric reflections in the  $2\theta$ - $\omega$  scans (Fig. 3a, c) differ between samples A and B, which means that they have different parameters of the crystal lattice of the GaN layer.

Moreover, besides the main high-intensity maxima, the  $2\theta$ - $\omega$   $(10\bar{1}2)$  scan for sample A (Fig. 3C) has an additional diffraction pattern (in the region of large Bragg angles). There is

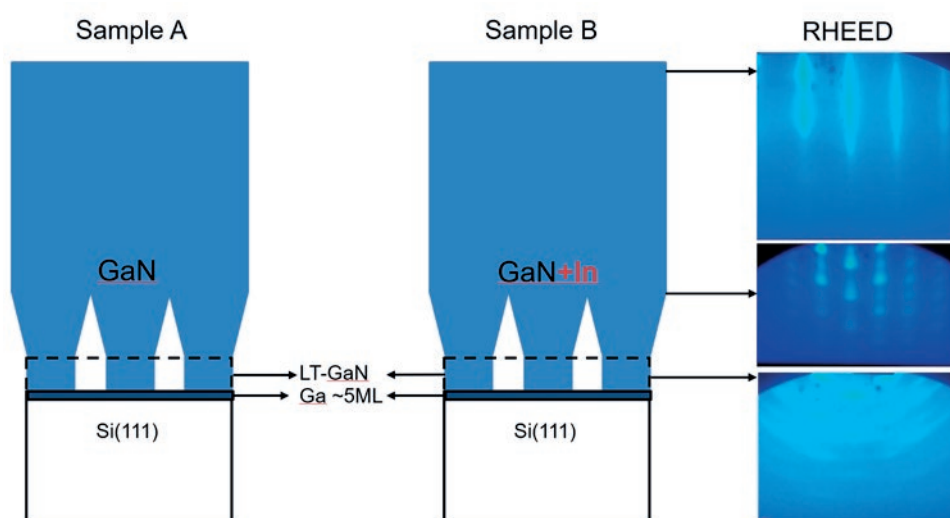


Fig. 1. Schematic representation of samples GaN/Si(111) heterostructures

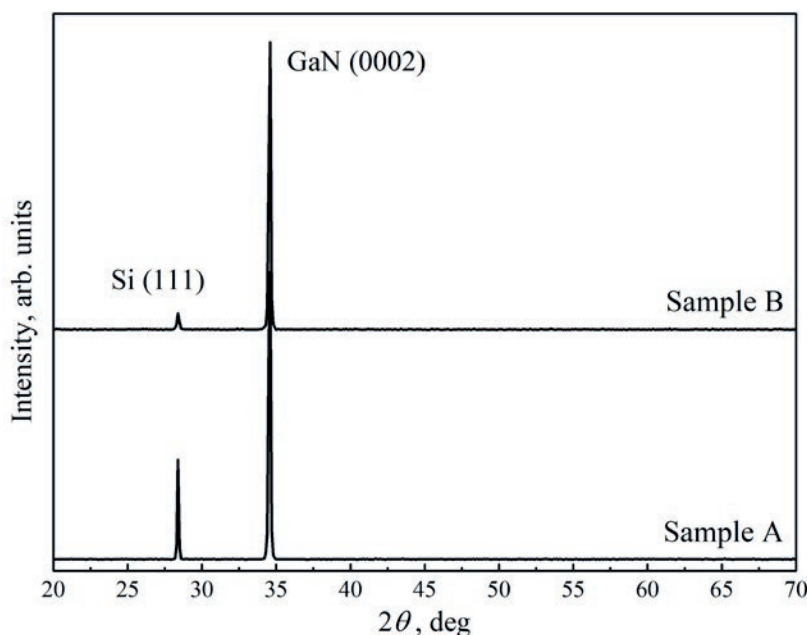


Fig. 2. XRD  $2\theta$ -scans for the GaN/Si(111) heterostructures

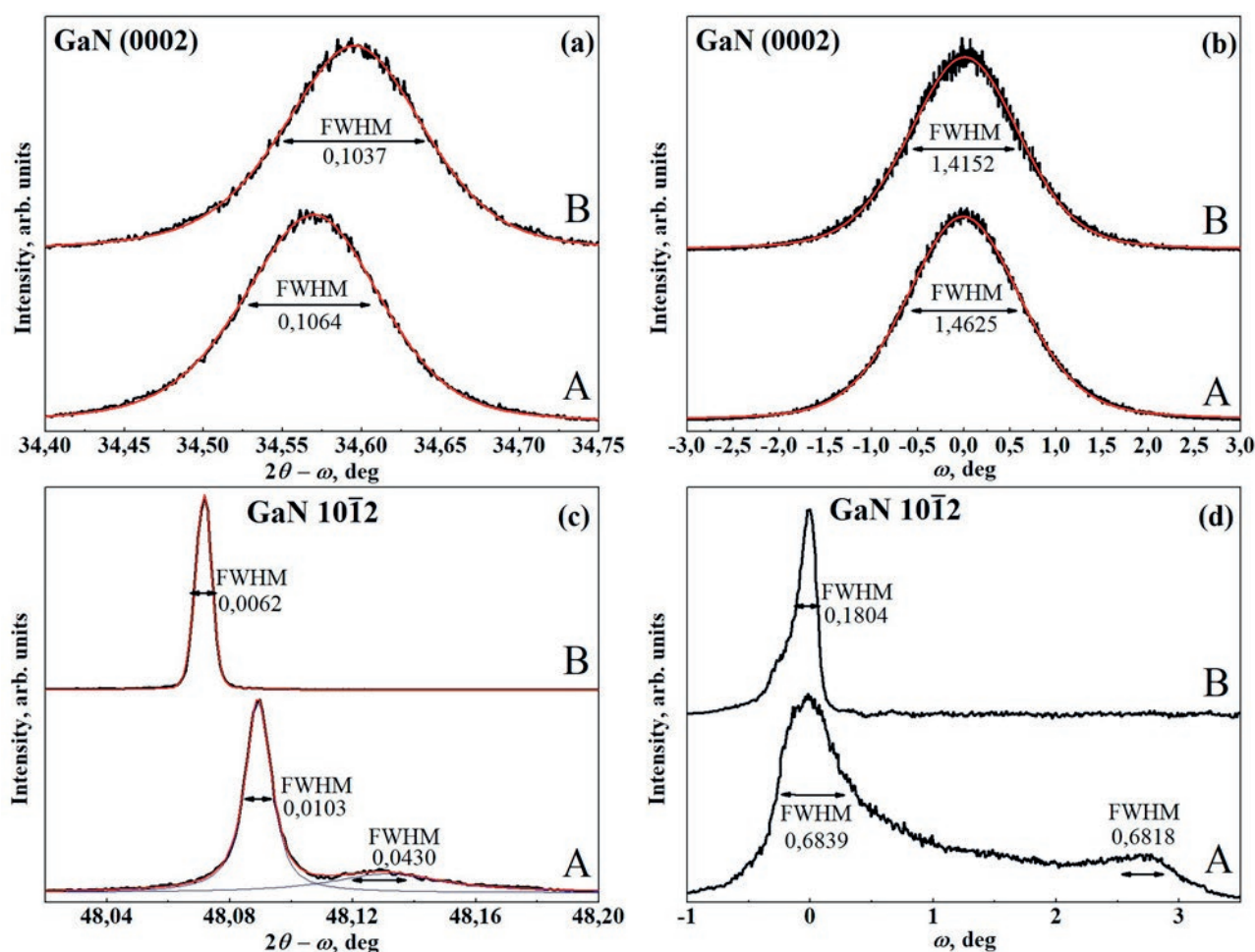


Fig. 3. XRD 2 $\theta$ -scans (a,c) and  $\omega$ -swing curves (b,d) GaN/Si(111) samples

also an additional low-intensity maximum at the (10 $\bar{1}2$ ) of the  $\omega$  rocking curve for sample A (Fig. 3d). These facts may indicate that a sublayer with a smaller lattice parameter than that of the main GaN layer was formed in sample A.

For each diffraction maximum, the full width at half maximum (FWHM) was determined using XRD scans. The analysis of FWHM values provided further information on the crystalline quality of the samples. Thus, the FWHM of the diffraction reflection in the 2 $\theta$ - $\omega$  scan showed the presence of inhomogeneous deformation and changes in the grains size of the sample. Additionally, the FWHM of the maximum in the  $\omega$  rocking curve provided information on the orientation of the crystallites in the epitaxial layer, i.e. mosaic structure.

The analysis of the obtained results (Fig. 3) revealed that the FWHMs of the main diffraction maximum in the 2 $\theta$ - $\omega$  and  $\omega$ -scans for the (0002) plane had similar values for samples A and B, while the FWHM of the (10 $\bar{1}2$ ) reflection was lower for sample B. This may also indicate that in the direction of growth of the GaN layer, both samples had the same relaxation values and degrees of mosaic structure, while in the growth plane these values, as well as the lattice parameters, differed between the samples. The measured FWHM (0002) values in the 2 $\theta$ - $\omega$  scans for samples A and B were 360 and 350 arcseconds, respectively. We compared the obtained values with those presented in the study by Jae-Hoon Lee et al. [8] where a high-quality GaN layer (~1.5  $\mu\text{m}$ ) with reduced stress and dislocation density was grown on Si substrate. As a result,

it can be concluded that the FWHM values for the (0002) plane were similar while the FWHM value for the (10 $\bar{1}2$ ) plane was much lower. Also, the FWHM values for the (0002) plane on the  $\omega$  rocking curves were much higher than the FWHM value in the  $2\theta$ - $\omega$  scans. It means that at the same value of the film's mosaic structure GaN layer should have better relaxation in the growth direction.

Asymmetric X-ray diffraction scans for the (10 $\bar{1}2$ ) plane provided information for directions coinciding with  $a$  and  $c$  axes of the wurtzite lattice [9]. The FWHM value for the (10 $\bar{1}2$ ) reflection was higher in the  $\omega$  scans than in the  $2\theta$ - $\omega$  scans. This indicates at a lower stress due to the lattice mismatch in this direction; however, it also means more pronounced mosaic structure. Moreover, the FWHM value for the (10 $\bar{1}2$ ) reflection in the  $\omega$ -scan for sample A was significantly higher than that one for sample B.

It is well known that an increase in the FWHM of X-ray reflections, which is associated with both the orientation and microdeformation of crystallites in the epitaxial layer, represents the formation and changes in the density of screw (c-type) dislocations along  $c$  crystal axis and edge (a-type) threading dislocations. In [10], it was shown that the values of the density of screw and edge dislocations in the epitaxial layers of nitrides can be estimated by  $\omega$  rocking curves based on the following relations [11]:

$$D_s = \frac{\beta_{0002}^2}{4.35b_s^2} \quad (1)$$

$$D_E = \frac{\beta_{10\bar{1}2}^2}{4.35b_E^2} \quad (2)$$

Here,  $\beta_{0002}$  and  $\beta_{10\bar{1}2}$  are the FWHMs for the symmetric and asymmetric omega scans, while  $b_s = 5.1864 \text{ \AA}$  and  $b_E = 3.1890 \text{ \AA}$  are the lengths of the Burgers vectors. The calculations showed (see Table 1) that the density of screw dislocations in the epitaxial layer of GaN in both samples was higher than that one of the edge dislocations. However, the density of screw and edge dislocations in sample B was lower than in the sample A.

HRXRD data were used to determine lattice constants  $a$  and  $c$  for the epitaxial layer with the wurtzite structure [12].

Experimentally obtained values of the lattice constants were used to determine the relaxation coefficient  $R$  of GaN layer relative to the Si substrate, the biaxial stress coefficient, and the residual stresses (see Table 1).

The lattice relaxation in the epitaxial layer can be calculated by the formula:

$$R = \frac{a_e - a_s}{a_0 - a_s} \quad (3)$$

where  $a_e$  is the lattice parameter measured experimentally;  $a_s$  is the lattice parameter equivalent to that one which the layer would take if it was completely deformed; and  $a_0$  is the lattice parameter which the layer would take in the bulk state.

The monocrystalline silicon (substrate) oriented along the (111) direction had the effective lattice parameter  $a_s = 3.84 \text{ \AA}$  [13]. The values of the lattice parameter for unstressed GaN were taken from previous studies:  $c_0 = 5.1864 \text{ \AA}$ ,  $a_0 = 3.1890 \text{ \AA}$  [14,15].

The obtained results (Table 1) indicate that GaN layer grown on a Si substrate by the proposed method was almost ~99% strain-free for the samples of both types.

Since the  $a$  parameter of the GaN wurtzite lattice is larger than the effective lattice parameter of the silicon substrate with (111) orientation, cooling of the sample after its growth is accompanied by appearance of biaxial deformation in the GaN epitaxial layer [16]. The in-plane biaxial stress  $\sigma_{xx}$  of GaN can be calculated as follows [17–19]:

$$\sigma_{xx} = -M\varepsilon_{xx}. \quad (4)$$

Deformations in the  $\varepsilon_{xx}$  plane (along the  $a$ -axis) and in the direction of the  $\varepsilon_{xx}$  growth (along the  $c$ -axis) were calculated as follows [20]:

$$\varepsilon_{xx} = \frac{a_e - a_0}{a_0}, \varepsilon_{zz} = \frac{c_e - c_0}{c_0} \quad (5)$$

$M$  is biaxial elastic modulus.

$$M = C_{11} + C_{12} - 2\frac{C_{13}^2}{C_{33}} \quad (6)$$

**Table 1.** Results of X-ray diffractometry, Raman and PL spectroscopy

Sample	Structure component	Lattice parameter, Å		Dislocation density		Relaxation coefficient, R, %	Level of residual biaxial stresses, $\sigma_{xx}$ , GPa
		$c_e$	$a_e$	Screw dislocations, $D_s$	Edge dislocations, $D_E$	–	
A	GaN	5.1850	3.1903	$5.1 \cdot 10^{-10}$	$3.1 \cdot 10^{-10}$	99.7 %	0.270
	GaN- bound	5.1850	3.1582	–	–	–	–
	Si	–	5.432	–	–	–	–
B	GaN	5.1813	3.1952	$5.0 \cdot 10^{-10}$	$2.1 \cdot 10^{-9}$	99.0%	0.930
	Si	–	5.427	–	–	–	–

According to (8), for GaN with a wurtzite lattice  $M \sim 479 \text{ ГПа}$ .

The calculations showed (see Table 1) that the level of residual in-plane biaxial stress for sample A was at  $\sim 270 \text{ МПа}$ , while for sample B it was almost three times higher and attained up to  $\sim 930 \text{ МПа}$ .

#### 4. Conclusions

The paper describes the structural features of the growth of GaN layers synthesized by PA MBE on silicon substrates without substrate nitridation and without the formation of an intermediate aluminum-containing layer.

High-resolution X-ray diffractometry was used to show that the suggested method can be used to grow strain-free GaN films.

It was found that in GaN layers grown directly on the Si substrate after the passivation of its surface with Ga atoms, the value of residual strain is of  $300 \text{ МПа}$ , while the use of indium atoms as a surfactant during the growth of the GaN layer results in a higher residual strain.

The obtained results are important for understanding the viability of the proposed approach for the formation of GaN layers directly integrated with Si without substrate nitridation and formation of an aluminum-containing buffer. This method opens up new opportunities for designing AlInN-based optoelectronic devices.

#### Contribution of the authors

The authors contributed equally to this article.

#### Conflict of interests

The authors declare that they have no known competing financial interests or personal relationships that could have influenced the work reported in this paper.

#### References

1. Li J., Xu Y., Tao J., ... Xu K. Study on nucleation and growth mode of GaN on patterned graphene by epitaxial lateral overgrowth. *Crystal Growth & Design*. 2023;23(8): 5541–5547. <https://doi.org/10.1021/acs.cgd.3c00171>
2. Almalawi D., Lopatin S., Edwards P. R., ... Roqan I. S. Simultaneous growth strategy of high-optical-efficiency GaN NWs on a wide range of substrates by pulsed laser deposition. *ACS Omega*. 2023;8(49): 46804–46815. <https://doi.org/10.1021/acsomega.3c06302>
3. Lim S. H., Bin Dolmanan S., Tong S. W., Liu H. Temperature dependent lattice expansions of epitaxial GaN-on-Si heterostructures characterized by in- and ex-situ X-ray diffraction. *Journal of Alloys and Compounds*. 2021;868: 159181. <https://doi.org/10.1016/j.jallcom.2021.159181>
4. Seredin P. V., Lenshin A. S., Zolotukhin D. S., Arsenyev I. N., Zhabotinskiy A. V., Nikolaev D. N. Impact of the substrate misorientation and its preliminary etching on the structural and optical properties of integrated GaAs/Si MOCVD heterostructures. *Physica E: Low-dimensional Systems and Nanostructures*. 2018;97: 218–225. <https://doi.org/10.1016/j.physe.2017.11.018>
5. Seredin P. V., Goloshchapov D. L., Lenshin A. S., Mizerov A. M., Zolotukhin D. S. Influence of por-Si sublayer on the features of heteroepitaxial growth and physical properties of  $\text{In}_x\text{Ga}_{1-x}\text{N}/\text{Si}(111)$  heterostructures with nanocolumn morphology of thin film. *Physica E: Low-dimensional Systems and Nanostructures*. 2018;104: 101–110. <https://doi.org/10.1016/j.physe.2018.07.024>
6. Mizerov A. M., Timoshnev S. N., Sobolev M. S., ... Bouravleuv A. D. Features of the initial stage of GaN growth on Si(111) substrates by nitrogen-plasma-assisted molecular-beam epitaxy. *Semiconductors*. 2018;52(12): 1529–1533. <https://doi.org/10.1134/S1063782618120175>



7. Vasilkova E. I., Pirogov E. V., Sobolev M. S., Ubiyovk E. V., Mizerov A. M., Seredin P. V. Molecular beam epitaxy of metamorphic buffer for InGaAs/InP photodetectors with high photosensitivity in the range of 2.2–2.6  $\mu\text{m}$ . *Condensed Matter and Interphases*. 2023;25(1): 20–26. <https://doi.org/10.17308/kcmf.2023.25/10972>
8. Seredin P. V., Glotov A. V., Domashevskaya E. P., Arsentyev I. N., Vinokurov D. A., Tarasov I. S. Structural features and surface morphology of  $\text{Al}_x\text{Ga}_{1-x}\text{In}_{1-x-y}\text{As}_y\text{P}_{1-z}/\text{GaAs}(1\ 0\ 0)$  heterostructures. *Applied Surface Science*. 2013;267: 181–184. <https://doi.org/10.1016/j.apsusc.2012.09.053>
9. Lee J.-H., Im K.-S. Growth of high quality GaN on Si (111) substrate by using two-step growth method for vertical power devices application. *Crystals*. 2021;11(3): 234. <https://doi.org/10.3390/cryst11030234>
10. Zheng C. D., Mo C. L., Fang W. Q., Jiang F. Y. Effect of the conduction type of Si (111) substrates on the performance of GaN MQW LED epitaxial films. *Advanced Materials Research*. 2013;750–752: 1029–1033. <https://doi.org/10.4028/www.scientific.net/AMR.750-752.1029>
11. Ene V. L., Dinescu D., Djourelou N., ... Andronescu E. Defect structure determination of GaN films in GaN/AlN/Si heterostructures by HR-TEM, XRD, and slow positrons experiments. *Nanomaterials*. 2020;10(2): 197. <https://doi.org/10.3390/nano10020197>
12. Lee H.-P., Perozek J., Rosario L. D., Bayram C. Investigation of AlGaIn/GaN high electron mobility transistor structures on 200-mm silicon (111) substrates employing different buffer layer configurations. *Scientific Reports*. 2016;6(1): 37588. <https://doi.org/10.1038/srep37588>
13. Xue J. J., Chen D. J., Liu B., ... Zhang J. P. Indium-rich InGaIn epitaxial layers grown pseudomorphically on a nano-sculpted InGaIn template. *Optics Express*. 2012;20(7): 8093. <https://doi.org/10.1364/OE.20.008093>
14. Ng T. K., Holguin-Lerma J. A., Kang C. H., ... Ooi B. S. Group-III-nitride and halide-perovskite semiconductor gain media for amplified spontaneous emission and lasing applications. *Journal of Physics D: Applied Physics*. 2021;54(14): 143001. <https://doi.org/10.1088/1361-6463/abd65a>
15. Morkoç H. *Handbook of nitride semiconductors and devices: materials properties, physics and growth*. 1st ed. Wiley; 2008. <https://doi.org/10.1002/9783527628438>
16. *Group IV elements, IV-IV and III-V compounds. Part a - lattice properties*. Madelung O., Rössler U., Schulz M. (eds.). Berlin/Heidelberg: Springer-Verlag; 2001; a1–7. <https://doi.org/10.1007/b60136>
17. Kisielowski C., Krüger J., Ruvimov S., ... Davis R. F. Strain-related phenomena in GaN thin films. *Physical Review B*. 1996;54(24): 17745–17753. <https://doi.org/10.1103/PhysRevB.54.17745>
18. Harutyunyan V. S., Aivazyan A. P., Weber E. R., Kim Y., Park Y., Subramanya S. G. High-resolution X-ray diffraction strain-stress analysis of GaN/sapphire heterostructures. *Journal of Physics D: Applied Physics*. 2001;34(10A): A35–A39. <https://doi.org/10.1088/0022-3727/34/10A/308>
19. Seredin P. V., Glotov A. V., Ternovaya V. E., ... Tarasov I. S. Effect of silicon on relaxation of the crystal lattice in MOCVD-hydride  $\text{Al}_x\text{Ga}_{1-x}\text{As}/\text{Si}/\text{GaAs}(100)$  heterostructures. *Semiconductors*. 2011;45(4): 481–492. <https://doi.org/10.1134/S106378261104021X>
20. Seredin P. V., Leiste H., Lenshin A. S., Mizerov A. M. Effect of the transition porous silicon layer on the properties of hybrid GaN/SiC/por-Si/Si(1 1 1) heterostructures. *Applied Surface Science*. 2020;508: 145267. <https://doi.org/10.1016/j.apsusc.2020.145267>
21. Li Z., Jiu L., Gong Y., ... Wang T. Semi-polar (11-22) AlGaIn on overgrown GaN on micro-rod templates: simultaneous management of crystal quality improvement and cracking issue. *Applied Physics Letters*. 2017;110(8): 082103. <https://doi.org/10.1063/1.4977094>

## Information about the authors

**Pavel V. Seredin**, Dr. Sci. (Phys.–Math.), Full Professor, Chair of Department of Solid State Physics and Nanostructures, Voronezh State University (Voronezh, Russian Federation).

<https://orcid.org/0000-0002-6724-0063>

[paul@phys.vsu.ru](mailto:paul@phys.vsu.ru)

**Olga K. Kosheleva**, postgraduate student, Department of Solid State Physics and Nanostructures, Voronezh State University (Voronezh, Russian Federation).

<https://orcid.org/0009-0002-0068-0002>

[olgak-98@yandex.ru](mailto:olgak-98@yandex.ru)

**Dmitry L. Goloshchapov**, Cand. Sci. (Phys.–Math.), Assistant Professor, Department of Solid State Physics and Nanostructures, Voronezh State University (Voronezh, Russian Federation).

<https://orcid.org/0000-0002-1400-2870>

[goloshchapov@phys.vsu.ru](mailto:goloshchapov@phys.vsu.ru)

**Nikita S. Buylov**, Cand. Sci. (Phys.–Math.), Educator, Department of Solid State Physics and Nanostructures, Voronezh State University (Voronezh, Russian Federation).

<https://orcid.org/0000-0003-1793-4400>

[buylov@phys.vsu.ru](mailto:buylov@phys.vsu.ru)

**Yaroslav A. Peshkov**, Laboratory Research Assistant, Department of Solid State Physics and Nanostructures, Voronezh State University (Voronezh, Russian Federation).

<https://orcid.org/0000-0003-0939-0466>

[tangar77@mail.ru](mailto:tangar77@mail.ru)

**Mizerov Andrey Mikhailovich**, Cand. Sci. (Phys.–Math.), Leading Researcher, Alferov University, (Saint Petersburg, Russian Federation).

<https://orcid.org/0000-0002-9125-6452>

[andreymizerov@rambler.ru](mailto:andreymizerov@rambler.ru)

**Sergey N. Timoshnev**, Cand. Sci. (Phys.–Math.), Leading Researcher, Alferov University (Saint Petersburg, Russian Federation).

<https://orcid.org/0000-0002-9294-3342>

[timoshnev@mail.ru](mailto:timoshnev@mail.ru)

*Maksim S. Sobolev*, Cand. Sci. (Phys.–Math.), Acting Head of the Laboratory of Nanoelectronics, Alferov University (Saint Petersburg, Russian Federation).

<https://orcid.org/0000-0001-8629-2064>  
sobolevsms@gmail.com

*Shukrilo Sh. Sharofidinov*, Cand. Sci. (Phys.–Math.), Researcher, Ioffe Physical Technical Institute, Russian Academy of Sciences (Saint Petersburg, Russian Federation).

<https://orcid.org/0000-0003-0354-5981>  
shukrillo71@mail.ru

*Received 16.10.2024; approved after reviewing 30.10.2024; accepted for publication 15.11.2024; published online 25.06.2025.*



## Original articles

Research article

<https://doi.org/10.17308/kcmf.2025.27/12808>

## Effect of the re-emitting layer of organic thin film on the efficiency of silicon solar cells

A. S. Tyutyunik✉, V. S. Gurchenko, A. S. Mazinov

V. I. Vernadsky Crimean Federal University,  
4 prospekt Vernadskogo, Simferopol 295007, Russian Federation

### Abstract

**Purpose:** Photovoltaic solar energy conversion technologies represent promising pathways to clean and renewable energy production. Research on organic solar cells is actively developing, especially in the last decade it has attracted scientific and economic interest driven by the rapid increase in energy conversion efficiency. In recent years, luminescent materials capable of converting a broad spectrum of light into photons of a specific wavelength have been synthesized and used to minimize losses in the solar cell-based energy conversion process. This paper presents a study of the optical and luminescent properties of thin films of copper complexes  $C_{62}H_{50}Cu_2I_2N_8P_2$ .

**Experimental:** It is proposed to use this material as a re-emitting layer on the surface of a solar cell in order to increase the coefficient of performance (COP) of the latter by converting energy from the ultraviolet range to the visible range. A study of the volt-ampere characteristics of a pure single-crystal solar cell and a cell with an re-emitting copper complex layer has been carried out.

**Conclusions:** It is shown that deposition of  $C_{62}H_{50}Cu_2I_2N_8P_2$  on the surface of solar cells allows increasing the efficiency of converters by 1.45 % in the ultraviolet range at low economic costs. Mechanisms for enhancing energy conversion are discussed and recent experimental results on similar studies are analyzed.

**Keywords:** Solar cell, Photovoltaic converters, Optical spectrum, Luminescence, Thin films, Copper complexes

**Funding Source:** The study was supported by the grant of the Russian Science Foundation No. 23-22-10007 and the region of Crimea.

**For citation:** Tyutyunik A. S., Gurchenko V. S., Mazinov A. S. Effect of the re-emitting layer of organic thin film on the efficiency of silicon solar cells. *Condensed Matter and Interphases*. 2025;27(2): 316–322. <https://doi.org/10.17308/kcmf.2025.27/12808>

**Для цитирования:** Тютюник А. С., Гурченко В. С., Мазинов А. С. Влияние переизлучающего слоя органической тонкой плёнки на КПД кремниевых солнечных батарей. *Конденсированные среды и межфазные границы*. 2025;27(2): 316–322. <https://doi.org/10.17308/kcmf.2025.27/12808>

✉ Andrey S. Tyutyunik, [tyutyunikas@mail.ru](mailto:tyutyunikas@mail.ru)

© Tyutyunik A. S., Gurchenko V. S., Mazinov A. S., 2025



The content is available under Creative Commons Attribution 4.0 License.

## 1. Introduction

The problem of finding alternative energy sources is very relevant nowadays, attempts are being made to make wider use of solar and other types of energy. Research on organic solar cells has evolved over the last 40 years, but especially in the last decade it has attracted scientific and economic interest driven by the rapid increase in energy conversion efficiency. This has been achieved through the introduction of new materials, improved manufacturing techniques and more sophisticated device designs [1]. Scientists estimate that between 2004 and 2030, annual global energy consumption will increase by more than 50 %. A commensurate increase in CO<sub>2</sub> emissions is expected, most of which is due to the burning of coal, the world's fastest growing energy source. Despite the projected steady increase in oil and gas prices, less than 10 % of global energy production in 2030 is projected to come from renewable energy sources such as hydroelectric, solar, wind, hydrothermal and biomass. To reduce global dependence on exhaustible natural resources and their environmentally hazardous burning, more scientific effort must be directed towards reducing the cost of renewable energy production. Current annual solar energy use is well below 1% of total energy use, while fossil fuels account for over 90 % of energy use. Before solar energy can be utilized on a large scale, more efficient photovoltaic systems need to be developed at lower costs [2–8].

The high cost of solar radiation conversion largely restrains the development of this area. A possible way to make it cheaper is to attract new low-cost materials and technical devices based on them that increase the efficiency of sunlight conversion [9]. Such systems can include photovoltaic concentrators, which are designed to increase the electrical energy obtained from the solar panel [10]. High optical concentration without excessive heating in a stationary system can be achieved using luminescent solar concentrators (LSC) [11–13]. Luminescent solar concentrators consist of a dye dispersed in a transparent waveguide. The incident light is absorbed by the dye and then re-emitted. The energy difference between absorption and emission prevents the dye from re-absorbing

light. Thus, luminescent solar concentrators can achieve high optical concentrations without tracking sunlight [14]. Unfortunately, the efficiency of fluorescent solar concentrators is limited by self-absorption losses.

In recent years, luminescent materials capable of converting a wide spectrum of light into photons of a specific wavelength have been synthesized and used to minimize losses in the solar cell-based energy conversion process [15]. This technique, called third generation solar photon conversion, involves the introduction of a passive luminescent layer in photovoltaic cells [16–18]. An important aspect of using this technology is that the spectral converters are easily applicable to existing solar cells with minor modifications, since the spectral converters and solar cells can be optimized independently. To improve the efficiency of single junction solar cells, three luminescence processes including upconversion, quantum reduction, and downconversion are being investigated to develop efficient photovoltaic devices. Trivalent lanthanide ions are prime candidates for efficient spectral conversion because of their rich energy level structure (known as the Dicke diagram), which allows photons to be easily manipulated [19–21]. In order to increase the efficiency of the initial solar cells within the framework of the conducted research, binuclear complexes of copper with pyridyltriazole were used as luminescent materials, namely, copper complex C<sub>62</sub>H<sub>50</sub>Cu<sub>2</sub>I<sub>2</sub>N<sub>8</sub>P<sub>2</sub> was considered [22].

## 2. Materials, methods and main idea

The basic idea of increasing the efficiency of a solar cell (SC) is to apply to the surface of the SC a thin film material having such optical properties that the material will transmit the main spectrum of the incident electromagnetic radiation. At the same time this material due to luminescent properties will convert a part of the spectrum from the region of low efficient operation of the solar cell to the region of the spectrum of more efficient operation of the SE. The realization of this task is possible thanks to the achievements in the field of organic and inorganic chemistry, which make it possible to create materials with specified optical properties. In particular, it is proposed to apply to the surface of the solar cell



a material having absorption in the ultraviolet range region and re-emission in the visible range region.

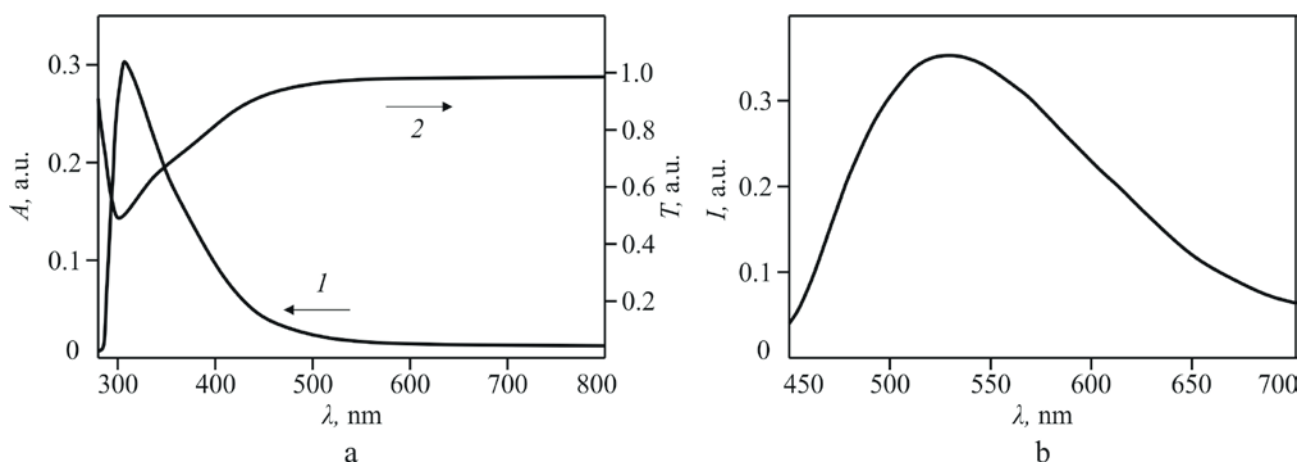
The objects of research were binuclear complexes of copper with pyridyltriazole, namely, the complex of  $\text{Cu C}_{62}\text{H}_{50}\text{Cu}_2\text{I}_2\text{N}_8\text{P}_2$  (b-phen). The methodology of synthesis of these materials is described in detail in [22]. Copper b-phen complexes are interesting materials due to their mechanochromic properties. When this material is mechanically pulverized, a shift of luminescence spectra from green to yellow area is observed. At the same time, this effect is reversible by mild annealing [22]. The second interesting property of this compound is the variation of the luminescence spectrum depending on the excitation wavelength. This phenomenon occurs in the excitation wavelength range of 385 to 435 nm with corresponding over-emission in the range of 508 to 595 nm. Note that the quantum yield of the compound  $\text{C}_{62}\text{H}_{50}\text{Cu}_2\text{I}_2\text{N}_8\text{P}_2$  is 28 % at room temperature and 55 %, at 77 K [22].

Absorption and transmission spectra were investigated using a GBC Cintra 4040 spectrophotometer. Tungsten and deuterium lamps were used as sources, which made it possible to realize the range of incident radiation from 250 to 800 nm with a slit width of 0.1–2 nm. Analyzing the absorption spectra of copper complexes, we note that the absorption maximum of these materials is in the range of 290–350 nm with a subsequent decline in the visible range (Fig. 1a). In turn, analyzing the transmission spectra, we emphasize the fact of almost complete

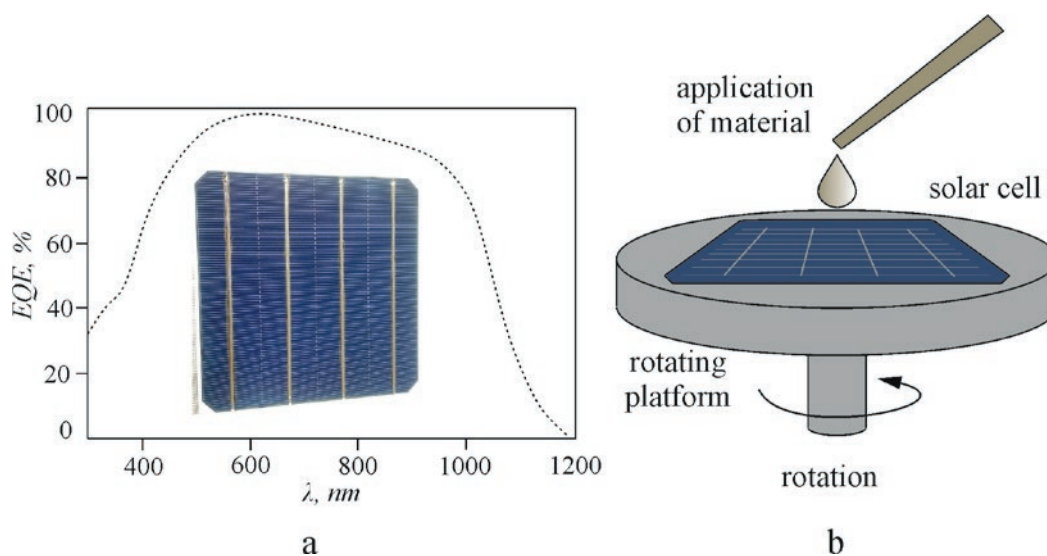
transmittance of electromagnetic radiation in the visible range and near-IR (Fig. 1a). Luminescence spectra were studied using a FluoroMax-4 instrument. In order to identify the optimal maximum of excitation radiation, a standard technique of pulse excitation, in which multiple irradiations of film structures are performed, was employed. Fig. 1b shows the luminescence spectrum of the copper b-phen complex at an excitation wavelength of 400 nm. Note that the luminescence maximum is observed at a wavelength of 530 nm (Fig. 1b).

The presented copper complexes fully meet the objective of increasing the efficiency of solar cells, but the thickness and homogeneity of the corresponding film is also an important factor. Therefore, the formation of b-phen thin films on the surface SE was carried out by centrifugation (Fig. 2b). Chloroform ( $\text{CHCl}_3$ ) was used to create a solution from the original solid-state, powdered copper complexes. The concentration of the starting substance in the solution was 1 mg/ml. The mass of powder materials was controlled by weighing on high-precision analytical scales HR-250AZ. In the process of material application, the rotational speed of PE-6900 centrifuge was brought to 1500–3000 rpm in steps of 500 rpm [23]. The volume applied per application cycle was 1 ml.

In this research, single-crystalline silicon solar cells created by diffusion technology with an efficiency of ~ 22 % were used (inset of Fig. 2a) [24]. Fig. 2a shows the quantum efficiency of the silicon solar cell. It is worth noting the decline



**Fig. 1.** Optical (a) absorption (1) and transmission (2) spectra and luminescence (b) of copper b-phen complexes



**Fig. 2.** Quantum efficiency of single crystal solar cell (a) scheme of deposition of copper b-phen complexes on solar cell by centrifugation (b)

in the conversion efficiency of the element in the UV range, which is due to such factors as the dissipation of part of the energy on phonons - transition to thermal energy, as well as recombination on the surface states of charge carriers [24].

An important factor in conducting measurements of the parameters of a pure solar cell and a luminescent-coated cell was strict adherence to the identity of the experimental conditions. The study of electrical parameters of solar cells was carried out using a Keysight B1500A semiconductor analyzer. Through volt-ampere characteristic analysis (VAC) and subsequent calculations, the main characteristics including efficiency and Fill factor (FF) were obtained. The measurements were carried out at a temperature of 20 °C. An LED matrix was used as an illumination source, the emission spectrum of which is in the range of 400–950 nm. The total incoming power was ~ 22 W/m<sup>2</sup>.

### 3. Results and discussion

The VAC was measured under two variations of the incident radiation, namely in the range from 400 to 950 nm and a power of 22 W/m<sup>2</sup>, as well as under incident radiation with a maximum wavelength of 400 nm and a power of 6 W/m<sup>2</sup>.

The choice of a separate narrow range of

incident radiation in the UV region is due to the excitation wavelength of the copper complexes.

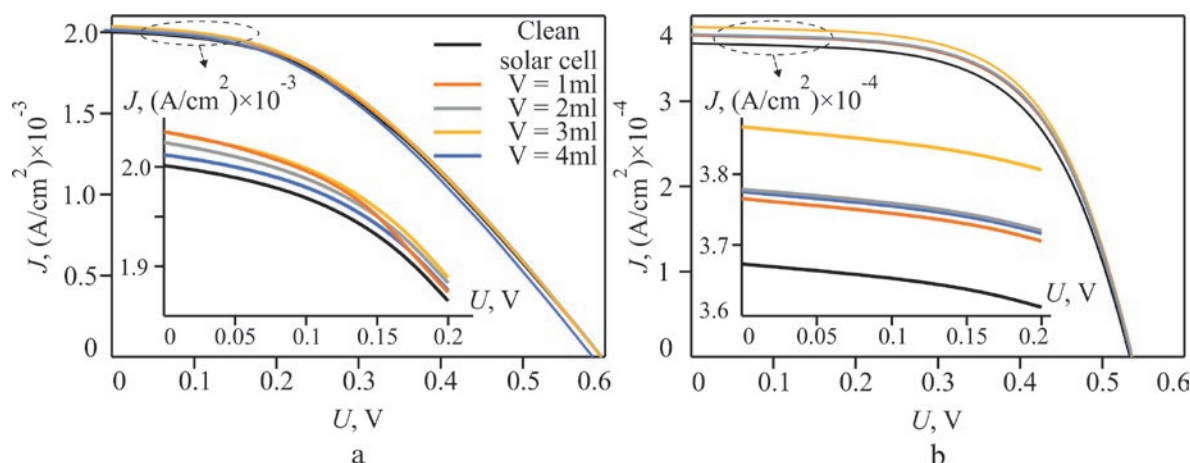
In Fig. 3 shows the VACs of both pure SE and with a surface layer of copper complex. In the course of the experiment, the thin film copper complex was applied layer by layer to the surface of the solar cell with the measurements of the VAC at each stage.

Analyzing the obtained results, we note that in the range of radiation 400-950 nm, the efficiency of pure single-crystalline solar cell was 21.74 %, whereas with the surface layer of copper complex, an increase in the efficiency of SE is observed (Fig. 3A). The maximum increase in the efficiency is seen when the volume of the deposited material  $V = 2$  ml, on the surface of the SE, the efficiency was 22.17 %.

For incident radiation with a maximum of 400 nm, the increase in efficiency of a solar cell with a surface over-emitting layer is more pronounced (Fig. 3b). The efficiency of the pure element in such a case was 19.76 %. In turn, when the volume of applied material  $V = 3$  ml, the efficiency was 21.21 %.

Photovoltaic conversion efficiency is defined as the ratio of the maximum electrical output power to the total incident power, and the solar cell fill factor is taken into account:

$$FF = \frac{P_{\max}}{U_{\text{oc}} I_{\text{sc}}}, \quad (1)$$



**Fig. 3.** Volt-ampere characteristics in the 400–950 nm range (a) and at  $\lambda = 400$  nm (b)

where  $FF$  – solar cell fill factor;  $P_{\max}$  – solar cell power;  $U_{OC}$  – solar cell no-load voltage;  $I_{SC}$  – solar cell short-circuit current.

The efficiency of a solar cell is in turn defined as:

$$\eta = \frac{P_{\max}}{ES}, \quad (2)$$

where  $E$  is the intensity of radiation falling on the solar cell;  $S$  is the surface area of the solar cell.

The measurement results as well as the calculated values of the solar cell parameters with and without the applied over-emitting coating are presented in Table 1 and 2 for the 400–950 nm range and the narrow range with a maximum at 400 nm, respectively.

#### 4. Conclusion

Thus the deposition of a thin film of copper complex  $C_{62}H_{50}Cu_2I_2N_8P_2$  on the surface of a

monocrystalline solar cell allowed to increase the efficiency of the solar cell by converting the energy from the ultraviolet range region to the visible range region. In particular, there is an increase in the short-circuit current of the SE and, as a consequence, an increase in efficiency.

The layer-by-layer application of the investigated material on the surface of the SE allowed determining the optimal ratio of the amount of applied material, while maximizing the efficiency. As a result, with incident radiation of 400–950 nm and volume of applied material in solution – 2 ml, we observe an efficiency gain of 0.43 %, an increase from 21.74 to 22.17 %. In turn, at incident radiation in the UV region with a maximum of 400 nm and the volume of applied material in solution – 3 ml, the efficiency gain is 1.45 %, an increase from 19.76 to 21.21 %. It is worth noting that further increase in the thickness of the surface layer of the copper complex leads to

**Table 1.** Solar cell parameters at incident wavelength of 400-950 nm

Parameter	Monocrystalline solar cell	1 layer of material	2 layer of material	3 layer of material	4 layer of material
$P_{\max}$ , mW	114.79	115.92	117.06	116.97	116.52
$U_{\max}$ , mV	325	325	325	325	325
$I_{\max}$ , mA	353.22	356.69	360.18	359.92	358.53
$U_{OC}$ , mV	595.25	595.22	595.80	595.37	595.14
$I_{SC}$ , mA	480.33	488.50	485.94	488.55	482.95
FF	0.401	0.398	0.404	0.402	0.405
$\eta$ , %	21.74	21.95	22.17	22.15	22.06
$E$ , mW/cm <sup>2</sup>	2.2	2.2	2.2	2.2	2.2
$S$ , cm <sup>2</sup>	240	240	240	240	240

**Table 2.** Solar cell parameters at an incident wavelength of 400 nm

Parameter	Monocrystalline solar cell	1 layer of material	2 layer of material	3 layer of material	4 layer of material
$P_{\max}$ , mW	28.47	29.66	29.90	30.56	29.80
$U_{\max}$ , mV	400	400	400	400	400
$I_{\max}$ , mA	71.17	74.17	74.77	76.41	74.51
$U_{oc}$ , mV	534.42	537.03	537.35	537.81	536.67
$I_{sc}$ , mA	88.15	90.36	90.69	92.80	90.60
FF	0.604	0.611	0.613	0.612	0.612
$\eta$ , %	19.77	20.6	20.76	21.22	20.69
$E$ , mW/cm <sup>2</sup>	0.6	0.6	0.6	0.6	0.6
$S$ , cm <sup>2</sup>	240	240	240	240	240

Where:  $\eta$  – efficiency of solar panel;  $P_{\max}$  – power of solar panel

parasitic absorption of this material in the visible range, which appreciably reduces the efficiency.

Traditional inorganic solar cell models based on Shockley's work have been widely used to understand the bulk heterojunction response of organic solar cells. While these models can be useful, there are key points that differ from traditional solar cell behavior. The competition of the two physical processes described above leads to the need for strict control of the application of the luminescent material on the surface of the SE while respecting the maximum efficiency of the latter. The presence of the luminescence peak of copper complexes at wavelengths of 530–550 nm opens obvious prospects for the application of the investigated material for GaAs photovoltaic cells, in which the conversion maximum occurs in this region. Among other things, the results in this paper are of significant interest in the space industry, where the share of the high-energy spectrum is much higher.

### Contribution of the authors

The authors contributed equally to this article.

### Conflict of interests

The authors declare that they have no known competing financial interests or personal relationships that could have influenced the work reported in this paper.

### References

- Hoppe H., Saricifti N. S. Organic solar cells: an overview. *Journal of Materials Research*. 2004;19(7): 1924–1945. <https://doi.org/10.1557/jmr.2004.0252>
- Roy S. S., Patra S. K. Synthesis and characterization of diferrocenyl conjugates: varying  $\pi$ -conjugated bridging ligands and its consequence on electrochemical communication. *European Journal of Inorganic Chemistry*. 2019;(16): 2193–2201. <https://doi.org/10.1002/ejic.201900114>
- Servaites J. D., Ratner M. A., Marks T. J. Organic solar cells: a new look at traditional models. *Energy & Environmental Science*. 2011;4(11): 4410–4422. <https://doi.org/10.1039/c1ee01663f>
- Yella A., Lee H.-W., Tsao H. N., Yi C., ... Gratzel M. Porphyrin-sensitized solar cells with cobalt (II/III)-based redox electrolyte exceed 12 percent efficiency. *Science*. 2011;334(6056): 629–634. <https://doi.org/10.1126/science.1209688>
- Kelzenberg M. D., Boettcher S. W., Petykiewicz J. A., ... Atwater H. A. Enhanced absorption and carrier collection in Si wire arrays for photovoltaic applications. *Nature Materials*. 2010;9(3): 239–244. <https://doi.org/10.1038/nmat2635>
- Huang K.-Y., Luo Y.-H., Cheng H.-M., Tang J., Huang J.-H. Performance enhancement of CdS/CdSe quantum dot-sensitized solar cells with (001)-oriented anatase TiO<sub>2</sub> nanosheets photoanode. *Nanoscale Research Letters*. 2019;14(1): 18. <https://doi.org/10.1186/s11671-018-2842-5>
- Peng K.-Q., Lee S.-T. Silicon nanowires for photovoltaic solar energy conversion. *Advanced Materials*. 2011;23(2): 198–215. <https://doi.org/10.1002/adma.201002410>
- Hochbaum A. I., Yang P. Semiconductor nanowires for energy conversion. *Chemical Reviews*. 2010;110(1): 527–546. <https://doi.org/10.1021/cr900075v>
- Wengeler L., Schmitt M., Peters K., Scharfer P., Schabel W. Comparison of large scale coating techniques for organic and hybrid films in polymer based solar cells. *Chemical Engineering and Processing: Process Intensification*. 2013;68: 38–44. <https://doi.org/10.1016/j.cep.2012.03.004>
- Currie M. J., Mapel J. K., Heidel T. D., Goffri S., Baldo M. A. High-efficiency organic solar concentrators for photovoltaics. *Science*. 2008;321(5886): 226–228. <https://doi.org/10.1126/science.1158342>
- Weber W. H., Lambe J. Luminescent greenhouse collector for solar radiation. *Applied Optics*. 1976;15(10): 2299–2300. <https://doi.org/10.1364/ao.15.002299>



12. Barnham K., Marques J. L., Hassard J., O'Brien P. Quantum-dot concentrator and thermodynamic model for the global redshift. *Applied Physics Letters*. 2000;76(9): 1197–1199. <https://doi.org/10.1063/1.125981>
13. Batchelder J. S., Zewail A. H., Cole T. Luminescent solar concentrators 2: experimental and theoretical analysis of their possible efficiencies. *Applied Optics*. 1981;20(21): 3733–3754. <https://doi.org/10.1364/ao.20.003733>
14. Smestad G., Ries H., Winston R., Yablonovitch E. The thermodynamic limits of light concentrators. *Solar Energy Materials*. 1990;21(2–3): 99–111. [https://doi.org/10.1016/0165-1633\(90\)90047-5](https://doi.org/10.1016/0165-1633(90)90047-5)
15. Huang X., Han S., Huang W., Liu X. Enhancing solar cell efficiency: the search for luminescent materials as spectral converters. *Chemical Society Reviews*. 2013;42(1): 173–201. <https://doi.org/10.1039/c2cs35288e>
16. Strümpel C., McCann M., Beaucarne G., ... Tobias I. Modifying the solar spectrum to enhance silicon solar cell efficiency – an overview of available materials. *Solar Energy Materials and Solar Cells*. 2007;91(4): 238–249. <https://doi.org/10.1016/j.solmat.2006.09.003>
17. Richards B. S. Luminescent layers for enhanced silicon solar cell performance: Down-conversion. *Solar Energy Materials and Solar Cells*. 2006;90(9): 1189–1207. <https://doi.org/10.1016/j.solmat.2005.07.001>
18. Shalav A., Richards B. S., Green M. A. Luminescent layers for enhanced silicon solar cell performance: up-conversion. *Solar Energy Materials and Solar Cells*. 2007;91(9): 829–842. <https://doi.org/10.1016/j.solmat.2007.02.007>
19. Eliseeva S. V., Bünzli J.-C. G. Lanthanide luminescence for functional materials and bio-sciences. *Chemical Society Reviews*. 2010;39(1): 189–227. <https://doi.org/10.1039/b905604c>
20. Huang C.-S., Jakubowski K., Ulrich S., ... Boesel L. F. Nano-domains assisted energy transfer in amphiphilic polymer conetworks for wearable luminescent solar concentrators. *Nano Energy*. 2020;76: 105039. <https://doi.org/10.1016/j.nanoen.2020.105039>
21. Van der Ende B. M., Aarts L., Meijerink A. Lanthanide ions as spectral converters for solar cells. *Physical Chemistry Chemical Physics*. 2009;11(47): 11081. <https://doi.org/10.1039/b913877c>
22. Gusev A., Kiskin M., Braga E., ... Linert W. Structure and emission properties of dinuclear copper(I) complexes with pyridyltriazole. *RSC Advances*. 2023;13(6): 3899–3909. <https://doi.org/10.1039/d2ra06986e>
23. Tyutyunik A. S., Gurchenko V. S., Mazinov A. S. Study of the electrochemical and electrical properties of Zn(II) pyrazolone-based azomethine complexes and their temperature dependences. *Inorganic Materials: Applied Research*. 2022;13(5): 1216–1222. <https://doi.org/10.1134/S2075113322050434>
24. Ejdelman B. L., Ejdelman K. B., Gudkov D. V., Polisan A. A. *Semiconductor photovoltaic converter*. Patent RF, no. 2750366. Publ. 28.06.2021, bull. no. 19.

\* Translated by author of the article

### Information about the authors

Andrey S. Tyutyunik, Cand. Sci. (Phys.–Math.), Research Fellow at the Department of Radiophysics and Electronics, Physical and Technical Institute, V. I. Vernadsky Crimean Federal University (Simferopol, Russian Federation).

<https://orcid.org/0000-0001-9017-9996>  
tyutyunikas@mail.ru

Vladimir S. Gurchenko, Research Fellow at the Department of Radiophysics and Electronics, Physical and Technical Institute, V. I. Vernadsky Crimean Federal University (Simferopol, Russian Federation).

<https://orcid.org/0000-0002-8270-3820>  
gurchenko\_v@mail.ru

Alim S. Mazinov, Dr. Sci. (Phys.–Math.), Assistant Professor, Head of the Department of Radiophysics and Electronics, Physical and technical institute, V. I. Vernadsky Crimean Federal University (Simferopol, Russian Federation).

<https://orcid.org/0000-0001-8015-8841>  
mazinovas@cfuv.ru

Received 10.07.2024; approved after reviewing 04.09.2024; accepted for publication 16.09.2024; published online 25.06.2025.



## Short communication

Short communication

<https://doi.org/10.17308/kcmf.2025.27/12878>

## Complexation processes in aqueous solutions of lead acetate and thiourea

V. N. Semyonov<sup>1</sup>, V. V. Volkov<sup>2</sup>, T. V. Samofalova<sup>1</sup>✉

<sup>1</sup>Voronezh State University,  
1 Universitetskaya pl., Voronezh 394018, Russian Federation

<sup>2</sup>Voronezh State Technical University,  
20-letiya Oktyabrya str., 84, Voronezh 394006, Russian Federation

### Abstract

**Purpose:** The aim of the article is to study the processes of complexation in aqueous solutions containing lead acetate and thiourea and to establish the optimal concentration regions for the existence of thiocarbamide coordination compounds.

**Modeling:** The study of ionic equilibria was carried out by means of theoretical calculation taking into account the stability constants of various complex forms. Slices of concentration dependences of fractions of coordination compounds on initial concentrations of lead ions and thiourea, as well as predominance diagrams and distribution diagrams in three-dimensional space were constructed using the COMSOL Multiphysics application package by the Newton-Raphson method.

**Conclusions:** concentration ranges of existence of coordination compounds formed in aqueous solutions of lead acetate and thiourea at varying concentrations of components have been determined. It was revealed that at low concentrations of lead salt in solution the homogeneously liganded thiourea complexes dominate. With increasing thiocarbamide concentration, the total fraction of homogeneously liganded and dissimilarly liganded thiourea coordination compounds increases.

**Keywords:** Thiourea coordination compounds, Complexation, Distribution diagrams, Predominance diagram, Lead sulfide films, Aerosol pyrolysis method

**For citation:** Semyonov V. N., Volkov V. V., Samofalova T. V. Complexation processes in aqueous solutions of lead acetate and thiourea. *Condensed Matter and Interphases*. 2025;27(2): 323–328. <https://doi.org/10.17308/kcmf.2025.27/12878>

**Для цитирования:** Семенов В. Н., Волков В. В., Самофалова Т. В. Процессы комплексообразования в водных растворах ацетата свинца и тиомочевина. *Конденсированные среды и межфазные границы*. 2025;27(2): 323–328. <https://doi.org/10.17308/kcmf.2025.27/12878>

✉ Tatyana V. Samofalova, e-mail: [TSamofalova@bk.ru](mailto:TSamofalova@bk.ru)

© Semyonov V. N., Volkov V. V., Samofalova T. V., 2025



The content is available under Creative Commons Attribution 4.0 License.

## 1. Introduction

Thiourea coordination compounds of lead are in demand in practical terms due to the possibility of their application as precursors in the preparation of lead sulfide films. Semiconductor films of narrow-gap PbS with a forbidden bandgap width of  $E_g = 0.41$  eV [1] are used in the fabrication of various photovoltaic and optoelectronic devices: photovoltaic converters, photodetectors, various sensors, IR detectors in the infrared region of the spectrum, and other devices [2–6].

Among a large number of methods for deposition of lead sulfide films with controlled crystalline structure and properties, chemical deposition from solutions and aerosol pyrolysis can be distinguished [7–11]. The method of aerosol pyrolysis of solutions of thiourea coordination compounds (TCC) allows the formation of a solid phase of metal sulfide in the process of thermal destruction of complex compounds on a heated substrate [12, 13]. The composition and structure of the initial coordination compound determines the type of crystal structure, optical, photoelectric and electrophysical properties of the deposited sulfide layers.

The processes of formation of coordination compounds in aqueous solutions of various lead and thiourea salts were previously studied and the domination regions of different TCC of lead were determined [10, 12, 14–16]. The spatial structure of the thiourea-acetate complex  $\text{Pb}((\text{NH}_2)_2\text{CS})_2(\text{mono-CH}_3\text{COO})_2$  was determined by quantum-chemical modeling in [17].

The aim of this work was to study the processes of complexation in aqueous solutions of lead acetate and thiourea and to establish the optimal concentration regions of thiocarbamide coordination compounds, which are precursors in the preparation of pyrolytic films of lead sulfide.

## 2. Modeling

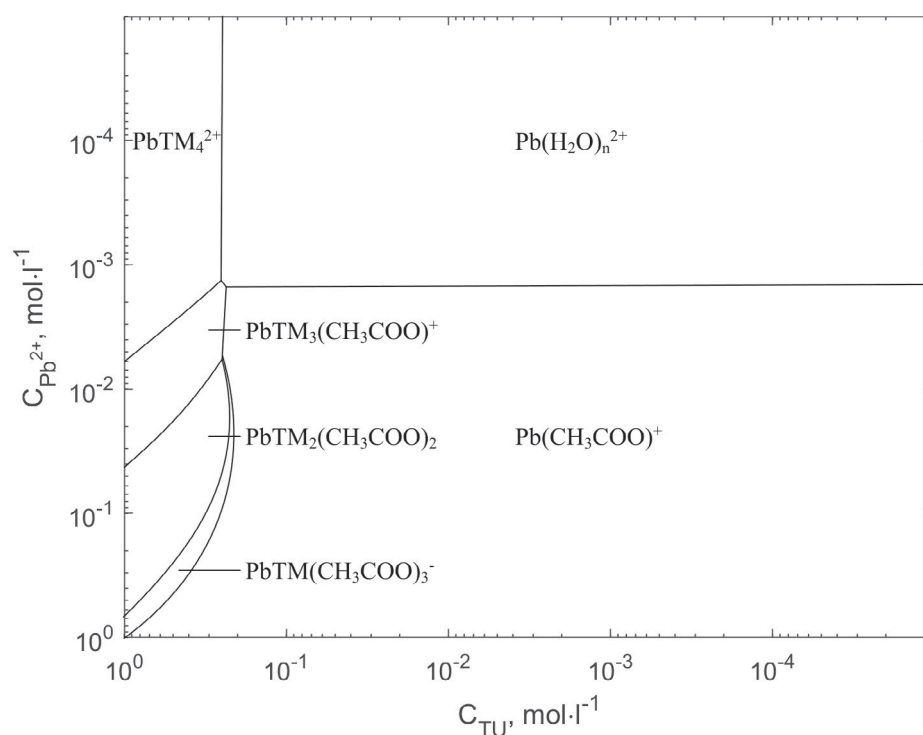
When studying the processes of complexation, we considered ionic equilibria in an aqueous solution of lead salt and thiourea (TM), calculated the fractions ( $\alpha$ ) of all complex forms present in it, constructed three-dimensional distribution diagrams and predominance diagram according to the method described in [10, 14, 16]. Based on the dependence of the molar fractions of complex compounds on the analytical concentration of

lead salt and thiocarbamide, the domination areas of specific complex forms were identified and the points (lines) where the fractions of the predominant coordination compounds in aqueous solution are equal were fixed.

From the presented diagram of the predominance of coordination compounds in the system “ $\text{Pb}(\text{CH}_3\text{COO})_2 - (\text{NH}_2)_2\text{CS}$ ” it can be seen that in low-concentration solutions ( $C_{\text{Pb}^{2+}} = 10^{-5} - 2 \cdot 10^{-3}$  mol/L and  $C_{\text{TM}} = 10^{-5} - 2 \cdot 10^{-1}$  mol/L) a wide region of existence of aquacomplexes of  $\text{Pb}(\text{H}_2\text{O})_n^{2+}$  is observed (Fig.). When increasing the concentration of lead acetate up to 1 mol/L in the same concentration range of thiourea, there is an increase in the proportion of complex ions  $\text{Pb}(\text{CH}_3\text{COO})^+$ . Thus, the specified range of concentrations of components of the initial solution “ $\text{Pb}(\text{CH}_3\text{COO})_2 - (\text{NH}_2)_2\text{CS}$ ” is not suitable for obtaining PbS films.

In the deposition of metal sulfide films, the formation of coordination compounds whose inner sphere includes thiourea is of greatest interest. Among thiourea coordination compounds in the aqueous solution of “ $\text{Pb}(\text{CH}_3\text{COO})_2 - (\text{NH}_2)_2\text{CS}$ ” the complex ions  $\text{PbTM}_4^{2+}$ ,  $\text{PbTM}_5(\text{CH}_3\text{COO})^+$ ,  $\text{PbTM}_2(\text{CH}_3\text{COO})_2$  are dominant. The maximum fractions of these complexes in solution have values of 0.87, 0.34, 0.33, 0.32, respectively. The distribution diagram in three-dimensional space and cross sections of lines of equal fractions for some complexes are given in [16, 18]. The fraction of lead hydroxocomplexes in the considered system does not exceed 0.03 %, their concentration sharply increases with increasing pH.

The studies have shown that of the other existing complex compounds in aqueous solution of lead acetate and thiourea,  $\text{PbTM}(\text{CH}_3\text{COO})_3^-$  ( $\alpha = 0.2$ ),  $\text{PbTM}_2^{2+}$  ( $\alpha = 0.14$ ),  $\text{PbTM}(\text{CH}_3\text{COO})^+$  ( $\alpha = 0.06$ ),  $\text{PbTM}(\text{CH}_3\text{COO})_2$  ( $\alpha = 0.06$ ) are relatively stable [16]. The maximum fraction of homogeneously liganded TCCs increases in the series  $\text{PbTM}_3^{2+} < \text{PbTM}_2^{2+} < \text{PbTM}^{2+} < \text{PbTM}_4^{2+}$ , and for the differently liganded complexes:  $\text{PbTM}_2(\text{CH}_3\text{COO})^+ < \text{PbTM}(\text{CH}_3\text{COO})_2 \approx \text{PbTM}(\text{CH}_3\text{COO})^+ < \text{PbTM}(\text{CH}_3\text{COO})_3^- < \text{PbTM}_2(\text{CH}_3\text{COO})_2 < \text{PbTM}_3(\text{CH}_3\text{COO})^+$ . It should be noted that of all the thiourea complex forms formed in aqueous solution of lead chloride and thiourea, the  $\text{PbTM}_4^{2+}$  ( $\alpha = 1$ ) is also predominant [14].



**Fig.** Diagram of the dominance of complex compounds in an aqueous solution of lead acetate and thiourea

The distribution diagrams were used to obtain data on the quantitative distribution of thiourea coordination compounds contained in the initial solution at a constant concentration of lead acetate and varying concentration of thiocarbamide. Thus, at the lead salt concentration of 0.1 mol/L, thiourea complexes with acetate ion in the inner sphere exist in solution, and their total fraction has values from 0.384 to 0.825 (Table). The total content of acetate TCCs increases with increasing thiourea concentration. At  $C_{\text{Pb}^{2+}} = 0.01$  mol/L, the initial solution contains all homogeneously

liganded thiourea complexes  $\text{Pb}(\text{TM})_m^{2+}$  as well as heterogeneously liganded  $\text{PbTM}_n(\text{CH}_3\text{COO})_m^{2-m}$ . With increasing thiourea content in the initial solution, the total fraction of all TCCs increases.

Analyzing the obtained results, it can be noted that the most probable precursors in the process of deposition of PbS films using different concentrations of lead salt can be complex forms of  $\text{PbTM}_4^{2+}$ ,  $\text{PbTM}^{2+}$ ,  $\text{PbTM}(\text{CH}_3\text{COO})_3^-$ ,  $\text{PbTM}_2(\text{CH}_3\text{COO})_2$ ,  $\text{PbTM}_3(\text{CH}_3\text{COO})^+$ . Varying the concentration of thiourea and lead acetate allows the formation of a complex of the desired

**Table.** Content of thiocarbamide coordination compounds at different concentrations of thiourea in solution ( $C_{\text{Pb}^{2+}} = 0.1$  mol/l)

Proportion of complexes	Concentration of thiourea, mol/l				
	0.2	0.4	0.6	0.8	1
$\text{PbTM}(\text{CH}_3\text{COO})^+$	0.040	0.041	0.034	0.019	0.009
$\text{PbTM}(\text{CH}_3\text{COO})_2$	0.048	0.048	0.047	0.038	0.026
$\text{PbTM}(\text{CH}_3\text{COO})_3^-$	0.145	0.183	0.190	0.198	0.180
$\text{PbTM}_2(\text{CH}_3\text{COO})^+$	0.014	0.018	0.018	0.017	0.015
$\text{PbTM}_3(\text{CH}_3\text{COO})^+$	0.035	0.082	0.198	0.215	0.278
$\text{PbTM}_2(\text{CH}_3\text{COO})_2$	0.102	0.193	0.238	0.310	0.317
Total proportion of thiourea complexes	0.384	0.565	0.725	0.797	0.825



composition in the initial solution for the synthesis of PbS films with controlled properties depending on the practical purpose of the formed layers [19]. Thus, at the stage of coordination compound formation in aqueous solution, “metal-sulfur” bonds are formed, which are fragments of the metal sulfide structure released during thermal decomposition of TCC on a heated substrate.

Thermolysis of homogeneously liganded thiocarbamide complexes  $\text{PbTM}^{2+}$ ,  $\text{PbTM}_2^{2+}$ ,  $\text{PbTM}_3^{2+}$ ,  $\text{PbTM}_4^{2+}$  leads to the deposition of more stoichiometric in composition PbS films with higher sulfur content. To obtain such samples it is necessary to use low concentrations of lead salt from  $10^{-5}$  to  $\sim 5 \cdot 10^{-2}$  mol/L, and thiourea from  $4 \cdot 10^{-2}$  to  $8 \cdot 10^{-1}$  mol/L.

In the concentration ranges of  $C_{\text{Pb}^{2+}} = 10^{-3} - 6.5 \cdot 10^{-1}$  mol/L and  $C_{\text{TM}} = 9 \cdot 10^{-2} - 1$ , acetate TCCs are formed in which the lead atom is linked by covalent bonds with the sulfur atom of the thiocarbamide molecule and the oxygen atom of the acetate ion. Thus, according to quantum-chemical calculations of the structure of the coordination compound  $\text{PbTM}_2(\text{CH}_3\text{COO})_2$ , the nearest environment of the metal atom is a strongly distorted tetrahedron of the composition  $\text{PbS}_2\text{O}_2$  [16]. During the thermal degradation of acetate complexes, oxygen enters the formed sulfide, replacing sulfur in the anionic sublattice ( $\text{O}_s$ ), which can affect its photovoltaic and electrophysical properties.

It was previously found [20] that oxygen impurities and oxide phases affect the mechanism of current transfer and photoconductivity in films of various sulfides. In the presence of oxygen in the samples, the potential barriers controlling the current transfer increase in the intergranular interlayers, and as a result, the electrical conductivity may decrease. The electrical conductivity and photosensitivity of PbS films are enhanced by annealing in air, during which oxygen adsorption on the sample surface, changes in its defect structure, and ordering of the crystalline structure of the sulfide [12, 19]. PbS films synthesized by aerosol pyrolysis of TCC solutions have a cubic structure regardless of the type of the initial thiourea complex [10, 17, 18].

Previous IR spectroscopic studies of TCC formed in a solution of lead acetate (0.1 mol/L)

and thiourea [15] showed that at three-, four-, and fivefold excess of  $(\text{NH}_2)_2\text{CS}$ , the coordination compound  $\text{PbTM}_2(\text{CH}_3\text{COO})_2$  predominates in the solution, while an excess of thiourea molecules remains in an unbound state. Also, with increasing concentration of  $(\text{NH}_2)_2\text{CS}$  in solution, the formation of PbS films with more developed surface topography and less dense packing of grains occurs [18]. Thus, to obtain high-quality lead sulfide layers, it is desirable not to exceed a fivefold excess of thiocarbamide in the initial solution.

The concentration of  $(\text{NH}_2)_2\text{CS}$  in the stock solution also affects the photoelectric and electrophysical properties of the sulfide films. According to [21], with increasing thiourea concentration in the initial solution, the resistivity and differential TEDS of the deposited PbS layers decrease, while the specific conductivity increases. It was also revealed in [22] that the use of different concentration ratios of lead acetate and thiourea allows to vary not only the resistivity of PbS films, but also their structural and morphological characteristics. According to the authors [23] an increase in the synthesis temperature leads to a decrease in the resistivity of pyrolytic lead sulfide layers.

### 3. Conclusion

On the basis of predominance diagrams and three-dimensional distribution diagrams, the domination regions of various coordination compounds formed in aqueous solutions of lead acetate and thiourea have been determined. It is established that the concentration range of  $C_{\text{Pb}^{2+}} = 10^{-5} - 1$  mol/L and  $C_{\text{TM}} = 10^{-5} - 2 \cdot 10^{-1}$  mol/L is not suitable for the preparation of lead sulfide films, since aqua- and acido complexes of  $\text{Pb}(\text{H}_2\text{O})_n^{2+}$  and  $\text{Pb}(\text{CH}_3\text{COO})^+$  predominate in it. It is shown that of all thiourea coordination compounds existing in solution, the complex forms dominate:  $\text{PbTM}_4^{2+}$ ,  $\text{PbTM}_2^{2+}$ ,  $\text{PbTM}_3(\text{CH}_3\text{COO})^+$ ,  $\text{PbTM}_2(\text{CH}_3\text{COO})_2$ . The maximum proportion of homogeneously liganded complexes increases in the series  $\text{PbTM}_5^{2+} < \text{PbTM}_2^{2+} < \text{PbTM}_3^{2+} < \text{PbTM}_4^{2+}$ , and for the dissimilarly liganded TCCs:  $\text{PbTM}_2(\text{CH}_3\text{COO})^+ < \text{PbTM}(\text{CH}_3\text{COO})_2 \approx \text{PbTM}(\text{CH}_3\text{COO})^+ < \text{PbTM}(\text{CH}_3\text{COO})_3^- < \text{PbTM}_3(\text{CH}_3\text{COO})^+ < \text{PbTM}_2(\text{CH}_3\text{COO})_2$ . When the concentration of thiourea in the stock solution

increases, the total fraction of thiourea complex compounds increases.

### Contribution of the authors

The authors contributed equally to this article.

### Conflict of interests

The authors declare that they have no known competing financial interests or personal relationships that could have influenced the work reported in this paper.

### References

1. *Fizicheskie velichiny. Spravochnik*\*. I. S. Grigor'eva, E. Z. Mejlihova (eds.). Moskva: Jenergoatomizdat Publ.; 1991. 1232 s. (in Russ.)
2. Varlashov I. B., Mitasov P. V., Miroshnikova I. N., Miroshnikov B. N., Mohammed H. S. H. Examination of phoyosensitive structures based on PbD by auger electron spectroscopy. *Vestnik Moskovskogo Energeticheskogo Instituta*. 2015;2: 103–107. (In Russ., abstract in Eng.). Available at: [https://www.elibrary.ru/download/elibrary\\_23378338\\_69530465.pdf](https://www.elibrary.ru/download/elibrary_23378338_69530465.pdf)
3. Akhmedov O. R., Guseinaliyev M. G., Abdullaev N. A., Abdullaev N. M., Babaev S. S., Kasumov N. A. Optical properties of PbS thin films. *Semiconductors*. 2016;50(1): 50–53. <https://doi.org/10.1134/S1063782616010036>
4. Abrakov D. D., Sulimov M. A., Rajkov D. V., Markov V. F., Ogorodnikov I. N. Experimental studies of photo-electric characteristics of photoresistors on the basis of lead sulfide. *Technosphere Safety*. 2015;4(9): 66–72. (In Russ., abstract in Eng.). Available at: <https://www.elibrary.ru/item.asp?id=25317094>
5. Uhuegbu C. C. Growth and characterization of lead sulphide thin film for solar cell fabrication. *Canadian Journal on Scientific and Industrial Research*. 2011;2(6): 230–241. Available at: [https://www.researchgate.net/publication/310147417\\_Growth\\_and\\_Characterization\\_of\\_Lead\\_Sulphide\\_Thin\\_Film\\_for\\_Solar\\_Cell\\_Fabrication](https://www.researchgate.net/publication/310147417_Growth_and_Characterization_of_Lead_Sulphide_Thin_Film_for_Solar_Cell_Fabrication)
6. Kouissa S., Djemel A., Aida M. S., Djouadi M. A. PbS infrared detectors: experiment and simulation. *Sensors & Transducers Journal*. 2015;193(10): 106–113. Available at: [https://www.sensorsportal.com/HTML/DIGEST/october\\_2015/Vol\\_193/P\\_2743.pdf](https://www.sensorsportal.com/HTML/DIGEST/october_2015/Vol_193/P_2743.pdf)
7. Markov V. F., Maskaeva L. N., Ivanov P. N. *Hydrochemical deposition of metal sulfide films: modeling and experiment*\*. Ekaterinburg: UrO RAN Publ.; 2006. 217 p. (in Russ.)
8. Maskaeva L. N., Mostovshchikova E. V., Markov V. F., ... Mikhailova A. I. Cobalt-doped chemically deposited lead-sulfide. *Semiconductors*. 2022;56: 91–100. <https://doi.org/10.1134/S1063782622010122>
9. Faraj M. G., Pakhuruddin M. Z. Deposited lead sulfide thin films on different substrates with chemical spray pyrolysis technique. *International Journal of Thin Film Science and Technology*. 2015;4(3): 215–217. <https://doi.org/10.12785/ijtfst/040310>
10. Semenov V. N., Ovechkina N. M., Krysin M. Yu., Volkov V. V., Samofalova T. V. Deposition of PbS films by pyrolysis of atomized solutions of lead Thiourea complexes. *Russian Journal of Applied Chemistry*. 2022;95: 264–269. <https://doi.org/10.1134/S1070427222020057>
11. Abdulnabi R. K. Using spray pyrolysis technique to prepare PbS lead sulfide thin films and study their structural and electrical properties as function of thickness. *International Journal of Soft Computing and Engineering*. 2016;6(4): 60–63. Available at: <https://www.ijscce.org/wp-content/uploads/papers/v6i4/D2902096416.pdf>
12. Semenov V. N. *The processes of formation of thin layers of semiconductor sulfides from thiourea complex compounds*\*. Doc. chem. sci. diss. Abstr. Voronezh. 2002. 355 p. (In Russ.)
13. Krunk M., Mellikov E. Metal sulfide thin films by chemical spray pyrolysis. *Proceedings of SPIE*. 2001; 4415: 60–65. <https://doi.org/10.1117/12.425472>
14. Semenov V. N., Volkov V. V., Pereslyckikh N. V. Complexation processes in «PbCl<sub>2</sub> – N<sub>2</sub>H<sub>4</sub>CS» aqueous solutions during deposition of lead sulphide films. *Condensed Matter and Interphases*. 2021;23(4): 543–547. <https://doi.org/10.17308/kcmf.2021.23/3673>
15. Semenov V. N., Karnushina V. A., Ovechkina N. M. Synthesis of lead thiourea acetate coordination compounds. *Proceedings of Voronezh State University. Series: Chemistry. Biology. Pharmacy*. 2016;(1): 25–29. (In Russ., abstract in Eng.). Available at: <https://www.elibrary.ru/item.asp?id=25910296&ysclid=lnjik6njw6427245614>
16. Semenov V. N., Nechaeva L. S., Ovechkina N. M., Volkov V. V. Formation of coordination compounds in the system «Pb(CH<sub>3</sub>COO)<sub>2</sub> – N<sub>2</sub>H<sub>4</sub>CS». *Bulletin of the Bashkir University*. 2014;19(3): 817–822. (In Russ., abstract in Eng.). Available at: <https://www.elibrary.ru/item.asp?id=22483478>
17. Semenov V. N., Naumov A. V., Nechaeva L. S., Malygina E. N. Lead thiocarbamide diacetate as a precursor for the precipitation of lead sulfide films. *Glass Physics and Chemistry*. 2020; 46(1): 78–83. <https://doi.org/10.1134/S1087659620010150>
18. Gannova E. A., Grechkina M. V., Semenov V. N., Lukin A. N., Ivkov S. A., Samofalova T. V. Deposition of lead sulfide films from «Pb(CH<sub>3</sub>COO)<sub>2</sub> – N<sub>2</sub>H<sub>4</sub>CS» aqueous solutions and their properties. *Condensed Matter and Interphases*. 2024;26(2): 238–246. <https://doi.org/10.17308/kcmf.2024.26/12070>
19. Samofalova T. V., Semenov V. N. Films based on a solid solution of CdS–ZnS system from thiourea coordination compounds and their properties. *Russian Journal of Applied Chemistry*. 2013;86(12): 1811–1818. <https://doi.org/10.1134/s1070427213120021>
20. Aleshin A. N., Burlak A. V., Mandel' V. E., Pasternak V. A., Tjurin A. V., Cukerman V. G. Photosensitive lead sulfide layers produced by spraying. *Inorganic Materials*. 1999;35(4): 322–324. Available at: <https://elibrary.ru/item.asp?id=13318157>
21. Karnushina V. A., Semenov V. N., Lukin A. N., Ovechkina N. M., Nikitin L. N. Properties of lead sulfide films deposited from a coordination compound [Pb(N<sub>2</sub>H<sub>4</sub>CS)<sub>2</sub>(CH<sub>3</sub>COO)<sub>2</sub>]. *Condensed Matter and Interphases*. 2017;19(2): 215–221. (In Russ., abstract in Eng.). Available at: <https://www.elibrary.ru/item.asp?id=29332700>
22. Veena E., Kasturi V. Bangera, Shivakumar G. K. Influence of lead precursor concentration on properties of spray deposited lead sulphide thin films. *International Journal of Pure and Applied Physics*. 2016;12(2): 97–112.

23. Rajashree C., Balu A. R., Nagarethinam V. S. Substrate temperature effect on the physical properties of spray deposited lead sulfide thin films suitable for solar control coatings. *International Journal of ChemTech Research*. 2014;6(1): 347-360.

\* Translated by author of the article

### Information about the authors

Victor N. Semenov, Dr. Sci. (Chem.), Professor, Chair of Department of General and Inorganic Chemistry, Voronezh State University (Voronezh, Russian Federation).

<https://orcid.org/0000-0002-4247-5667>  
office@chem.vsu.ru

Vitaly V. Volkov, Cand. Sci. (Phys.- Math.), Associate Professor of the Department of Structural Mechanics, Voronezh State Technical University (Voronezh, Russian Federation).

<https://orcid.org/0000-0003-1114-984X>  
kotlac@yandex.ru

Tatyana V. Samofalova, Cand. Sci. (Chem.), Associate Professor of the Department of General and Inorganic Chemistry, Voronezh State University (Voronezh, Russian Federation).

<https://orcid.org/0000-0002-4277-4536>  
TSamofalova@bk.ru

Received 04.10.2024; approved after reviewing 25.10.2024; accepted for publication 15.11.2024; published online 25.06.2025.



# Condensed Matter and Interphases

Kondensirovannye Sredy i Mezhfaznye Granitsy  
<https://journals.vsu.ru/kcmf/>

## Chronicle

<https://doi.org/10.17308/kcmf.2025.27/12934>

### Pavel Pavlovich FEDOROV (April 16, 1950 – March 31, 2025)

Professor DSc Pavel Pavlovich Fedorov, 74, passed away suddenly on March 31, 2025. He was an outstanding materials scientist, chemical engineer, and inventor of several new optical materials.

In addition to chemistry and physics, Pavel Pavlovich was actively interested in geology, anthropology, philosophy and history. In addition, he authored poetry under the pseudonym of Fedorov-Schastlivtsev.

Pavel Pavlovich inherited his interest in physical and chemical analysis and phase equilibria from his father, Prof. Pavel Il'ich Fedorov, to whom he dedicated his book "My Father: Documented Story".

The breadth of Pavels' scientific interests is partially reflected in his monographs, Fedorov P. P. Archaic Thinking: Yesterday, Today, Tomorrow (3-rd edition, essentially revised and supplemented), Moscow, Lenand, 2017, and Fedorov P. P. Where is the Boundary between Science and Pseudoscience? Quantitative Criterion and Features of Pseudoscience, Moscow, Lenand, 2019.

Pavel P. Fedorov graduated from M. V. Lomonosov Moscow Institute of Fine Chemical Technology with an MS degree in chemical engineering in 1972, while majoring in chemical technology of rare and trace elements. Upon graduation, Prof. Fedorov dedicated his entire professional life to scientific research and teaching activities.

Pavel Pavlovich successfully defended his PhD thesis titled "Study of the phase diagrams of



$\text{CaF}_2\text{-(Y,Ln)F}_3$  systems and polymorphism of rare earth trifluorides" (1977) and his DSc thesis titled "High-temperature chemistry of the condensed state of systems with rare earth trifluorides as a basis for obtaining new materials" (1991). In 2000, he attained the rank of full professor of crystallography and crystal physics.

After graduation, Pavel P. Fedorov worked at A. V. Shubnikov Institute of Crystallography of the Russian Academy of Sciences from 1972 to 2003, where he advanced in his career, starting as a laboratory assistant, eventually becoming a leading research fellow. From 2003, Prof. Fedorov was affiliated with the Scientific Center for Laser Materials and Technology at A. M. Prokhorov General Physics Institute of the Russian Academy



The content is available under Creative Commons Attribution 4.0 License.



of Sciences, where he served as the leading research fellow, group leader, and laboratory head of the laboratory for nanomaterials technology for photonics, head of the nanotechnology department, and chief research fellow.

Over the span of his extensive career Pavel Pavlovich published more than 1,000 research papers (including 33 reviews), and 5 textbooks, and authored an additional 31 patents.

In addition to his extensive publications, Prof. Fedorov was a prolific mentor, serving as a scientific advisor for more than 30 MS theses, 9 PhD theses, and a scientific consultant for 3 DSc theses.

Prof. Fedorov contributed to various areas of materials sciences, where he obtained unique results informing such fields as:

1. Features of heterovalent isomorphism in crystals and glasses.
2. Thermodynamic theory of morphotropy and bifurcation theory for phase diagrams of the binary systems, where he predicted and experimentally detected the saddle points on the melting surfaces of the ternary solid solutions.
3. More than 200 different phase diagrams of binary and ternary systems.
4. Generalization of the Tiller criterion for morphological stability of a flat crystallization front.

5. Technology for the synthesis of fluoride laser ceramic materials.

Pavel P. Fedorov focused his research papers specifically at application of the methods of physical and chemical analysis as well as studies of phase equilibria of various substances. In order to enhance such studies, he conducted “Physical and Chemical Analysis and Thermodynamics of Heterogeneous Equilibria” seminars at M. V. Lomonosov Institute of Fine Chemical Technology and taught the corresponding classes to undergraduate students. Later, under Prof. Fedorov’s guidance, the “Physical and at Chemical Processes in Condensed Matter and Interphases” conference (Voronezh, Russia) included a special section titled “Development of Methods of Physical and Chemical Analysis for Substances and Materials”.

The most important results, obtained by Prof. Fedorov in the aforementioned areas prior to 2020, were published in two monographs: Fedorov P. P. Etudes in physical and chemical analysis (collection of papers), Moscow, Science, 2019 (191 pp.) and Fedorov P. P. Etudes in crystal chemistry and crystal growth (collection of papers), Moscow, Science, 2020 (241 pp.)

Pavel Pavlovich was well-recognized within the scientific community, receiving numerous decorations and honorable citations for his scientific publications. This included the special



Prof. Pavel P. Fedorov delivers his presentation at VIII All-Russian Conference with International Participation “PHYSICO-CHEMICAL PROCESSES IN CONDENSED MEDIA AND AT INTERPHASE BOUNDARIES – FAGRAN-2018”, dedicated to 100-th anniversary of Voronezh State University, October, 2018.



Voronezh, September, 2024.

prize of the USSR Academy of Sciences and Czechoslovakia Academy of Sciences (1989), Guo Moruo Medal of the Chinese Academy of Sciences (1988), Paul Hagenmuller Medal (Bordeaux, France, 2018), 300-th Anniversary of the Russian Academy of Sciences Medal (2024), “100 best Russian Inventions” special citations of Federal Service for Intellectual Property Special Citations (2012 and 2013), Elsevier Outstanding Reviewer Citations (2012 and 2013), special citation for significant contribution in development of science and industry in the City of Moscow (2018).

Pavel Pavlovich also made significant contributions in the editorial activity of “Nanosystems: Physics, Chemistry, Mathematics”, “Inorganic Materials”, and “Condensed Matter and Interphases” scientific periodicals.

Pavel Pavlovich’s passing is an irreplaceable loss for “Condensed Matter and Interphases” journal. He was an active member of editorial board and unflinching reviewer. He was also a famous scientist, publishing his papers in

top international periodicals, so his insight and experience were priceless. The high scientific quality of his papers, published in our journal, enhanced the standing of our journal in international bibliographic databases and undoubtedly had a positive effect on the citation of our publications. Thus, P. P. Fedorov and E. G. Yarotskaya review paper “Zirconium Dioxide. Review” (Condensed Matter and Interphases, 2021, volume 23, issue 2, pp. 169-187; DOI: 10.17308/kcmf.2021.23/3427) still remains the most highly cited article published in our journal.

The most important issue is that Prof. Pavel P. Fedorov was a great friend and a valued colleague, and he will remain in such a capacity in the hearts of his staff at Voronezh State University, Department of Chemistry.

Everyone, who personally knew Pavel Pavlovich, will remember him as a very talented scientist, skilled advisor, patient mentor and great human being.

A. A. Alexandrov, O. K. Alimov, A. E. Baranchikov, S. Ch. Batygov, T.B. Bekker, M. A. Borik, I. I. Buchinskaya, V. M. Buznik, E. V. Chernova, M. E. Doroshenko, A. V. Egorysheva, Yu. A. Ermakova, S. A. Filatova, E. A. Garibin, S. V. Garnov, K. S. Gavrichev, T. Yu. Glazunova, V. V. Glushkov, V. K. Ivanov, N. A. Ivanovskaya, V. A. Kamynin, D. G. Kochiev, A. E. Kokh, K. A. Kokh, N. G. Kononova, V. A. Konyushkin, S. L. Korableva, A. V. Kulebyakin, S. V. Kuznetsov, V. A. Logacheva, E. E. Lomonova, A. A. Luginina, V. L. Manomenova, V. A. Myzina, A. N. Nakladov, K. N. Nischev, A. S. Nizamutdinov, A. G. Papashvili, A. I. Popov, P. A. Popov, V. Yu. Proydakova, M. S. Pudovkin, A. A. Pynenkov, E. B. Rudneva, V. V. Semashko, V. N. Semenov, R. L. Simoneaux, N. I. Sorokin, V. A. Stasyuk, N. Yu. Tabachkova, V. B. Tsvetkov, S. N. Ushakov, M. A. Uslamina, A. A. Volchek, A. E. Voloshin, V. V. Voronov, D. S. Yasyrkina, A. I. Zagumennyi, R. M. Zakalukin, A. S. Zakharova, A. Y. Zavrzhnov, E. V. Zharikov



# ВЕКТОН-ЦЕНТР

ВСЕ НЕОБХОДИМОЕ ДЛЯ ВАШЕЙ ЛАБОРАТОРИИ

- ✓ лабораторное оборудование
- ✓ лабораторная мебель
- ✓ химические реактивы
- ✓ лабораторная посуда



## Вектон-Центр исполнит любой каприз для вашей лаборатории

Общество с ограниченной ответственностью «Вектон-Центр» было основано в 2007 году как представительство крупнейшей компании ЗАО «ВЕКТОН», г. Санкт-Петербург, которая уже более 20 лет занимается производством химических реактивов.

Первоначально основным направлением работы компании была поставка химических реактивов, посуды и расходных материалов для лабораторий. Сейчас мы занимаемся комплексным оснащением лабораторий практически во всех отраслях Российской промышленности, образования и науки. Мы готовы предоставить широкий ассортимент лабораторной мебели и оборудования различного назначения для применения в пищевой, тяжелой и легкой промышленности, а так же в нефтегазовой отрасли.

Современные потребности лабораторий предъявляют высокие требования к качеству используемого оборудования, химических реактивов и расходных материалов. Компания «Вектон-Центр» готова предложить лучшую продукцию для осуществления поставленных задач. Мы предъявляем высокие требования не только к поставляемой продукции, но и к работающему персоналу.

Сотрудники компании могут оказать профессиональную консультацию при подборе лабораторного оборудования, лабораторной мебели, химреактивов, посуды и расходных материалов для лабораторий.

## 6 причин для сотрудничества с нами



**С нами надежно и спокойно**  
мы не исчезнем завтра с рынка - с 2007 года стабильно растем и развиваемся



**С нами удобно**  
это действительно удобно, когда можно купить все необходимое в одном месте



**Разные варианты оплаты**  
предоплата по договору в размере 100%, 50/50, 30/70 или отсрочка



**С нами выгодно**  
предлагаем оптимальные цены, работаем по прайсам производителей



**Любые варианты доставки**  
самовывоз, транспортная компания или с помощью наших машин



**Система скидок и поощрений** для наших постоянных клиентов

Для вас и за вас решим даже самые сложные задачи по комплексному оснащению лабораторий, созданию лабораторий под ключ, подбору оптимального оборудования под ваши цели с учетом технических требований.

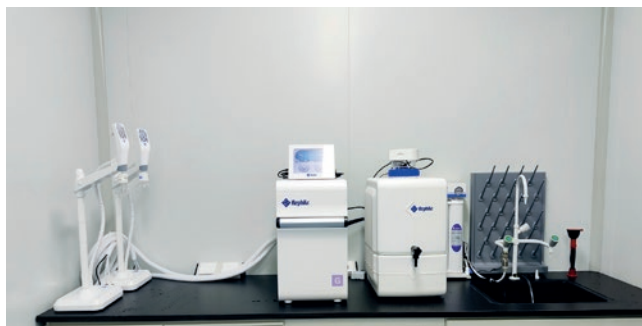
---



**Простые и сложные химические соединения, наборы**



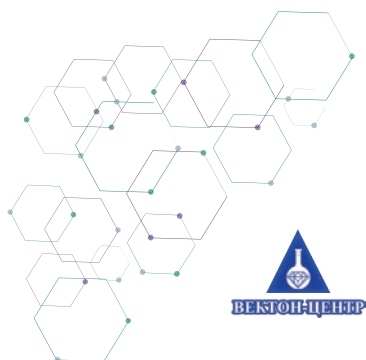
**Лабораторный пластик, стекло, принадлежности**



**Общелабораторное и аналитическое оборудование**



**Лабораторная мебель различных конфигураций и цветов**



**Если вы согласны с тем, что время - деньги, приходите к нам за решением своих задач по оснащению лаборатории!**

**Задать вопросы или оставить заявку вы можете любым удобным способом:**

по телефонам +7 (473) 260-20-54, +7 (473) 232-40-49  
или по электронной почте [vektionvm@list.ru](mailto:vektionvm@list.ru)

Подробную информацию о нас вы найдете на сайте [www.vektionvm.ru](http://www.vektionvm.ru)  
Адрес офиса: г. Воронеж, 394026, проспект Труда, 48/5, 2 этаж





комплексное оснащение и  
снабжение лабораторий

- оборудование
- мебель
- посуда
- расходные материалы

Компания “ПроЛаб-Трейд” с 2013 года помогает решать различные задачи по оснащению химических лабораторий на производствах, в образовательных учреждениях и науке. Найти оптимальное решение, сочетающее в себе приемлемую цену без потери качества, - главная цель нашей работы.



Больше 10 лет мы занимаемся как комплексным оснащением новых лабораторий, так и дооснащением существующих. Огромный опыт и знания, накопленные за все время работы, позволяют нам четко выполнять обязательства и экономить ваш бюджет.

Многолетнее партнерство с ведущими Российскими и зарубежными производителями дает возможность нашим заказчикам получать необходимое лабораторное оборудование, мебель, посуду и расходные материалы по ценам производителей, а также гарантирует качество поставляемых товаров, подтвержденное соответствующей документацией.

## Заказать в одном месте все, что нужно для вашей лаборатории, - это удобно!



грамотный подбор  
оборудования  
от специалистов с  
опытом работы  
10+ лет



доставка в любой  
регион России



собственное производство  
лабораторного  
оборудования и посуды  
OmnisLab



официальные дилеры и  
представители  
производителей (ЛОИП, Simple  
PRO, Смоленское СКТБ СПУ,  
BIOSAN, Mettler Toledo, Unico,  
Минимед и др.)



постоянный  
участник  
Госзакупок



ПроЛаб-Трейд



## ПОДБЕРЕМ ДЛЯ ВАС



### Лабораторное оборудование

- весовое оборудование
- термостаты
- сушильные шкафы
- муфельные печи
- шейкеры
- мешалки магнитные
- оборудование для хроматографии
- анализаторы влажности
- спектрометры и спектрофотометры
- ламинарные боксы
- стерилизаторы и многое другое



### Лабораторная мебель

- вытяжные шкафы
- столы специализированные
- столы-мойки
- столы на опорных тумбах
- стеллажи к столам
- тумбы хранения
- шкафы хранения
- зонты вытяжные
- технологические стойки к лабораторным столам
- вспомогательное оборудование и многое другое



### Лабораторная посуда из стекла и пластика

- колбы конические, круглодонные, мерные и др.
- воронки лабораторные
- воронки делительные
- стаканы высокие и низкие
- банки из светлого и темного стекла с винтовыми и притертыми крышками
- пипетки
- чашки Петри и многое другое

**Поделитесь с нами своей задачей по оснащению лаборатории и мы обязательно поможем вам сэкономить время, деньги и нервы!**

Открыты для общения с Пн по Пт с 9.00 до 18.00 по мск времени.

#### Наш офис в Москве

г. Москва, ул. Кольская, д. 1

+7 (495) 210-34-35

info@plt-lab.ru



**ПроЛаб-Трейд**

www.plt-lab.ru

#### Наш офис в Краснодаре

г.Краснодар, ул. Уральская, д.126Б

+7 (861) 248-88-01

prolabtrejd.3@list.ru